**Caltech Ph.D. Thesis**

# Oxygen Isotope Studies of the Petrogenesis of Hawaiian Lavas and a Theoretical Study on Equilibrium Thermodynamics of Multiply-substituted Isotopologues

Zhengrong Wang

Thesis Advisor: John Eiler

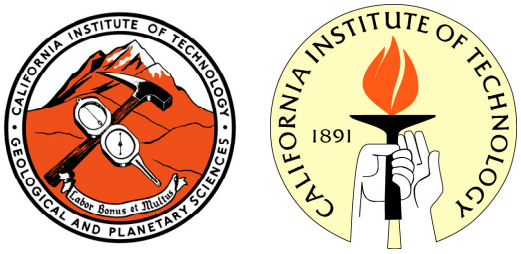


Division of Geological and Planetary Sciences

California Institute of Technology

Pasadena

2005

# OXYGEN ISOTOPE STUDIES OF THE PETROGENESIS OF HAWAIIAN LAVAS
# AND
# A THEORETICAL STUDY ON EQUILIBRIUM THERMODYNAMICS OF MULTIPLY-SUBSTITUTED ISOTOPOLOGUES

Thesis by

**Zhengrong Wang**

In Partial Fulfillment of the Requirements

for the Degree of

Doctor of Philosophy

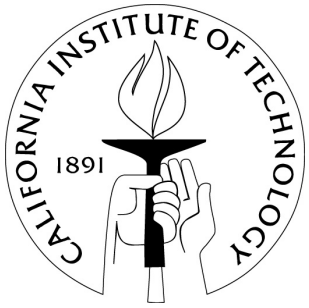


California Institute of Technology

Pasadena, California

2005

(Defended April 5, 2005)

© 2005

Zhengrong Wang

All Rights Reserved

*To My wife, Xiaolan Wu,*

*and my parents, Shusong & Faxiang Wang*

# ACKNOWLEDGEMENTS

Here, I want to bow my thanks to many people who have made a strong impact on my studies and six years of life at Caltech. First of all, I am grateful to my thesis advisor, Prof. John Eiler, whose encouragement, patience, mentoring and confidence in me have made a big difference during this biggest transition of my life from a student to a scientist. I want to thank Prof. Paul Asimow, whose talent and enthusiasm greatly inspired me throughout my graduate studies at Caltech. I also want to thank Prof. Hugh Taylor, who has made a bridge between now and the "old days", and enlightened me on the theoretical basics and fundamentals of stable isotope geochemistry.

I also want to thank the following Professors for facilitating my studies at Caltech and illuminating for me the mystery world of science: Professors. Jess Adkins, Michael Brown, Donald Burnett, Kenneth Farley, George Rossman, Edward Stolper, Jason Saleeby, Alex Sessions, Joann Stock, Paul Wennberg, Brian Wernicke, Yuk Yung, Peter Goldreich, Leon Silver, Peter Wyllie, Yuk Yung, Gerald Wasserburg, Rudy Marcus, and Mitchio Okumura. A lot of learning also took place in the Petrology Reading Group and the Stable Isotope Reading Group and I am indebted to them.

I sincerely appreciate the help and friendship of Mike Baker, Chi Ma, Chris Baumgartner, Jed Mosenfelder, Sally Newmann, Greg Holk, Mike Spicuzza, Edwin Schauble, Elisabeth Johnson, Paula Smith, Ronit Kessel, Sujoy & Sarah Mukhopadhyay, Ilya Bindeman, Hagit Afek, Lingsen Zeng, Jing Liu, Julie O'Leary, Prosenjit Ghosh, Laura Robinson, David Shuster, Paula Smith, Arnold Gail, Kanani Lee, Xianglei Huang, Chao Li, Weifu Guo, Sidao Ni, Desheng Wang, Wei-Chen Chen, Yi-Qin Gao, Qiang

Yang, Jiantao Wang, Huirong Ai, Lun Li, Zhenyu Li, Laura Baker, Selene Eltgroth, Sara Miller, Elisabeth Nadin, Chen ji, Cheng Jin, Liang Zhao, Lisa Welp, Kaiwen Xia, Huiyu Li, Zhonghua Yang, Huirong Ai, Eh Tan, Zhimei Yan, Ying Tan, The-Ru Song, Qinya Liu, Hao-Te Hsu, Xinling Wang, Xin Liu, Hualin Ye and Yindi Jing. They have made my life at Caltech more colorful and wonderful.

This thesis greatly benefited from my collaboration with Amy J. Jurewicz, Mike Fitzsimmons, Zhongyuan Ren, Prof. Mike Garcia, Eiichi Takahashi, and comments from Alexander Sobolev, Fred Frey, Shichun Huang and K. Muehlenbachs.

I would like to thank Wafa Abouchami, Albrecht W. Hofmann, Z. Fekiacova, Vincent Salters, and Mark Kurz for sharing with us unpublished data. This thesis is part of a group effort to study Hawaiian lavas. I appreciate all participants in HSDP-II and KSDP for their great work, and the database team of GEOROC website for making my work easier.

Finally, I would like to express my sincere thanks to my wife, Xiaolan Wu, and my parents, Shusong & Faxiang Wang, who constantly supported me emotionally and spiritually, and kept me in a good mood even when the filament of the Mass-Spectrometer burned out; when some mystery leak was hidden in the vacuum line; when capillaries or glass tubes were broken for no good reason; and when frustrations were about to take over. They are my pleasure and happiness incarnate.

# ABSTRACT

Temporal oxygen isotope variations have been discovered in both Mauna Kea and Koolau volcanoes after detailed studies of the Hawaiian Scientific Drilling Project (HSDP-phase II) and Koolau Scientific Drilling Project (KSDP). In both volcanoes, oxygen isotope compositions of olivine phenocrysts all converge to 'Mauna Loa-like' values from depleted or enriched composition, respectively and yet, the interpretations are totally different. In the studies of HSDP core, many lines of geochemical evidences strongly indicate that low-$\delta^{18}O$ values characteristic of Kea trend Hawaiian lavas are the product of contamination by hydrothermally altered rocks in the volcanic edifice. In the studies of KSDP core and submarine Koolau landslides, a full diversity of $\delta^{18}O$ values correlate with trace element and radiogenic isotope compositions of host lavas. These correlations are interpreted as reflecting mixing between partial melts of high-$\delta^{18}O$ and normal-$\delta^{18}O$ components. A magma mixing model has been constructed to simultaneously explain the oxygen isotope, major element, trace element and radiogenic isotope variations defined by these correlations. This model indicates that the Koolau shield-building lavas are mixtures of 75~100% melt of mantle peridotite with 0~25% eclogite melt, the protolith of which is Mid-Ocean Ridge Basalt (MORB) with Depleted Mantle Model (DMM) age of at least 1.8±0.3 billions years. $\delta^{18}O$ value of this eclogite component is predicted to be 11.3±1.5‰, implying it is an upper crustal (layer 1 or 2) basalt or gabbro with a low-temperature alteration history; contains a small amount of sediment; and has experienced partial melting before forming eclogite.

I also derived a method for systematically evaluating clumped-isotope effects in the abundances of all isotopologues in thermodynamically equilibrated populations of $O_2$, CO, $N_2$, NO, $CO_2$ and $N_2O$ between 1000 and 193 to 77 K. This method uses Urey-type algorithms to evaluate partition functions and equilibrium constants of isotope exchange reactions, and simultaneously solves for abundance of each isotopologue of a given molecule constrained by all independent equilibria. Calculation results show that, in most cases, multiply-substituted isotopologues of these mono-molecular gases are predicted to be enriched relative to stochastic (random) distributions by ca. 1 to 2 per mil at earth-surface temperatures.

# Table of Contents

# List of illustrations

# INTRODUCTION

My thesis research includes two intellectually separate parts: 1) oxygen isotope studies of the petrogenesis of Hawaiian lavas; and 2) a theoretical study on equilibrium thermodynamics of multiply-substituted isotopologues.

## PART 1. OXYGEN ISOTOPE STUDIES OF THE PETROGENESIS OF HAWAIIAN LAVAS

Oxygen isotope compositions of many crustal rocks differ significantly from mantle peridotites due to water-rock interaction and weathering (dissolution-precipitation) at near-earth surface temperatures. Therefore, oxygen isotopes can be used to identify crustal components that contribute to the petrogenesis of mantle-derived magmas, either as ancient subducted source components or as contaminants added during passage through crustal magma conduits (TAYLOR and SHEPPARD, 1986; EILER, 2001).

It has long been recognized that Hawaii lavas are characterized by $\delta^{18}O$ values significantly lower than Mid-Ocean-Ridge-Basalts (e.g., KYSER, 1986; MUEHLENBACHS, 1986; TAYLOR, 1986; TAYLOR and SHEPPARD, 1986; EILER, 2001). This property was attributed to a variety of possible causes, including $^{18}O$-depletion of the lower mantle presumed to feed the Hawaiian plume (HARMON and HOEFS, 1995) or a source component of $^{18}O$-depleted recycled lower oceanic crust (HAURI, 1996; LASSITER and HAURI, 1998), although the scattered nature of observed oxygen isotope variations precluded a detailed formulation or tests of these ideas. Prior to the start of my thesis research, EILER et al., (1996a, 1996b) showed that $\delta^{18}O$ values of olivines in Hawaiian subaerial shield building tholeiites vary systematically among the various volcanoes and correlate with trace element and radiogenic isotope compositions. In particular, olivines in lavas from most Loa trend volcanoes (Loihi, Mauna Loa, Hualalai, W. Molokai, and

Kauai) are similar to olivines in oxygen isotope exchange equilibrium with MORBs (ca. 5.1±0.1‰), or in the case of Koolau and Lanai (home to the most 'enriched' radiogenic isotope signatures in Hawaiian lavas), are higher in $\delta^{18}O$ values than MORBs. In contrast, olivines in most lavas from Kea trend volcanoes (Kilauea, Mauna Kea, Kohala, and Haleakala) are $^{18}O$-depleted compared to MORBs. EILER et al. (1996b) suggested that $^{18}O$-enriched lavas from Koolau and Lanai sampled a recycled upper crustal source component, and this interpretation was adopted in more or less modified form by subsequent studies (e.g., DUCEA et al., 2002). In contrast, the cause of $^{18}O$-depleted compositions was debated. EILER et al., 1996b) suggested they reflected contamination by the Pacific plate; LASSITER and HAURI (1998) suggested they reflected the presence of an $^{18}O$-depleted source component in the Hawaiian plume (e.g., recycled lower section of oceanic crust), and GARCIA et al. (1998) suggested that at least a sub-set of them (recent lavas from Pu`u O`o) sampled an $^{18}O$-depleted component from the volcanic edifice.

The major portion of my thesis research focused on testing alternative hypotheses for the origin of oxygen isotope variations in Hawaiian lavas by conducting detailed studies of the temporal evolution of oxygen isotope compositions of Mauna Kea and Koolau volcanoes -- the low-$\delta^{18}O$ and high-$\delta^{18}O$ extremes -- and by developing and applying a laser-based micro-analytical tool for measuring intra-crystalline oxygen isotope variations in individual phenocrysts.

My first important finding was that olivine phenocrysts from the submarine section of Mauna Kea volcano have $\delta^{18}O$ values similar to those in common mantle peridotites and in equilibrium with MORBs (5.01 ± 0.07‰, in Chapter 1); i.e., Mauna Kea lavas from below the submarine/subaerial transition lack the $^{18}O$-depletion thought to be

characteristic of Kea trend volcanoes based on studies of subaerial lavas. Significantly, no similar break in radiogenic isotope composition is observed, suggesting the variation in oxygen isotope composition is not related to a secular change in the plume source. Second, I found that microphenocrysts of olivines from both subaerial and submarine volcanoes are systematically lower in $\delta^{18}O$ values than macrophenocryst olivines in the same and related lavas, and that microphenocrysts are in oxygen isotope exchange equilibrium with co-existing glass, whereas macrophenocrysts are not. Together, this suggests time-evolution of the $\delta^{18}O$ values of Mauna Kea lavas between early precipitation of coarse, magnesian phenocrysts and late precipitation of fine, Fe-rich microphenocrysts. Finally, *in situ* measurements of $\delta^{18}O$ studies on individual olivine phenocrysts from subaerial Mauna Loa lavas reveal that the $\delta^{18}O$ values of their parental melts decreased monotonically over the course of their crystallization differentiation, from initial values that were indistinguishable from normal MORBs (in Chapter 3). Taken together, these findings strongly indicate that low-$\delta^{18}O$ values characteristic of Kea trend Hawaiian lavas are the product of contamination by hydrothermally altered rocks in the volcanic edifice. This result effectively disproves the previous hypothesis that the Hawaiian plume contains a recycled low-$\delta^{18}O$ component, and makes it highly unlikely that subaerial Hawaiian lavas sample large proportions of deep Pacific lithosphere. Moreover, it provides a detailed view of the past volcanological processes in the Hawaiian volcanic edifice.

Detailed studies of lavas with high $\delta^{18}O$ values at Koolau volcano yielded a very different result (in Chapter 4). Basaltic lavas from the KSDP core (collected 381-511 mbsl) contain olivines with $\delta^{18}O$ values (5.39±0.1‰) higher than typical upper mantle

peridotites and Mauna Loa lavas (5.17±0.11‰). Younger basalts (collected at 304-359 mbsl) have olivines with even higher $\delta^{18}O$ values (5.56±0.05‰), similar to olivines from plagioclase-spinel peridotite xenoliths collected on Oahu (5.51±0.05) and approaching exceptionally high values previously reported for subaerial (Makapu`u) Koolau lavas (5.89±0.12). Olivines from dredged samples (including subaerial landslides and submarine Koolau volcano) show a wide range of $\delta^{18}O$ values (5.2~6.0‰). Unlike the Mauna Kea series, this full diversity of $\delta^{18}O$ values, across all three sample suites (drill core; subaerial lavas; submarine land slides) correlate with trace element and radiogenic isotope compositions of host lavas, defining a compositional continuum from a high-$\delta^{18}O$, extremely enriched end member toward a more normal $\delta^{18}O$, 'Mauna Loa-like' composition. I interpret this trend as reflecting mixing between partial melts of high-$\delta^{18}O$ components and normal-$\delta^{18}O$ components of the Hawaiian plume, and have constructed a model to simultaneously explain the oxygen isotope, major element, trace element and radiogenic isotope variations defined by this trend. This model indicates that the Koolau shield building lavas are mixtures of 75-100% melt of mantle peridotite with 0-25% eclogite melt, the protolith of which is Mid-Ocean Ridge Basalt (MORB) with Depleted Mantle Model (DMM) age of at least 1.8 ± 0.3 billion years. $\delta^{18}O$ values of this eclogite component can be predicted to be 11.3 ± 1.5‰, implying it is an upper crustal (layer 1 or 2) basalt or gabbro with a low-temperature alteration history; contains a small amount of sediment; and has experienced partial melting before forming eclogite.

Finally, much of my work on the petrogenesis of Hawaiian lavas made use of a 157 nm UV laser fluorination system that I developed over the course of my thesis research (in Chapter 2). This system is capable of *in situ* oxygen isotope analyses of minerals and

glasses with spatial resolution on the order of 100~200 μm and precision on the order of ±0.1 to 0.2 ‰ (1σ).

## PART 2. THEORETICAL STUDY ON EQUILIBRIUM THERMODYNAMICS AND KINETICS OF MULTIPLY-SUBSTITUTED ISOTOPOLOGUES

In the last chapter, I studied the theory of clumped isotope effects on the abundances of multiply-substituted isotopologues. Heavy stable isotopes are not randomly distributed among molecules in thermodynamically equilibrated mono-molecular gases (e.g., $O_2$, $N_2$, or $CO_2$), but instead, preferentially concentrate into bonds with each other (e.g., $^{18}O$-$^{18}O$, $^{15}N$-$^{15}N$, etc.). This occurs because such bonds have exceptionally low zero-point energies and thus are comparatively more stable. This zero point energy effect is subtle (typically at per-mil level), but has recently been shown to be measurable (EILER and SCHAUBLE, 2004). The abundances of isotopologues of molecular gases containing more than one rare isotope ("multiply-substituted isotopologues") could be used for a variety of geochemical applications including geothermometry, and such applications will require a sound understanding of these zero-point energy effects. I derived a method for systematically evaluating their influence in the abundances of all isotopologues in thermodynamically equilibrated populations of $O_2$, CO, $N_2$, NO, $CO_2$ and $N_2O$ between 1000 and 193 to 77 K. This method uses Urey-type algorithms (based on simple harmonic oscillator and rigid rotor model, UREY, 1947) to evaluate partition functions and equilibrium constants of isotope exchange reactions, and simultaneously solves for abundance of each isotopologue of a given molecule constrained by all independent equilibria. I also examined the accuracy of the Urey-type models by comparison with

direct summations over all experimentally or empirically determined energy levels to calculate partition functions. This comparison is only made for CO and $CO_2$ due to limitations in spectroscopic data, but in these cases, there are no significant differences among methods. Calculation results also show that, in most cases, multiply-substituted isotopologues are predicted to be enriched relative to stochastic (random) distributions by ca. 1 to 2 per mil at earth-surface temperatures. This deviation, defined as $\Delta_i$ for isotopologue i, generally increases linearly with 1/T at temperatures < 500 K, and with $1/T^2$ at temperatures > 500 K. An exception is $N_2O$, which shows complex temperature dependences and 10's of per-mil enrichments or depletions of abundances for some isotopologues. These theoretical calculations provide a basis for discriminating between fractionations controlled by equilibrium thermodynamics and other sorts of isotopic fractionations in the budgets of atmospheric gases. Moreover, because abundances of multiply-substituted isotopologues in thermodynamically equilibrated populations of molecules vary systematically with temperature, they can be used as geothermometers. Such thermometers are unusual in that they involve homogeneous rather than heterogeneous equilibria (e.g., isotopic distribution in gaseous $CO_2$ alone, rather than differences in isotopic composition between $CO_2$ and coexisting water). Also, multiple, independent thermometers exist for all molecules having more than one multiply-substituted isotopologue (e.g., thermometers based on abundances of $^{18}O^{13}C^{16}O$ and $^{18}O^{12}C^{18}O$ are independent); thus, temperatures estimated by this method can be tested for internal consistency.

## REFERENCES

Ducea M., Sen G., Eiler J., and Fimbres J. (2002) Melt depletion and subsequent metasomatism in the shallow mantle beneath Koolau volcano, Oahu (Hawaii). *Geochemistry Geophysics Geosystems* **3**.

Eiler J. M. (2001) Oxygen isotope variations of basaltic lavas and upper mantle rocks. In *Stable Isotope Geochemistry*, Vol. 43, pp. 319-364. Mineralogical Society of America.

Eiler J. M., Farley K. A., Valley J. W., Hofmann A. W., and Stolper E. M. (1996b) Oxygen isotope constraints on the sources of Hawaiian volcanism. *Earth and Planetary Science Letters* **144**(3-4), 453-467.

Eiler J. M. and Schauble E. (2004) $^{18}O^{13}C^{16}O$ in Earth's atmosphere. *Geochimica et Cosmochimica Acta* **68**(23), 4767-4777.

Eiler J. M., Valley J. W., and Stolper E. M. (1996a) Oxygen isotope ratios in olivine from the Hawaii Scientific Drilling Project. *Journal of Geophysical Research-Solid Earth* **101**(B5), 11807-11813.

Garcia M. O., Ito E., Eiler J. M., and Pietruszka A. J. (1998) Crustal contamination of Kilauea Volcano magmas revealed by oxygen isotope analyses of glass and olivine from Pu'u O'o eruption lavas. *Journal of Petrology* **39**(5), 803-817.

Harmon R. S. and Hoefs J. (1995) Oxygen-isotope heterogeneity of the mantle deduced from global $^{18}O$ systematics of basalts from different geotectonic settings. *Contributions to Mineralogy and Petrology* **120**(1), 95-114.

Hauri E. H. (1996) Major-element variability in the Hawaiian mantle plume. *Nature* **382**(6590), 415-419.

Kyser T. K. (1986) Stable isotope variations in the mantle. *Reviews in Mineralogy* **16**, 141-164.

Lassiter J. C. and Hauri E. H. (1998) Osmium-isotope variations in Hawaiian lavas: evidence for recycled oceanic lithosphere in the Hawaiian plume. *Earth and Planetary Science Letters* **164**(3-4), 483-496.

Muehlenbachs K. (1986) Alteration of the oceanic-crust and the $^{18}O$ History of Seawater. *Reviews in Mineralogy* **16**, 425-444.

Taylor H. P. (1986) Igneous rocks 2: isotopic case-studies of circum-pacific magmatism. *Reviews in Mineralogy* **16**, 273-317.

Taylor H. P. and Sheppard S. M. F. (1986) Igneous rocks 1: processes of isotopic fractionation and isotope systematics. *Reviews in Mineralogy* **16**, 227-271.

Urey H. C. (1947) The thermodynamic properties of isotopic substances. *J. Chem. Soc. (London)*, 561-581.

# PART 1. OXYGEN ISOTOPE STUDIES OF THE PETROGENESIS OF HAWAIIN LAVAS

# CHAPTER 1

# OXYGEN ISOTOPE GEOCHEMISTRY OF THE SECOND HSDP CORE

Zhengrong Wang, Nami E. Kitchen, and John M. Eiler

Division of Geological and Planetary Sciences, California Institute of Technology, Pasadena, California, USA

(*Published in Geochemistry Geophysics Geosystems* **4**, art. no.-8712., 2003)

**ABSTRACT**

Oxygen isotope ratios were measured in olivine phenocrysts (~ 1 mm diameter), olivine microphenocrysts (generally ~ 100 to 200 μm diameter), glass, and/or matrix from 89 samples collected from depths down to 3079.7 m in the second, and main, HSDP core (HSDP-2). Olivine phenocrysts of 11 samples from Mauna Loa and 34 samples from the submarine section of Mauna Kea volcano have $\delta^{18}O$ values that are similar to one another (5.11 ± 0.10‰, 1σ, for Mauna Loa; 5.01 ± 0.07‰, for submarine Mauna Kea) and within the range of values typical of olivines from oceanic basalts ($\delta^{18}O$ of ~ 5.0 to 5.2‰). In contrast, $\delta^{18}O$ values of olivine phenocrysts from 20 samples taken from the subaerial section of Mauna Kea volcano (278 to 1037 mbsl) average 4.79 ± 0.13‰. Microphenocrysts in both the subaerial (n = 2) and submarine (n = 24) sections of Mauna Kea are on average ~ 0.2‰ lower in $\delta^{18}O$ than phenocrysts within the same stratigraphic interval; those in submarine Mauna Kea lavas have an average $\delta^{18}O$ value of 4.83 ± 0.11‰. Microphenocrysts in submarine Mauna Kea lavas and phenocrysts in Mauna Loa lavas are the only population of olivines considered in this study that are typically in oxygen isotope exchange equilibrium with coexisting glass or groundmass. These data confirm the previous observation that the stratigraphic boundary between Mauna Loa and Mauna Kea lavas defines a shift from "normal" to unusually low $\delta^{18}O$ values. Significantly, they also document that the distinctive $^{18}O$-depleted character of subaerial Mauna Kea lavas is absent in phenocrysts of submarine Mauna Kea lavas. Several lines of evidence suggest that little if any of the observed variations in $\delta^{18}O$ can be attributed to subsolidus alteration or equilibrium fractionations accompanying partial melting or crystallization. Instead, they reflect variable

proportions of an $^{18}O$-depleted source component or contaminant from the lithosphere and/or volcanic edifice that is absent in or only a trace constituent of subaerial Mauna Loa lavas, a minor component of submarine Mauna Kea lavas, and a major component of subaerial Mauna Kea lavas. Relationships between the $\delta^{18}O$ of phenocrysts, microphenocrysts, and glass or groundmass indicate that this component (when present) was added over the course of crystallization-differentiation. This process must have taken place in the lithosphere and most likely at depths of between ~ 5 and 15 km. We conclude that the low-$\delta^{18}O$ component is either a contaminant from the volcanic edifice that was sampled in increasingly greater proportions as the volcano drifted off the center of the Hawaiian plume or a partial melt of low-$\delta^{18}O$, hydrothermally altered peridotites in the shallow Pacific lithosphere that increasingly contributed to Mauna Kea lavas near end of the volcano's shield building stage. The first of these alternatives is favored by the difference in $\delta^{18}O$ between subaerial and submarine Mauna Kea lavas, whereas the second is favored by systematic differences in radiogenic and trace element composition between higher and lower $\delta^{18}O$ lavas.

## 1. INTRODUCTION

Rocks recovered by the second HSDP core ("HSDP-2") provide the first opportunity to examine a large fraction of the temporal evolution of a single oceanic intraplate volcano. In this paper, we document and discuss the significance of oxygen isotope variations of olivines and coexisting phases in rocks recovered by this core.

At the outset of this study, more was known about the oxygen isotope geochemistry of Hawaiian lavas than of any other basaltic volcanic center, with the possible exception

of Iceland (KYSER et al., 1981; KYSER et al., 1982; GARCIA et al., 1989; GARCIA et al., 1993; HARMON and HOEFS, 1995; EILER et al., 1996a; EILER et al., 1996b; GARCIA et al., 1998). These previous studies showed that many Hawaiian lavas have low $\delta^{18}O$ values ($\equiv [^{18}O/^{16}O/0.0020052 - 1]\cdot 1000$) compared to most terrestrial basalts, and that this characteristic is most strongly expressed in shield-building lavas of the "Kea trend" volcanoes (i.e., Kilauea, Mauna Kea, Kohala and Haleakala). Several hypotheses have been put forward to explain this phenomenon, including (1) $^{18}O$ depletion of primitive lower-mantle that is presumed to core the Hawaiian plume (HARMON and HOEFS, 1995), (2) entrainment of $^{18}O$-depleted, recycled oceanic lithosphere within the Hawaiian plume (LASSITER and HAURI, 1998), (3) contamination of Hawaiian magmas by $^{18}O$-depleted rocks in the current Pacific lithosphere (EILER et al., 1996b), and (4) contamination of Hawaiian magmas by hydrothermally altered, low-$\delta^{18}O$ rocks in the volcanic edifice (suggested by GARCIA et al., 1998 for recent Pu'u O'o lavas; the significance of this process for other Hawaiian lavas has not been explored).

In this study, we analyzed oxygen isotope compositions of olivines and coexisting phases from subaerial Mauna Loa lavas, both subaerial and submarine Mauna Kea lavas, and hyaloclastites and intrusives in the submarine Mauna Kea section. These data confirm the previous observation (EILER et al., 1996a) that the stratigraphic boundary between Mauna Loa and Mauna Kea marks a shift from "normal" to unusually low $\delta^{18}O$ values, respectively. Additionally, we find that coarse olivine phenocrysts in submarine Mauna Kea lavas and hyaloclastites are "normal" in $\delta^{18}O$ rather than $^{18}O$-depleted like subaerial Mauna Kea lavas. Finally, we find there is a systematic difference in $\delta^{18}O$ between coarse phenocrysts and microphenocrysts in the submarine Mauna Kea lavas --

the former are similar in $\delta^{18}O$ to other oceanic basalts, whereas the latter are distinctly lower in $\delta^{18}O$. We discuss several models for these stratigraphic trends and examine them in light of geochemical and petrologic data presented in other articles in this theme (BLICHERT-TOFT et al., 2003; BRYCE and DEPAOLO, 2003; EISELE et al., 2003; FEIGENSON et al., 2003; GARCIA et al., 2003; HUANG and FREY, 2003).

## 2. SAMPLING AND ANALYTICAL TECHNIQUES

Oxygen isotope ratios were analyzed in olivines, glass and/or groundmass from 89 samples of 88 tholeiites and one alkalic basalt in the HSDP-2 core from depths down to 3079.7 m below sea level (mbsl); these data are presented in Table 1. Our sampling of the submarine Mauna Kea section includes 27 pillow lavas, 21 hyaloclastites, 7 massive and 3 intrusive rocks. We refer to pillow basalts, massive lava flows and hyaloclastites as "lavas" in the remainder of this paper unless we wish to make a particular distinction among these subtypes of basalts. Most samples below 560 mbsl are from splits of the geochemical reference suite also analyzed in the accompanying articles in this theme. Samples from above 560 mbsl were collected by the authors from the portion of the HSDP-2 core stored at Caltech, and were generally taken from within 1.5 m of a reference suite sample; the exception is sample SR0133-0.04, which is 4.4 m below the sample SR0131-6.92 from the geochemical reference suite. All of our samples were taken from within a stratigraphic unit sampled by the geochemical reference suite. Further details for correlating our samples with those in other papers are given in Table 1.

All mineral, glass and groundmass separates were prepared by crushing, sieving, ultrasonicating in distilled water or 1N HCl, ultrasonicating in ethanol, drying, and

handpicking under a binocular microscope. Mineral, glass and groundmass fragments containing visible inclusions and alteration products were discarded during handpicking.

Most data are for large (≥ 1 mm) phenocrysts of olivine. However, we also recovered and analyzed fine-grained (usually ~ 100 to 200 μm diameter) separates of olivine microphenocrysts from 26 samples. We only separated microphenocrysts from lavas that are poor in coarser phenocrysts in order to avoid the possibility of mistaking small fragments of phenocrysts for microphenocrysts. The separated microphenocrysts are more susceptible to subsolidus alteration and might have formed by a different generation of olivine crystallization from that which formed coarse phenocrysts. Therefore, we distinguish between these two groups of olivine analyses in Table 1, all figures and throughout our discussion. Previous studies of the petrography and mineral chemistry of Hawaiian lavas have shown that coarse olivine phenocrysts and/or xenocrysts are relatively magnesian (forsterite contents between ~ 88 and 86%) and many are strained -- suggesting that they formed relatively early in the differentiation history of their host lavas or other magmas in the Hawaiian edifice and spent some time as components of cumulate piles before being brought to the surface (CLAGUE et al., 1995; BAKER et al., 1996). In contrast, microphenocrysts are less magnesian (typical forsterite contents of ~ 82 to 80%, extending down to ~ 50% on grain rims) and are inferred to be relatively late-stage precipitates from their host lavas. We checked that differences between these two populations previously identified in thin sections correspond to differences between our "phenocryst" versus "microphenocryst" mineral separates by making electron microprobe measurements of splits from two of our samples (Table 2). Our separated phenocrysts from sample SR0762-4.60 have forsterite contents of ~ 87.3 ± 0.8 mole%, whereas our

separated microphenocrysts from sample SR0907-1.65 have cores with ~ 81.6 ± 0.5 mole% forsterite.

Glass separates were recovered from thin rims surrounding olivine phenocrysts in hyaloclastites or from thick glassy rinds of pillow basalts. Analyzed glass fragments were dark brown and semitransparent; fragments that appeared altered (e.g., opaque and lacking glassy luster) were not analyzed. "Matrix" separates consisted of fine-grained aggregates of glass and minerals. Two separates of matrix from sample SR0157-7.17 were analyzed: one having a particle size of 200 to 300 μm ("matrix-a"; consisting of dark gray aggregates of glass and mafic minerals) and one having a size <150 μm ("matrix-b"; consisting of light gray aggregates dominated by plagioclase). The first of these is most like matrix and glass recovered from other samples and is the measurement from this sample plotted and discussed in the following sections.

All mineral, glass and matrix separates were analyzed by laser fluorination at the California Institute of Technology using methods previously described by EILER et al. (2000a, 2000b) and based on methods described by SHARP (1990) and VALLEY et al. (1995). A total of 67 UWG-2 (garnet), 33 SCO2 (olivine), 15 SCO3 (olivine) and 26 ALV526 (glass) standards were analyzed interspersed with analyses of samples. Results for these standards are as follows: UWG-2 = 5.77 ± 0.10‰, SCO2 = 5.25 ± 0.09‰, SCO3 = 5.31 ± 0.08‰ and ALV526 = 5.36 ± 0.09‰ (all standard deviations refer to long-term reproducibility of raw measurements and are 1$\sigma$); these values compare with accepted values of: UWG-2 = 5.80‰, SCO2 = 5.25‰, SCO3 = 5.35‰ and ALV526 = 5.40‰ (Valley et al., 1995; Eiler et al., 2000a; 2000b). All $\delta^{18}O$ values for unknowns measured on a given day were corrected by the difference between measured

Table 1. Oxygen Isotope Compositions of Materials From the HSDP-2 Core [a]

| Sample | Depth[b] (mbsl) | Unit [c] | Rock Type [d] | Material | $\delta^{18}O$ (‰) | 1 σ | Note[e] |
|---|---|---|---|---|---|---|---|
| SR0008-3.12 | 9.7 | U0002 | Mauna Loa subaerial | Olivine | 5.13 | 0.05 | W |
| SR0023-2.90 | 34.1 | U0006 | Mauna Loa subaerial | Olivine | 5.15 | 0.02 | W |
| | | | | Matrix | 5.36 | 0.13 | W |
| SR0031-0.52 | 45.5 | U0007 | Mauna Loa subaerial | Olivine | 5.14 | 0.05 | W |
| | | | | Glass | 5.42 | 0.08 | W |
| SR0036-2.18 | 53.7 | U0008 | Mauna Loa subaerial | Olivine | 5.02 | 0.11 | W |
| SR0066-0.13 | 98.8 | U0018 | Mauna Loa subaerial | Olivine | 4.93 | 0.06 | W |
| SR0067-0.33 | 100.4 | U0018 | Mauna Loa subaerial | Olivine | 5.02 | 0.05 | W |
| SR0098-0.00 | 177.1 | U0028 | Mauna Loa subaerial | Olivine | 5.27 | 0.05 | W |
| SR0100-7.33 | 185.6 | U0029 | Mauna Loa subaerial | Olivine | 5.14 | 0.10 | W |
| SR0104-5.46 | 197.5 | U0032 | Mauna Loa subaerial | Olivine | 5.14 | 0.04 | W |
| SR0113-6.56 | 222.4 | U0036 | Mauna Loa subaerial | Olivine | 5.25 | 0.05 | W |
| SR0118-0.40 | 234.9 | U0037 | Mauna Loa subaerial | Olivine | 5.05 | 0.06 | W |
| SR0133-0.04 | 278.8 | U0048 | Mauna Kea subaerial | Olivine | 4.78 | 0.07 | W |
| | | | | Glass | 4.36 | 0.10 | W |
| SR0136-6.33 | 290.0 | U0053 | Mauna Kea subaerial | Olivine | 4.64 | 0.07 | W |
| | | | | Glass | 4.13 | 0.06 | W |
| SR0137-6.08 | 293.0 | U0053 | Mauna Kea subaerial | Olivine | 4.60 | 0.02 | W |
| *SR0141-8.83* | *306.0* | *U0056* | *Mauna Kea subaerial* | *Olivine* | *4.49* | *0.09* | *W* |
| | | | | Matrix | 4.39 | 0.02 | W |
| SR0148-8.67 | 326.7 | U0060 | Mauna Kea subaerial | Olivine | 4.77 | 0.15 | W |

Table 1. (Continued)

| Sample | Depth[b] (mbsl) | Unit [c] | Rock Type [d] | Material | $\delta^{18}O$ (‰) | 1 σ | Note[e] |
|---|---|---|---|---|---|---|---|
| SR0157-7.17 | 353.2 | U0061 | Mauna Kea subaerial | Olivine | 4.60 | 0.04 | W |
| | | | | Matrix-a | 4.74 | 0.10 | W |
| | | | | Matrix-b | 5.11 | 0.02 | W |
| SR0175-5.21 | 398.0 | U0073 | Mauna Kea subaerial | Olivine | 4.71 | 0.10 | W |
| SR0184-4.25 | 421.5 | U0076 | Mauna Kea subaerial | Olivine | 4.65 | 0.04 | W |
| SR0193-1.83 | 444.1 | U0080 | Mauna Kea subaerial | Olivine | 4.66 | 0.08 | W |
| | | | | Matrix | 4.67 | 0.03 | W |
| SR0206-0.30 | 469.3 | U0084 | Mauna Kea subaerial | Olivine | 4.97 | 0.05 | W |
| SR0213-3.58 | 492.5 | U0088 | Mauna Kea subaerial | Olivine | 4.72 | 0.15 | W |
| SR0222-3.67 | 516.6 | U0092 | Mauna Kea subaerial | Olivine | 4.77 | 0.03 | W |
| SR0233-1.08 | 542.9 | U0094 | Mauna Kea subaerial | Olivine | 4.71 | 0.12 | W |
| SR0267-6.85 | 615.8 | U0107 | Mauna Kea subaerial | Olivine | 4.97 | 0.09 | R |
| SR0276-7.85 | 636.0 | U0110 | Mauna Kea subaerial | Olivine | 4.78 | 0.15 | R |
| SR0328-3.10 | 759.8 | U0127 | Mauna Kea subaerial | Olivine | 4.71 | 0.16 | R |
| SR0346-5.60 | 812.7 | U0136 | Mauna Kea subaerial | Olivine | 4.93 | 0.13 | R |
| SR0354-7.75 | 833.9 | U0138 | Mauna Kea subaerial | Olivine | 5.06 | 0.07 | R |
| SR0372-2.80 | 871.2 | U0142 | Mauna Kea subaerial | Olivine | 4.62 | 0.07 | R |
| SR0379-3.00 | 888.4 | U0144 | Mauna Kea subaerial | Olivine | 4.89 | 0.09 | R |
| SR0423-3.65 | 1012.4 | U0157 | Mauna Kea subaerial | Olivine | 4.89 | 0.06 | R |
| *SR0431-8.50* | *1037.7* | *U0160* | *Mauna Kea subaerial* | *Olivine* | *4.72* | *0.08* | *R* |
| SR0455-7.40 | 1098.2 | U0179 | Massive | Olivine | 4.95 | 0.08 | R |

Table 1. (Continued)

| Sample | Depth[b] (mbsl) | Unit [c] | Rock Type [d] | Material | $\delta^{18}O$ (‰) | 1 σ | Note[e] |
|---|---|---|---|---|---|---|---|
| SR0512-4.70 | 1294.4 | U0194 | Hyaloclastite | Olivine | 5.15 | 0.06 | S |
| | | | | Glass | 5.06 | 0.05 | S |
| SR0531-4.40 | 1352.6 | U0198 | Massive | Olivine | 4.95 | 0.06 | R |
| SR0545-8.35 | 1394.9 | U0198 | Hyaloclastite | Olivine | 4.95 | 0.02 | R |
| SR0548-8.00 | 1404.1 | U0199 | Massive | Olivine | 5.05 | 0.08 | R |
| SR0560-7.50 | 1435.4 | U0202 | Hyaloclastite | Olivine | 5.03 | 0.02 | R |
| SR0582-10.00 | 1497.7 | U0207 | Massive | Olivine | 5.01 | 0.09 | R |
| | | | | Glass | 5.10 | 0.06 | R |
| SR0594-8.70 | 1521.4 | U0213 | Massive | Olivine | 4.98 | 0.15 | R |
| SR0596-5.55 | 1526.3 | U0214 | Hyaloclastite | Olivine | 5.01 | 0.15 | S |
| SR0603-8.90 | 1548.2 | U0216 | Hyaloclastite | Olivine | 4.98 | 0.07 | R |
| SR0622-7.10 | 1581.2 | U0218 | Hyaloclastite | Olivine | 5.01 | 0.15 | R |
| SR0655-4.00 | 1678.7 | U0238 | Hyaloclastite | Olivine | 4.99 | 0.07 | R |
| SR0664-5.10 | 1705.5 | U0238 | Hyaloclastite | Olivine | 5.02 | 0.08 | R |
| SR0675-6.90 | 1739.3 | U0243 | Hyaloclastite | Olivine | 5.02 | 0.08 | R |
| SR0683-5.75 | 1763.2 | U0245 | Massive | Olivine | 5.14 | 0.07 | R |
| *SR0686-5.1* | *1771.6* | *U0248* | *Hyaloclastite* | *Olivine* | *4.78* | *0.05* | *C* |
| | | | | Glass | 5.17 | 0.05 | C |
| *SR0696-8.4* | *1797.4* | *U0254* | *Hyaloclastite* | *Olivine* | *4.99* | *0.10* | *C* |
| | | | | Glass | 5.14 | 0.11 | C |

Table 1. (Continued)

| Sample | Depth[b] (mbsl) | Unit [c] | Rock Type [d] | Material | $\delta^{18}O$ (‰) | 1 σ | Note[e] |
|---|---|---|---|---|---|---|---|
| *SR0697-8.1* | *1800.2* | *U0254* | *Hyaloclastite* | *Olivine* | *4.79* | *0.10* | *C* |
| | | | | Glass | 5.30 | 0.17 | C |
| *SR0698-5.6* | *1802.5* | *U0255* | *Hyaloclastite* | *Olivine* | *4.90* | *0.13* | *C* |
| | | | | Glass | 4.66 | 0.10 | C |
| *SR0699-5.55* | *1805.7* | *U0256* | *Hyaloclastite* | *Olivine* | *4.83* | *0.05* | *C* |
| | | | | Glass | 5.24 | 0.05 | C |
| SR0709-13.35 | 1852.0 | U0261 | Hyaloclastite | Olivine | 5.02 | 0.02 | R |
| SR0714-11.55 | 1883.6 | U0263 | Intrusive | Olivine | 5.08 | 0.11 | R |
| SR0720-18.25 | 1921.6 | U0268 | Intrusive | Olivine | 4.95 | 0.08 | R |
| SR0741-7.90 | 2009.8 | U0278 | Pillow | Olivine | 4.99 | 0.08 | R |
| SR0750-12.45 | 2062.7 | U0283 | Pillow | Olivine | 4.97 | 0.03 | R |
| SR0756-13.2 | 2098.6 | U0284 | Pillow | Olivine | 5.03 | 0.08 | R |
| SR0762-4.60 | 2123.7 | U0284 | Pillow | Olivine | 4.99 | 0.16 | R |
| *SR0768-11.20* | *2157.4* | *U0285* | *Hyaloclastite* | *Olivine* | *4.72* | *0.05* | *R* |
| | | | | Glass | 5.07 | 0.05 | R |
| *SR0778-3.20* | *2218.2* | *U0287* | *Hyaloclastite* | *Olivine* | *5.10* | *0.11* | *R* |
| | | | | Glass | 5.13 | 0.07 | R |
| *SR0780-20.80* | *2236.7* | *U0288* | *Pillow* | *Olivine* | *4.75* | *0.05* | *R* |
| | | | | Glass | 5.15 | 0.07 | R |
| *SR0792-6.20* | *2285.2* | *U0290* | *Pillow* | *Olivine* | *4.84* | *0.05* | *R* |
| | | | | Glass | 5.22 | 0.05 | R |

Table 1. (continued)

| Sample | Depth[b] (mbsl) | Unit [c] | Rock Type [d] | Material | $\delta^{18}O$ (‰) | 1 σ | Note[e] |
|---|---|---|---|---|---|---|---|
| *SR0796-6.70* | *2300.2* | *U0290* | *Pillow* | *Olivine* | *5.05* | *0.03* | *R* |
| | | | | Glass | 5.39 | 0.07 | R |
| *SR0800-13.20* | *2321.6* | *U0291* | *Pillow* | *Olivine* | *4.94* | *0.05* | *R* |
| *SR0807-3.70* | *2340.7* | *U0292* | *Pillow* | *Olivine* | *4.88* | *0.08* | *R* |
| | | | | Glass | 5.20 | 0.05 | R |
| *SR0814-14.40* | *2357.0* | *U0292* | *Pillow* | *Olivine* | *4.69* | *0.08* | *R* |
| *SR0814-17.60* | *2357.4* | *U0292* | *Pillow* | *Olivine* | *4.83* | *0.14* | *W* |
| *SR826-13.8* | *2411.4* | *U0293* | *Pillow* | *Olivine* | *4.82* | *0.04* | *W* |
| *SR0826-20.60* | *2414.1* | *U0293* | *Pillow* | *Olivine* | *4.71* | *0.08* | *R* |
| *SR829-3.40* | *2426.7* | *U0293* | *Pillow* | *Olivine* | *4.76* | *0.14* | *W* |
| | | *U0293* | *Hyaloclastite* | *Olivine* | *4.78* | *0.05* | *W* |
| *SR0836-5.80* | *2467.3* | *U0295* | *Pillow* | *Olivine* | *4.81* | *0.05* | *R* |
| SR0837-4.20 | 2472.8 | U0296 | Pillow | Olivine | 5.03 | 0.05 | W |
| | | U0296 | Hyaloclastite | Olivine | 5.04 | 0.05 | W |
| SR0843-8.70 | 2511.5 | U0302 | Massive | Olivine | 4.99 | 0.05 | W |
| SR0846-2.80 | 2525.4 | U0303 | Hyaloclastite | Olivine | 4.88 | 0.06 | R |
| SR0860-8.10 | 2615.0 | U0310e | Pillow | Olivine | 5.01 | 0.02 | R |
| *SR0871-13.00* | *2654.1* | *U0312* | *Pillow* | *Olivine* | *4.87* | *0.02* | *R* |
| *SR0891-15.10* | *2730.2* | *U0316* | *Pillow* | *Olivine* | *4.84* | *0.04* | *R* |
| *SR0896-2.40* | *2759.3* | *U0319* | *Hyaloclastite* | *Olivine* | *4.76* | *0.08* | *R* |
| SR0899-4.40 | 2770.9 | U0320 | Pillow | Olivine | 4.84 | 0.05 | R |

Table 1. (continued)

| Sample | Depth[b] (mbsl) | Unit [c] | Rock Type [d] | Material | $\delta^{18}O$ (‰) | 1 σ | Note[e] |
|---|---|---|---|---|---|---|---|
| *SR0907-1.65* | *2789.9* | *U0321* | *Pillow* | *Olivine* | *4.65* | *0.07* | *R* |
| SR0913-2.4 | 2825.8 | U0327 | Intrusive | Olivine | 4.93 | 0.15 | R |
| SR0916-1.15 | 2837.6 | U0330 | Pillow | Olivine | 5.04 | 0.05 | R |
| | | | | Matrix | 5.06 | 0.09 | R |
| SR0930-15.85 | 2919.5 | U0333 | Pillow | Olivine | 5.14 | 0.02 | R |
| SR0939-18.10 | 2961.0 | U0335a | Pillow | Olivine | 5.08 | 0.02 | R |
| SR0954-8.00 | 3009.2 | U0339 | Pillow | Olivine | 4.98 | 0.04 | R |
| SR0964-4.30 | 3058.0 | U0340e | Pillow | Olivine | 5.02 | 0.13 | R |
| *SR0967-2.75* | *3068.9* | *U0343a* | *Pillow* | *Olivine* | *4.94* | *0.08* | *R* |

**a**: Italicized entries are data for olivine microphenocrysts, all other olivine analyses are for coarse (1 mm and larger) olivine phenocrysts; **b:** Depth is in meters below sea level (mbsl); **c** : Units defined by the HSDP-2 stratigraphic column; **d**: Petrological description from the HSDP-2 core log; **e** : **W**, sampled by authors; **R**, from the HSDP-2 reference suite; **C**, sampled by Caroline Seaman; **S**, sampled by Sujoy Mukhopadhyay.

Table 2. Magnesium numbers of representative grains from olivine separates

| | Average |
|---|---|
| Coarse Phenocrysts; Sample SR0762-4.60 | |
| 88.6; 86.6; 87.6; 87.6; 87.9; 88.4; 88.6; 87.9; 87.1; 87.5; 86.9; 87.0; 86.0 | 87.3 ± 0.8 |
| Microphenocrysts; Sample SR0907-1.65 | |
| 82.0; 81.3; 81.1; 82.2; 80.8; 81.9; 82.0 | 81.6 ± 0.5 |

and accepted values for standards on that day. All measurements of unknown samples were replicated, generally in duplicate but some between three and seven times; standard deviations for each sample are reported in the Table 1. Olivines from a few samples were not replicated to within our nominal analytical precision, suggesting that they are isotopically heterogeneous. These samples do not appear to be outliers to any of the stratigraphic or geochemical trends discussed below. We analyzed olivines from two to four different samples in each of nine stratigraphic units (units U0018, U0053, U0238, U0254, U0284, U0290, U0292, U0293, and U0296); average values for of $\delta^{18}O$ olivine for the related samples are usually within analytical uncertainty of one another, suggesting at least these individual units are isotopically homogeneous. The $\delta^{18}O$ values of olivine from pillow basalt are indistinguishable from those of immediately adjacent hyaloclastites in units U0293 and U0296.

## 3. RESULTS

### 3.1. OXYGEN ISOTOPE STRATIGRAPHY OF THE HSDP-2 CORE

Olivines from the HSDP-2 core have $\delta^{18}O$ values of between 4.49 and 5.27‰ (averaged for each sample; Table 1 and Figure 1a; minima and maxima for individual measurements, before averaging by hand sample, are 4.36 and 5.43‰). These ranges are similar to those observed in the ~ 1 km HSDP pilot core (e.g., 4.64 to 5.39‰ when averaged for each sample; EILER et al., 1996a) and are within the range of values typical of all Hawaiian lavas other than shield-building Koolau and Lanai tholeiites (which are higher in $\delta^{18}O$, Eiler et al., 1996b).

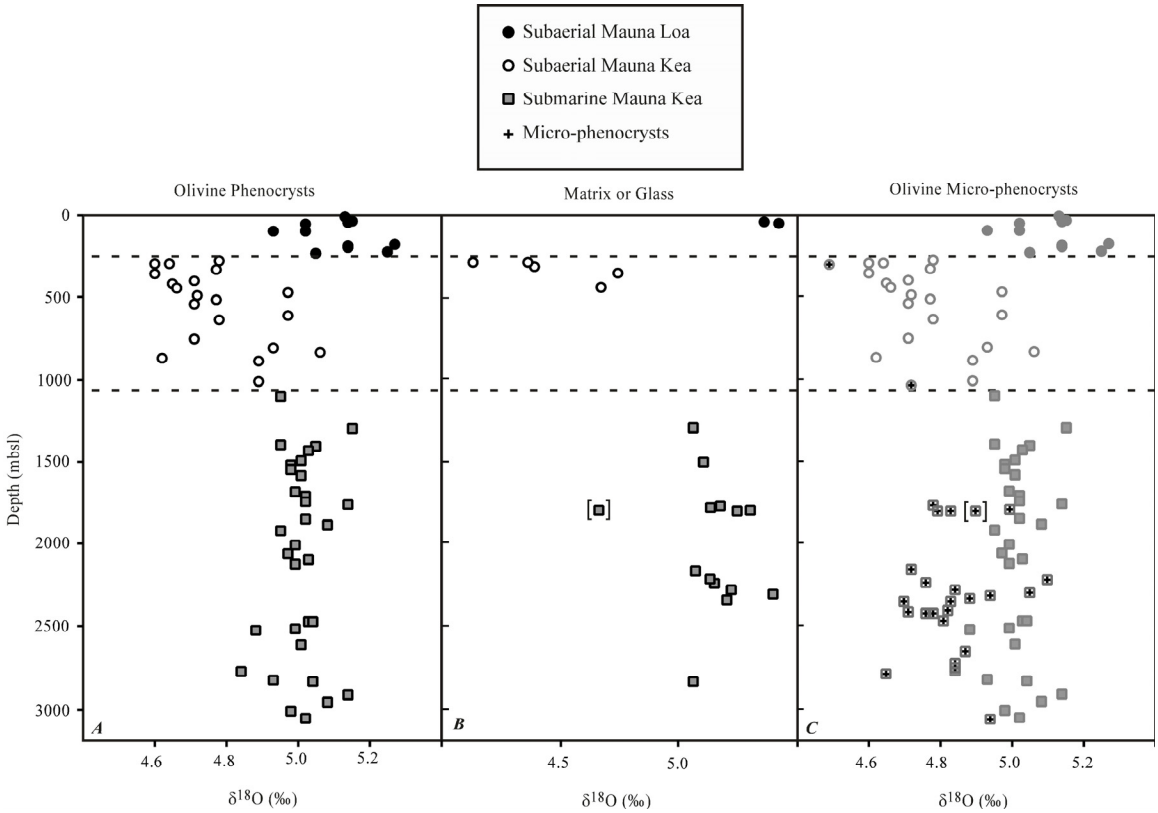


**Figure 1**. Stratigraphic profiles of the oxygen isotope compositions of materials from the HSDP-2 core, including (A) olivine phenocrysts; (B) glass and nominally fresh volcanic groundmass; and (C) microphenocrysts (data for olivine phenocrysts are reproduced from panel A as faint gray symbols). See legend for symbols used in this and following figures.

Olivine phenocrysts (i.e., as distinct from microphenocrysts) from eleven samples of subaerial Mauna Loa lavas (between 0 and 246 mbsl) and 34 samples of submarine Mauna Kea lavas (greater than 1061 mbsl) have $\delta^{18}O$ values that are similar to one another (5.11 ± 0.10‰, 1σ, versus 5.01 ± 0.07‰, 1σ, respectively) and typical of olivines from other oceanic basalts (EILER et al., 1997; EILER et al., 2000a; EILER et al., 2000b). In contrast, olivine phenocrysts from 20 samples of subaerial Mauna Kea lavas (between

246 to 1061 mbsl) have $\delta^{18}O$ values averaging 4.79 ± 0.13‰, 1σ, a lower extreme of 4.60‰, and include many samples having $\delta^{18}O$ values below the lower limits defined by phenocrysts from other sections of the core. Olivine phenocrysts from one sample of alkali basalt from the uppermost portion of the Mauna Kea section of the core (SR133-0.04) have a $\delta^{18}O$ value of 4.78 ± 0.07‰ -- indistinguishable from tholeiitic lavas in the same section of the core. There is no obvious difference in $\delta^{18}O$ of olivine phenocrysts between hyaloclastites and pillows in a given interval of the core (Table 1). None of the intrusives or massive units has low $\delta^{18}O$ olivine phenocrysts (Table 1).

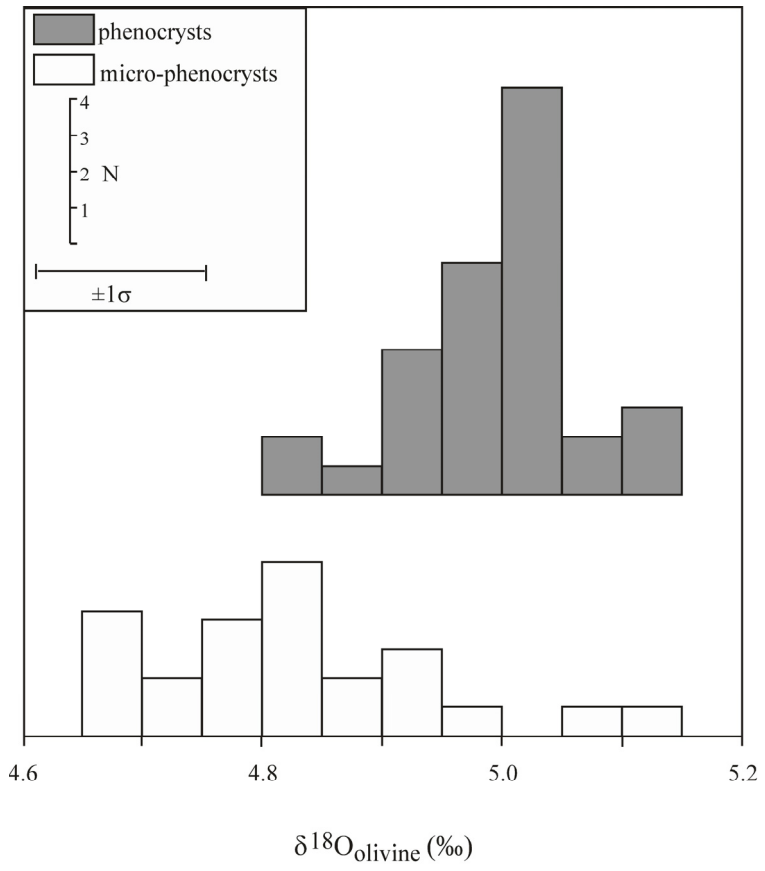


**Figure 2.** Histograms illustrating the distribution of $\delta^{18}O$ values for coarse olivine phenocrysts and olivine microphenocrysts in submarine Mauna Kea lavas. Note that microphenocrysts are, on average, ~ 0.2‰ lower in $\delta^{18}O$ than phenocrysts.

The stratigraphy of $\delta^{18}O$ values for matrix and glass (Figure 1b) resembles that described above for olivine phenocrysts: the $\delta^{18}O$ values of Mauna Loa lavas and submarine Mauna Kea lavas are relatively high and, with one exception, constant, whereas those for subaerial Mauna Kea lavas are relatively low. However, there are several significant features unique to data for matrix and glass: (1) the range of $\delta^{18}O$ values for matrix and glass is greater -- by approximately 50%, relative -- than that for olivine phenocrysts; (2) the average values for matrix and glass in Mauna Loa (5.39‰) and submarine Mauna Kea samples (5.13‰) are higher than the averages for coexisting or stratigraphically adjacent olivine phenocrysts -- in the direction of the equilibrium melt-olivine fractionation -- whereas the average value for matrix and glass in subaerial Mauna Kea samples (4.46‰) is less than that of related olivine phenocrysts -- opposite the direction of the equilibrium fractionation; (3) $\delta^{18}O$ values for matrix and glass in submarine Mauna Kea lavas overlap but often fall below the range typical of mid ocean ridge basalt glasses (~ 5.3 to 5.8‰, EILER et al., 2000b; EILER, 2001; COOPER et al., 2004), whereas olivine phenocrysts in this interval are generally within the range typical of olivine in oceanic basalts; and (4) there is one notable outlier to the otherwise tightly grouped population of glasses in the submarine Mauna Kea section (sample SR697-8.1 from 1802.5 mbsl). This sample contains olivine microphenocrysts that are isotopically similar to those in other submarine Mauna Kea lavas and is not unusual in other aspects of its geochemistry (STOLPER et al., 2004). We distinguish this unusual sample on all plots where it appears by placing brackets around its symbol.

The stratigraphy of $\delta^{18}O$ values for olivine microphenocrysts (Figure 1c) resembles that described above for olivine phenocrysts (Figure 1a) and matrix or glass (Figure 1b)

in that the two subaerial Mauna Kea samples (4.49 and 4.72‰) are lower in $\delta^{18}O$ than the average value for submarine Mauna Kea samples (4.85‰). However, the most noticeable feature of the data for microphenocrysts is that they are consistently lower in $\delta^{18}O$ than phenocrysts in stratigraphically adjacent lavas. In particular, throughout the submarine section of Mauna Kea, all olivine phenocrysts are within or closely approach the lower end of the range typical of oceanic basalts (~ 5.0 to 5.2‰) whereas microphenocrysts are generally below that range. Histograms illustrating the contrast in $\delta^{18}O$ between phenocrysts and microphenocrysts in the submarine section of Mauna Kea are provided in Figure 2.

We further examine the relationship between $\delta^{18}O$ values of olivines and host glass or matrix in Figure 3. This plot contains a thick gray line of slope 1 corresponding to a fractionation of 0.4‰ between matrix or glass on one hand and olivine on the other. This is our best estimate of the high-temperature equilibrium fractionation between basaltic melt and olivine based on previous studies of basaltic lavas and experimental studies of oxygen isotope partitioning among melts, glasses, minerals and vapors (ANDERSON et al., 1971; MUEHLENBACHS and KUSHIRO, 1974; MUEHLENBACHS and BYERLY, 1982; MATTHEWS et al., 1998; EILER, 2001; APPORA et al., 2003). All lavas in which olivine and melt are in high-temperature isotopic equilibrium should plot on or near this line and those that do not have been disturbed by change in $\delta^{18}O$ of olivine, melt, glass and/or matrix groundmass after olivine crystallization. Of phenocryst-glass/matrix pairs, only the two Mauna Loa samples closely approach the equilibrium fractionation and all Mauna Kea samples have fractionations that are significantly too low or even reversed (i.e.,

opposite in sign to equilibrium value). In contrast, eight of twelve microphenocryst-glass/matrix pairs are indistinguishable from the equilibrium fractionation.

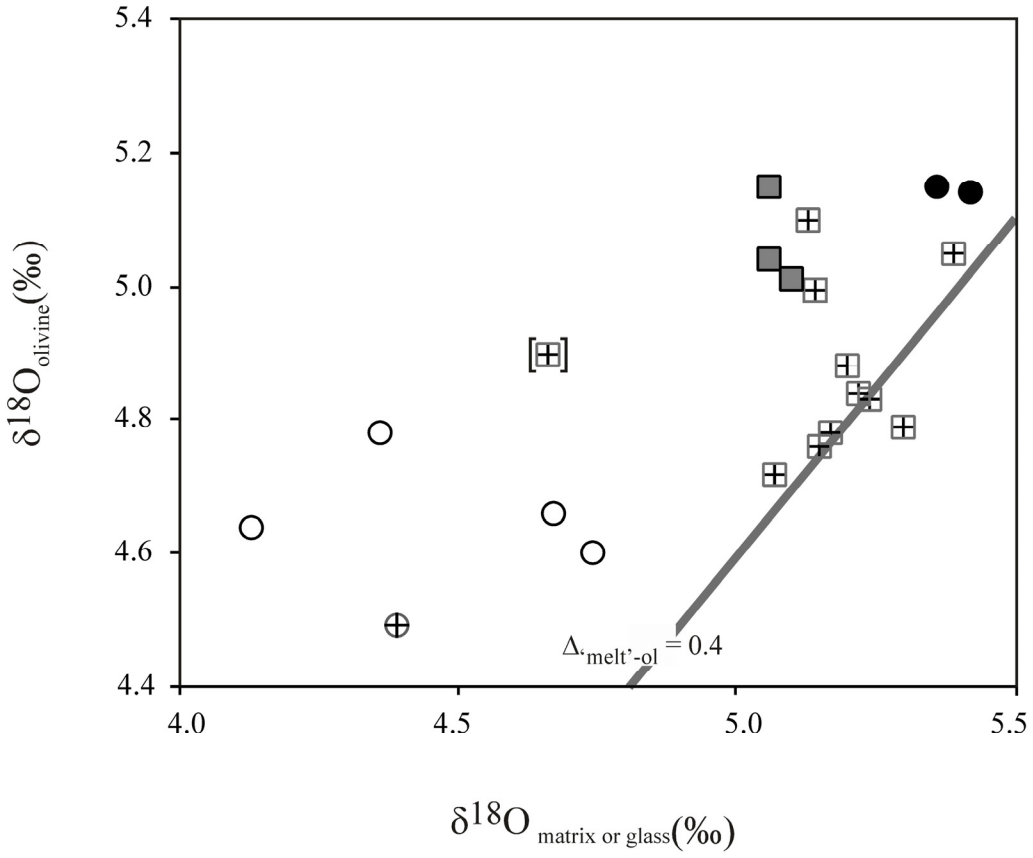


**Figure 3.** Comparison of $\delta^{18}O$ values measured for olivine phenocrysts or microphenocrysts (vertical axis) to those measured for host glass or groundmass (horizontal axis). Symbols are as in Figure 1. The diagonal gray line is the inferred equilibrium olivine-melt fractionation for basalt at magmatic temperatures; see EILER, 2001) for data and references on which this estimate is based. Most microphenocryst -- host pairs are in high-temperature isotopic equilibrium, whereas phenocryst -- host pairs generally have inferred melt-olivine fractionations that are too small or reversed. The maximum departure from equilibrium (i.e., greatest distance from the gray line) is larger for low-$\delta^{18}O$ samples than for higher $\delta^{18}O$ samples. Disequilibrium fractionations observed in many samples in this study are similar to those previously observed for unaltered Pu'u O'o lavas (GARCIA et al., 1998).

### 3.2. Comparison of Oxygen Isotope Compositions With Other Geochemical Variables

Figure 4 reproduces values of $\varepsilon_{Hf}$ (4a), $^{3}He/^{4}He$ (4b), $^{208}Pb^{*}/^{206}Pb^{*}$ (4c), and Sm/Yb (4d) from the HSDP-2 core (data are taken from Blichert-Toft et al., 2003; Eisele et al., 2003; Kurz et al., 2004; Huang and Frey, 2003, and Feigenson et al., 2003). The index $^{208}Pb^{*}/^{206}Pb^{*}$ is calculated following Galer and Onions (1985). We combined Pb isotope data from Blichert-Toft et al. (2003) and Eisele et al. (2003) to construct Figure 4c; Blichert-Toft et al. (2003) document that these two data sets yield closely similar values of $^{208}Pb^{*}/^{206}Pb^{*}$ for the same samples. In addition, Figure 5 reproduces the distributions of $SiO_2$ contents for submarine Mauna Kea glasses or inferred for subaerial Mauna Kea whole rocks, after normalization for olivine accumulation. These data are taken from Stolper et al. (2004).

There are several similarities and differences between the stratigraphy of $\delta^{18}O$ values (Figure 1) and that of other geochemical variables plotted in Figures 4 and 5:

**1.** The boundary between Mauna Loa and Mauna Kea lavas, at which we observe a sharp change from "normal" to unusually low $\delta^{18}O$ values for all analyzed materials, is also a change from less to more radiogenic Hf and He isotope ratios, and from lower to higher $^{208}Pb^{*}/^{206}Pb^{*}$ values and Sm/Yb ratios. These differences are the same as those previously observed at the same stratigraphic boundary in the HSDP pilot hole (Eiler et al., 1996a; Hofmann and Jochum, 1996; Lassiter et al., 1996) and are consistent with the contrast in oxygen isotopes and other geochemical indices between Mauna Loa and Mauna Kea shield-building lavas exposed at the surface (Eiler et al., 1996b, and references therein). Fractionation-normalized $SiO_2$ contents (Figure 5) were not estimated

for Mauna Loa lavas in the HSDP-2 core (STOLPER et al., 2004). However, previous work suggests this boundary likely marks a significant decrease in silica going down-core from Mauna Loa to Mauna Kea (e.g., HAURI, 1996).

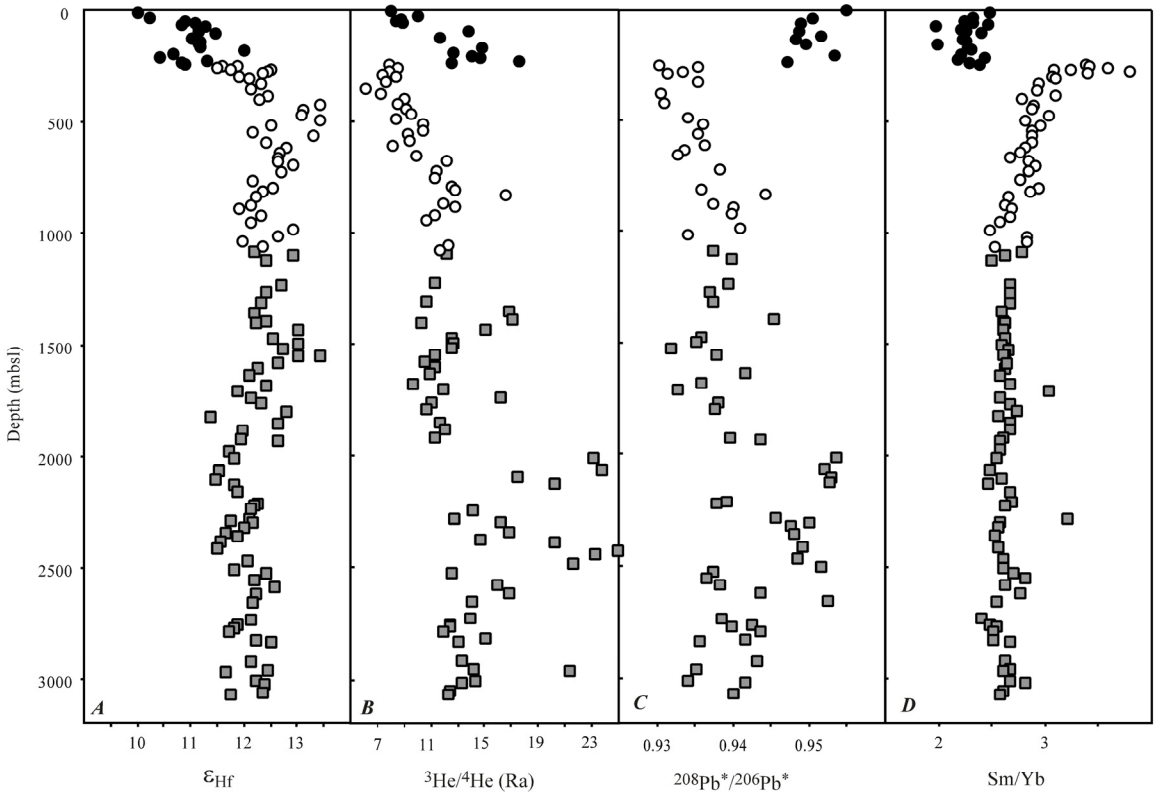


**Figure 4.** Stratigraphic variations in $\varepsilon_{Hf}$ (BLICHERT-TOFT et al., 2003), $^{3}He/^{4}He$ (KURZ et al., 2004), $^{208}Pb^{*}/^{206}Pb^{*}$ (based on data from BLICHERT-TOFT et al., 2003; EISELE et al., 2003; FEIGENSON et al., 2003), and Sm/Yb (FEIGENSON et al., 2003) in the HSDP-2 core. See text and Figure 1 for comparisons with the oxygen isotope stratigraphy.

**2**. The boundary between subaerial and submarine Mauna Kea lavas marks a change in the average oxygen isotope composition of olivine phenocrysts, microphenocrysts, matrix and glass (Figure 1). This change is particularly clear for the olivine phenocryst data, which are the largest and most densely spaced subset of our measurements (Figure

1a). $^{3}He/^{4}He$, Sm/Yb ratios and $^{208}Pb^{*}/^{206}Pb^{*}$ values of subaerial Mauna Kea lavas are also different, on average, than those of submarine Mauna Kea lavas (Figure 4), and thus variations in O, He and Pb isotopes and rare earth element ratios might be caused by similar processes. However, the changes in He and Pb isotopes and Sm/Yb ratios across the subaerial/submarine transition and through the subaerial section are relatively smooth, perhaps caused by a gradual temporal trend, whereas the change in $\delta^{18}O$ of olivine phenocrysts appears relatively sharp. Therefore, it also seems possible that these stratigraphic trends have different causes and are only fortuitously correlated with one another.

**3.** The distribution of fractionation-corrected $SiO_2$ contents changes sharply across the subaerial/submarine transition (STOLPER et al., 2004) (see also Figure 5). In particular, submarine Mauna Kea lavas are characterized by two distinct populations of $SiO_2$ contents, referred to by STOLPER et al., 2004) as the high-$SiO_2$ and low-SiO2 series. Neither of these populations contains anomalously low-$\delta^{18}O$ olivine phenocrysts (the $\delta^{18}O$ values of glass and microphenocrysts are also similar in both). Intermediate $SiO_2$ contents are rare in the submarine section of the core and are always associated with extensive degassing, leading STOLPER et al. (2004) to suggest they could be mixtures of high-$SiO_2$ and low-$SiO_2$ magmas that only encounter one another in a shallow magma reservoir. In contrast, subaerial Mauna Kea tholeiites have a unimodal distribution of intermediate $SiO_2$ contents (i.e., between the low-$SiO_2$ and high-$SiO_2$ submarine populations), with a long tail of low-$SiO_2$ compositions extending toward alkaline post-shield lavas. We find it striking that the transition from bimodal to uni-modal $SiO_2$

contents occurs at the submarine/subaerial transition, and thus coincides with the transition from normal to anomalously low-$\delta^{18}O$ olivine phenocrysts.

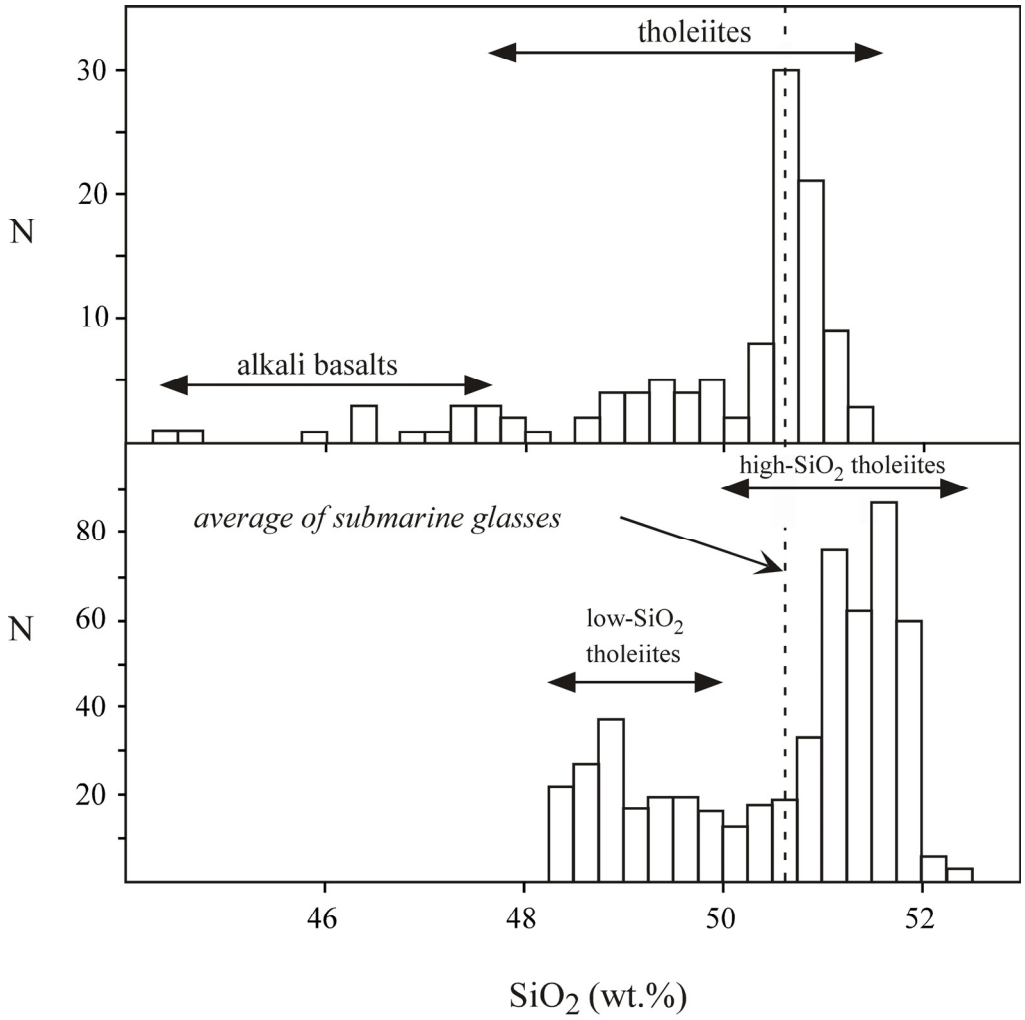


**Figure 5.** Histograms illustrating the distribution in fractionation-normalized $SiO_2$ contents of submarine Mauna Kea glasses (lower columns) and subaerial basalts (upper columns). Data from STOLPER et al. (2004). Note that submarine lavas are characterized by a bimodal population of higher and lower-$SiO_2$ lavas. In contrast, subaerial lavas have a unimodal distribution with an average equal to the mean of all submarine lavas.

**4.** There are two intervals of exceptionally high $^{3}He/^{4}He$ ratios and $^{208}Pb^{*}/^{206}Pb^{*}$ values between 1950 and 2500 mbsl (Figures 4b and 4c). These intervals are discussed at

length in several articles in this theme (BLICHERT-TOFT et al., 2003; EISELE et al., 2003; KURZ et al., 2004). There is no obvious anomaly in the $\delta^{18}O$ of any one analyzed material (phenocryst, microphenocryst, glass or matrix) within the narrow stratigraphic intervals having anomalous He and Pb isotope ratios.

**5.** Two intervals of the submarine section of the core are anomalous in their major element chemistry: (1) glasses between 1765 and 1810 mbsl are anomalously rich in $K_2O$; and (2) glasses between 2235 and 2280 mbsl are unusual in several respects consistent with them being products of unusually low degrees of mantle melting (STOLPER et al., 2004). There is no obvious relationship between $\delta^{18}O$ of glass or microphenocrysts and $K_2O$ over this first interval, although it is noteworthy that it includes sample SR0698-5.6, which has exceptionally low $\delta^{18}O$ glass and an exceptionally low glass-olivine fractionation (Figures 1b and 3). Only one of our samples (SR0780-20.80) is from within the second interval, but we note there is a systematic stratigraphic trend in several radiogenic isotope ratios over the larger, overlapping interval of ~ 2150 to 2500 mbsl (Figure 6). Six samples from this larger interval were analyzed for oxygen isotope composition of glass, and appear to decrease in $\delta^{18}O$ with decreasing depth, correlated with increases in $\varepsilon_{Nd}$ and $\varepsilon_{Hf}$ and decreases in $^{3}He/^{4}He$ and $^{87}Sr/^{86}Sr$ with decreasing depth (Figure 6; note the stratigraphic trend in $\varepsilon_{Hf}$ appears more complex at the top and bottom of this interval than do those of other radiogenic isotope ratios). While these trends might reflect coupled, gradual changes over time, note that this interval contains discontinuities in the stratigraphy of $SiO_2$ and a layer of fine-grained sand that might mark a significant change in deposition rate (STOLPER et al., 2004).

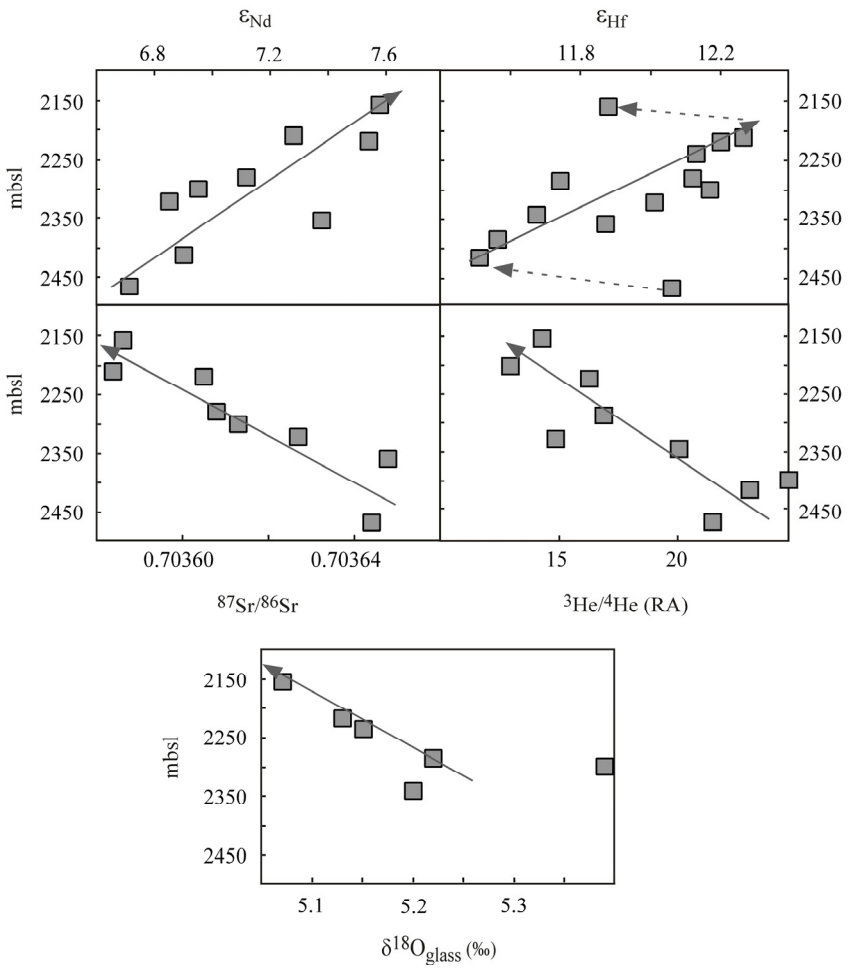


**Figure 6.** Stratigraphic variations in $\varepsilon_{Nd}$ (BRYCE and DEPAOLO, 2003), $\varepsilon_{Hf}$, $^{87}Sr/^{86}Sr$, $^{3}He/^{4}He$ and $\delta^{18}O$ glass over an interval in the submarine Mauna Kea section that is characterized by unusually coherent, monotonic trends in radiogenic isotope composition, perhaps due to unusually simple mixing relationships between isotopically distinct sources. The $\delta^{18}O$ value of glass over this interval decreases monotonically with decreasing depth, suggesting all stratigraphic trends reflect increasing contributions from a component that is relatively low in $\delta^{18}O$, $^{87}Sr/^{86}Sr$ and $^{3}He/^{4}He$ and relatively high in $\varepsilon_{Nd}$ and $\varepsilon_{Hf}$. Such simple stratigraphic trends are not seen elsewhere in the Mauna Kea section of the core, either because they are obscured elsewhere by more complex mixing relationships (e.g., involving three or more end-members, EISELE et al., 2003), or because they are fortuitous here and do not reflect real coupling of these isotopic systems.

We further examine relationships between oxygen isotopes and other geochemical variables by plotting $\delta^{18}O$ versus various major-element, trace element and radiogenic isotope indices measured on whole rock splits and glasses from the same samples or nearby samples from the same units (Figures 7a–7e). Figures 7a–7d show that variations in $\delta^{18}O$ of olivine phenocrysts (filled and unfilled circles and squares) are loosely but consistently correlated with other geochemical variables, and that these correlations are defined both by differences between Mauna Loa and Mauna Kea lavas and by variations among Mauna Kea lavas alone. In Figures 7a–7c, these correlations consist of three overlapping but distinguishable groups — (1) Mauna Loa, (2) submarine Mauna Kea, and (3) subaerial Mauna Kea—that differ from one another in average values of $\delta^{18}O$ of olivine phenocrysts and in the other plotted variable. The sense of these trends is that decreasing $\delta^{18}O$ is associated with decreasing $Al_2O_3/TiO_2$, increasing Sm/Yb, and decreasing V/Ti (the significance of which is discussed below). Figure 7d has a somewhat different appearance: Mauna Loa lavas and submarine Mauna Kea lavas span a large range of generally high $^3He/^4He$ ratios with "normal" values of $\delta^{18}O$ for olivine phenocrysts, whereas subaerial Mauna Kea lavas define a distinct group that is anomalously low in both $\delta^{18}O$ and $^3He/^4He$. This figure has the same topology as a plot of $\delta^{18}O$olivine versus 3He/4He for all Hawaiian shield-building lavas (EILER et al., 1996b). Data for olivine microphenocrysts generally conform to the trends defined by olivine phenocrysts in Figures 7a–7d; however, four submarine Mauna Kea lavas are exceptions having olivine microphenocrysts with $\delta^{18}O$ values ~ 0.2‰ lower than olivine phenocrysts in chemically similar (and stratigraphically close) lavas.

Figure 7e compares the $\delta^{18}O$ values of submarine Mauna Kea glasses to MgO contents of glasses from the same units measured by electron microprobe (STOLPER et al., 2004). For comparison, we also show data for recent lavas from the Pu'u O'o vents on Kilauea's east rift zone (GARCIA et al., 1998). Except the anomalous sample SR0698-5.6 (indicated by brackets), the total range in $\delta^{18}O$ for Mauna Kea glasses (0.32‰) is a small multiple of analytical precision (0.07‰). Nevertheless, they define a positive correlation with MgO (i.e., decreasing MgO is associated with decreasing $\delta^{18}O$). A stronger positive correlation is defined by the more compositionally diverse Pu'u O'o lavas. This trend is offset toward lower $\delta^{18}O$ values at any given MgO content when compared to submarine Mauna Kea glasses, but is otherwise similar. The anomalous submarine Mauna Kea glass from sample SR0698-5.6 falls on the trend defined by Pu'u O'o glasses. Finally, we cannot plot matrix samples from subaerial Mauna Kea lavas on Figure 7e because there is no simple way to estimate their MgO contents excluding accumulated olivine. However, these samples appear to have undergone similar extents of differentiation as submarine lavas (STOLPER et al., 2004) and are consistently ~ 0.5‰ lower in $\delta^{18}O$ than submarine glasses; thus they likely also fall near the trend defined by Pu'u O'o glasses.

Trends in Figure 7e indicate that decreasing $\delta^{18}O$ values (from nominally normal toward anomalously low) are associated with increasing degrees of crystallization-differentiation. This result is important for the interpretation of our data because it suggests that the dominant process controlling variations in $\delta^{18}O$ is caused by, or at least correlated with, magmatic differentiation rather than partial melting and/or variations among mantle sources. It is difficult to determine whether the same trend exists for the larger data set of olivine phenocrysts and microphenocrysts because the $Mg^{\#}$ of each

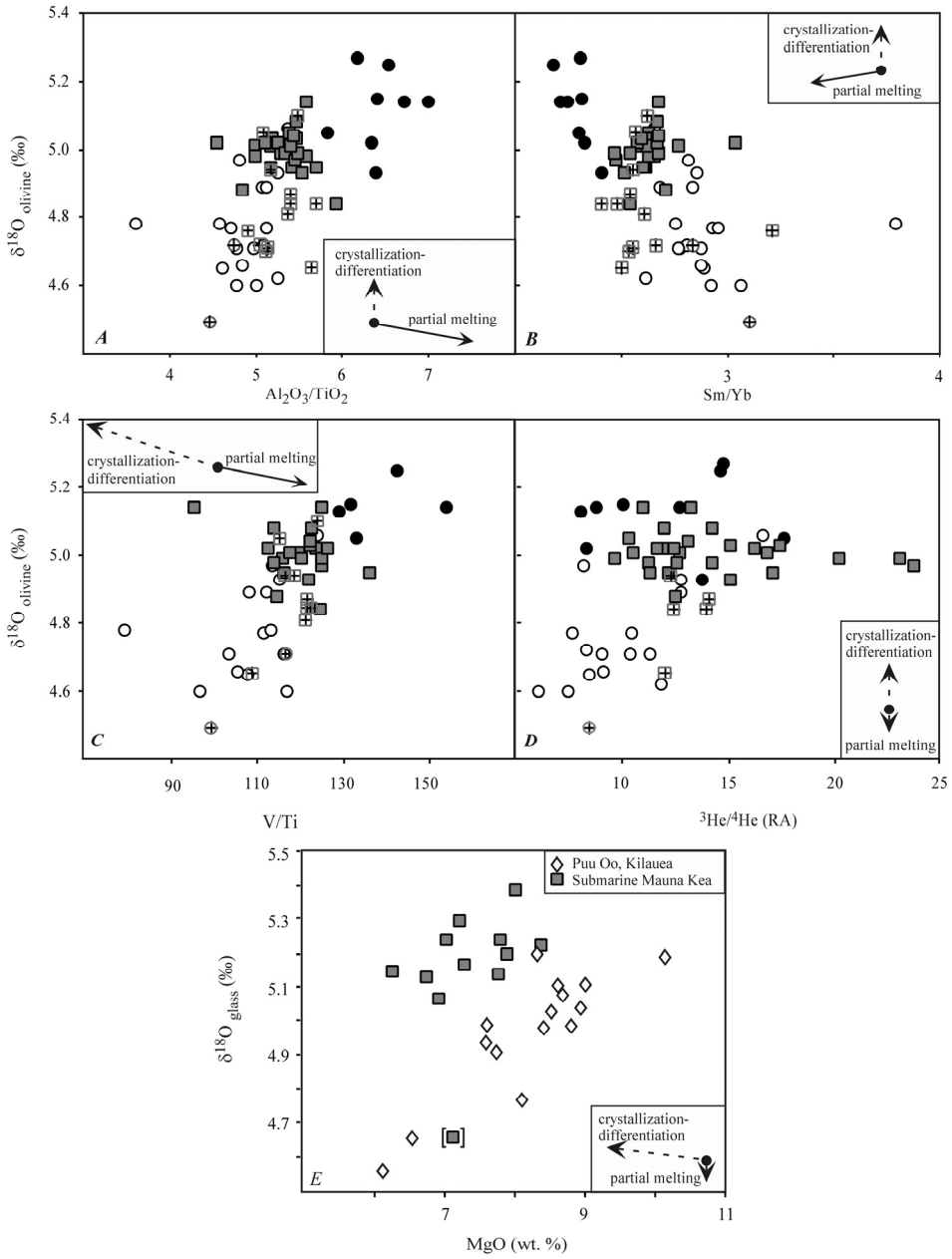


**Figure 7.** Comparison of $\delta^{18}O$ values for phenocrysts and microphenocrysts from the HSDP-2 core with elemental abundances and radiogenic isotope compositions of host lavas. Panels A through D are plotted using symbols given in Figure 1. Panel E also uses these symbols for submarine Mauna Kea lavas, and shows data for recent lavas from Pu'u O'o (Kilauea; taken from GARCIA et al., 1998) as open diamonds.

analyzed grain is not known. However, recall that magnesian, coarse olivines presumably crystallized from higher-MgO liquids than did more iron-rich microphenocrysts; thus, the difference in $\delta^{18}O$ between these two populations (Figure 2) is consistent with the trends in Figure 7e. Finally, the V/Ti ratio should decrease in residual magma during precipitation of olivine ± chromian spinel (GREEN, 1994), and neither element is sufficiently compatible for small amounts of accumulated olivine to overwhelm this signal. Therefore, the positive trend in Figure 7c is consistent, at least in direction, with trends in Figure 7e.

Finally, we further illustrate geochemical differences between relatively high- and relatively low-$\delta^{18}O$ lavas using plots of Sm/Yb, $Al_2O_3/TiO_2$ and Pb isotope composition versus one another (Figure 8), on which arrows indicate the direction of decreasing average $\delta^{18}O$ between these groups (based on Figures 1 and 7) and plotted fields permit comparison of these trends with compositions of Pacific MORBs and/or post-shield and post-erosional Hawaiian lavas (HEGNER et al., 1986; WEST and LEEMAN, 1987; WHITE et al., 1987; KENNEDY et al., 1991; SCHIANO et al., 1997; LASSITER et al., 2000). Figures 8a and 8b show that the transition from higher to lower $\delta^{18}O$ values is associated with a shift in major-element, minor-element and radiogenic isotope composition toward those of post-shield and post-erosional basalts, which have been suggested to sample a source related to local asthenospheric and/or lithospheric mantle (e.g., CHEN and FREY, 1983; see also FEIGENSON et al., 2003 and HUANG and FREY, 2003). It is counterintuitive that this component should be characterized by high Sm/Yb because the oceanic asthenosphere and lithospheric mantle are lower in this ratio than putative plume sources (see discussion by LASSITER and HAURI, 1998). This can be explained if the high Sm/Yb,

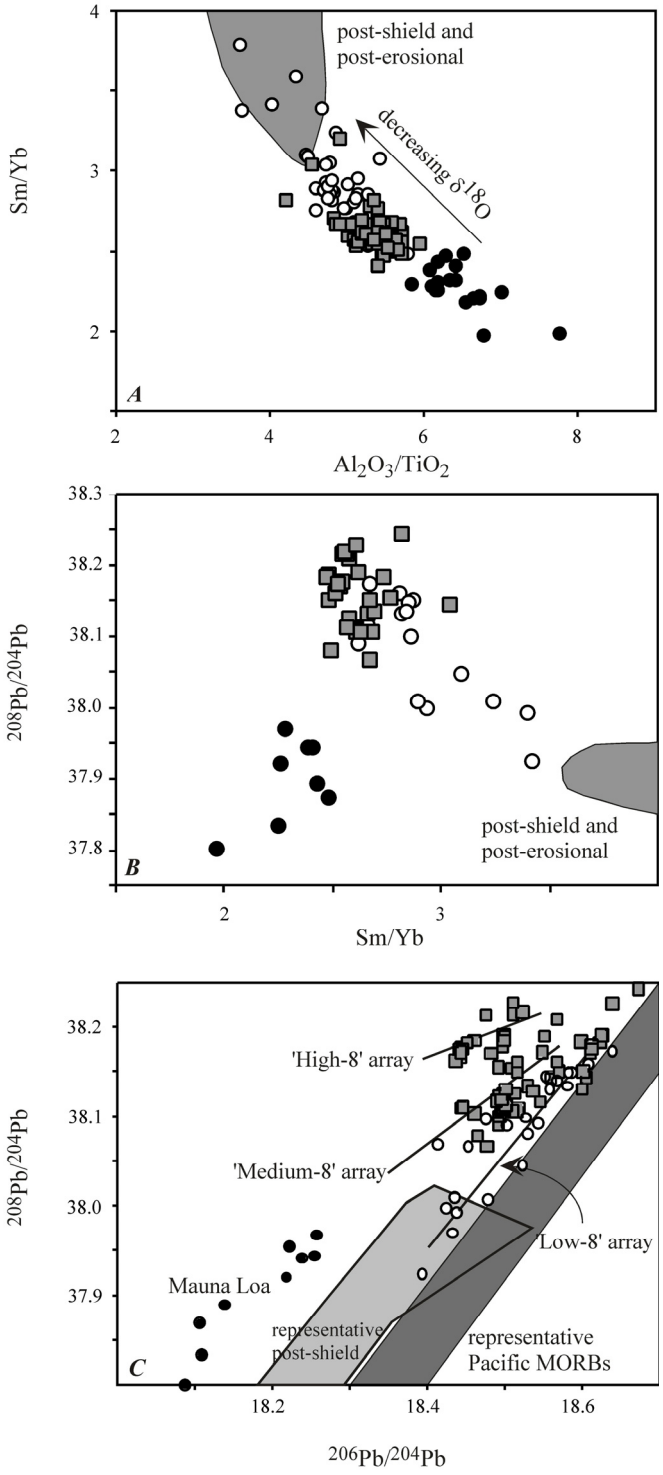


**Figure 8.** Comparison of Sm/Yb ratios with $Al_2O_3/TiO_2$ (panel A) and $^{208}Pb/^{204}Pb$ (panel B) in HSDP-2 lavas (data from FEIGENSON et al., 2003; RHODES and VOLLINGER, 2004, and BLICHERT-TOFT et al., 2003). In both cases, subaerial Mauna Kea lavas (the lowest-$\delta^{18}O$ subset of the HSDP-2 core) are offset toward the field of compositions defined by post-shield and post-erosional Hawaiian basalts (gray fields; data from CHEN and FREY, 1983; HEGNER et al., 1986; WEST and LEEMAN, 1987; KENNEDY et al., 1991; LASSITER et al., 2000, and references therein).

isotopically MORB-like component is a low-degree lithospheric and/or asthenospheric melt, such that its abundance ratios of moderately incompatible elements are fractionated with respect to their sources (CHEN and FREY, 1983).

EISELE et al., (2003) organize Pb isotope variations in HSDP-2 lavas into three groups -- "High-8", "Middle-8", and "Low-8"—each of which defines a linear trend in a plot of $^{208}Pb/^{204}Pb$ versus $^{206}Pb/^{204}Pb$ (Figure 8c). Lavas with anomalously low-$\delta^{18}O$ coarse olivine phenocrysts are only found in subaerial Mauna Kea lavas, which fall only on the "Low-8" array. This result suggests that the Pb isotope composition of a low-$\delta^{18}O$ component contributing to Hawaiian lavas has a $^{206}Pb/^{204}Pb$ ratio of ~ 18.4 to 18.5 and falls on or below the Low-8 array in Figure 8c. This is less radiogenic, but similar in $^{208}Pb^*/^{206}Pb^*$, to the composition suggested for the Kea component by Eiler (1996b). EISELE et al., (2003) suggest that the highest $^{206}Pb/^{204}Pb$ ratios in Figure 8c, where all three Pb isotope arrays converge, are a signature of recycled oceanic crust in the Hawaiian plume. There are no samples with low $\delta^{18}O$ phenocrysts at these most radiogenic compositions, suggesting that this component is not the cause of low $\delta^{18}O$ olivine values. Similarly, several articles in this theme (BLICHERT-TOFT et al., 2003; EISELE et al., 2003; FEIGENSON et al., 2003; KURZ et al., 2004) suggest that relatively thorogenic Pb isotope compositions (the "High-8" array) are a distinctive property of a plume component. Our data provide no evidence that this signature is associated with low $\delta^{18}O$ olivine values. EISELE et al., 2003) discovered "Low-8" Pb isotope array — a signature that does appear to be associated with low $\delta^{18}O$ olivine values — is not discussed at length in other articles in this theme. However, both FEIGENSON et al. (2003) and HUANG and FREY (2003) suggest that it is associated with relatively low degrees of

melting of the edges of the Hawaiian plume, the composition of which might be influenced by the upper-mantle sources of MORBs.

## 4. DISCUSSION

### 4.1. EVALUATION OF THE EFFECTS OF AQUEOUS ALTERATION

Differences in $\delta^{18}O$ between fine and coarse grains of the same mineral (Figures 1c and 2) and deviations of interphase fractionations from high-temperature equilibrium (Figure 3) can be characteristic of weathered or hydrothermally altered rocks (RYERSON et al., 1989; GAZIS et al., 1996; HOLT and TAYLOR, 1998). On the other hand, Pu'u O'o lavas are unambiguously unaltered -- many were collected minutes to hours after eruption -- and are also characterized by microphenocrysts with $\delta^{18}O$ values lower than coarse olivine phenocrysts from other Kilauea lavas (EILER et al., 1996b; GARCIA et al., 1998) and by olivine-glass fractionations that are ~ 0.5‰ out of equilibrium (GARCIA et al., 1998). Therefore, at least some Hawaiian lavas undergo magmatic processes that produced oxygen isotope systematics like those we observe for HSDP-2 samples.

Several lines of evidence suggest the variations we observe in the HSDP-2 core reflect magmatic rather than subsolidus processes: (1) individual samples, and in some cases even entire stratigraphic units, are nearly homogeneous in $\delta^{18}O$ for any one phase (e.g., olivine phenocrysts in the submarine section); (2) stratigraphic variations in $\delta^{18}O$ are subtle (~ 1‰) and change systematically across major boundaries (e.g., the Mauna Loa/Mauna Kea contact); and (3) most (eight of eleven) measured fractionations between glass and microphenocrysts closely conform to high-temperature equilibrium. In contrast, weathering and hydrothermal alteration typically produce shifts in $\delta^{18}O$ of many per mil,

heterogeneity on all scales (from individual grains to many meters), and departures from high-temperature equilibrium fractionation that are largest for the most susceptible materials like glass and fine-grained minerals (e.g., VALLEY and GRAHAM, 1993; EILER et al., 1995; GAZIS et al., 1996; HOLT and TAYLOR, 1998). Finally, (4) values of $\delta^{18}O$ in the HSDP-2 core are uncorrelated with minor-element indices that are sensitive to aqueous alteration (e.g., Rb/Ba, Rb/K, and $K_2O/P_2O_5$ , see HUANG and FREY, 2003).

### 4.2 RELATIONSHIPS BETWEEN PHENOCRYSTS AND HOST LAVAS

Most coarse olivine phenocrysts in HSDP-2 lavas are in some sense xenocrystic because they have oxygen isotope compositions out of equilibrium with their host lavas. These grains are also usually too forsterite-rich to be in Fe/Mg exchange equilibrium with their host lavas and often contain kink-bands, suggesting they resided in cumulate piles prior to entrainment in their host lavas -- both observations that have been used to suggest they are xenocrysts (e.g., CLAGUE et al., 1995; BAKER et al., 1996). However, when interpreting the isotopic compositions of these grains, it is important to distinguish between two possibilities: (1) Hawaiian magmas might vary in $\delta^{18}O$ over the course of their crystallization-differentiation history, such that early formed olivine phenocrysts record one point in that evolution and late-formed phenocrysts and matrix another point. In this case, the coarse, magnesian olivine crystals are related to their host lavas even if they are not in isotopic equilibrium with them at the time of eruption. (2) Alternatively, coarse, magnesian olivine crystals might have precipitated from an unrelated magma in the volcanic edifice and later been entrained in their host lavas prior to eruption; in this case, coarse olivine crystals have no direct relationship to host lavas. Correlations

between the $\delta^{18}O$ of olivine phenocrysts and lithophile-element geochemistry of host lavas provide one means of testing between these alternatives. The existence of such correlations in Figures 7a–7d suggest the first of these alternatives is the case (note that similar arguments apply to the interpretation of Os and He isotope data, which are dominated by coarse olivine crystals (LASSITER and HAURI, 1998; KURZ et al., 2004).

### 4.3. OXYGEN ISOTOPE FRACTIONATION DURING CRYSTALLIZATION AND PARTIAL MELTING

Figures 2, 3, and 7e provide evidence that processes of crystallization-differentiation are associated in some way with variations in $\delta^{18}O$. In this section, we ask whether these variations could be caused by high-temperature, equilibrium fractionations between crystals and melt. EILER (2001) shows that crystallization of olivine ± spinel leads to subtle increases in $\delta^{18}O$ values of residual basaltic melts (~ 0.1‰ for ~ 20% crystallization); further cotectic crystallization of olivine plus clinopyroxene and/or plagioclase leads to minimal additional changes in $\delta^{18}O$ until after olivine is no longer a liquidus phase. The approximate predicted trend of $\delta^{18}O$ and other geochemical indices for these models are shown in Figures 7a–7e as dashed arrows pointing in the direction of increasing extent of crystallization. These predicted changes are nearly orthogonal to observed trends. Similarly, crystallization-differentiation alone produces increases in $\delta^{18}O$ over the course of differentiation; therefore it cannot explain the observation in Figures 2 and 3 that olivine microphenocrysts (generally late-formed, CLAGUE et al., 1995) are lower in $\delta^{18}O$ than olivine phenocrysts (generally early formed, CLAGUE et al., 1995). We conclude that fractional crystallization may be correlated with processes that

change $\delta^{18}O$, but that equilibrium fractionations between solid and melt are not the cause of those relationships.

Magmas parental to HSDP-II lavas were generated by a range of extents of melting of their mantle sources, and there are statistically significant correlations between $\delta^{18}O$ values of phenocrysts and geochemical indices that are sensitive to extent of melting (e.g., Sm/Yb, $Al_2O_3/TiO_2$; V/Ti could also vary with extent of melting; Figures 7a–7c and 8a). Therefore, we consider whether high-temperature equilibrium fractionations between melts and residual solids during partial melting could generate the oxygen isotope variations we observe. EILER, 2001 shows that partial melting of lherzolites can generate a total range in $\delta^{18}O$ of product melt of only 0.10‰ over the course of up to 30 wt.% partial melting. The correlations between $\delta^{18}O$ and other geochemical indices predicted by such calculations are shown in Figures 7a–7e as solid arrows pointing in the direction of increasing extent of melting. These model predictions are obviously at odds with the trends we observe. Moreover, fractionations accompanying partial melting would not be expected to generate systematic isotopic differences between olivine phenocrysts and microphenocrysts (Figure 2). We conclude that partial melting of isotopically homogeneous peridotite is incapable of producing the oxygen isotope variations we observe.

### 4.4. POSSIBLE SOURCES OF LOW-$\delta^{18}O$ COMPONENTS

The preceding discussion establishes that the oxygen isotope stratigraphy of the HSDP-2 core principally reflects differences in $\delta^{18}O$ among the mantle sources and/or lithospheric contaminants of Hawaiian lavas rather than subsolidus alteration, fractional

crystallization and/or partial melting. In this section we discuss amounts and identities of components that could have led to these oxygen isotope variations.

Most mantle rocks and mantle-derived magmas span a narrow range in $\delta^{18}O$ that we have referred to as "normal" throughout preceding sections of this paper (i.e., $\delta^{18}O$ olivine between ~ 5.0 and 5.2‰, or $\delta^{18}O$ melt of 5.4 to 5.6‰; EILER, 2001). Because a wide range of ultramafic rocks have $\delta^{18}O$ values in this range, little specific is implied about the mantle sources of basalts that also have such values, other than that they lack recycled crustal materials in abundances greater than a few percent. However, where values outside this range are observed, they provide relatively specific constraints on the origin and amounts of isotopically anomalous materials in the sources of those lavas. In this context, the important finding of this study is that olivine phenocrysts in subaerial Mauna Kea lavas and both olivine microphenocrysts and host glass or matrix throughout Mauna Kea are lower in $\delta^{18}O$ than this "normal" range.

The only major earth reservoir known to have a $\delta^{18}O$ value significantly less than average mantle is the hydrosphere, and rocks only take on this value as a result of high-temperature water-rock interaction. The greatest volume of low-$\delta^{18}O$ rocks produced by this process are in the oceanic lithosphere, which undergoes extensive hydrothermal alteration at ridges (SHANKS, 2001). These low-$\delta^{18}O$ signatures persist long after the lithosphere has cooled (GREGORY and TAYLOR, 1981). Furthermore, there is evidence that these signatures survive subduction and are mixed into the mantle (GARLICK et al., 1971). It is poorly known, but important to our discussion, how deep in the ocean lithosphere low-$\delta^{18}O$ rocks exist. These compositions are common in the gabbroic portions of most characterized sections of ocean crust (MUEHLENBACHS, 1986), but it is

unclear whether ultramafic rocks beneath the petrologic MOHO are also commonly low in $\delta^{18}O$. On one hand, permeabilities decrease dramatically at these depths and limit fluid infiltration (WALTHER and ORVILLE, 1982), so low $\delta^{18}O$ values are not expected. On the other hand, some ophiolites contain low $\delta^{18}O$ ultramafic rocks that could have acquired their oxygen isotope signatures before obduction (MILLER et al., 2001), so aqueous alteration might penetrate deep in the ocean lithosphere despite expectations. Finally, active volcanoes frequently support meteoric hydrothermal systems, particularly in portions of their edifices having extensional structures. These systems are believed to be the principle sources of $^{18}O$-depleted crustal contaminants responsible for low $\delta^{18}O$ values in Icelandic lavas (e.g., EILER et al., 2000c), and have been proposed as a contributor to (although perhaps not the only cause of) low $\delta^{18}O$ values in recent Kilauea lavas (GARCIA et al., 1998).

A key aspect of all low-$\delta^{18}O$ components is that they must be sampled in large mass fractions to produce measurable decreases in the $\delta^{18}O$ of basaltic lavas. For example, the contrast between even the lowest-$\delta^{18}O$ portions of the oceanic lithosphere (~ 0‰) and average mantle is only ~ 5‰, and thus, lavas must sample at least 10% of such materials as subducted components of their mantle sources or as shallow-level contaminants in order to reach $\delta^{18}O$ olivine values of ~ 4.5‰. Hydrothermally altered rocks in subaerially exposed volcanic edifices can be lower in $\delta^{18}O$ than 0‰ (down to ~ -5 to -10‰) due to the influence of low-$\delta^{18}O$ meteoric water and boiling processes; in these cases, proportionally smaller amounts of contamination (i.e., ~ 6 to 3%, respectively) would be required to produce measurable shifts in the $\delta^{18}O$ of erupted lavas.

## 4.5. Link Between Crystallization and the Abundance of Low-$\delta^{18}O$ Component(s)

Two key features of our results are (1) the abundance of the low-$\delta^{18}O$ component led not only to variations in $\delta^{18}O$ of erupted lavas, but also to oxygen isotope disequilibrium between components of those lavas (Figures 1c, 2, and 3), and (2) $\delta^{18}O$ values of glasses (Figure 7e) and perhaps phenocrysts (Figure 7c) are correlated with chemical indices that are sensitive to crystallization-differentiation. In this section, we propose a model that quantitatively explains these observations as consequences of progressive addition of low-$\delta^{18}O$ component (whatever its origin) to Hawaiian magmas over the course of their crystallization-differentiation.

Figure 9 summarizes the essential features of our model, including the extent of crystallization and identity of phases crystallizing from primary basaltic magma parental to HSDP-2 lavas (Figure 9a; calculated using the MELTs algorithm, assuming the Baker et al., 1996 estimate for primary Mauna Kea magma, a pressure of 1000 bars and oxygen fugacity controlled by the QFM buffer), the amount of low-$\delta^{18}O$ component mixed into that magma during its crystallization-differentiation (Figure 9b; assuming several representative cases detailed below), and the Mg# of olivine grown from that magma at any point in the differentiation/mixing process (Figure 9c; based on output of the calculated fractionation-crystallization path for primary Mauna Kea magma illustrated in Figure 9a). For the purposes of simplicity, we assume that the low-$\delta^{18}O$ component is mafic in composition, so that it does not substantially dilute the MgO content of basaltic magmas into which it is mixed. All three variables are plotted versus model magmatic

temperature (decreasing to the right), which is a useful proxy for order of increasing extent of differentiation.

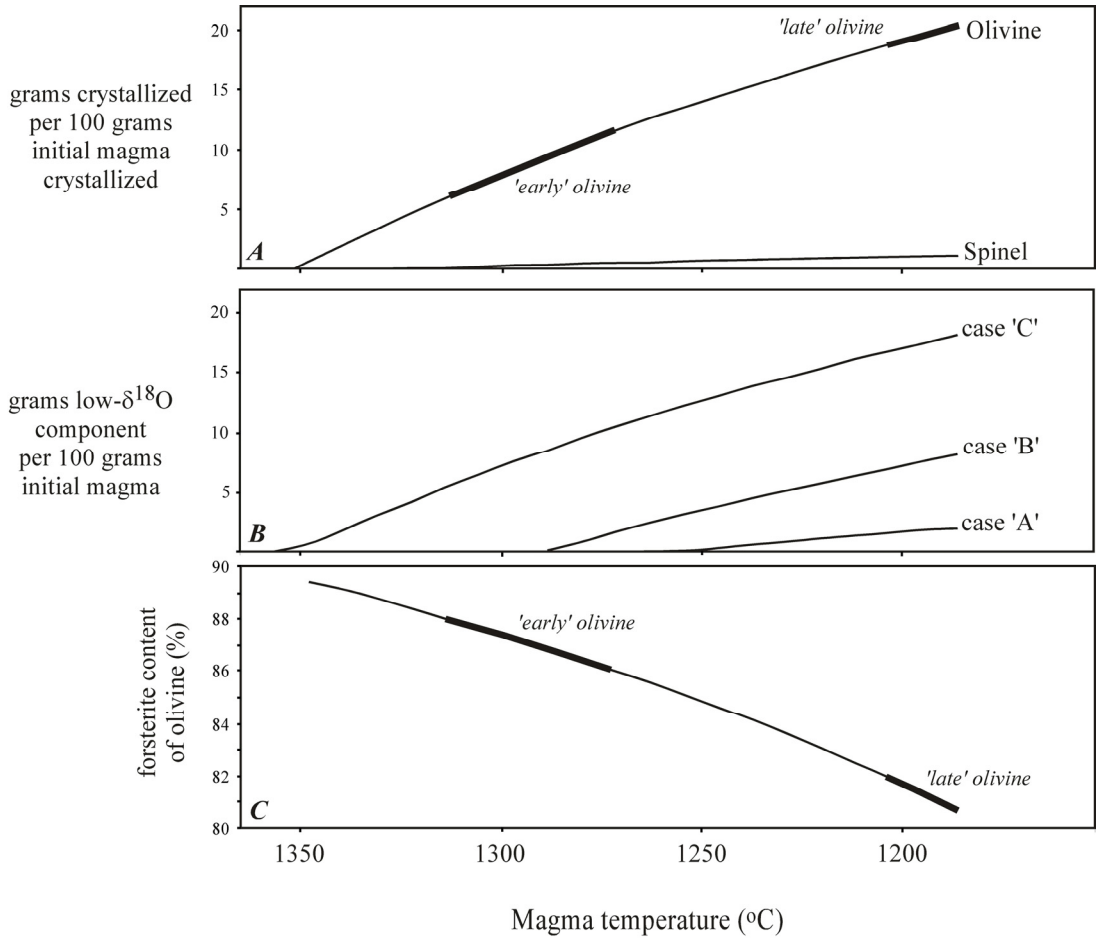


**Figure 9.** Outline of the essential features of our proposed model for simultaneous crystallization-differentiation and mixing with a low-$\delta^{18}O$ component. Amounts, identities and mineral-chemistries of crystallizing phases are calculated using the MELTs algorithm (GHIORSO et al., 1994) assuming an initial Mauna Kea magma given by BAKER et al., 1996. Amounts of low-$\delta^{18}O$ component added over the course of crystallization-differentiation are prescribed for each of three cases (A, B, and C), as shown. Heavy line segments in panels A and C show the populations of "early" and "late" olivine we consider as approximate model predictions for phenocrysts and microphenocrysts, respectively.

Systems undergoing processes of combined crystallization and mixing can vary in relative timing of the two processes and in the total amount of admixed component. To illustrate such variations, we show three cases: addition of low $\delta^{18}O$ component is small in extent and begins late in the history of olivine crystallization (case A); addition of low-$\delta^{18}O$ component is moderate in extent and begins after approximately half the crystallizing assemblage has precipitated (case B); and addition of low-$\delta^{18}O$ component is large in extent and begins early in the history of olivine crystallization (case C). Other combinations are possible; these were chosen because they are plausible and, as is shown below, lead to a range of oxygen isotope systematics that resembles our data. We assume that the maximum amount of low-$\delta^{18}O$ component that can be added in case C is controlled by the heat budget of a system undergoing assimilation/fractional crystallization (i.e., the latent heat of fusion of mafic, low-$\delta^{18}O$ component is less than or equal to the latent heat of crystallization of the precipitating assemblage plus the specific heat change of cooling magma). However, this limit need not apply to systems in which the heat liberated by one generation of magmas contributes to melting contaminants that are mixed into another generation of magmas (BAKER et al., 1996). Thus, larger amounts of low-$\delta^{18}O$ component could be added even if it is a lithospheric contaminant.

The important feature of this model is that both olivine crystallization and addition of low-$\delta^{18}O$ component take place gradually and simultaneously. As a result, the first-formed olivine grows from magma containing less low-$\delta^{18}O$ component than does the last-formed olivine, and, assuming early formed olivine cannot isotopically re-equilibrate with host magma (reasonable given the slow rates of oxygen self-diffusion in olivine; RYERSON et al., 1989), only the last olivine to crystallize is in oxygen-isotope equilibrium

with the erupted host lava. For the purposes of discussion and comparison with our data, we discriminate between two populations of olivine that form at different stages of the model differentiation process: "early" olivines having forsterite contents of 88 to 86% and "late" olivines having forsterite contents of 82 to 80%. These two populations are marked in Figures 9a and 9c as heavy black line segments. The "early" olivines were chosen to have forsterite contents comparable to those of the most abundant coarse olivine phenocrysts in Hawaiian lavas (CLAGUE et al., 1995; BAKER et al., 1996; Table 2) and reasonably represent the predictions of our model for phenocryst data (Figure 1a). The "late" olivines were chosen to have forsterite contents comparable to those of skeletal, equant and resorbed microphenocrysts in Hawaiian lavas (CLAGUE et al., 1995; BAKER et al., 1996; Table 2) and reasonably represent the predictions of our model for microphenocryst data (Figure 1c; Table 2).

By assigning $\delta^{18}O$ values to the primary melt and the low-$\delta^{18}O$ component, and by adopting existing constraints on oxygen isotope fractionations associated with olivine crystallization (EILER, 2001), the model outlined in Figure 9 predicts the differences in $\delta^{18}O$ between early and late formed phenocrysts, between phenocrysts and final (i.e., post-differentiation) host melt, and the relationship between melt -- phenocryst fractionations and the amount of low-$\delta^{18}O$ component added, and the relationship between MgO and $\delta^{18}O$ in erupted melt. We adopted values of 5.5‰ for primary melt (equal to the $\delta^{18}O$ of normal MORBs and similar to the matrix of a Mauna Loa lava analyzed in this study) and a value of 0‰ for the low-$\delta^{18}O$ component. This value is at the lower end of the range for hydrothermally altered mafic and ultramafic rocks near the base of the oceanic crust (MUEHLENBACHS, 1986; MILLER et al., 2001) and their

subducted equivalents (GARLICK et al., 1971), and is within the range expected for hydrothermally altered rocks in Kilauea's east rift zone (GARCIA et al., 1998). Thus it is a single model value that provides reasonable predictions regardless of the source (plume, lithosphere, or edifice) of low-$\delta^{18}O$ component. In reality, a range of $\delta^{18}O$ values is expected of any of the possible low-$\delta^{18}O$ components, and this model is expected to fit only the directions and approximate magnitudes of observed trends and ranges.

Figure 10a illustrates our model's predictions for the locations of "early" and "late" olivines on a plot of $\delta^{18}O_{olivine}$ versus $\delta^{18}O_{melt}$. This figure is plotted at the same scale as Figure 3 and data from Figure 3 are reproduced as faint gray symbols. Ranges predicted for "early" olivines in case A (minor mixing), B (moderate mixing) and C (extensive mixing) are shown as black boxes and labeled according to the model case they represent. "Late" olivines are always predicted to fall on or near the equilibrium line of slope 1; italicized letters mark the predicted locations on that line for cases A, B and C. Our model quantitatively reproduces all the first-order features of our data: phenocrysts, like model "early" olivine, fall above and to the left of the equilibrium line, and are further from that line in low-$\delta^{18}O_{melt}$ lavas than in high-$\delta^{18}O_{melt}$ lavas (i.e., the lowest $\delta^{18}O$ phenocrysts are preferentially found in exceptionally low-$\delta^{18}O$ hosts). This latter detail is predicted by our model but would not be expected if phenocrysts were accidental xenocrysts that crystallized from higher-$\delta^{18}O$ magmas unrelated to their host. Furthermore, most microphenocrysts, like model "late" olivine, fall on the equilibrium line and are ~ 0.2‰ lower in $\delta^{18}O$ than phenocrysts from related lavas (we presume the few exceptions are small olivine grains that we classified as microphenocrysts but are not the last olivines to grow from their host). Finally, the difference in $\delta^{18}O$ between early

and late olivines is expected to increase as the $\delta^{18}O$ of host melt decreases -- also consistent with the data in Figure 3.

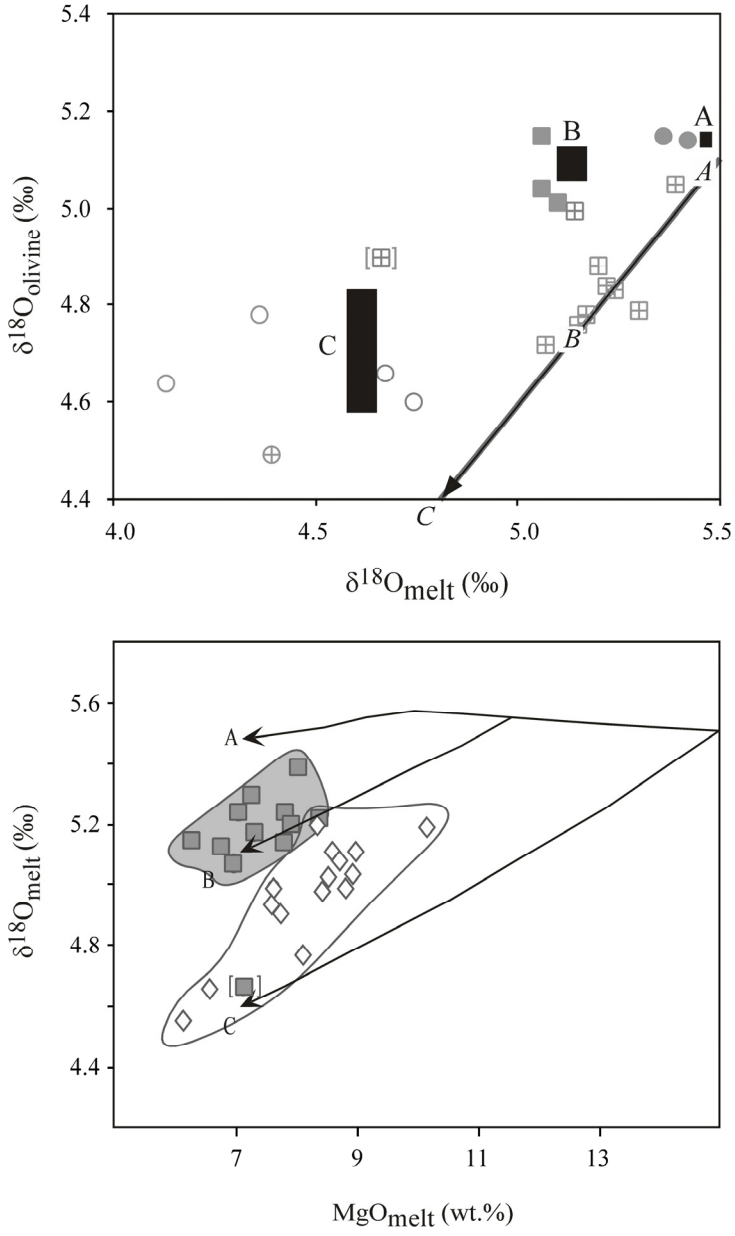


**Figure 10.** Comparison of our observations with the predictions of the model outlined in Figure 9, assuming initial melt has a $\delta^{18}O$ of 5.5‰ (comparable to NMORBs and in equilibrium with typical olivine in oceanic basalts (EILER, 2001) and the low-$\delta^{18}O$ component has a $\delta^{18}O$ of 0‰ (at the lower end of the range for hydrothermally altered

oceanic lithosphere and its subducted equivalents and within the range possible for materials in the Hawaiian volcanic edifice). Figure 10a plots our model predictions in the same way data is plotted in Figure 3. Black squares show model predictions for "early" olivine for cases A, B and C (as labeled). The black arrow shows the predicted change in $\delta^{18}O$ of melt and coexisting, equilibrated olivine with increasing amounts of differentiation and mixing; italicized letters show the locations on that line of predictions for "late" olivine for cases A, B and C. Figure 10b plots our model predictions in the same was data is plotted in Figure 7e. In this case, model predictions for melt are shown for cases A, B and C (as labeled). In both cases, gray symbols reproduce data from Figures 3 and 7e, respectively.

Figure 10b illustrates our model's predictions for the relationships between $\delta^{18}O$ and MgO of melt over the course of combined crystallization-differentiation and mixing with low-$\delta^{18}O$ component; lines for cases A, B and C are marked. Data for Mauna Kea and Pu'u O'o glasses are reproduced from Figure 7e as faint gray symbols; fields surround each data set for added clarity. Figure 10b covers a broader scale than Figure 7e in order to encompass model predictions for more primitive glasses that might eventually be found and analyzed for $\delta^{18}O$. As in Figure 10a, model trends provide a satisfactory explanation for the observed trends. In detail, model B appears to provide the best fit to data for submarine Mauna Kea lavas (as in Figure 10a), whereas cases intermediate between models B and C appear to provide better fits to data from Pu'u O'o and the anomalous submarine Mauna Kea sample, SR0698-5.6 (as is the case for that sample and subaerial Mauna Kea samples in Figure 10a).

We conclude on the basis of the preceding discussion that the addition of low-$\delta^{18}O$ component to magmas parental to HSDP-2 lavas was gradual and took place while they

were undergoing fractional crystallization of olivine. This is a powerful constraint on the origin of the low-$\delta^{18}O$ component and the processes by which it was sampled because of the limited depth range over which Hawaiian basalts undergo crystallization-differentiation. Oceanic intraplate basalts generally differentiate within the lithosphere. It has been argued that they often do so at pressures of ~ 10 to 20 kb (~ 35 to 70 km depth, or within the lower lithospheric mantle) based on the importance of clinopyroxene fractionation in their differentiation (ALBAREDE, 1992). However, Hawaiian tholeiites generally lack clear evidence of clinopyroxene fractionation (e.g., CLAGUE et al., 1995; HUANG and FREY, 2003). Their differentiation is instead dominated until its latest stages by olivine. Fluid-inclusion barometry indicates that this olivine generally forms at pressures less than or equal to ~ 5 kb (~ 15 km -- approximately the depth to the MOHO beneath Mauna Kea (e.g., ROEDDER, 1965). ANDERSON and BROWN, 1993 suggest, on the basis of $CO_2$ contents of olivine-hosted melt inclusions, that most olivine crystallization takes place at pressures near 2 kb. This corresponds to a depth of ~ 5 to 6 km—within the volcanic edifice of a fully grown Hawaiian volcano or perhaps within the underlying Cretaceous crust in a younger and smaller one. In light of these arguments, our data appear to require that the low-$\delta^{18}O$ component (whatever its origin) was added to HSDP-2 magmas while they resided in the upper portions of the Cretaceous lithosphere (approximately at or above the MOHO) and/or the volcanic edifice.

## 5. SUMMARY AND CONCLUSIONS REGARDING THE PETROGENESIS OF LOW-$\delta^{18}O$ HSDP-II LAVAS

The most significant interpretations we put forward in preceding sections are summarized and briefly elaborated upon in the following paragraphs:

• Oxygen isotope compositions of handpicked olivine, glass and groundmass from HSDP-II lavas, including interphase fractionations, largely or entirely reflect magmatic rather than subsolidus processes and are not dominantly controlled by high-temperature equilibrium fractionations accompanying partial melting and/or crystallization-differentiation. Those compositions can reflect mixing between magmas having normal $\delta^{18}O$ and magmas and/or assimilants having anomalously low $\delta^{18}O$. Candidates for the low-$\delta^{18}O$ component include hydrothermally altered oceanic lithosphere in the Pacific plate, subducted fragments of hydrothermally altered oceanic lithosphere entrained in the Hawaiian plume, or hydrothermally altered components of the Hawaiian volcanic edifice.

• The low-$\delta^{18}O$ component(s) was added over the course of crystallization-differentiation of higher-$\delta^{18}O$ magma. This restricts the mixing process to depths within ~ 15 km of the surface -- the depth interval of olivine crystallization.

• Low-$\delta^{18}O$ component is present, but low in abundance and only detectable in late-stage differentiation products (i.e., glass and microphenocrysts, but not coarse, magnesian phenocrysts) in submarine Mauna Kea lavas. In contrast, the low-$\delta^{18}O$ component is high in abundance and detected in the earliest differentiation products throughout subaerial Mauna Kea lavas.

• Anomalously low-$\delta^{18}O$ olivine phenocrysts appear suddenly at the subaerial/submarine transition in Mauna Kea. This sharp transition is mirrored by a

change in the distribution of fractionation-normalized $SiO_2$ contents (from bimodal in the submarine section to unimodal in the subaerial section).

• Low-$\delta^{18}O$ signatures are correlated with other geochemical indices that are associated with low-degree melting of upper mantle and/or lithosphere on the margins of the Hawaiian plume (CHEN and FREY, 1983; BLICHERT-TOFT et al., 2003; HUANG and FREY, 2003). Most such correlations are defined by the contrast between average compositions of subaerial and submarine Mauna Kea lavas (Figures 7a–7d and 8); in this case, we believe these correlations could reflect either unique geochemical properties of a low-$\delta^{18}O$ component, or a coincidence that a low-$\delta^{18}O$ component is sampled in greater abundance at the same time that primary magmas are changing in composition for other reasons. In addition, an interval of the submarine Mauna Kea section (between 2150 and 2350 mbsl) records correlated stratigraphic trends in $\delta^{18}O$ and various radiogenic isotope ratios (Figure 6); this observation suggests that low-$\delta^{18}O$ values are derived from a component with relatively MORB-like geochemistry that can be present at any time in Mauna Kea's evolution.

• There is no evidence that anomalously low $\delta^{18}O$ values are associated with highly anomalous, presumably plume-derived radiogenic isotope compositions (i.e., high $^{208}Pb^*/^{206}Pb^*$, $^3He/^4He$, and $^{87}Sr/^{84}Sr$; low $\varepsilon_{Nd}$ and $\varepsilon_{Hf}$).

Our results are difficult to reconcile with the interpretation that low $\delta^{18}O$ values in Hawaiian lavas are derived from a component of the Hawaiian plume (HARMON and HOEFS, 1995; HAURI, 1996; BLICHERT-TOFT et al., 1999; LASSITER et al., 2000). In particular, it is difficult to envision why a low $\delta^{18}O$ source component would be sampled in increasingly larger amounts over the course of low-pressure crystallization-

differentiation. Furthermore, one would expect lavas rich in low-$\delta^{18}O$ component, if it consists of ancient, recycled lithosphere, to have exotic radiogenic isotope compositions (e.g., high $^{206}Pb/^{204}Pb$, EISELE et al., 2003) rather than the observed modest shifts toward compositions resembling modern MORBs. Finally, the only positive evidence previously cited for the plume origin of this component was based on it having a lower εHf value than normal MORBs (BLICHERT-TOFT et al., 2003). However, KEMPTON et al. (2000) and CHAUVEL and BLICHERT-TOFT (2001) recently showed that Pacific MORBs are unusually low in $\varepsilon_{Hf}$, ranging down to values similar to Mauna Kea lavas (i.e., Hf isotope data alone are consistent with local asthenosphere, local lithosphere, or the plume as sources of the low-$\delta^{18}O$ component). Therefore, while we recognize that one could construct a model describing our results in terms of a low-$\delta^{18}O$ plume component, there is no evidence clearly in favor of this hypothesis and several observations appear to argue against it. We instead focus our attention on two models involving contamination in the lithosphere or volcanic edifice, which we think can more plausibly explain a wider range of our data. These models are schematically illustrated in Figure 11 and explained in the following paragraphs.

### 5.1. COUPLED EVOLUTION OF MANTLE SOURCES AND SHALLOW VOLCANIC PLUMBING (FIGURE 11A)

The end of Mauna Kea's period of shield building volcanism could have involved two temporal trends: (1) gradually increasing contributions of a "normal"- $\delta^{18}O$, low-degree melt of the asthenosphere and/or lithospheric mantle beneath Hawaii as the volcano moved away from the plume axis (HUANG and FREY, 2003) and (2) gradually increasing

degrees of contamination by low-$\delta^{18}O$ rocks in the volcanic edifice, such as occurs today in Kilauea's east rift zone (GARCIA et al., 1998). These two different processes need not be correlated with one another, but one can imagine how they could be. As the volcano grows and ages, it moves off the plume axis and taps greater proportions of low degree melts from the plume edges. Simultaneously, the edifice gets larger so that subaerially exposed rift zones and their low-$\delta^{18}O$ hydrothermal systems make up more of their upper several kilometers. Thus, the population of lavas tapping the largest proportion of source components from the plume edges or the over-riding plate will be exposed to the lowest-$\delta^{18}O$ rocks in the volcanic edifice through which they erupt.

This hypothesis provides an explanation for evidence that low-$\delta^{18}O$ component is added to Mauna Kea magmas gradually over the course of their differentiation (Figures 2 and 7e) because the heat required to melt crustal assimilants is expected to be, in part, balanced by the latent heat of crystallization of phenocrysts (e.g., ALDANMAZ et al., 2000; BINDEMAN and VALLEY, 2001) and the low-$\delta^{18}O$ component is only available in the crustal environments where most crystallization takes place. It also provides an explanation for why the subaerial/submarine transition is a sharp break in oxygen isotope composition of phenocrysts (Figure 1a), but only roughly coincides with the start of gradual changes in radiogenic isotope and trace element geochemistry (Figure 4): The lower limit in $\delta^{18}O$ of hydrothermally altered rocks in submarine volcanoes is ~ 0‰ (the value for seawater), whereas subaerial volcanoes can contain hydrothermally altered rocks with $\delta^{18}O$ values down to ~ -10 to -15‰ caused by interaction with meteoritic precipitation and products of low-pressure boiling processes (GARCIA et al., 1998, and references therein). Thus, the change in $\delta^{18}O$ across the subaerial/submarine transition in

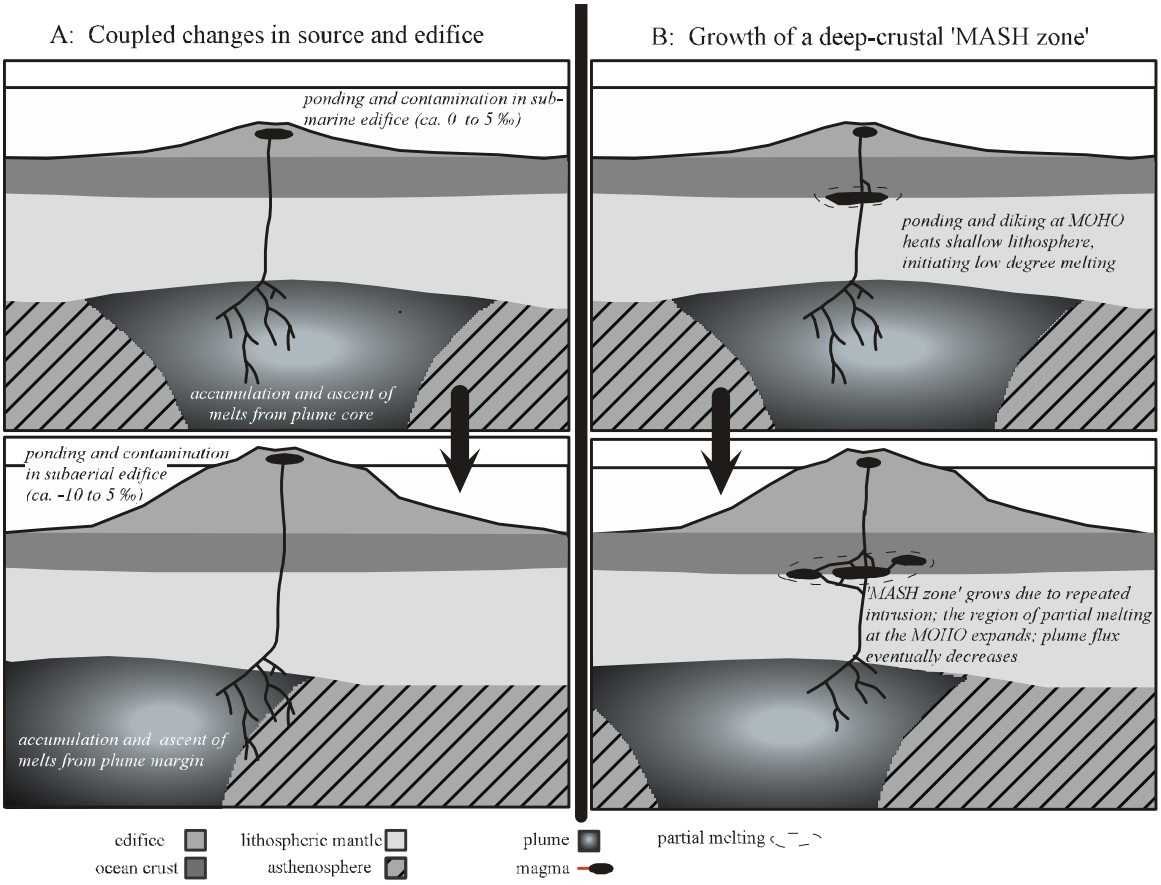


**Figure 11.** Cartoons illustrating two proposed models for the temporal evolution of Mauna Kea that are consistent with the oxygen isotope geochemistry and other geochemical properties of its lavas. In the first model (A; the top panel shows an early stage of the volcano's evolution and the bottom panel shows the end of shield-building volcanism), aging of the volcano is associated with two processes: increasing proportions of low-degree melt from the cool outer margins of the plume (the composition of which is influenced by mixing with upper mantle) and/or the lithospheric mantle, and simultaneously increasing amounts of contamination by low-$\delta^{18}O$ volcanic edifice in the subaerial rift zones through which magmas pass. According to this model, correlations between $\delta^{18}O$ and other geochemical properties (e.g., Figures 6, 7, and 8) are fortuitous or result from the fact that both processes are increasingly important over the same span of the volcano's life. In the second model (B; the top panel shows an early stage of the

volcano's evolution and the bottom panel shows the end of shield-building volcanism), low degree melt of the shallow lithosphere is generated in a "MASH zone" near the petrologic MOHO (HILDRETH and MOORBATH, 1988). The proportional contribution of that melt to erupted lavas increases with time as a result of gradual heating of the "MASH-zone" by repeated intrusion combined with decreased magma flux as the volcano drifts off the plume axis. Both models are consistent with existing constraints but have advantages and disadvantages. The first calls on processes known to occur in the shallow plumbing systems of Hawaiian volcanoes (GARCIA et al., 1998) but requires special pleading to produce geochemical trends (Figures 6 through 8). The second explains these geochemical trends but calls on a process that is little explored in oceanic intraplate settings, and requires a significant fraction of olivine crystallization occurs at great depths (~10 to 15 km).

Mauna Kea could reflect a sudden increase in the contrast in $\delta^{18}O$ between its primary magmas and hydrothermally altered rocks in its volcanic edifice. Finally, this model could help understand the change in modality of fractionation-normalized $SiO_2$ contents across the subaerial/submarine transition (Figure 5). STOLPER et al. (2004) suggest that intermediate $SiO_2$ magmas could be mixtures of the high- and low-$SiO_2$ magmas that define the bimodal population that dominates the submarine section. Furthermore, they note that intermediate $SiO_2$ submarine glasses are always degassed and suggest this might signify that magma mixing only takes place in high-level crustal magma chambers. If so, the drop in $\delta^{18}O$ and shift in modality of $SiO_2$ contents could indicate that the submarine/subaerial transition coincides with the establishment of long-lived, shallow crustal magma reservoirs where mixing, degassing and assimilation take place before eruption. Note, however, that submarine hyaloclastites presumably formed by subaerial eruptions that broke apart at the shore (i.e., they too erupted through shallow magma

reservoirs; MOORE, 2001), and thus it is hard to understand why there are no hyaloclastites with anomalously low-$\delta^{18}O$, coarse olivine phenocrysts typical of subaerial Mauna Kea lavas (Figure 1a).

If the model illustrated in Figure 11a is correct, low-$\delta^{18}O$ lavas are evidence for the passage of magmas through hydrothermally active parts of their volcanic edifices and thus they provide insight on the past volcanology and hydrology of Hawaii. The broadest, consistent feature of oxygen isotope variations among Hawaiian lavas is that those from Kea trend volcanoes (Kilauea, Mauna Kea, Kohala and Haleakala) are often lower in $\delta^{18}O$ than typical terrestrial basalts whereas those from Loa trend volcanoes (Loihi, Mauna Loa, Hualalai, Lanai, Koolau, and perhaps Kauai) are not. Previously, this difference has been interpreted to reflect greater contributions to magmas parental to "Kea trend" lavas of a low-$\delta^{18}O$ source component in the Hawaiian plume or over-riding Cretaceous Pacific lithosphere (EILER et al., 1996b; LASSITER and HAURI, 1998). If, instead, low $\delta^{18}O$ values are acquired during their transit through the volcanic edifices through which they erupt, the systematic difference in $\delta^{18}O$ between the Loa and Kea lavas requires a different explanation. One simple possibility is that Kea trend volcanoes have abundant low-$\delta^{18}O$, hydrothermally altered rocks within their volcanic edifices during their subaerial evolution whereas Loa trend volcanoes do not. This difference could be a consequence of the fact that the northeast sides of the Hawaiian islands receive more rain than their southwest sides (i.e., so vigorous hydrothermal systems are only present in rift zones trending toward the northeastern shores). However, large parts of Mauna Loa do receive significant amounts of rain, and thus requires that there is a threshold in amount of rainfall, currently not understood, below which vigorous

hydrothermal systems cannot develop. A further weakness of this hypothesis is that, except under special circumstances, contamination in volcanic edifices involves minimal contrasts in most geochemical properties between magmas and contaminants (because the latter are solidified and altered equivalents of the former). Therefore, this model requires that correlations between $\delta^{18}O$ and various lithophile-element abundance ratios and radiogenic isotope ratios (Figures 6 through 8) are fortuitous.

### 5.2. A "MASH" ZONE BENEATH HAWAII (FIGURE 11B)

The low-$\delta^{18}O$ component could be a low-degree melt of the Cretaceous Pacific crust and/or shallow lithospheric mantle that mixes into Hawaiian magmas as they begin to differentiate at depths near the MOHO. The best analogy with such deep-crustal contamination processes could be the "MASH"-zones ("Melting-Assimilation-Storage-Homogenization") suggested to exist in lower crustal magmatic systems at convergent margins (HILDRETH and MOORBATH, 1988). These systems are characterized by repeated intrusion of mantle-derived basalt near the MOHO, producing a complex of dikes and sills that heats and partially melts intervening septa of pre-existing lower-crustal and upper mantle rocks. Mixing of these partial melts into the intruding basalts produces hybrid magmas. In continental convergent margins, this process leads to siliceous hybrid magmas because the quartzo-feldspathic crustal rocks produce $SiO_2$-rich partial melt. In this case, one might expect this process to lead to systematically higher fractionation-normalized $SiO_2$ in low $\delta^{18}O$ lavas, in contrast with our observations (Figures 1 and 5). However, similar systems active near the oceanic MOHO might instead produce low-degree partial melt of mafic and ultramafic rock types, which could have smaller major-

element contrasts with invading plume-derived magmas and thus produce less obvious changes in major element chemistry.

This hypothesis could be consistent with our conclusion that low-$\delta^{18}O$ component was added to Mauna Kea magmas over the course of their differentiation, but only if olivine crystallization occurs at depths within the lithosphere and below the volcanic edifice (~10 to 15 km). Hawaiian magmas crystallize olivine over a range of depths, the upper end of which is consistent with this restriction and the lower end of which (~ 0 to 5 km) is not. It would be challenging but possible to determine the $\delta^{18}O$ values of individual olivine crystals from known crystallization depths; we suggest such measurements are an attractive goal for testing and/or elaborating this hypothesis.

Perhaps the greatest strength of the model illustrated in Figure 11b is that it explains the association of low-$\delta^{18}O$ values with relatively low $^{3}He/^{4}He$ and low $^{208}Pb^{*}/^{206}Pb^{*}$ at moderate $^{206}Pb/^{204}Pb$ (Figures 7 and 8), and is consistent with evidence suggesting the low-$\delta^{18}O$ component is relatively low in $^{87}Sr/^{86}Sr$ and high in $\varepsilon_{Hf}$ (Figure 6). All of these isotopic shifts are consistent with addition to primary Hawaiian magmas of a component derived from the local asthenosphere and/or lithosphere (EISELE et al., 2003; HUANG and FREY, 2003; KURZ et al., 2004).

Major-element and rare earth-element data for these samples, as well as previous Os isotope data for samples from the HSDP-I core, place restrictions on this model. The lowest $\delta^{18}O$ values in Mauna Kea lavas are associated with low $Al_2O_3/TiO_2$ and high Sm/Yb ratios, consistent with them sampling a component resembling post shield and post-erosional lavas (Figures 7 and 8). These characteristics can be explained by low degrees of melting of an ultramafic source (CHEN and FREY, 1983; HIROSE and KUSHIRO,

1993; BAKER et al., 1995; FEIGENSON et al., 2003). Furthermore, previous work shows that low-$\delta^{18}O$ Hawaiian lavas have Os isotope compositions like those of most other terrestrial basalts rather than relatively radiogenic compositions expected of old basaltic rocks. This also suggests the low-$\delta^{18}O$ component is ultramafic (or very young, as in the model discussed in the previous section). Therefore, in the context of the model depicted in Figure 11b, the low-$\delta^{18}O$ component must come from olivine-rich rocks in the Pacific plate, where intrusion and gradual heating produces low degree melts that mix with infiltrating plume-derived magma. In the context of this model, the stratigraphic trend in geochemistry of the upper ~ 1/3 of the Mauna Kea section reflects greater proportions of lithospheric melt in deep magmatic plumbing systems as the volcano moves off the plume axis and the flux of plume-derived magma decreases.

The principle weakness of the model discussed in this section is that it provides no obvious explanation for the relatively sharp decrease in $\delta^{18}O$ of coarse olivine phenocrysts going from the submarine to subaerial Mauna Kea sections, nor the similarity between oxygen-isotope stratigraphy and the modality of fractionation-normalized $SiO_2$ (Figure 5).

Both of the models examined above provide explanations of some observations but not others. Therefore, we conclude that low-$\delta^{18}O$ values of Hawaiian magmas reflect contamination rather than a low-$\delta^{18}O$ plume component, but that the origin of those contaminants and the places and mechanisms by which they were incorporated remain an open question. Future studies that could help discriminate between these models include (1) comparisons of the oxygen isotope geochemistry of rift zones on Mauna Loa and Kilauea (which should vary systematically with geography if the model illustrated in

Figure 11a is correct) and (2) studies of the relationship between crystallization pressure, Mg# and $\delta^{18}O$ in individual olivine phenocrysts, which could establish whether low-$\delta^{18}O$ phenocrysts form at the high-pressures required of the model in Figure 11b, or only at the low pressures indicated by the model in Figure 11a.

Finally, we emphasize that the preceding conclusions are based on the geochemical properties of low-$\delta^{18}O$ Mauna Kea lavas and should not be generalized to apply to the processes responsible for anomalously high $\delta^{18}O$ values previously found in Koolau and Lanai lavas (EILER et al., 1996b). These values were initially interpreted to reflect the presence of a high-$\delta^{18}O$, recycled crustal component in the Hawaiian plume -- a conclusion supported by subsequent radiogenic isotope studies (LASSITER and HAURI, 1998; BLICHERT-TOFT et al., 1999). Furthermore, DUCEA et al. (2002) subsequently discovered anomalously high-$\delta^{18}O$ mantle xenoliths from Oahu having radiogenic isotope compositions indicating they were infiltrated and metasomatized by plume-derived melt. Thus the high-$\delta^{18}O$, "Koolau-like" signature must have been carried by plume-derived melts before they ascended through the lithosphere.

## ACKNOWLEDGMENTS

We thank all participants in the Hawaiian Scientific Drilling Project for their work in recovering, documenting and preparing the HSDP II core. We particularly thank authors of accompanying articles in this theme for providing us their data prior to its publication and Caroline Seamen for helping disseminate those data. We thank Paul Asimow for his help in performing calculations using the MELTS program, and H.P. Taylor, George Rossman, Edwin Schauble, Liz Johnson, Ronit Kessel and Sujoy Mukhopadhyay for

helpful discussions of this and related work. We thank Mike Garcia, Don DePaolo and an anonymous reviewer for helpful comments on the initial draft of this manuscript. This research was partially supported by National Science Foundation grants OCE-0095897 and OCE-0112132.

**REFERENCES**

Albarede F. (1992) How deep do common basaltic magmas form and differentiate. *Journal of Geophysical Research-Solid Earth* **97**(B7), 10997-11009.

Aldanmaz E., Pearce J. A., Thirlwall M. F., and Mitchell J. G. (2000) Petrogenetic evolution of late Cenozoic, post-collision volcanism in western Anatolia, Turkey. *Journal of Volcanology and Geothermal Research* **102**(1-2), 67-95.

Anderson A. T. and Brown G. G. (1993) $CO_2$ contents and formation pressures of some Kilauean melt inclusions. *American Mineralogist* **78**(7-8), 794-803.

Anderson A. T., Clayton R. N., and Mayeda T. K. (1971) Oxygen isotope thermometry of mafic igneous rocks. *Journal of Geology* **79**(6), 715-720.

Appora I., Eiler J. M., Matthews A., and Stolper E. M. (2003) Experimental determination of oxygen isotope fractionations between $CO_2$ vapor and soda-melilite melt. *Geochimica et Cosmochimica Acta* **67**(3), 459-471.

Baker M. B., Alves S., and Stolper E. M. (1996) Petrography and petrology of the Hawaii Scientific Drilling Project lavas: Inferences from olivine phenocryst abundances and compositions. *Journal of Geophysical Research-Solid Earth* **101**(B5), 11715-11727.

Baker M. B., Hirschmann M. M., Ghiorso M. S., and Stolper E. M. (1995) Compositions of near-solidus peridotite melts from experiments and thermodynamic calculations. *Nature* **375**(6529), 308-311.

Bindeman I. N. and Valley J. W. (2001) Low-$\delta^{18}O$ rhyolites from Yellowstone: Magmatic evolution based on analyses of zircons and individual phenocrysts. *Journal of Petrology* **42**(8), 1491-1517.

Blichert-Toft I., Frey F. A., and Albarede F. (1999) Hf isotope evidence for pelagic sediments in the source of Hawaiian basalts. *Science* **285**(5429), 879-882.

Blichert-Toft J., Weis D., Maerschalk C., Agranier A., and Albarede F. (2003) Hawaiian hot spot dynamics as inferred from the Hf and Pb isotope evolution of Mauna Kea volcano. *Geochemistry Geophysics Geosystems* **4**.

Bryce J. G. and DePaolo D. J. (2003) Sr and Nd isotope stratigraphy of the second HSDP core. *Geochemistry Geophysics Geosystems* **submitted**.

Chauvel C. and Blichert-Toft J. (2001) A hafnium isotope and trace element perspective on melting of the depleted mantle. *Earth and Planetary Science Letters* **190**(3-4), 137-151.

Chen C. Y. and Frey F. A. (1983) Origin of Hawaiian tholeiite and alkalic basalt. *Nature* **302**(5911), 785-789.

Clague D. A., Moore J. G., Dixon J. E., and Friesen W. B. (1995) Petrology of submarine lavas from Kilaueas Puna Ridge, Hawaii. *Journal of Petrology* **36**(2), 299-349.

Cooper K. M., Eller J. M., Asimow P. D., and Langmuir C. H. (2004) Oxygen isotope evidence for the origin of enriched mantle beneath the mid-Atlantic ridge. *Earth and Planetary Science Letters* **220**(3-4), 297-316.

Ducea M., Sen G., Eiler J., and Fimbres J. (2002) Melt depletion and subsequent metasomatism in the shallow mantle beneath Koolau volcano, Oahu (Hawaii). *Geochemistry Geophysics Geosystems* **3**.

Eiler J. M. (2001) Oxygen isotope variations of basaltic lavas and upper mantle rocks. In *Stable Isotope Geochemistry*, Vol. 43, pp. 319-364. Mineralogical Soc America.

Eiler J. M., Crawford A., Elliott T., Farley K. A., Valley J. W., and Stolper E. M. (2000a) Oxygen isotope geochemistry of oceanic-arc lavas. *Journal of Petrology* **41**(2), 229-256.

Eiler J. M., Farley K. A., Valley J. W., Hauri E., Craig H., Hart S. R., and Stolper E. M. (1997) Oxygen isotope variations in ocean island basalt phenocrysts. *Geochimica et Cosmochimica Acta* **61**(11), 2281-2293.

Eiler J. M., Farley K. A., Valley J. W., Hofmann A. W., and Stolper E. M. (1996b) Oxygen isotope constraints on the sources of Hawaiian volcanism. *Earth and Planetary Science Letters* **144**(3-4), 453-467.

Eiler J. M., Gronvold K., and Kitchen N. (2000c) Oxygen isotope evidence for the origin of chemical variations in lavas from Theistareykir volcano in Iceland's northern volcanic zone. *Earth and Planetary Science Letters* **184**(1), 269-286.

Eiler J. M., Schiano P., Kitchen N., and Stolper E. M. (2000b) Oxygen-isotype evidence for recycled crust in the sources of mid-ocean-ridge basalts. *Nature* **403**(6769), 530-534.

Eiler J. M., Valley J. W., Graham C. M., and Baumgartner L. P. (1995) Ion microprobe evidence for the mechanisms of stable-isotope retrogression in high-grade metamorphic rocks. *Contributions to Mineralogy and Petrology* **118**(4), 365-378.

Eiler J. M., Valley J. W., and Stolper E. M. (1996a) Oxygen isotope ratios in olivine from the Hawaii Scientific Drilling Project. *Journal of Geophysical Research-Solid Earth* **101**(B5), 11807-11813.

Eisele J., Abouchami W., Galer S. J. G., and Hofmann A. W. (2003) The 320 kyr Pb isotope evolution of Mauna Kea lavas recorded in the HSDP-2 drill core. *Geochemistry Geophysics Geosystems* **4**.

Feigenson M. D., Bolge L. L., Carr M. J., and Herzberg C. T. (2003) REE inverse modeling of HSDP2 basalts: Evidence for multiple sources in the Hawaiian plume. *Geochemistry Geophysics Geosystems* **4**.

Galer S. J. G. and Onions R. K. (1985) Residence time of thorium, uranium and lead in the mantle with implications for mantle convection. *Nature* **316**(6031), 778-782.

Garcia M. O., Ito E., Eiler J. M., and Pietruszka A. J. (1998) Crustal contamination of Kilauea Volcano magmas revealed by oxygen isotope analyses of glass and olivine from Pu'u O'o eruption lavas. *Journal of Petrology* **39**(5), 803-817.

Garcia M. O., Jorgenson B. A., Mahoney J. J., Ito E., and Irving A. J. (1993) An evaluation of temporal geochemical evolution of Loihi summit lavas - results from Alvin submersible dives. *Journal of Geophysical Research-Solid Earth* **98**(B1), 537-550.

Garcia M. O., Muenow D. W., Aggrey K. E., and Oneil J. R. (1989) Major element, volatile, and stable isotope geochemistry of Hawaiian submarine tholeiitic glasses. *Journal of Geophysical Research-Solid Earth and Planets* **94**(B8), 10525-10538.

Garcia M. O., Pietruszka A., and Rhodes J. M. (2003) A petrologic perspective of Kilauea volcano's summit magma reservoir. *Journal of Petrology* **44**(12), 2313-2339.

Garlick G. D., Macgrego I. D., and Vogel D. E. (1971) Oxygen isotope ratios in eclogites from kimberlites. *Science* **172**(3987), 1025-1030.

Gazis C., Taylor H. P., Hon K., and Tsvetkov A. (1996) Oxygen isotopic and geochemical evidence for a short-lived, high-temperature hydrothermal event in the Chegem caldera, Caucasus mountains, Russia. *Journal of Volcanology and Geothermal Research* **73**(3-4), 213-244.

Ghiorso M. S., Hirchmann M. M., and Sack R. O. (1994) New software models thermodynamics of magmatic systems. *Eos Trans. AGU Fall meeting* **75**, 571-576.

Green T. H. (1994) Experimental studies of trace-element partitioning applicable to igneous petrogenesis - sedona 16 Years later. *Chemical Geology* **117**(1-4), 1-36.

Gregory R. T. and Taylor H. P. (1981) An oxygen isotope profile in a section of Cretaceous oceanic-crust, Samail Ophiolite, Oman - evidence for $\delta^{18}O$ Buffering of the oceans by deep (less-than 5 Km) seawater-hydrothermal circulation at Mid-Ocean Ridges. *Journal of Geophysical Research* **86**(NB4), 2737-2755.

Harmon R. S. and Hoefs J. (1995) Oxygen-isotope heterogeneity of the mantle deduced from global $^{18}O$ systematics of basalts from different geotectonic settings. *Contributions to Mineralogy and Petrology* **120**(1), 95-114.

Hauri E. H. (1996) Major-element variability in the Hawaiian mantle plume. *Nature* **382**(6590), 415-419.

Hegner E., Unruh D., and Tatsumoto M. (1986) Nd-Sr-Pb isotope constraints on the sources of west Maui volcano, Hawaii. *Nature* **319**(6053), 478-480.

Hildreth W. and Moorbath S. (1988) Crustal contributions to arc magmatism in the Andes of central Chile. *Contributions to Mineralogy and Petrology* **98**(4), 455-489.

Hirose K. and Kushiro I. (1993) Partial melting of dry peridotites at high-pressures: determination of compositions of melts segregated from peridotite using aggregates of diamond. *Earth and Planetary Science Letters* **114**(4), 477-489.

Hofmann A. W. and Jochum K. P. (1996) Source characteristics derived from very incompatible trace elements in Mauna Loa and Mauna Kea basalts, Hawaii Scientific Drilling Project. *Journal of Geophysical Research-Solid Earth* **101**(B5), 11831-11839.

Holt E. W. and Taylor H. P. (1998) $^{18}O/^{16}O$ mapping and hydrogeology of a short-lived (approximate to 10 years) fumarolic (> 500 $^{o}C$) meteoric-hydrothermal event in the upper part of the 0.76 Ma Bishop Tuff outflow sheet, California. *Journal of Volcanology and Geothermal Research* **83**(1-2), 115-139.

Huang S. and Frey F. A. (2003) Trace element abundances of Mauna Kea basalt from phase 2 of the Hawaii Scientific Drilling Project: Petrogenetic implications of correlations with major element content and isotopic ratios. *Geochemistry Geophysics Geosystems* **4**.

Kempton P. D., Fitton J. G., Saunders A. D., Nowell G. M., Taylor R. N., Hardarson B. S., and Pearson G. (2000) The Iceland plume in space and time: a Sr-Nd-Pb-Hf

study of the North Atlantic rifted margin. *Earth and Planetary Science Letters* **177**(3-4), 255-271.

Kennedy A. K., Kwon S. T., Frey F. A., and West H. B. (1991) The isotopic composition of postshield lavas from Mauna-Kea volcano, Hawaii. *Earth and Planetary Science Letters* **103**(1-4), 339-353.

Kurz M. D., Curtice J., Lott D. E., and Solow A. (2004) Rapid helium isotopic variability in Mauna Kea shield lavas from the Hawaiian Scientific Drilling Project. *Geochemistry Geophysics Geosystems* **5**.

Kyser T. K., Oneil J. R., and Carmichael I. S. E. (1981) Oxygen isotope thermometry of basic lavas and mantle nodules. *Contributions to Mineralogy and Petrology* **77**(1), 11-23.

Kyser T. K., Oneil J. R., and Carmichael I. S. E. (1982) Genetic relations among basic lavas and ultramafic nodules - evidence from oxygen isotope compositions. *Contributions to Mineralogy and Petrology* **81**(2), 88-102.

Lassiter J. C., DePaolo D. J., and Tatsumoto M. (1996) Isotopic evolution of Mauna Kea volcano: Results from the initial phase of the Hawaii Scientific Drilling Project. *Journal of Geophysical Research-Solid Earth* **101**(B5), 11769-11780.

Lassiter J. C. and Hauri E. H. (1998) Osmium-isotope variations in Hawaiian lavas: evidence for recycled oceanic lithosphere in the Hawaiian plume. *Earth and Planetary Science Letters* **164**(3-4), 483-496.

Lassiter J. C., Hauri E. H., Reiners P. W., and Garcia M. O. (2000) Generation of Hawaiian post-erosional lavas by melting of a mixed lherzolite/pyroxenite source. *Earth and Planetary Science Letters* **178**(3-4), 269-284.

Matthews A., Stolper E. M., Eiler J. M., and Epstein S. (1998) Oxygen isotope fractionation among melts, minerals, and rocks. *Min. Mag.* **62A**, 971-972.

Miller J. A., Cartwright I., Buick I. S., and Barnicoat A. C. (2001) An O-isotope profile through the HP-LT Corsican ophiolite, France and its implications for fluid flow during subduction. *Chemical Geology* **178**(1-4), 43-69.

Moore J. G. (2001) Density of basalt core from Hilo drill hole, Hawaii. *Journal of Volcanology and Geothermal Research* **112**(1-4), 221-230.

Muehlenbachs K. (1986) Alteration of the oceanic-crust and the $^{18}O$ history of seawater. *Reviews in Mineralogy* **16**, 425-444.

Muehlenbachs K. and Byerly G. (1982) $^{18}O$-enrichment of silicic magmas caused by crystal fractionation at the Galapagos spreading center. *Contributions to Mineralogy and Petrology* **79**(1), 76-79.

Muehlenbachs K. and Kushiro I. (1974) Oxygen isotope exchange and equilibrium of silicates with $CO_2$ or $O_2$. *Year Book Carnegie Inst. Washington* **71**, 232-236.

Rhodes J. M. and Vollinger M. J. (2004) Composition of basaltic lavas sampled by phase-2 of the Hawaii Scientific Drilling Project: Geochemical stratigraphy and magma types. *Geochemistry Geophysics Geosystems* **5**.

Roedder E. (1965) Liquid $CO_2$ inclusions in olivine-bearing nodules and phenocrysts from basalts. *American Mineralogist* **50**(10), 1746-&.

Ryerson F. J., Durham W. B., Cherniak D. J., and Lanford W. A. (1989) Oxygen diffusion in olivine - effect of oxygen fugacity and implications for creep. *Journal of Geophysical Research-Solid Earth and Planets* **94**(B4), 4105-4118.

Schiano P., Birck J. L., and Allegre C. J. (1997) Osmium-strontium-neodymium-lead isotopic covariations in mid-ocean ridge basalt glasses and the heterogeneity of the upper mantle. *Earth and Planetary Science Letters* **150**(3-4), 363-379.

Shanks W. C. (2001) Stable isotopes in seafloor hydrothermal systems: vent fluids, hydrothermal deposits, hydrothermal alteration, and microbial processes. In *Stable Isotope Geochemistry*, Vol. 43, pp. 469-525. Mineralogical Soc America.

Sharp Z. D. (1990) A laser-based micro-analytical method for the *in situ* determination of oxygen isotope ratios of silicates and oxides. *Geochimica et Cosmochimica Acta* **54**(5), 1353-1357.

Stolper E., Sherman S., Garcia M., Baker M., and Seaman C. (2004) Glass in the submarine section of the HSDP2 drill core, Hilo, Hawaii. *Geochemistry Geophysics Geosystems* **5**.

Valley J. W. and Graham C. M. (1993) Cryptic grain-scale heterogeneity of oxygen isotope ratios in metamorphic magnetite. *Science* **259**(5102), 1729-1733.

Valley J. W., Kitchen N., Kohn M. J., Niendorf C. R., and Spicuzza M. J. (1995) UWG-2, a garnet standard for oxygen isotope ratios: strategies for high precision and accuracy with laser heating. *Geochimica et Cosmochimica Acta* **59**(24), 5223-5231.

Walther J. V. and Orville P. M. (1982) Volatile production and transport in regional metamorphism. *Contributions to Mineralogy and Petrology* **79**(3), 252-257.

West H. B. and Leeman W. P. (1987) Isotopic evolution of lavas From Haleakala crater, Hawaii. *Earth and Planetary Science Letters* **84**(2-3), 211-225.

White W. M., Hofmann A. W., and Puchelt H. (1987) Isotope geochemistry of Pacific Mid-ocean Ridge basalt. *Journal of Geophysical Research-Solid Earth and Planets* **92**(B6), 4881-4893.

# CHAPTER 2.

# *IN SITU* OXYGEN ISOTOPE ANALYSIS BY EXCIMER LASER (157NM) FLUORINATION TECHNIQUE AND ITS APPLICATION TO GEOLOGICAL PROBLEMS

Zhengrong Wang, John M. Eiler, Amy J. Jurewicz and Nami E. Kitchen

Division of Geological and Planetary Sciences, M/C 100-23,

California Institute of Technology, Pasadena, CA 91125, USA

(*wzhr@gps.caltech.edu*, *eiler@gps.caltech.edu*, *jurewicz@gps.caltech.edu*)

**ABSTRACT**

We developed an excimer laser (157 nm) fluorination technique, including gas handling system and isotope-ratio mass spectrometry method, for the *in situ* measurement of oxygen isotope compositions of anhydrous rock-forming minerals. This system is experimentally demonstrated to be capable of measuring $\delta^{18}O$ values of single grain minerals (including olivine, clinopyroxene, anorthite, and quartz) and minerals in rock sections with a high precision ( ± 0.2‰ for $\delta^{18}O$ and ± 0.3‰ for $\delta^{17}O$). The $O_2$ yields from most of these minerals after ablation and fluorination are very close to 100%, except feldspars which will react with $F_2$ gas at room temperatures. Compared with $CO_2$ infra-red laser fluorination techniques, this excimer laser system significantly reduces the material size per analysis (10~100 μg, vs. 1-2 mg), and increases the spatial resolution (100~500 μm spots). It also shows great potential to measure $\delta^{18}O$ values of hard-to-fluorinate minerals such as chromite. Application of this technique to the study of intra-grain, oxygen isotope heterogeneity in lavas from Borgarhraun, Iceland reveals both oxygen isotope equilibrium and disequilibrium phenomena. We then used this phenomenon to constrain the residence time for the magma mixtures.

## 1. INTRODUCTION

During the last decade, significant effort has been devoted to developing excimer laser-based techniques and determining precise oxygen isotope compositions of minerals or rocks of geological interests at microscopic scale (WIECHERT and HOEFS, 1995; RUMBLE et al., 1997; FARQUHAR and RUMBLE, 1998; RUMBLE and SHARP, 1998; YOUNG et al., 1998; YOUNG et al., 1998; FIEBIG et al., 1999; WIECHERT et al., 2002). The ultimate

goal of these continued developments is to facilitate the joint study of geological samples using oxygen isotopes along with other geochemical tracers on the same materials, thereby constraining geological processes in detail. These methods have many advantages over conventional and infrared-laser fluorination methods, including reduced sample size and improved spatial resolution. It has been demonstrated that the excimer laser fluorination method is able to make high precision ($1\sigma \sim 0.2‰$ for $\delta^{18}O$) *in situ* oxygen isotope measurement on silicate minerals (WIECHERT and HOEFS, 1995; RUMBLE et al., 1997; FARQUHAR and RUMBLE, 1998; RUMBLE and SHARP, 1998; YOUNG et al., 1998; YOUNG et al., 1998; FIEBIG et al., 1999; WIECHERT et al., 2002).

Excimer lasers previously used for these techniques include KrF (248 nm), ArF (193 nm), frequency-quadrupled Nd-YAG lasers (266 nm), and frequency-doubled Cu-vapor lasers (255.3/289.1 nm) (RUMBLE and SHARP, 1998). These lasers generate photons with energies between 4.7 eV to 6.4 eV, which are able to break up Si-O bonds (~ 5 eV) without significant heating (heating-induced temperature gradient is known to cause isotope fractionation; ELSENHEIMER and VALLEY, 1992; RUMBLE and HOERING, 1994). In this study, we systematically investigate the use of a 157 nm excimer laser beam with photon energy of 7.9 ev to conduct oxygen isotope analyses. In principle, this laser is able to more efficiently break up Si-O bonds without isotopic fractionation, and therefore might be preferable for studying most rock-forming minerals, including those that are transparent to mid-UV light (e.g., Quartz; WIECHERT and HOEFS, 1995). It also has the potential to produce an even smaller spot than commonly-used lasers since the size limit of a focused spot of light is proportional to its wavelength (RUMBLE and SHARP, 1998). However, the increase in the spatial resolution in the measurement of oxygen isotope

composition poses great challenges in measuring nano-mole gas samples produced by excimer laser ablation and fluorination. The Irm-GC-MS technique is frequently used to solve these problems (MERRITT et al., 1994; MERRITT and HAYES, 1994; YOUNG et al., 1998). Here, we describe a gas handling technique and continuous flow Irm-MS system which can satisfy these requirements and precisely analyze 80 ~ 200 nanomole $O_2$ gas. Some geological applications of this technique are also described.

## 2. INSTRUMENTATION AND CALIBRATON

Figure 1 presents schematic illustrations of our excimer laser (157nm) fluorination system. It consists of three major parts: a) an excimer laser ablation system; b) a gas purifying and handling system; and c) mass-spectrometry system. In the laser ablation system, we use an LPF® 202 excimer laser (type 157, Lambda Physik), which utilizes 95% He and 5% $F_2$ mixed working gas to produce 157 nm photons with pulse energy of 75 mJ at 26 kV and 10 Hz, maximum average power of 1.5 W and repetition rate range of 1~20 Hz. The beam optics are similar to those described for a 193 nm laser ablation system by WIECHERT et al. (2002). A stainless steel pedestal sits in the sample chamber to hold the sample at the height of the laser's focal plane; it serves a secondary purpose of reducing the gas-filled volume of the laser chamber, and thus reducing the amount of reagent needed to maintain a given pressure. The gas-filled space of the chamber plus the flexible tubing connecting it to the gas-handling line is about 20.5 cc. The sample chamber is accessed through a $MgF_2$ window, which is sealed to the chamber by Kalrez® $F_2$-resistant O-ring. A constant flow of $N_2$ gas flushes over the outside of the $MgF_2$

window to prevent absorption of the laser beam by $O_2$ gas in air (the stopping distance of our laser beam in air is a few centimeters).

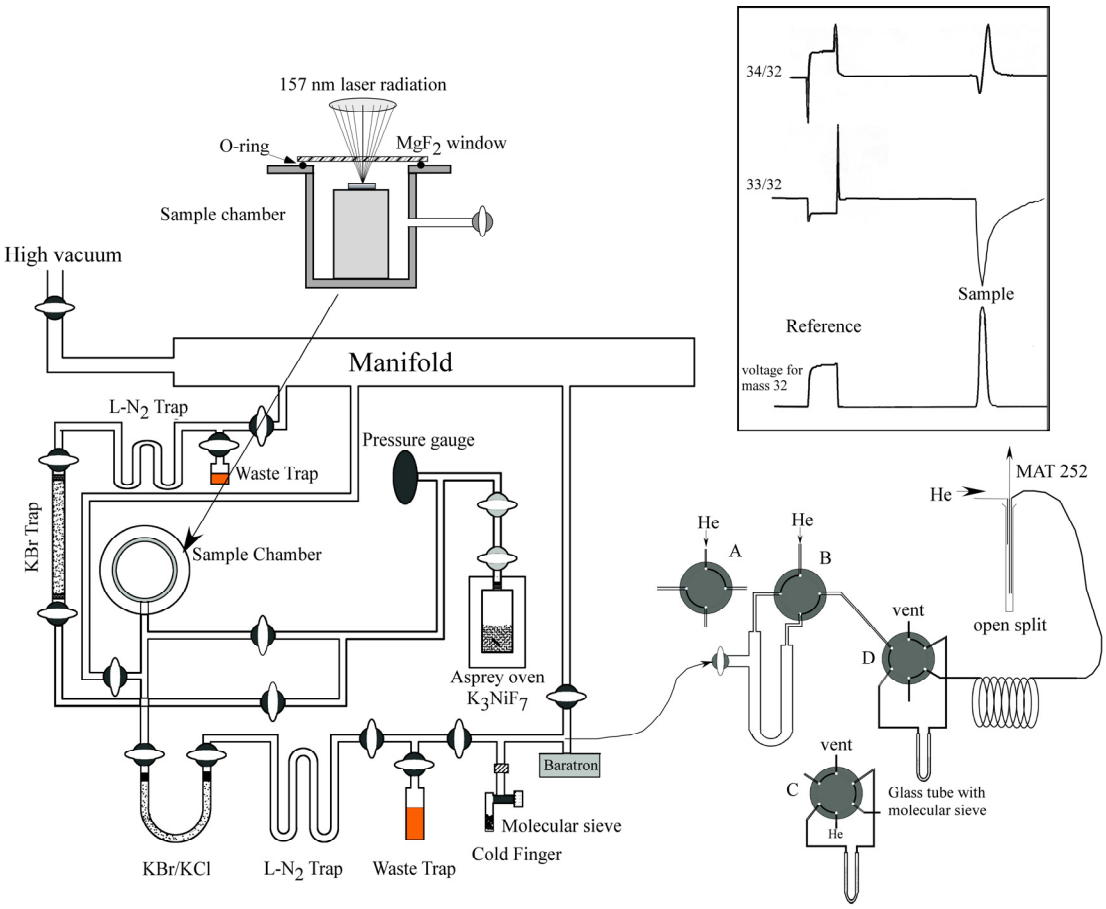


**Figure 1.** Schematics of the excimer laser (157 nm) fluorination system. It consists of three sections: a) an excimer laser ablation system; b) a gas purifying and handling system; and c) mass-spectrometry system. The main optical alignment is similar to that described by WIECHERT et al. (2002). In the stainless steel chamber sits a gold-plated pedestal. Top part of sample chamber is sealed by $MgF_2$ window via a Kalrez® $F_2$-resistant O-ring. Each time, ~ 25 µmol of $F_2$ gas is introduced into the chamber from a pool of purified $F_2$ gas in the Asprey oven (Asprey, 1976). After ablation and fluorination in the sample chamber, $F_2$ gas is removed from $O_2 + F_2$ mixtures by slowly passing through KBr/KCl and liquid nitrogen trap. Oxygen gas produced during laser ablation will finally be absorbed in the 3Å molecular sieves. Collected oxygen gases will either be measured using modified dual-inlet system off-line or using continuous flow system. In the continuous flow system, position A

is in expansion mode, combination of B and D is in cryogenic-focus mode, and position C is in measurement mode. Sample gas is tapped at open split by MAT-252, using Conflow-II interface. Oxygen isotope composition is measured by comparing the sample gas peak with standard gas from bellows of MAT-252.

Samples -- either single crystals or small slabs of rock -- are prepared for analysis by polishing down to a 1.0 μm grit, and then either placed loose on the pedestal or, for small samples that move when ablated, attached to the pedestal using copper tape (3 M® double sided copper tape, copper coated with thin film of acrylic adhesives). Before the experiment, the sample chamber is pumped to $10^{-7}$ torr and pretreated using $F_2$ until the blank is less than 10% of sample gas. This normally takes at least one week. At the beginning of each analysis, approximately 25 μmol of $F_2$ gas is introduced into the chamber from a reservoir of $F_2$ that has been purified by uptake and release from an Asprey oven (ASPREY, 1976). During ablation, pulses of UV light (1 ~ 20 Hz) irradiate the polished surface. The ablated material reacts with $F_2$ gas, forms fluoride and precipitates at the edge of the plume shown in the margin of the pedestal. After the ablation is complete, unreacted $F_2$ plus product $O_2$ gas are slowly leaked through a KBr/KCl trap (to remove $F_2$) and a liquid nitrogen trap (to remove $Br_2$, $Cl_2$ and other products that pass the KBr/KCl trap). The remaining oxygen gas is then absorbed on 3 Å molecular sieves held at liquid nitrogen temperature. Collected oxygen gases is then analyzed for its oxygen isotope composition using either a modified dual-inlet system (when sample size is larger than 0.8 μmol) or a continuous flow system (when the sample is between 50~200 nmol). Ablation time is controlled to be either 8~12 min or 1~3 min depending on what systems are chosen for isotope ratio measurements.

## 2.1 STANDARD GAS CALIBRATION

Our oxygen-isotope analyses were standardized by comparison with two nominally pure $O_2$ gases. The first $O_2$ gas, Ref-I, is from an ultra-high purity compressed $O_2$ cylinder manufactured by Air Liquide; $\delta^{18}O$ value of this $O_2$ gas standard is calibrated to be 24.91±0.07‰, determined by analyzing $CO_2$ produced by quantitative reaction of this $O_2$ gas with pure graphite (the $CO_2$ analysis was, in turn, standardized by comparison with $CO_2$ produced by phosphoric acid digestion of NBS-19 calcite). The $\delta^{17}O$ value of this standard gas was calibrated by comparison with $O_2$ generated by $CO_2$-laser fluorination of 22 natural terrestrial silicates and oxides, including San Carlos olivines, UWG-2 garnet, magnetite, NBS30 biotite, brazil quartz, and rhyolite (SHARP, 1990; VALLEY et al., 1995; EILER et al., 1996). These materials define a slope of 0.523 when regressed following the power-law expression, approximately corresponding to $\partial(\delta^{17}O)/\partial(\delta^{18}O)$ (MILLER, 2002). This value is comparable to slopes determined in other labs for the terrestrial fractionation line (TFL, MATSUHISA et al., 1978; LI and MEIJER, 1998; MILLER et al., 1999; MILLER, 2002), and we infer that our data also lie on that line (as expected for all common terrestrial silicates and oxides). The Ref-1 standard gas has a $\Delta^{17}O$ value of -0.30 ± 0.07 relative to the TFL determined in our lab, corresponding to a $\delta^{17}O$ value of 12.70 ± 0.13‰. This result is consistent with our $O_2$ reference gas being derived from atmospheric $O_2$ (THIEMENS et al., 1995; LUZ et al., 1999).

The second standard, Ref-II, was produced by heating CuO at 900 ºC and collecting the evolved $O_2$. The isotopic composition of this gas was calibrated against Ref-I to have $\delta^{18}O$ values of 13.2±0.10‰, and $\Delta^{17}O$ values of -0.15±0.07‰, which is between TFL and

our Ref-I as shown in Figure 2, indicating $O_2$ gas in the air is partly the source for making this CuO.

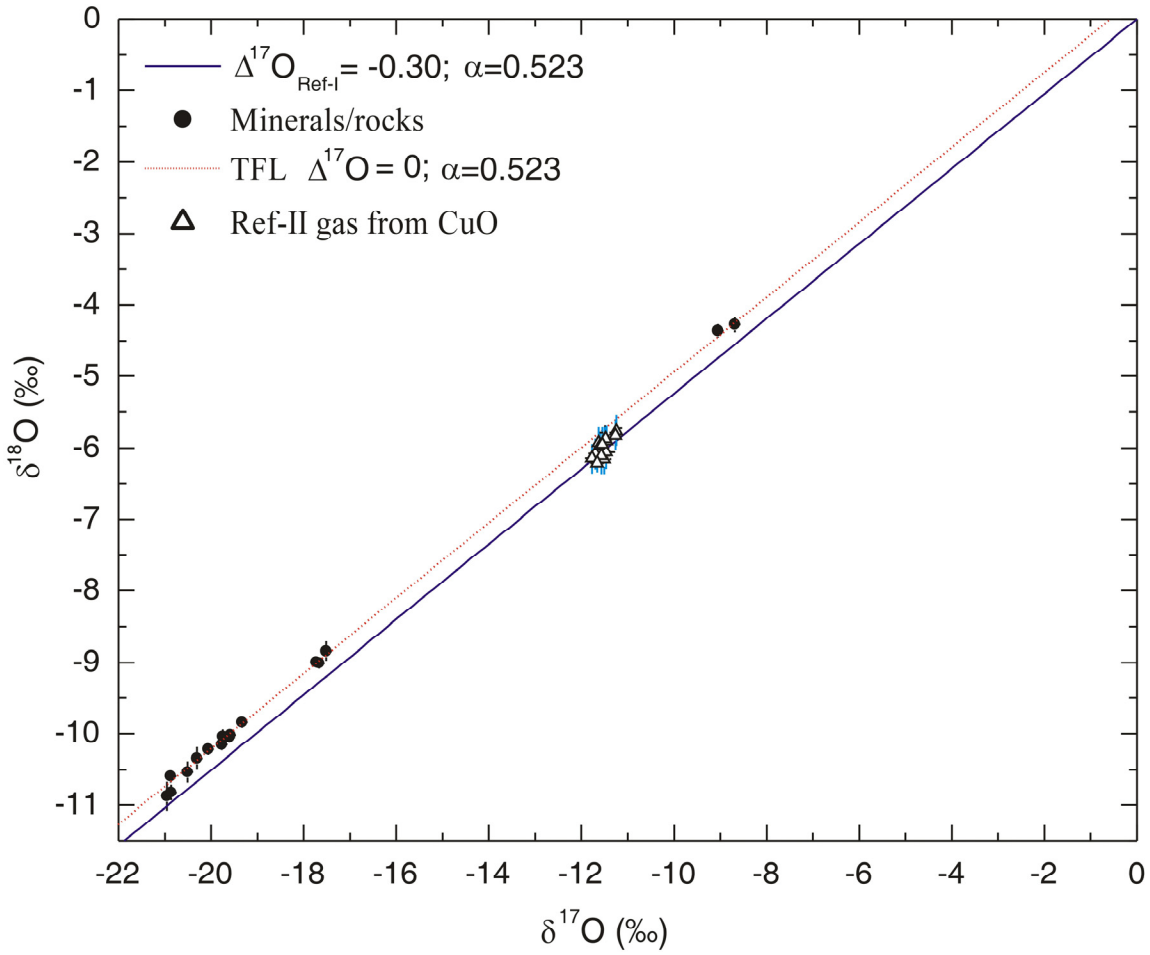


**Figure 2.** Calibration of standard $O_2$ gas. Our long term standard $O_2$ gas is from an ultra-high purity compressed $O_2$ cylinder manufactured by Air Liquide. Relative to this standard, solid circles are oxygen isotope composition of $O_2$ gas extracted from San Carlos olivines, UWG-2 garnet, magnetite, NBS30 biotite, brazil quartz, and rhyolite, using infra-red laser fluorination method (SHARP, 1990; VALLEY et al., 1995; EILER et al., 1996). Our $O_2$ standard gas is lying below this terrestrial fractionation line defined by these minerals and rock samples by 0.3 ‰. Up-triangle symbols are our intermediate standard (Ref-II) extract from CuO at 900 °C.

All isotopic analyses of $CO_2$ were made using a Finnigan MAT-251, and all isotopic analyses of $O_2$ were made using a Finnigan MAT-252 and a modified dual-inlet system described below.

### 2.2 MODIFIED DUAL-INLET SYSTEM

We installed a cold finger filled with 3Å molecular sieves onto the inlet system of our Finnigan MAT-252 mass-spectrometer in order to achieve acceptably-high sample pressure in the source for ~ 1.0 μmol samples. This cold finger is directly connected with the source of the mass spectrometer by a flexible metal capillary and crimp (i.e., the cold finger lies between the sample bellows and sample capillary included in the standard dual inlet system of the Finnigan MAT-252). Analyses are made by freezing the sample into this cold finger at liquid nitrogen temperature, closing the valve between the bellows and cold-finger, heating the molecular sieve to release the $O_2$ gas and making it flow through the capillary to the source. This configuration can measure samples of $O_2$ as small as ~ 0.8 μmol with ~ 0.2‰ precision for $\delta^{18}O$, and ~ 0.3‰ for $\delta^{17}O$. Figure 3a shows the results of 'zero-enrichment' analyses (comparison of two aliquots of the same gas) as a function of the temperature to which the molecular sieve was heated or frozen when releasing the sample. We find significantly elevated $\Delta^{17}O$ values when the molecular sieve is heated to greater than 100°C. We suspect this reflects contamination of sample gas by water, fragments of which recombine with $O_2$ in the mass spectrometer source, producing $^{16}O_2H^+$ and interfering with $^{16}O^{17}O$ (there is no $F_2$ gas involved in any stage of these measurements, and so it is implausible that the contaminant is a fragmentation product of $NF_3$; RUMBLE et al., 1997; CLAYTON and MAYEDA, 1983). When the

temperature of molecular sieve is adjusted to between -50 and 60°C, $\Delta^{17}O$ values are constant and approximately accurate, but $\delta^{18}O$ values of released gas vary by close to 1 ‰, suggesting fractionation during desorption. These anomalies also do not correlate with the amount of gas being analyzed (Figure 3b). Our measurements appear to be accurate and precise for both $\delta^{18}O$ and $\Delta^{17}O$ when the molecular sieve is heated to 80˚C to release $O_2$.

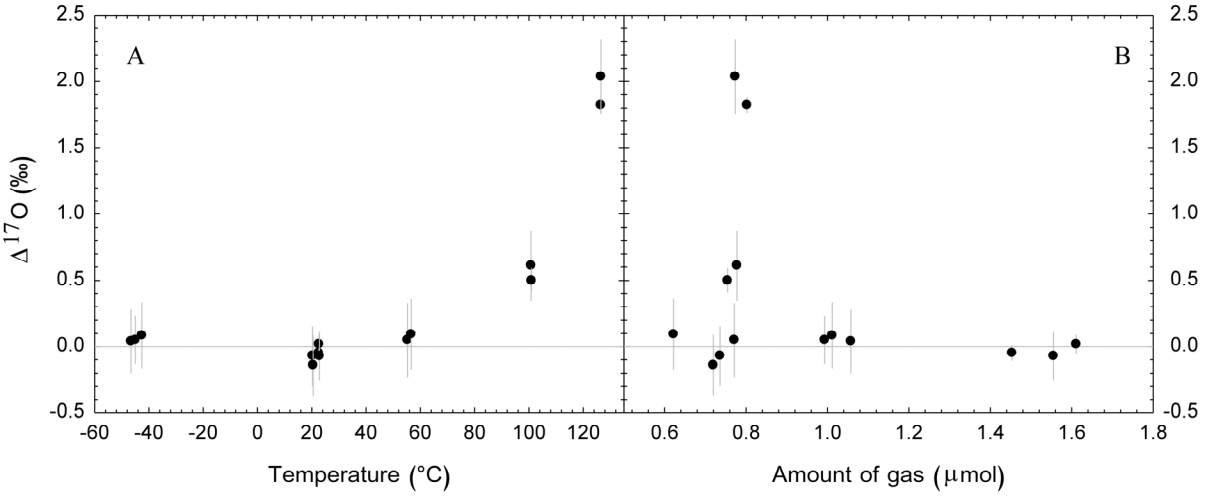


**Figure 3.** The relationship between $\Delta^{17}O$ and **A:** the temperature of the molecular sieve; **B:** the amount of gas measured. All symbols are for one gas sample (Ref-II).

### 2.3 CONTINUOUS-FLOW-IRM-MS SYSTEM

Analyses of small (sub-μmol) samples of $O_2$ gas are made using a continuous-flow system illustrated in Figure 1. In this case, analyte oxygen gas after purification in the KBr/KCl trap is expanded into a U-shaped section of quarter-inch stainless-steel tubing attached to a four-way valve set to position **'A'** (as indicated in Figure 1). Several minutes are allowed for the expanded gas to equilibrate in pressure and homogenize in isotopic composition, after which we close the valve that isolates this U-trap from the rest of the vacuum line, set the four-way valve to position '**B'**, and set the six-way valve to

position 'D'. Analyte $O_2$ gas is then entrained by Helium carrier gas and cryo-focused in a fine glass tube filled with the dry 3 Å molecular sieve held at liquid nitrogen temperature. After $O_2$ is completely condensed on the molecular sieve (typically after about 8 min at a He flow rate of 6 ~ 8 cc/min), the six-way-valve is switched to position '**C'** and the molecular sieve trap is warmed by removing the liquid nitrogen bath and immersing in a dry ice + acetone slush at -78°C. Oxygen gas is desorbed from the molecular sieve and carried in the He stream into an open split, where a fraction of it is injected into the source of a Finnigan MAT-252 mass-spectrometer. The standard gas used to calibrate these continuous flow measurements (either Ref-I or Ref-II) is introduced to the ion source from the standard bellow using Conf-II interface.

The precision of measurements made using our carrier-gas system are sensitive to the following factors: 1) the He carrier gas must be $H_2O$-free in order for our measurements of $\delta^{17}O$ to be accurate; we suspect this is because $^{16}O_2H^+$ interferes with $^{16}O^{17}O^+$ as discussed in the last section; 2) the capillary in the vent port of the six-way valve (at **B** and **D** configuration) needs to be long to prevent back-flow of atmospheric $O_2$ into the U-shaped tubing when the six-way valve is first switched from position **D** to position **B**. We immerse the vent capillary into liquid nitrogen to further reduce the opportunity for such contamination; 3) if $O_2$ is released from the molecular sieve at temperatures outside the range -72 to -78 °C, precision and accuracy degrade due to changes in the peak shape (either too broad or too sharp); and 4) the flow rate of He gas going to mass spectrometer has to be maintained within the range 3.5 to 5.0 cc/min.

The configuration described above routinely measures 50 ~ 200 nmol samples of $O_2$ with precisions of ±0.15‰ (1σ) for $\delta^{18}O$ and ±0.20‰ for $\delta^{17}O$ (and ±0.07‰ for $\Delta^{17}O$).

Oxygen isotope compositions of $O_2$ in small samples of bulk air can also be measured using this configuration and technique because $N_2$ is released more slowly than $O_2$ when the molecular sieve is warmed to dry ice + ethanol/acetone slush temperatures, and therefore does not interfere with oxygen isotope measurements. However, $H_2O$ in bulk air must be completely removed from the molecular sieve between measurements. The volume of this U-shaped tubing is about 60% of the total volume of the vacuum system for expansion. Therefore, it is generally possible to analyze each sample a second time by recovering the remaining 40% of the sample excluded from the U-shaped tube during expansion. Tests show that the reproducibility of such duplicate analyses is within the analytical precision of each analysis (that is, our expansions do not fractionate the analyte $O_2$). Our homemade open split has a maximum tapping efficiency of about 60%, and analyses of our reference gases using the procedure described above for samples demonstrates that the open split produces no isotopic fractionation.

Each of the two configurations described above (dual inlet and continuous flow) has advantages and disadvantages. Dual-inlet analyses can measure the same sample of $O_2$ gas many times with relatively high precision. However, more than 0.8 μmol of $O_2$ gas are required for analysis, calling for longer ablation times and larger spot-sizes. The continuous flow method requires only 50~200 nmol of $O_2$ gas, which can be generated in just about 1~3 minutes of ablation from a spot as small as about 100 μm on a side, but is less precise and sensitive to contamination.

## 3. ANALYTICAL RESULTS AND DISCUSSION

Table 1 presents the results of analyses of several silicate reference materials (including previously described intra- and inter-laboratory standards, and materials characterized for this study). The precision of our measurements of San Carlos olivine (an intra-laboratory standard described in EILER et al., 1996) is typically ±0.2‰ (1σ) in $\delta^{18}O$, and ±0.3‰ in $\delta^{17}O$ (1σ). Other minerals tend to have higher standard deviations, either due to sample heterogeneity (as previously found by *in situ* analyses of hydrothermal quartz; FIEBIG et al., 1999) and for other reasons (e.g., tendency of alkali feldspars to react at room temperature with $F_2$ reagent). We will discuss them in greater detail below.

Table 1 Summary of analytical results on minerals from 2001 to 2004

| | Studied using UV laser | | | Studied using infrared laser | |
|---|---|---|---|---|---|
| | $\delta^{18}O$(measured) | 1σ | n | | |
| Using dual in-let system | | | | | |
| Amelia Albite | 10.8 | 0.30 | 76 | **$** | **$** |
| San Carlos olivine | 5.3 | 0.20 | 60 | 5.28 | 0.04 |
| Brazil Quartz | 16.7 | 1.11 | 24 | | |
| South Carolina Chromite | 3.5 | 0.21 | 2 | -1.20 | 0.12 |
| $An_{70}$ | 6.0 | 0.18 | 12 | 6.11 | 0.03 |
| Orthoclase | 6.6 | 0.15 | 2 | | |
| Using continuous flow systems | | | | | |
| UVSCO1 (San Carlos) | 5.2 | 0.2 | 40 | 5.28 | 0.07 |
| UVSCO2 (San Carlos) | 5.1 | 0.2 | 38 | 5.18 | 0.07 |

**$**: measured by SIMs to be 10.8±0.5 (EILER et al., 1997)

### 3.1 OXYGEN YIELDS

We determined the molarities of $O_2$ produced by laser fluorination by measuring the intensity of the mass-32 beam in the same mass spectrometer used for stable isotope analysis, the sensitivity of which was calibrated by analysis of manometrically prepared $O_2$ gas standards. We then determined the relative yield of $O_2$ by comparing these measured molarities with the amount of $O_2$ expected based on sample weight loss during ablation (Table 2; Figures 4 and 5). Weight loss was measured by CAHN 29 -- an automatic electro-balance (± 0.1μg) -- and the expected amount of gas produced was calculated from mineral stoichiometry. All samples are weighted directly after cleaning the sample using dust-off at the end of the experiment. Control samples for each type of mineral are used (italic font in Table 2) to monitor the weight increase due to the deposition of fluorination residues and the weight loss due to fluorination reaction at room temperature. For alkali feldspars (Amelia Albite and K-feldspar), these control samples show significant positive weight loss even without ablation due to prolonged pre-treatment before analysis, so their yields shown in Table 2 are significantly underestimated. For other minerals, they generally show negative weight loss. This extra-weight comes from the precipitation of fluorination product during ablation. SEM analyses show they are mostly fluorite aggregates. Since these extra-weights are smaller than 5% of the weight loss, they will limit the precision of this yield measurement to be within ± 5%.

Anorthite, olivine, clinopyroxene and chromite typically have yields near 100 ± 5%, which suggests complete reaction between ablated material and the ambient $F_2$ atmosphere. Measured yields for quartz vary between 80 and 105%. We suspect that yields lower than 100 % for quartz are a result of its relative transparence to 157 nm

Table 2. Yield measurement for different minerals by weight loss

| Sample | Weight loss[&] (μg) | Gas produced[#] (μmol) | Yield (%) | Gas produced per shot (nmol) |
|---|---|---|---|---|
| K-feldspar | | | | |
| K-1 | 1157.3 | 0.554 | 3.3 | |
| *K-2* | *462.2* | | | |
| Amelia Albite | | | | |
| A-1 | 309.8 | 0.652 | 13.8 | |
| A-2 | 494.4 | 0.692 | 9.2 | |
| *A-3* | *257.2* | | | |
| Anorthite ($An_{70}$) | | | | |
| An-1 | 28.3 | 0.417 | 100.5 | 2.78 |
| *An-2* | *-1.8* | | | |
| Brazil quartz | | | | |
| Q-1 | 30.4 | 0.415 | 82.1 | 2.77 |
| Q-2 | 33.0 | 0.523 | 95.2 | 3.49 |
| Q-3 | 42.3 | 0.717 | 101.8 | 4.78 |
| Q-4 | 35.0 | 0.564 | 96.9 | 3.76 |
| Q-5 | 50.5 | 0.808 | 96.2 | 5.39 |
| Q-6 | 48.8 | 0.774 | 95.3 | 5.16 |
| Q-7 | 79.6 | 1.216 | 91.8 | 8.11 |
| Q-8 | 70.1 | 1.085 | 93.0 | 7.23 |
| Q-9 | 75.3 | 1.173 | 93.6 | 7.82 |
| Q-10 | 51.1 | 1.014 | 105.2 | 6.76 |
| *Q-11* | *-0.3* | | | |

Table 2. (Continued)

| Sample | Weight loss[&] (μg) | Gas produced[#] (μmol) | Yield (%) | Gas produced per shot (nmol) |
|---|---|---|---|---|
| *Q-12* | *0.9* | | | |
| *Q-13* | *-0.5* | | | |
| San Carlos Olivine ($Fo_{90}$) | | | | |
| SCO-1 | 14.7 | 0.188 | 95.8 | 1.25 |
| SCO-2 | 34.0 | 0.451 | 99.5 | 3.00 |
| San Carlos CPX (assuming diopside) | | | | |
| SCC-1 | 34.6 | 0.489 | 102.0 | 3.26 |
| *SCC-2* | *-0.3* | | | |
| *SCC-3* | *-0.6* | | | |
| South Carolina Chromite | | | | |
| SCCH-1 | 39.1 | 0.365 | 104.5 | 2.43 |

**&**: Weight loss is measured by CAHN 29 -- an automatic electro-balance (± 0.1μg). The expected amount of gas produced is calculated from stoichiometry of minerals; the amount of $O_2$ gas produced is inferred from calibrated molarities by the voltage of cup 32 in the MAT-252.

radiation. At the end of a laser ablation analysis of a polished slab of quartz, we find an etched pit on both the front and back sides of the slab which never happened for other minerals. The pit formed on the under side of the slab is likely caused by reflection of the transmitted laser light off the gold-coated stainless steel pedestal, driving ablation on the under-side of the quartz. If the material ablated from the back of the quartz slab are harder to react with $F_2$ (e.g., because of limited access to $F_2$ reagent and short-path length to a surface where it can plate out), then relatively little $O_2$ gas will be formed. Yields in

excess of 100% are unusual and only slightly above expectations; we suspect they reflect analytical blanks and errors in yield measurements.

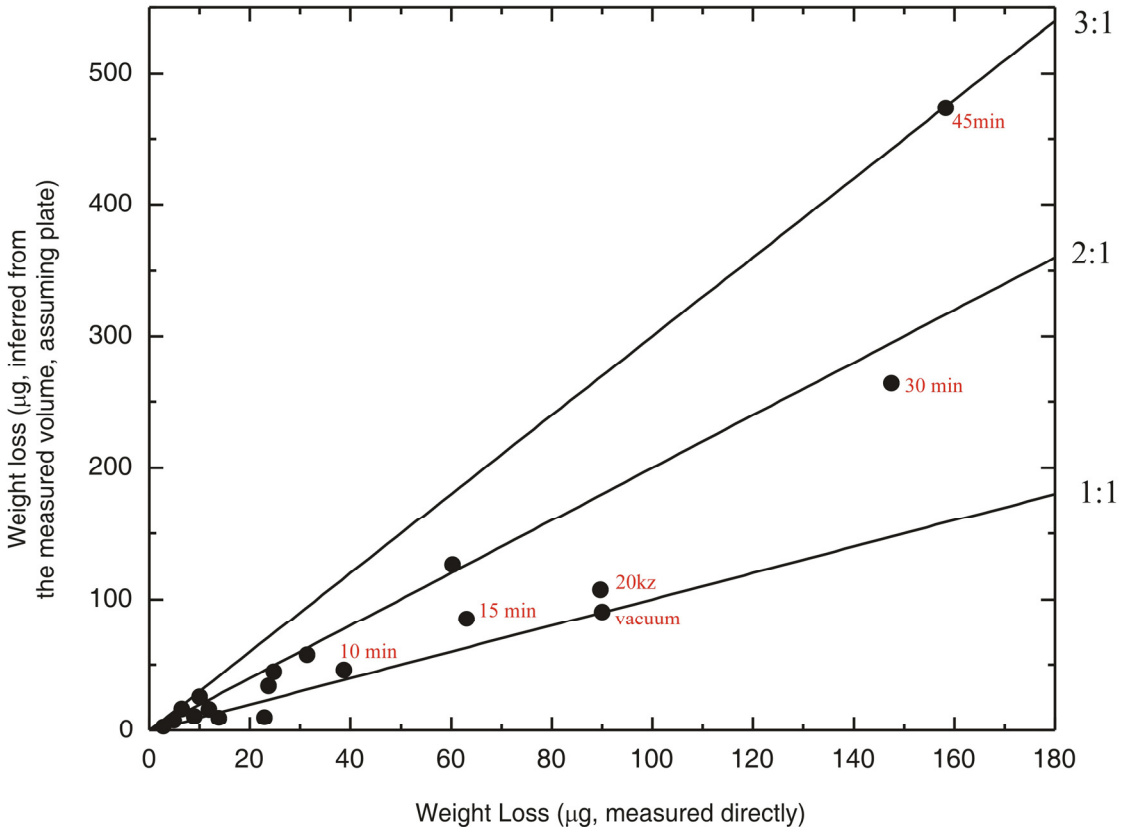


**Figure 4.** Measured weight loss before and after laser ablation compared with weight loss inferred from the geometry of the laser pits assuming a plate shape. The depth of the pit is measured using the focal point of the microscope. This comparison can infer the shape the laser pit, e.g., 1:1 implies it is a plate, 3:1 implies it is a pyramid. All experiments are conducted on Brazil quartz grains.

Yield measurements using weight loss method are much more precise than from volume measurements because the pit shape is variable depending on the laser duration and power, concentration of $F_2$ in the laser tube, focus, time of ablation, and the vacuum of the sample chamber. Figure 4 shows the direct measurement of weight loss for Brazil

quartz compared with estimation from density and the geometry of pits assuming they are plates. Those pits are produced by rastering the laser beam over a typically 400 × 500 μm

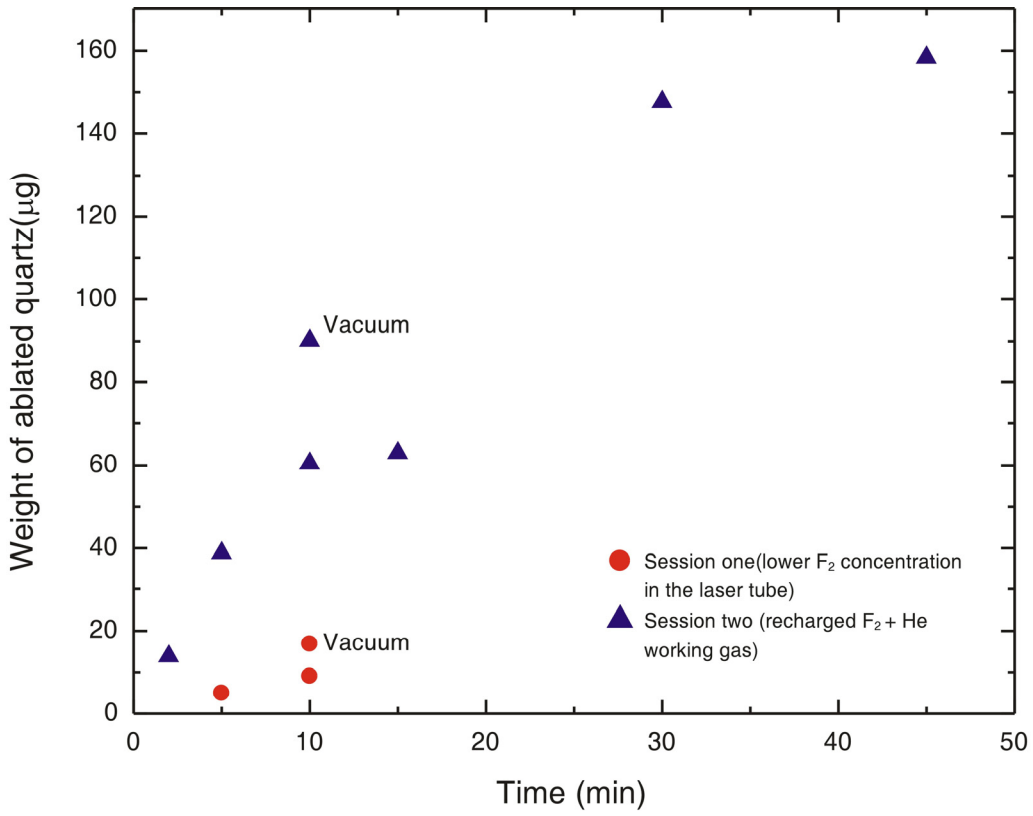


**Figure 5.** Variation of excimer laser ablation rate of quartz with laser and sample chamber conditions.

rectangle area with depth from 20 to 500 μm. The ratio of the expected over the measured weight loss tells us about the shape of the pit, i.e., 1:1 means the pit is roughly a plate, and 3:1 means the pit is roughly a pyramid, which is hard to tell from direct observation. Figure 4 also shows the ablation efficiency decreases as ablation time increases, which is presumably caused by the loss of focus and the increase of gas pressure in the chamber. Figure 5 shows $F_2$ concentration in the laser tube affects the ablation efficiency, and $F_2$ gas in the sample chamber absorbs UV-photon energies and reduces the ablation rate.

### 3.2 ABLATION MECHANISM

The yield measurements indicate that the ablated material reacts completely, or nearly completely, with reagent $F_2$ to yield $O_2$ gas and metal fluorides. Previous studies of *in situ* laser fluorination in an $F_2$ atmosphere have suggested that $O_2$ is produced by expansion of a plume of hot plasma (or particles/gas with high kinetic energy) into the cold $F_2$ atmosphere (FARQUHAR and RUMBLE, 1998; YOUNG et al., 1998). Alternatively, one can imagine that fragments and melt-droplets ejected from the sample surface by detonation, fusion, and/or evaporation might react with the $F_2$ atmosphere due to their ratios of surface area to volume. We performed several experiments that discriminate between these alternate mechanisms. First, we ablated San Carlos olivine in vacuum (without $F_2$ reagent) and produced far less than the normal amount of $O_2$ gas (equivalent to ~5% yield). This $O_2$ gas was pumped out of the sample chamber, and then we performed a second ablation of the same grain under an $F_2$ atmosphere (as normal). This time, the yield was about 150 % and the $\delta^{18}O$ value of product $O_2$ was about 4.0‰ lower than the expected value. We interpret this as evidence that fine-grained metal oxide precipitates that are formed by quenching of the ablated plume in vacuum undergo only partial reaction, yielding $^{18}O$-poor $O_2$ (perhaps due to a kinetic isotope effect that manifests itself when the fluorination reaction is incomplete). Another experiment only introduces $F_2$ into the chamber after the first ablation in vacuum. It yields about 30% gas of what is expected from a typical ablation session in $F_2$ atmosphere, and the $\delta^{18}O$ value is about 6.0‰ lower than expected. These experiments indicate that the fine powders of the ablated chunks/particles are very reactive with $F_2$, even at room temperature. However, fluorination cannot be completed after particles precipitate. It truly requires an

interaction between an activated $F_2$ gas and high energy ablated particles to complete these reactions.

It is well-known photochemistry that $O_2$ will dissociate after radiation by deep UV light ($\lambda < 243$ nm, for ArF and He + $F_2$ lasers) to form O· radicals which will later incorporate with $O_2$ to form $O_3$. The formation of $O_3$ could result in mass-independent fractionation (THIEMENS and HEIDENREICH, 1983). However, $O_3$ effects have not been identified in any previous studies (FIEBIG et al., 1999) or this study. This can be understood by the fact that the reaction rate for $O\cdot + F_2 \rightarrow OF + F\cdot$ is much faster than the reaction $O\cdot + O_2 \rightarrow O_3$ at room temperature. The second order rate constants for $O\cdot + O_2 + M \rightarrow O_3 + M$ is about $6 \times 10^{-34}$ $cm^6/molecule^2 \cdot s$ (ATKINSON et al., 2004), whereas for $O(1D) + F_2 \rightarrow OF + F\cdot$, it is $1.0 \times 10^{-16}$ $cm^3/molecule \cdot s$ (ARUTYUNOV, 1979). The formed F· radical will continuously react with $O_2$ to form $O_2F$ with a third order reaction rate of $4.41 \times 10^{-33}$ $cm^6/molecule^2 \cdot s$ (DEMORE, 1997) slightly larger than the rate to form $O_3$. Even if $O_3$ is formed by chance, $O_3$ will dissociate with a relatively fast rate due to the existence of F· radical (second order rate constants for reaction $O_3 + \cdot F \rightarrow O_2 + OF$, is $2.19 \times 10^{-11} cm^3/molecule \cdot s$, DEMORE, 1997).

### 3.3 COATING EXPERIMENT

One of the key difficulties in making excimer laser fluorination measurements is minimizing the contribution of the analytical blank to the sample gas (with a typical goal of reducing it to less than 10 %). This is particularly challenging for continuous-flow measurements, where the sample size is a fraction of a micromole. The simplest way of reducing analytical blanks is by prolonged high-vacuum pumping and pre-fluorination

time (which we do for about a week for most sample types). This limits the productivity of *in situ* laser fluorination methods, and is insufficient for many sample types (e.g, fine-grained rock sections, and those composed of particularly reactive minerals). For these reasons, we have explored the possibility of reducing analytical blank by coating samples with thin layers of metals that are relatively un-reactive with $F_2$ gas (including Au, Al, Cu, Ni, Cr and Ti).

We deposited layers of these metals up to 3000 Å thick on $CaF_2$, $SiO_2$, and glass wafers, and on quartz and olivine crystals. Unfortunately, these thin coatings (including Al, the most reflective metal for 157 nm UV photons and commonly used as coats for mirrors to reflect UV light) were typically ablated and peeled off the sample surface after a single laser burst at the fluence needed for geochemical analysis by laser ablation. This was true with or without adhesion coats. Therefore, it was impractical to make the hole in the mask smaller than the diameter of the laser unless we could plate the target with much thicker and stronger coatings. We also noted that this peeling effect could be mitigated using a thick (1 μm), multilayer aluminum-chrome-aluminum coating. The aluminum absorbed and dissipated the laser energy by reflection and melting at low temperatures while the thin (100 Å) chrome interlayer tended to focus the beam a little bit. However this particular multilayer technique was not pursued, as it was deemed inefficient and impractical because this 157 nm laser will penetrate through a several-micron thick target.

Tests on quartz wafers showed that we could implement lithographic coatings on well-polished geological samples using standard semiconductor photoresists and exposures under a light microscope. If the microscope had both transmitted and reflectance capabilities, the “holes” in the coating could be strategically placed.

Accordingly, we could coat an entire sample except for the one or two grains that we want to analyze.

In response to our failure at finding photo-resistant thin coatings, we also experimented with machining of 1 mm-thick metal foils (Au, Al, Cu, Ni, Cr and Ti) that can shield 157 nm deep UV light at the requisite 1.5 watts. This approach was successful, but naturally limited by the spatial scale of our ability to machine holes and slots in foils, and thus, is generally coarser than our target spatial scale of ca. 10 μm.

A polished grain of San Carlos olivine was partially masked with a 3000 Å Ti-Au coating. Oxygen isotope analyses on both the coated and uncoated sides were performed by laser-ablation fluorination technique. Analytical results show that the coating did not alter the measured oxygen isotopic ratios beyond analytical uncertainty ($1\sigma \approx 0.2$ ‰ in $\delta^{18}O$). Scanning Electron Microscope (SEM) analysis of ablated pits showed that reaction products of both coated and uncoated grain portions consist of the commonly observed mixture of metal-fluoride aggregates. Further comparison between basalt sections with Ti-Au coats (170 Å Ti and 2000 Å Au) and without coating showed that "masking" reduces the pumping and $F_2$ pre-treatment time by half, lowers the analytical blank during laser ablation by a factor of three, and therefore, allows us to apply the technique to unusually reactive sample types (e.g., volcanic groundmass, meteorite matrix, and sedimentary rocks).

### 3.4 ANALYZING CHROMITE

The spot size of this 157 nm laser can be controlled up to 300 μm in diameter by adjusting the size of the aperture. We typically use spots with 80~100 μm in diameter.

For the dual-inlet systems, a 400×500 μm rectangle area is scanned to produce ~ 1 μmol $O_2$ gas, while for the continuous flow system, laser beam is stationary. These allow us to investigate the homogeneity of single crystal or rock sections, and thereby, broaden our view of geological processes. Two of these applications are discussed in Section 5. However, there are other applications that take advantage of the special properties of the laser ablation reaction itself, independent of the issue of spatial resolution.

Values of $\delta^{18}O$ of chromite measured by infra-red laser fluorination technique are generally significantly lower than those measured on the same material by conventional resistance-heated fluorination, and are lower than expected, based on simple models of the reduced partition coefficients of oxides (ZHENG, 1991, CLAYTON and KIEFFER, 1991). This discrepancy has been attributed to grain size effects during laser-fluorination analyses (FOUILLAC and GIRARD, 1996), although similar effects found in that study for quartz have been subsequently shown to reflect details of their method and not an intrinsic property of laser fluorination reactions (SPICUZZA et al., 1998). We examined the causes of these analytical artifacts for chromite and whether laser fluorination driven by 157 nm radiation can circumvent those artifacts.

We first separated magnetite grains from Soledad canyon (massif rock with 90% of fine grained metallic magnetite; might be associated with granodiorite), and mixed them with variable amounts of Cr metal (with purity of 99.9%). Some of the mixtures were heated under vacuum using a 50 W $CO_2$ laser so that the Cr metal and magnetite could react to form intermediate compounds (e.g., chromite); others are only mechanical mixtures. Figure 6 presents the results of $CO_2$-laser fluorination analyses of these materials. Most of mixtures, whether they are pre-heated or not have $\delta^{18}O$ values lower

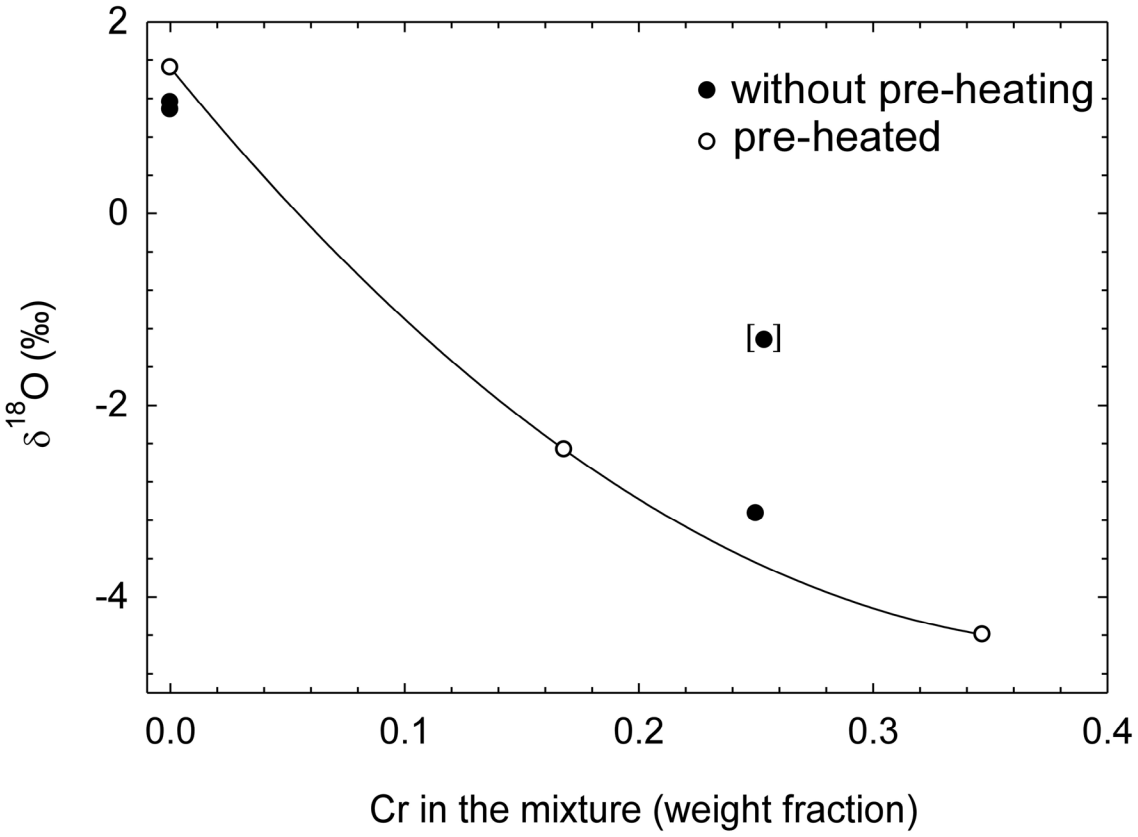


**Figure 6.** Effect of Cr on $\delta^{18}O$ values of Cr and magnetite mixtures measured using infrared laser fluorination techniques.

than the pure magnetite starting material, and their $\delta^{18}O$ values roughly correlate with the proportion of Cr in the mixture. One outlier (bracket circle) is the result of an analysis in which the sample 'jumped' during lasing -- a phenomenon that is often associated with partial reaction and inaccurate results. The yields of these experiments are generally 55 ~ 70% of that expected from stoichiometry and mixing-fraction of magnetite. One of the possible explanations for this phenomena is the formation of a series of Cr, O, and F/Br compounds such as $CrF_2O_2$, $CrBr_2O_2$ and $CrF_xO$ (x=1-5) which prevent quantitative extraction of $O_2$ into the gas phase.

Natural chromites typically contain ≥ 40 wt% of Cr metal, and thus, the phenomena we observe for analyses of magnetite-Cr mixtures provide a reasonable explanation of the low $\delta^{18}O$ values obtained by IR-laser fluorination of chromite. Finally, we measured the $\delta^{18}O$ values of two chromite samples from South Carolina using both the IR-laser fluorination technique and our new 157-nm *in situ* laser fluorination technique. These chromites are associated with meta-ultramafic rocks (e.g., meta-dunite), and are typically tens of microns in size. Since they are closely associated with olivine, the $\delta^{18}O$ values can be predicted to be ~ 3.9 ‰ if we assume olivine is in oxygen isotope exchange equilibrium with chromite at ~1200°C and the fractionation factor between chromite and forsterite is similar to between magnetite and forsterite olivine, based on the fractionation factors by CLAYTON and KIEFFER (1991). The fractionation factor calculated by ZHENG (1991) suggests it is even closer to olivine than magnetite by a couple of a tenths per mil.

We selected hundreds of grains from these samples and treated them with HF at 80 ~ 100°C for three hours. Impurities of silicate minerals attached on those chromites completely dissolved in warm HF. We picked out euhedral chromite after this treatment and loaded them for laser fluorination measurement. The $\delta^{18}O$ values measured by infrared laser fluorination technique are -1.2 ± 0.1‰ -- associated with low $O_2$ yields -- whereas the UV laser fluorination method results in $\delta^{18}O$ values of 3.5±0.2 ‰ and yields are close to 100% (Tables 1 and 2). While we do not independently know the $\delta^{18}O$ values of these chromites (and likely cannot without an inter-laboratory calibration effort, as no well-characterized chromite oxygen isotope standards exist), these results suggest that 157 nm laser fluorination yields essentially circumvents the analytical artifacts associated with IR-laser fluorination. We suspect this is because the plasma generated by 157 nm

laser ablation fully dissociates Cr-O bonds, and the Cr ions quantitatively quench to $CrF_3$, providing no opportunity to form Cr-O-F compounds. It is possible that the 157 nm laser will be similarly useful in improving the accuracy of $\delta^{18}O$ analyses of other hard-to-fluorinate materials (e.g., phosphates).

## 4. APPLICATION

### 4.1 *IN SITU* OXYGEN ISOTOPE STUDIES OF MINERALS FROM ICELAND

Iceland is famous for the large variations in $\delta^{18}O$ of its lavas (-6 ~ +10‰, TAYLOR and SHEPPARD, 1986; MUEHLENBACHS et al., 1972; MUEHLENBACHS et al., 1974). The petrogenesis of $^{18}O$-depleted primitive lavas has been a long-standing controversy, with one school of thought ascribing their exotic oxygen isotope compositions to a low-$\delta^{18}O$ component in their mantle sources, and another suggesting that component is a crustal contaminant added during fractional crystallization processes (NICHOLSON et al., 1991; EILER et al., 2000; EILER, 2001; MACLENNAN et al., 2003 GRONVOLD, 2000; GEE et al., 1998). Figure 8 compiles all previous $\delta^{18}O$ measurements of olivine, plagioclase and clinopyroxene minerals from Iceland using infra-red laser fluorination techniques (GEE et al., 1998; EILER et al., 2000; HANSEN and GRONVOLD, 2000; MACLENNAN et al., 2003). These data show that $\delta^{18}O$ values of olivines in Iceland lavas vary from 3.5 (well below the range typical of mantle olivine) to 5.4 ‰ (at the upper end of the normal range) (EILER, 2001). Furthermore, the phenocrysts in lava flows are not as heterogeneous as those in gabbroic and wehrlitic nodules (e.g., in Figure 9). Olivine phenocrysts from Borgarhraun have a peak at about 4.5‰ and with a limited range between 4.3 ~ 5.3‰ (EILER et al., 2000), whereas olivines in nodules vary between 3.4 ~ 5.3‰ (MACLENNAN

et al., 2003). Similar differences between data for phenocrysts and nodules exist for clinopyroxene and plagioclase.

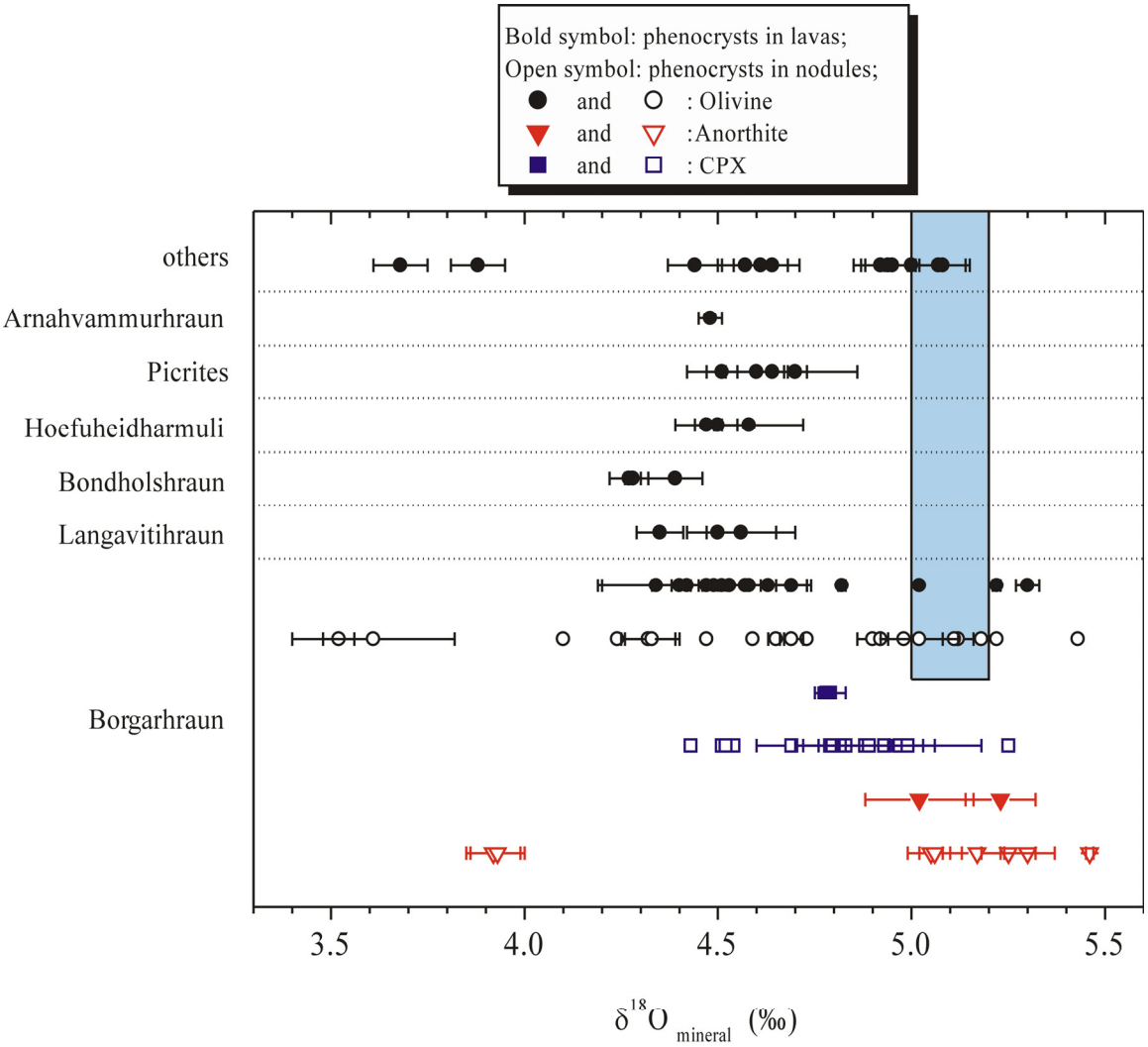


**Figure 7.** Compilation of $\delta^{18}O$ studies on minerals from Iceland (Gee et al., 1998; Eiler et al., 2000; Hansen and Gronvold, 2000; Maclennan et al., 2003**)**

We used the 157-nm laser fluorination technique described here to characterize the intra-crystalline oxygen isotope variations of plagioclase and clinopyroxene phenocrysts from Borgarhraun lava, 98-M1 (EILER et al., 2000). Selected grains were polished on one side, and analyzed using the dual-inlet system described above. The results are shown in

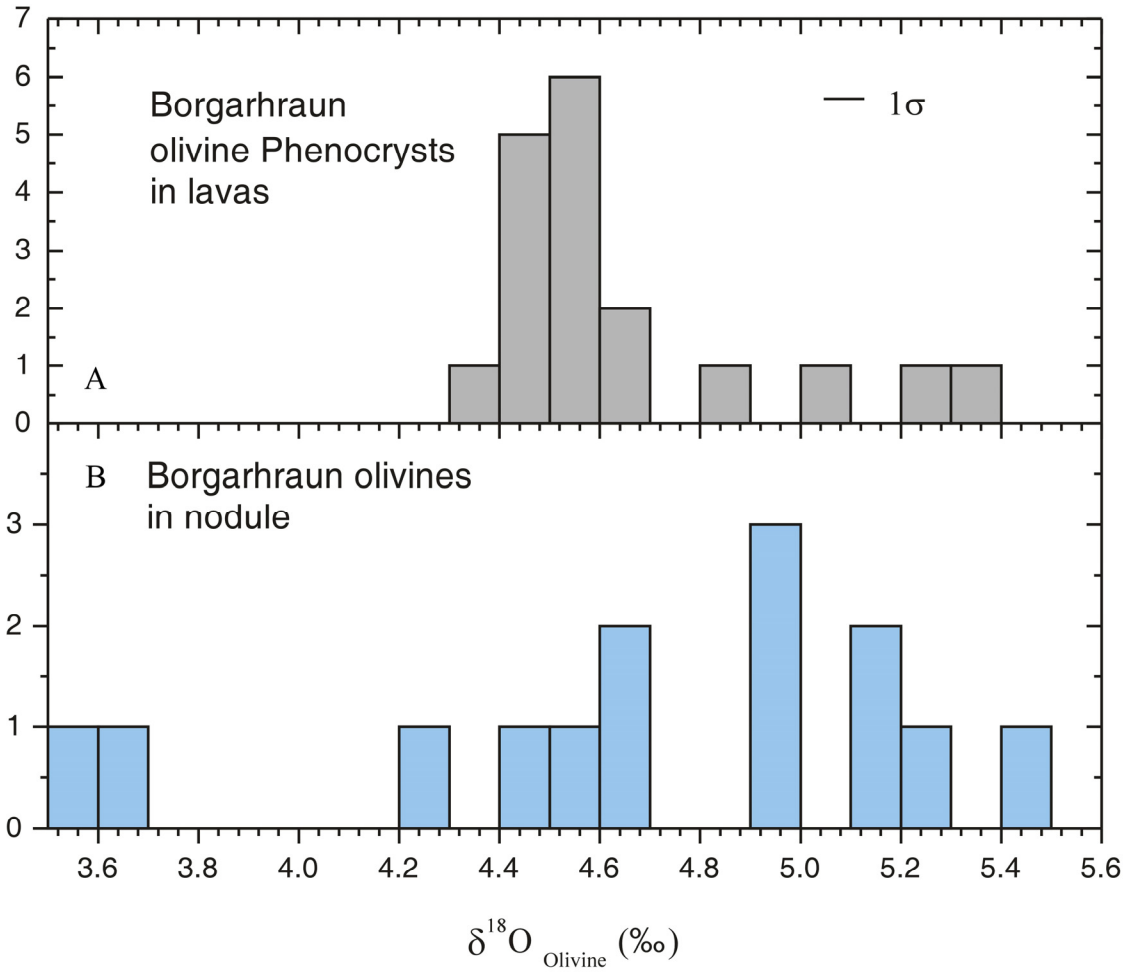


**Figure 8.** Histogram of $\delta^{18}O$ values of olivines from lavas (A) and from wehrlitic nodules in Borgarhraun volcano, Iceland.

Figures 10 and 11. One poly-crystalline aggregate of clinopyroxene (Figure 10), is homogeneous in $\delta^{18}O$ within analytical precision, and approximately in oxygen isotope exchange equilibrium with olivines from the same rock ($\Delta_{cpx\text{-}ol}$ averages ~0.4‰; these pyroxenes and olivines are also in Fe-Mg exchange equilibrium at magmatic temperatures; MACLENNAN et al., 2003). Micro-olivine phenocrysts in the matrix are $Fo_{74\text{-}76}$; plagioclase is $An_{67\text{-}77}$; and CPX micro-phenocrysts have higher concentration of Fe with $Mg^{\#}$ of only 70 to 75. This assemblage should correspond to very late

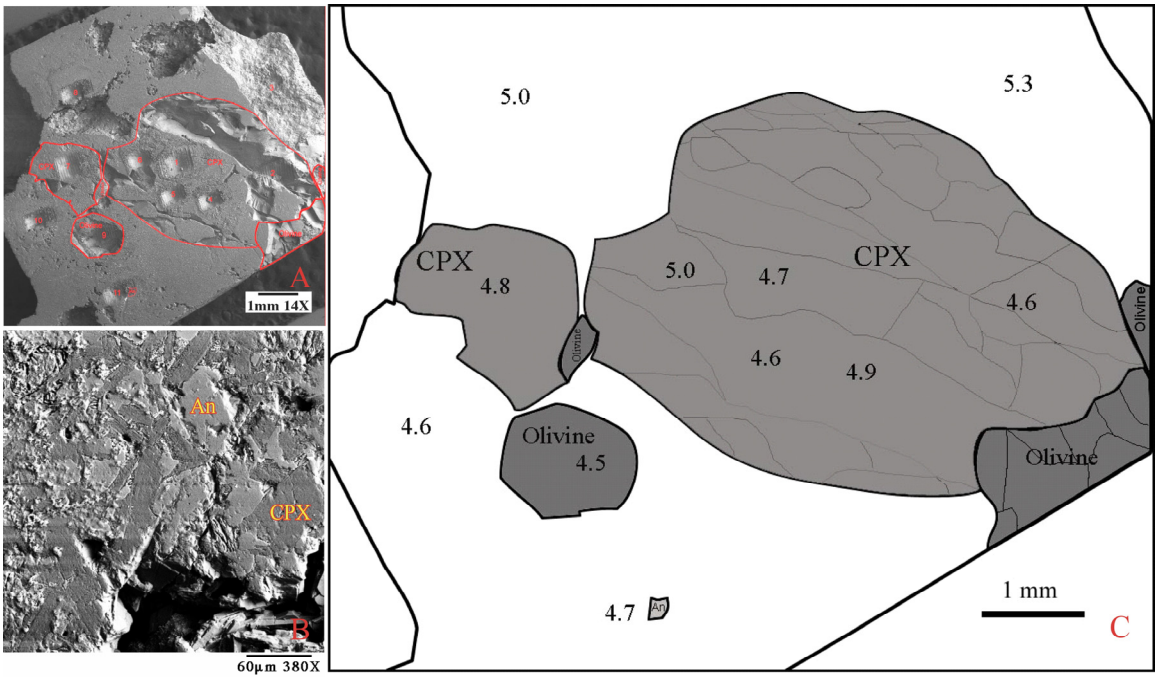


**Figure 9.** Examples of *in situ* oxygen isotope study on a rock section from Borgarhraun, Iceland. Millimeter sized olivine ($Fo_{85\text{-}90}$) and clinopyroxenes ($Mg^{\#}$ of 88~89.8) macrophenocrysts. **A:** back-scatter image of the rock section and the excimer laser pit; **B:** high magnification of the basaltic texture and micro-phenocrysts CPX + An; **C:** a schematic drawing of image A and the oxygen isotope composition.

crystallization processes. The matrices surrounding this CPX are inhomogeneous, but averagely are in oxygen isotope equilibrium with CPX crystals. This sample tells us that the $^{18}O$-depleted component was added to this lava before the crystallization of these MgO rich crystals.

Figure 11 shows *in situ* measurements of a ~3 mm diameter aggregate of anorthite grains from the same lava. This anorthite is $An_{87\text{-}91}$, and also crystallized early in the differentiation history of the magma (likely just after the start of crystallization of magnesian olivine and pyroxene). However, the oxygen isotope systematics of this

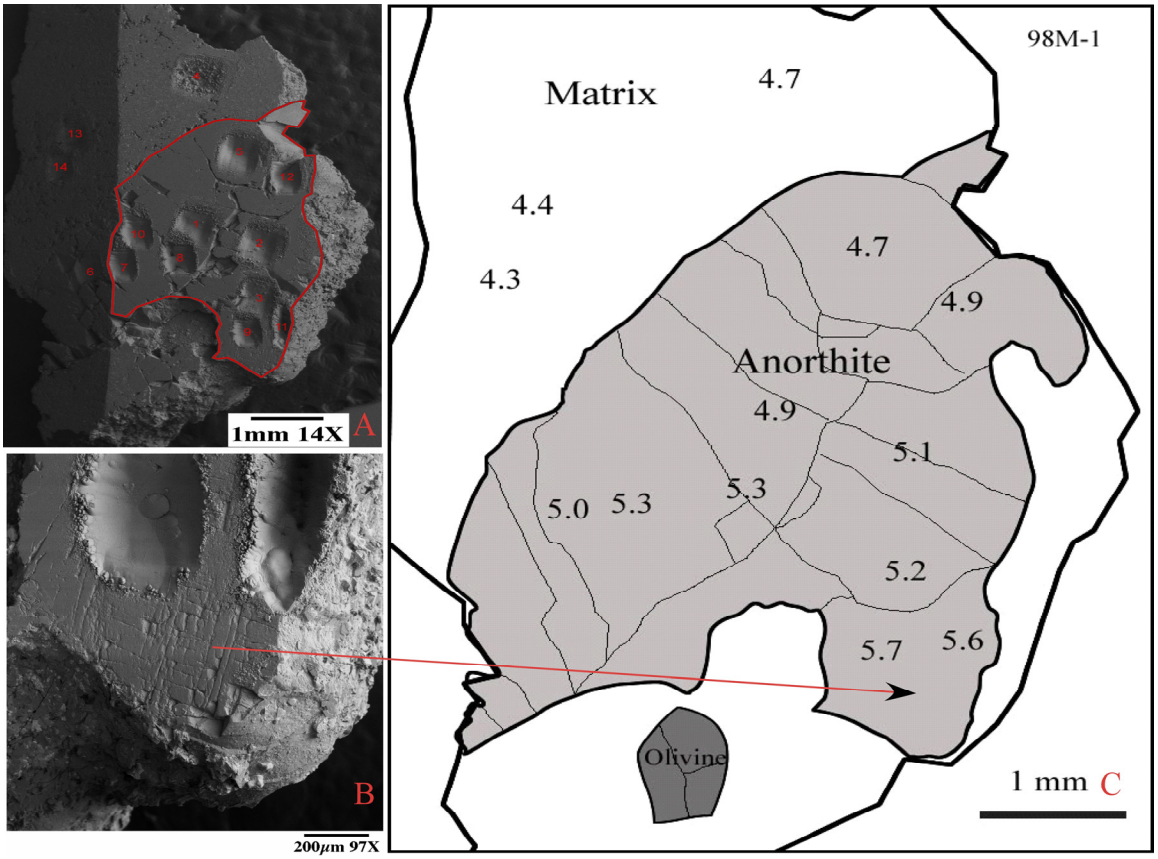


**Figure 10.** *In situ* oxygen isotope study on a millimeter sized plagioclase ($An_{87-90}$) embedded in a rock section from Borgarhraun, Iceland. **A:** back-scatter image of the rock section and the excimer laser pits; **B:** high magnification of the lattice-like cleavage texture associated with relatively enriched $^{18}O$ composition; **C:** a schematic drawing of image A and the oxygen isotope composition.

aggregate are very different from those of clinopyroxene (above): $\delta^{18}O$ values vary between 4.7 (close to equilibrium with co-existing low-$\delta^{18}O$ olivine, pyroxene and groundmass) and ~5.7‰ (far higher than equilibrium, and similar to plagioclase in typical basaltic lavas). Note that the higher-$\delta^{18}O$ grain is riddled with pronounced lattice-like cleavages, whereas lower-$\delta^{18}O$ grains are uncleaved. The contrast in $\delta^{18}O$ between the cleaved and uncleaved grains in this aggregate suggests to us that the high-$\delta^{18}O$ crystal was added to the magma as an assimilant prior to being overgrown by low-$\delta^{18}O$

plagioclase, which precipitated in oxygen isotope exchange equilibrium with co-existing pyroxenes and olivines (above). The preservation of oxygen isotope contrasts between adjacent xenocrystic and phenocrystic plagioclase crystals places constraints on the duration of time between entrainment of the higher-$\delta^{18}O$ xenocryst and eruption of the lava.

To the first order, the time for diffusion controlled oxygen isotope homogenization should require $t > \frac{r^2}{4D_{An}^{oxygen}(T)}$, where t is time, r is the radius of the crystal, and D is the oxygen self-diffusion coefficient in the mineral (An). If r = 1.5 mm, T=1200°C, and expression of $D_{An}^{oxygen}$ as a function of temperature from ELPHICK et al. (1988), then the time *t* is at most 5 kys.

### 4.2 OXYGEN ISOTOPE STUDIES OF OLIVINES FROM SUBAERIAL MAUNA KEA LAVAS

We also conducted a study on analyzing single-grain olivines from subaerial Mauna Kea lavas using continuous flow systems. This study reveals the correlation between forsterite content and oxygen isotope composition, and indicates that contamination by meteoric-water-altered rocks in the volcanic edifice plays an important role in the formation of the $^{18}O$ depleted lavas from subaerial Mauna Kea shields. The details of this work are described in the next chapter.

## 5. CONCLUSION

Our excimer laser (157 nm) fluorination technique is experimentally demonstrated to be capable of measuring the $\delta^{18}O$ values of single grain minerals (olivine, clinopyroxene,

anorthite, quartz, and chromite) and minerals in rock sections with high precision (±0.2‰ for $\delta^{18}O$ and ±0.3‰ for $\delta^{17}O$). The $O_2$ yields from most of these minerals after ablation and fluorination are very close to 100%. Compared with $CO_2$ infra-red laser fluorination techniques, this excimer laser system significantly reduces the material size per analysis (10~100 μg, vs. 1-2 mg), and increases the spatial resolution (100~500 μm spots). It also shows great potential to measure $\delta^{18}O$ values of hard-to-measure minerals such as chromite. Application of this technique to the study of intra-grain, oxygen isotope heterogeneity in lavas from Borgarhraun, Iceland reveals both oxygen isotope equilibrium and disequilibrium phenomena.

**ACKNOWLEDGEMENTS**

We would like to thank H.P Taylor, Edwin Schauble, Greg Holk, and Mike Spicuzza for valuable information and suggestions during the development of this system; George Rossman for offering us precious minerals for measurements and helpful discussion; Dan McKenzie for Iceland samples and comments; Ed Stolper for allowing us to sample HSDP drill core; and Mike Fitzsimmons for helping us to make various kinds of coatings. This work is partially sponsored by the President Fund from JPL, and funding from NSF.

**REFERENCES**

Arutyunov V. S. B., S.N.; Chaikin, A.M. (1979) Homogeneous and heterogeneous decay of oxygen and bromine atoms in the presence of molecular fluorine. *Kinet. Catal.* **20**.

Asprey L. B. (1976) The preparation of very pure fluorine gas. *J. Fluor. Chem.* **7**, 359-361.

Atkinson R., Baulch D. L., Cox R. A., Crowley J. N., Hampson R. F., Hynes R. G., Jenkin M. E., Rossi M. J., and Troe J. (2004) Evaluated kinetic and photochemical data for atmospheric chemistry: Volume I - gas phase reactions of Ox, HOx, NOx and SOx species. *Atmos. Chem. Phys.* **4**, 1461-1738.

Clayton R. N. and Kieffer S. W. (1991) Oxygen isotopic thermometer calibrations. In *Stable Isotope Geochemistry: A Tribute to Samuel Epstein*, Vol. Special Publication No. 3 (ed. J. Hugh P. Taylor, J. R. O'Neil, and I. R. Kaplan). The Geochmical Society.

Clayton R. N. and Mayeda T. K. (1983) Oxygen isotopes in eucrites, shergottites, nakhlites, and chassignites. *Earth and Planetary Science Letters* **62**, 1-6.

DeMore W. B. S., S.P.; Golden, D.M.; Hampson, R.F.; Kurylo, M.J.; Howard, C.J.; Ravishankara, A.R.; Kolb, C.E.; Molina, M.J. (1997) Chemical kinetics and photochemical data for use in stratospheric modeling (Evaluation number 12). *JPL Publication* **97-4**, 1-266.

Eiler J. M. (2001) Oxygen isotope variations of basaltic lavas and upper mantle rocks. *Reviews in Mineralogy & Geochemistry* **43**, 319-364.

Eiler J. M., Farley K. A., Valley J. W., Hofmann A. W., and Stolper E. M. (1996) Oxygen isotope constraints on the sources of Hawaiian volcanism. *Earth and Planetary Science Letters* **144**(3-4), 453-467.

Eiler J. M., Graham C., and Valley J. W. (1997) SIMS analysis of oxygen isotopes: Matrix effects in complex minerals and glasses. *Chemical Geology* **138**(3-4), 221-244.

Eiler J. M., Gronvold K., and Kitchen N. (2000) Oxygen isotope evidence for the origin of chemical variations in lavas from Theistareykir volcano in Iceland's northern volcanic zone. *Earth and Planetary Science Letters* **184**(1), 269-286.

Elphick S. C., Graham C. M., and Dennis P. F. (1988) An ion probe study of anhydrous oxygen diffusion in anorthite: A comparison with hydrothermal data and some geological implications. *Contrib. Mineral.Petrol* **100**(4), 490-495.

Elsenheimer D. and Valley J. W. (1992) *In situ* oxygen isotope analysis of feldspar and quartz by Nd-Yag laser microprobe. *Chemical Geology* **101**(1-2), 21-42.

Farquhar J. and Rumble D., III. (1998) Comparison of oxygen isotope data obtained by laser fluorination of olivine with KrF excimer laser and $CO_2$ laser. *Geochimica et Cosmochimica Acta* **62**(18), 3141-3149.

Fiebig J., Wiechert U., Rumble D., III, and Hoefs J. (1999) High-precision *in situ* oxygen isotope analysis of quartz using an ArF laser. *Geochimica et Cosmochimica Acta* **63**(5), 687-702.

Fouillac A. M. and Girard J. P. (1996) Laser oxygen isotope analysis of silicate/oxide grain separates: Evidence for a grain size effect? *Chemical Geology* **130**(1-2), 31-54.

Gee M. A. M., Thirlwall M. F., Taylor R. N., Lowry D., and Murton B. J. (1998) Crustal processes: Major controls on Reykjanes Peninsula lava chemistry, SW Iceland. *Journal of Petrology* **39**(5), 819-839.

Hansen H. and Gronvold K. (2000) Plagioclase ultraphyric basalts in Iceland: the mush of the rift. *Journal of Volcanology and Geothermal Research* **98**(1-4), 1-32.

Li W. J. and Meijer H. A. J. (1998) The use of electrolysis for accurate small delta, $\delta^{17}O$ and small delta, $\delta^{18}O$ isotope measurements in water. *Iso. Env. Health Stud* **34**, 349-369.

Luz B., Barkan E., Bender M. L., Thiemens M. H., and Boering K. A. (1999) Triple-isotope composition of atmospheric oxygen as a tracer of biological productivity. *Nature* **400**, 547-550.

Maclennan J., McKenzie D., Gronvold K., Shimizu N., Eiler J. M., and Kitchen N. (2003) Melt mixing and crystallization under Theistareykir, northeast Iceland. *Geochemistry Geophysics Geosystems* **4**.

Matsuhisa Y., Goldsmith J. R., and Clayton R. N. (1978) Mechanisms of hydrothermal crystallization of quartz at 250°C and 15 kbar. *Geochim. Cosmochim. Acta* **42**, 173–182.

Merritt D. A., Brand W. A., and Hayes J. M. (1994) Isotope-Ratio-Monitoring Gas-Chromatography Mass-Spectrometry - Methods for isotopic calibration. *Organic Geochemistry* **21**(6-7), 573-583.

Merritt D. A. and Hayes J. M. (1994) Factors controlling precision and accuracy in Isotope-Ratio-Monitoring Mass-Spectrometry. *Analytical Chemistry* **66**(14), 2336-2347.

Miller M. F. (2002) Isotopic fractionation and the quantification of $^{17}O$ anomalies in the oxygen three-isotope system: An appraisal and geochemical significance. *Geochimica et Cosmochimica Acta* **66**(11), 1881-1889.

Miller M. F., Franchi I. A., Sexton A. S., and Pillinger C. T. (1999) High precision delta $^{17}O$ isotope measurements of oxygen from silicates and other oxides: Method and applications. *Rapid Communications in Mass Spectrometry* **13**(13), 1211-1217.

Muehlenbachs K., Anderson A. T., and Sigvalda G. (1974) Low-$^{18}O$ basalts from Iceland. *Geochimica et Cosmochimica Acta* **38**(4), 577-588.

Muehlenbachs K., Sigvalda G., and Anderson A. T. (1972) Origins of $^{18}O$-poor volcanic-rocks from Iceland. *Transactions-American Geophysical Union* **53**(4), 556-&.

Nicholson H., Condomines M., Fitton J. G., Fallick A. E., Gronvold K., and Rogers G. (1991) Geochemical and isotopic evidence for crustal assimilation beneath Krafla, Iceland. *Journal of Petrology* **32**(5), 1005-1020.

Rumble D. and Hoering T. C. (1994) Analysis of oxygen and sulfur isotope ratios in oxide and sulfide minerals by spot heating with a carbon-dioxide laser in a fluorine atmosphere. *Accounts of Chemical Research* **27**(8), 237-241.

Rumble D., III, Farquhar J., Young E. D., and Christensen C. P. (1997) *In situ* oxygen isotope analysis with an excimer laser using $F_2$ and $BrF_5$ reagents and $O_2$ gas as analyte. *Geochimica et Cosmochimica Acta* **61**(19), 4229-4234.

Rumble D. and Sharp Z. D. (1998) Laser microanalysis of silicates for $^{18}O/^{17}O/^{16}O$ and of carbonates for $^{18}O/^{16}O$ and $^{13}C/^{12}C$ ratios. *Reviews in Economic Geology* **7**, 99-119.

Sharp Z. D. (1990) A laser-based micro-analytical method for the *in situ* determination of oxygen isotope ratios of silicates and oxides. *Geochimica et Cosmochimica Acta* **54**(5), 1353-1357.

Spicuzza M. J., Valley J. W., Kohn M. J., Girard J. P., and Fouillac A. M. (1998) The rapid heating, defocused beam technique: A $CO_2$-laser-based method for highly precise and accurate determination of delta $^{18}O$ values of quartz. *Chemical Geology* **144**(3-4), 195-203.

Taylor H. P. and Sheppard S. M. F. (1986) Igneous rocks 1. Processes of isotopic fractionation and isotope systematics. *Reviews in Mineralogy* **16**, 227-271.

Thiemens M. H. and Heidenreich J. E., III. (1983) The mass-independent fractionation of oxygen: A novel isotope effect and its possible cosmochemical implications. *Science* **219**(4588), 1073-1075.

Thiemens M. H., Jackson T., Zipf E. C., Erdman P. W., and Egmond C. v. (1995) Carbon dioxide and oxygen isotope anomalies in the mesosphere and stratosphere. *Science* **270**, 969-972.

Valley J. W., Kitchen N., Kohn M. J., Niendorf C. R., and Spicuzza M. J. (1995) UWG-2, a garnet standard for oxygen isotope ratios: Strategies for high precision and accuracy with laser heating. *Geochimica et Cosmochimica Acta* **59**(24), 5223-5231.

Wiechert U., Fiebig J., Przybilla R., Xiao Y., and Hoefs J. (2002) Excimer laser isotope-ratio-monitoring mass spectrometry for *in situ* oxygen isotope analysis. *Chemical Geology* **182**(2-4), 179-194.

Wiechert U. and Hoefs J. (1995) An excimer laser-based micro analytical preparation technique for *in situ* oxygen isotope analysis of silicate and oxide minerals. In *Geochimica et Cosmochimica Acta*, Vol. 59 (eds. D. A. Vanko and P. E. Brown), pp. 4093-4101. Pergamon.

Young E. D., Coutts D. W., and Kapitan D. (1998) UV laser ablation and irm-GCMS microanalysis of $^{18}O/^{16}O$ and $^{17}O/^{16}O$ with application to a calcium-aluminium-rich inclusion from the Allende meteorite. *Geochimica et Cosmochimica Acta* **62**(18), 3161-3168.

Young E. D., Fogel M. L., Rumble D., III, and C. H. T. (1998) Isotope-ratio-monitoring of $O_2$ for micro-analysis of $^{18}O/^{16}O$ and $^{17}O/^{16}O$ in geological materials. *Geochimica et Cosmochimica Acta* **62**(18), 3087-3094.

Zheng Y. F. (1991) Calculation of oxygen isotope fractionation in metal-oxides. *Geochimica et Cosmochimica Acta* **55**(8), 2299-2307.

# CHAPTER 3.

# INSIGHTS INTO THE ORIGIN OF LOW-$\delta^{18}$O BASALTIC MAGMAS IN HAWAII REVEALED FROM *IN SITU* MEASUREMENTS OF OXYGEN ISOTOPE COMPOSITION OF SINGLE-GRAIN OLIVINES

Zhengrong Wang and John M. Eiler

Division of Geological and Planetary Sciences, M/C 100-23,

California Institute of Technology, Pasadena, CA 91125, USA

(*wzhr@gps.caltech.edu*, *eiler@gps.caltech.edu*)

**ABSTRACT**

*In situ* measurements of oxygen isotope composition and element concentrations in olivines were conducted on Mauna Loa and subaerial Mauna Kea lavas from the HSDP-2 (Hawaiian Scientific Drilling Project, phase II) drill core. Values of $\delta^{18}O$ passively correlate with Fo contents of olivines from Mauna Kea lavas, indicating that low-$\delta^{18}O$ components were gradually added to magmas parental to those lavas during their crystallization-differentiation histories. This result suggests that low-$\delta^{18}O$ components are contaminants from the volcanic edifice or lithosphere rather than plume components. Models of assimilation-fractional crystallization (AFC) processes can reproduce our observations if the $\delta^{18}O$ values of crustal contaminants decrease sharply at the submarine - subaerial transition in Mauna Kea lavas, and if Mauna Loa lavas are either uncontaminated or contaminated only by rocks that are 'normal' in $\delta^{18}O$ value. We suggest that the differences in oxygen isotope systematics among Mauna Loa, submarine Mauna Kea and subaerial Mauna Kea lavas principally reflect the sources and amounts of water available to hydrothermal systems in the volcanic edifice.

**INTRODUCTION**

Subaerial shield-building tholeiitic lavas from the Hawaiian volcanoes of Kilauea, Mauna Kea, Kohala and Haleakala commonly contain olivine phenocrysts having $\delta^{18}O$ values of ca. 4.4 to 5.0 ‰ -- lower than those typical of upper mantle olivines or olivine phenocrysts in most other basaltic Hawaiian lavas (ca. 5.0 to 5.4‰, Mattey et al., 1994; Eiler, 2001). This $^{18}O$-depletion is most extreme and best documented in the subaerial section of Mauna Kea volcano (Wang et al., 2003) and the Pu'u O'o eruption of Kilauea

volcano (Garcia et al., 1998). Smaller numbers of analyses of glass and plagioclase phenocrysts co-existing with these olivines show them to be $^{18}O$-depleted as well, compared to those same phases in most other terrestrial basalts, and also show that an unusually large proportion of low-$\delta^{18}O$ Hawaiian lavas exhibit disequilibrium olivine-glass oxygen isotope fractionations (Wang et al., 2003; Eiler, 2001).

Several hypotheses have been put forward to explain the origin of low $\delta^{18}O$ values in some Hawaiian lavas including: 1) $^{18}O$-depletion of primitive lower-mantle that is presumed to core the Hawaiian plume (Harmon and Hoefs, 1995); 2) entrainment of $^{18}O$-depleted, recycled lower oceanic lithosphere within the Hawaiian plume (Lassiter and Hauri, 1998); 3) contamination of Hawaiian magmas by $^{18}O$-depleted rocks in the current Pacific lithosphere (Eiler et al., 1996b; Gaffney et al., 2004); and 4) contamination of Hawaiian magmas by hydrothermally altered, low-$\delta^{18}O$ rocks in the volcanic edifice (Garcia et al., 1998; Wang et al., 2003). It is important to discriminate these possibilities because of the different implications each has for the interpretation of other geochemical properties of Hawaiian lavas, for the 'plumbing' of the Hawaiian volcanic edifice and underlying lithosphere, and for the structure and composition of the Hawaiian plume.

Hawaiian lavas contain diverse textural types of olivine phenocrysts and/or xenocrysts, including un-deformed coarse phenocrysts, kink-banded coarse phenocrysts, rods, aggregates, and micro-phenocrysts (e.g., Garcia, 1996). Wang et al. (2003) found that micro-phenocrysts in submarine Mauna Kea lavas are commonly in oxygen isotope exchange equilibrium with co-existing glass or groundmass and are systematically lower in $\delta^{18}O$ values than coarse phenocrysts. That is, although coarse phenocrysts are lower in $\delta^{18}O$ values than those in most terrestrial basalts and peridotites, they are not as low as

micro-phenocrysts and not low enough to be in oxygen isotope exchange equilibrium with host magmas. Wang et al. (2003) suggested that this difference between phenocrysts and micro-phenocrysts reflects the fact that: 1) low $\delta^{18}O$ components were added to Mauna Kea lavas gradually over the course of their crystallization-differentiation histories; 2) coarse phenocrysts crystallized early in this process, sampling relatively little of those components; and 3) micro-phenocrysts crystallized later, sampling relatively large amounts of those components. This interpretation is consistent with differences in Fo content between coarse phenocrysts and micro-phenocrysts. However, this correlation between oxygen isotope composition and Fo content is subtle because oxygen isotope studies using infrared laser fluorination technique can only be carried out on phenocryst and micro-phenocryst mixtures due to the sample size limitation. Furthermore, textural evidence that some coarse olivines are xenocrysts also permits that they might have originally precipitated from some other, entirely unrelated magma. In this case, differences in $\delta^{18}O$ between phenocrysts and microphenocrysts might not accurately reflect the differentiation history of any one magma, and thus provide no indication for the relationship between differentiation and low-$\delta^{18}O$ components.

In this study, we document variations in $\delta^{18}O$ value and elemental abundances within individual coarse grain olivines from subaerial Mauna Kea lavas, measured by *in situ* UV laser fluorination and electron microprobe, respectively. We show that $\delta^{18}O$ values decrease with decreasing Fo contents within individual coarse olivines, that micro-phenocrysts lie on the extension of this trend of $\delta^{18}O$ vs. Fo content defined by coarse phenocrysts, and that the most magnesian cores of coarse phenocrysts are actually 'normal' in $\delta^{18}O$ (i.e., lacking any evidence for low- $\delta^{18}O$ components), even in lavas

having low $\delta^{18}O$ values when averaged over multiple grains. These results support the interpretation that Mauna Kea lavas are generated with 'normal' $\delta^{18}O$ values, and acquire low $\delta^{18}O$ components gradually throughout their crystallization-differentiation histories. We develop a quantitative model for such a process and discuss its relevance for understanding previous studies of oxygen isotope variations in Hawaiian lavas.

## SAMPLING AND ANALYSIS

We selected eight coarse olivine grains from four subaerial Mauna Kea lavas and five grains from two subaerial Mauna Loa lavas; all sampled lavas are from the HSDP-2 core. Selected grains were tabular and had widths between about 2 and 5 mm, and thickness between about 0.8 and 1.5 mm. These grains were polished to remove approximately half their thicknesses, revealing a cross-section through the core of each grain, and then mounted on a slab of $BaF_2$ using copper tape (3 M® double sided copper tape, copper coated with thin film of acrylic adhesives). We then analyzed the oxygen isotope compositions of portions of their polished surfaces by 157 nm Excimer laser fluorination technique. Details of our methods are given in Chapter 2, which are modified from those previously described by Wiechert et al. (2002), Young et al. (1998) and Rumble et al. (1997). Our measurements were standardized by the analysis of two grains of San Carlos olivine (designated 'UVSCO1' and 'UVSCO2'). Fragments of each of these grains were measured for $\delta^{18}O$ values using the previously established infrared laser fluorination method (Sharp, 1990; Valley et al., 1995; Eiler et al., 2000a), yielding $\delta^{18}O$ values of 5.28±0.07‰ for UVSCO1 and 5.18±0.07‰ for UVSCO2. Sixteen analyses of UVSCO1 using our *in situ* UV laser fluorination technique yielded an average $\delta^{18}O$ value of 5.2 ±

0.2‰, and fifteen analyses of UVSCO2 yielded an average $\delta^{18}O$ value of 5.1 ± 0.2‰. On this basis, we have corrected our *in situ* UV laser fluorination analyses of unknown olivines by 0.1 ‰, and we infer that each analysis has an external precision of ±0.2 ‰, 1σ.

After oxygen isotope analysis, each olivine grain was recovered from the UV laser fluorination chamber, slightly re-polished to remove adhered fluorination products, then coated with carbon and analyzed for major and minor element composition using an electron microprobe (JXA-733) at Caltech. These analyses included four or five measurements of spots surrounding each hole ablated for oxygen isotope analysis. JXA-733 is operated at an accelerating voltage of 15 kV and beam current of 25 nA. Data were corrected using the CITZAF program (Armstrong, 1995). The oxide total for each measurement averages 99.8±0.5%.

**RESULTS**

All oxygen isotope analyses and the average major and minor element composition of olivine immediately surrounding each laser pit are reported in Table 1 and plotted in Figure 1. Individual electron microprobe analyses used to calculate average major and minor element compositions are available on request from the corresponding author.

Values of $\delta^{18}O$ values for olivine grains from the subaerial section of Mauna Loa vary between 5.1 and 5.3‰ -- homogeneous within the analytical precision of our technique and similar to the average $\delta^{18}O$ value of olivines from non-Hawaiian basalts and peridotites. In contrast, olivines recovered from subaerial Mauna Kea lavas vary in $\delta^{18}O$

Table 1. Results of *in situ* analysis for oxygen isotope composition, Fo contents and select major elements for individual coarse olivine grains from subaerial section of Mauna Kea lavas, and multiple olivine grain averages from submarine section of Mauna Kea lavas, HSDP2. (Refer to Wang et al., 2003 for detailed petrologic description)

| Sample | $\delta^{18}O^{*}$ (‰) | $\delta^{17}O^{\&}$ (‰) | Fo (%) | NiO (%) | $Cr_2O_3$ (%) | MnO (%) | CaO (%) |
|---|---|---|---|---|---|---|---|
| Subaerial section of Mauna Loa | | | | | | | |
| SR0098-0.00 | | | | | | | |
| Grain-19 | 5.3 | 2.6 | 89.5±0.3 | 0.46±0.04 | 0.12±0.03 | 0.13±0.01 | 0.23±0.01 |
| Grain-20 | 5.3 | 2.5 | 89.3±0.1 | 0.45±0.01 | 0.10±0.02 | 0.13±0.01 | 0.22±0.01 |
| SR0104-5.46 | | | | | | | |
| Grain-12 | 5.1 | 2.5 | 89.6±0.1 | 0.48±0.03 | 0.12±0.01 | 0.14±0.01 | 0.21±0.01 |
| Grain-13 | 5.3 | 2.6 | 89.7±0.1 | 0.48±0.02 | 0.11±0.03 | 0.12±0.02 | 0.20±0.01 |
| Grain-14 | 5.2 | 2.5 | 89.7±0.2 | 0.45±0.02 | 0.10±0.02 | 0.14±0.02 | 0.21±0.01 |
| Subaerial section of Mauna Kea | | | | | | | |
| SR0157-7.17 | | | | | | | |
| Grain-10 | 4.7 | 2.3 | 88.2±0.1 | 0.41±0.01 | 0.07±0.04 | 0.12±0.01 | 0.24±0.01 |
| SR0267-6.85 | | | | | | | |
| Grain-13 | 4.9 | 2.6 | 88.5±0.1 | 0.44±0.02 | 0.07±0.03 | 0.13±0.02 | 0.22±0.01 |
| SR0276-7.85 | | | | | | | |
| Grain-15-spot-1 | 4.7 | 2.3 | 88.2±0.2 | 0.41±0.04 | 0.10±0.01 | 0.14±0.01 | 0.23±0.01 |
| Grain-15-spot-2 | 4.6 | 2.7 | 87.8±0.2 | 0.38±0.02 | 0.06±0.04 | 0.13±0.03 | 0.22±0.01 |
| Grain-15-spot-3 | 4.7 | 2.7 | 88.2±0.2 | 0.45±0.01 | 0.07±0.01 | 0.14±0.02 | 0.23±0.01 |
| SR0284-2.40 | | | | | | | |
| Grain-7-spot-1 | 4.8 | 2.5 | 89.0±0.2 | 0.52±0.05 | 0.09±0.01 | 0.13±0.03 | 0.21±0.01 |

Table 1 (Continued)

| Sample | $\delta^{18}O^{*}$ (‰) | $\delta^{17}O^{\&}$ (‰) | Fo (%) | NiO (%) | $Cr_2O_3$ (%) | MnO (%) | CaO (%) |
|---|---|---|---|---|---|---|---|
| Grain-7-spot-2 | 5.0 | 2.5 | 89.8±0.2 | 0.51±0.04 | 0.06±0.02 | 0.10±0.02 | 0.20±0.01 |
| Grain-8 | 5.0 | 2.5 | 89.9±0.2 | 0.47±0.04 | 0.07±0.03 | 0.10±0.02 | 0.19±0.01 |
| Grain-1 | 4.9 | 2.4 | 89.7±0.2 | 0.53±0.01 | 0.06±0.01 | 0.14±0.01 | 0.20±0.01 |
| Grain-2-spot-1 | 5.2 | 2.5 | 90.2±0.1 | 0.51±0.03 | 0.08±0.01 | 0.12±0.01 | 0.21±0.01 |
| Grain-2-spot-2 | 4.9 | 2.4 | 90.2±0.1 | 0.52±0.04 | 0.09±0.01 | 0.12±0.01 | 0.20±0.01 |
| Grain-3 | 5.2 | 2.6 | 89.8±0.2 | 0.51±0.02 | 0.10±0.04 | 0.13±0.01 | 0.21±0.02 |
| Multiple grain averages of two submarine Mauna Kea samples | | | | | | | |
| SR0141-4.60 | 4.49±0.09 | | 84.5±2.3 | 0.30±0.05 | 0.05±0.03 | 0.21±0.03 | 0.26±0.03 |
| SR0431-1.65 | 4.72±0.08 | | 86.6±1.6 | 0.38±0.06 | 0.06±0.03 | 0.18±0.03 | 0.26±0.04 |
| Multiple grain averages of two submarine Mauna Kea samples | | | | | | | |
| SR0762-4.60$^{@}$ | 4.99±0.16 | | 87.3±0.8 | 0.40±0.04 | 0.08±0.02 | 0.15±0.04 | 0.24±0.03 |
| SR0907-1.65$^{\#}$ | 4.65±0.07 | | 81.6±0.5 | 0.22±0.03 | 0.06±0.02 | 0.22±0.02 | 0.28±0.01 |

*: 1σ for $\delta^{18}O$ is 0.2‰; &: 1σ for $\delta^{17}O$ is 0.3‰; @: only phenocryst data are listed here, microphenocryst data please refer to supplemental materials; #: only microphenocrysts exist in this sample, for individual measurement, please refer to supplemental materials.

from 'normal' values near 5.2‰ down to significantly $^{18}O$-depleted values near 4.6 ‰. This range covers most of that exhibited by olivines from all Hawaiian lavas, with the exception of systematically higher values typical of Koolau and Lanai.

Figure 1 shows the relationship between CaO wt% and Fo (forsterite) content of phenocryst and microphenocryst samples for this study, compared with previous measurements of olivine grains from other Hawaiian lavas. The phenocryst grains define

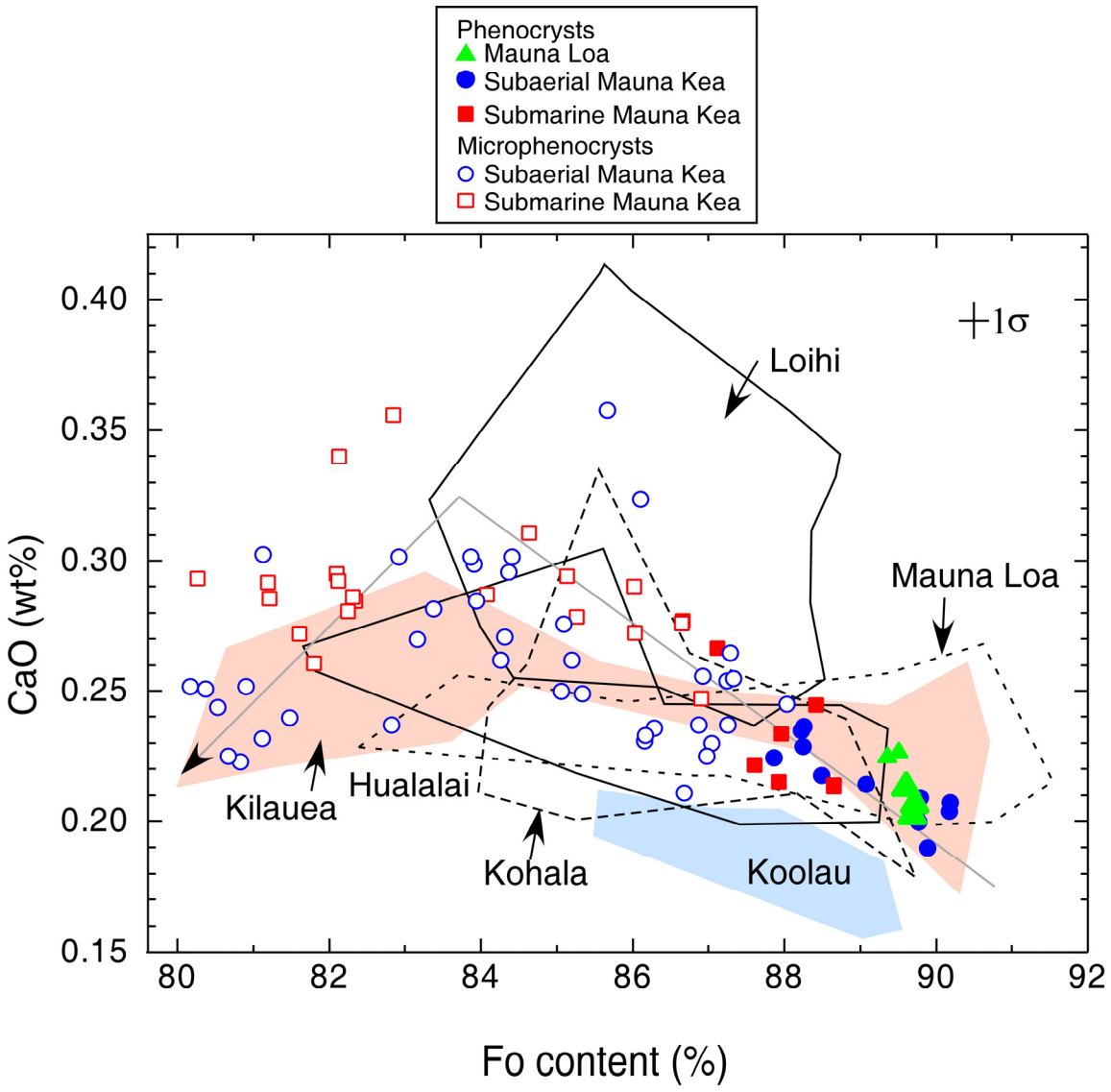


**Figure 1**. Variation of CaO concentrations with Fo contents of single-grain olivines from Mauna Kea and Mauna Loa lavas, compared with picrites from Loihi, Mauna Loa, Koolau, Kohala, Hualalai and Kilauea (Norman and Garcia, 1999) outlined as domains. Solid line with an arrow sketches approximately the variation trend of CaO with Fo for Mauna Kea sample. This trend is systematically lower than that calculated by MELTs program (Ghiorso et al., 1994) by a factor of 1.5.

a trend of increasing CaO with decreasing Fo content when Fo > 0.84, and a trend of decreasing CaO with decreasing Fo when Fo < 0.84. These trends are consistent with

crystallization-differentiation processes predicted for cooling parental Mauna Kea lavas (Baker et al., 1996), i.e., olivine grains with Fo > 0.84 only coexist with spinel (~1%), but olivines with Fo < 0.84 will coexist with clinopyroxene ± plagioclase. As expected, all our phenocryst samples are within the olivine-control area, while some of the microphenocrysts are in the multiple-saturation area. Importantly, the olivines analyzed in this study lie on the crystallization-differentiation trends defined by other Kea trend Hawaiian lavas, and thus likely are phenocrysts rather than xenocrysts entrained from the mantle underlying Hawaii. Finally, note that most olivine micro-phenocrysts (< 100 μm) have Fo < 0.87, and thus precipitated late in the history of crystallization-differentiation, whereas coarse phenocrysts (normally > 600 μm) generally have Fo > 0.87 and precipitated relatively early in that differentiation history when host magmas were saturated in olivine only.

Figure 2 plots the relationship between $\delta^{18}O$ values and Fo contents of olivine phenocryst analyzed in this study, and compares this relationship with average $\delta^{18}O$ values and Fo contents previously determined for bulk mineral separates of phenocrysts and microphenocrysts from Mauna Loa and Mauna Kea lavas. Three trends can be identified: 1) Subaerial Mauna Loa lavas exhibit little variations in $\delta^{18}O$ values with decreasing Fo contents and no systematic correlation between these two variables; 2) Submarine Mauna Kea lavas exhibit a gentle decrease in $\delta^{18}O$ with decreasing Fo content; and 3) subaerial Mauna Kea lavas exhibit a sharp decrease in $\delta^{18}O$ with decreasing Fo content. Thus, $\delta^{18}O$ values of olivine phenocrysts from all three of the studied stratigraphic sections converge to a single value of about 5.1±0.1 ‰ -- comparable to olivines in most mantle peridotites and basalts -- when Fo contents of olivines approach

0.90, and fan out to lower values with decreasing Fo contents, following slopes that systematically differ among the three suites.

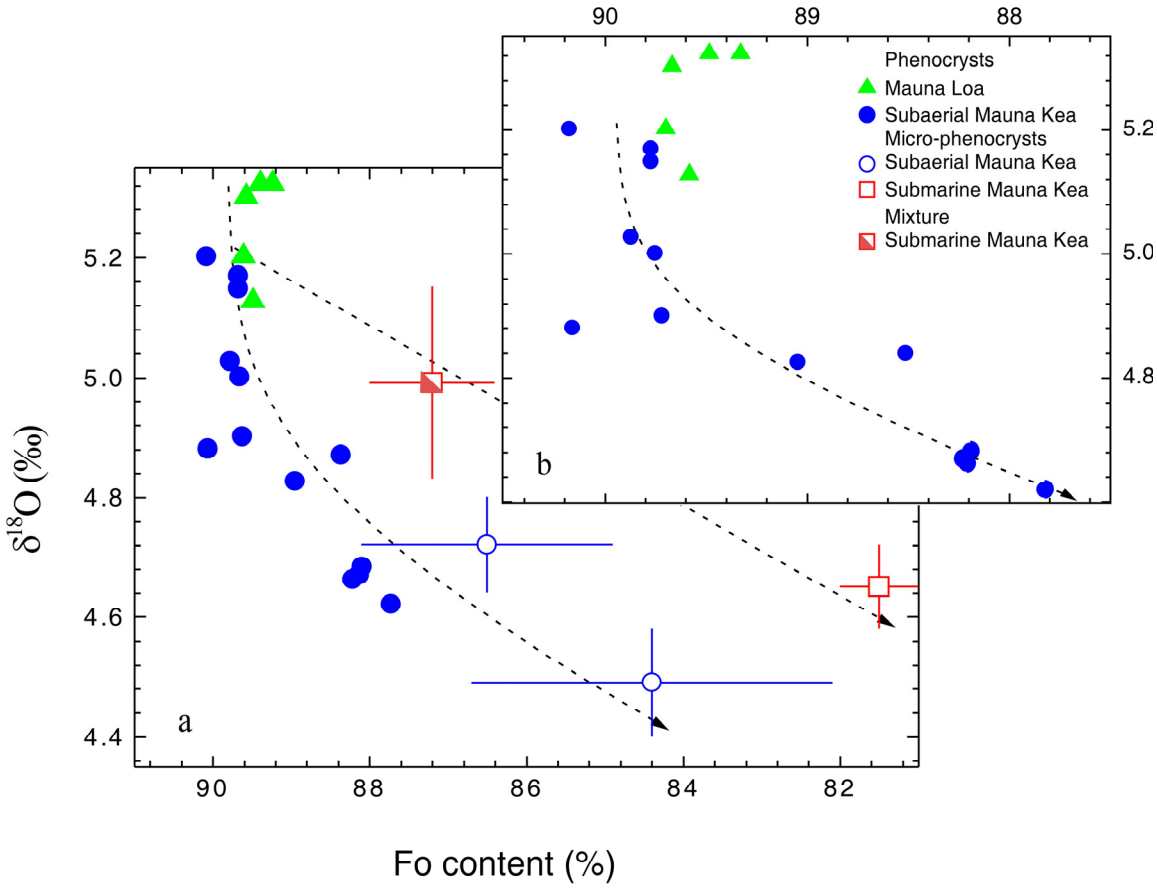


**Figure 2.** **a.** Comparison of $\delta^{18}O$ values with Fo contents of single-grain olivines from Mauna Kea and Mauna Loa lavas (data listed in Table 1). Those data that are averages of multiple-grain measurements have relatively bigger error bars in Fo contents; curve is to emphasize positive correlation; **b.** a blow-up of data for subaerial section of Mauna Loa and Mauna Kea volcanoes.

## DISCUSSION

A straightforward interpretation of these results is that primary magmas, parental to all the lavas we examined, began their differentiation histories having $\delta^{18}O$ values equal to each other and to other typical basalts, and increasingly diverged from one another in

$\delta^{18}O$ value over the course of their crystallization-differentiation history. That is, Mauna Loa lavas remained approximately constant in $\delta^{18}O$ during differentiation, submarine Mauna Kea lavas decreased monotonically and subtly in $\delta^{18}O$ with increasing differentiation, and subaerial Mauna Kea lavas decreased monotonically and strongly in $\delta^{18}O$ with increasing degrees of differentiation. However, these oxygen isotope variations cannot be attributed to isotopic fractionations between precipitated minerals and residual melts because models of crystallization-differentiation of basalts predict subtle ($\leq$0.05 ‰) increases rather than decreases in $\delta^{18}O$ over the relevant range in the extent of differentiation (Eiler, 2001), and because all three of the studied suites of lavas share broadly similar differentiation histories (Figure 1), yet differ markedly from one another in oxygen isotope systematics (Figure 2). Instead, the oxygen isotope variations we observed must reflect additions of variable amounts of low-$\delta^{18}O$ components to subaerial and submarine Mauna Kea lavas during their crystallization-differentiation histories.

However, we can imagine diverse ways in which this mixing/differentiation process could have occurred. For example, only one low-$\delta^{18}O$ component might have been sampled by both subaerial and submarine Mauna Kea lavas, but different amounts of that component were added for a given amount of crystallization (i.e., more for subaerial lavas; less for submarine lavas). Alternatively, the lavas we have studied might have sampled a variety of additive components in roughly constant proportion to the amount of crystallization that the lava had undergone, but those components had diverse $\delta^{18}O$ values (i.e., a moderately low $\delta^{18}O$ component was added to submarine Mauna Kea lavas, a very low $\delta^{18}O$ component was added to subaerial Mauna Kea lavas, and perhaps similar amounts of a 'normal' $\delta^{18}O$ component was added to Mauna Loa lavas). We can also

imagine that the low-$\delta^{18}O$ component(s) might come from any number of different sources such as rocks from the Pacific lithosphere, or Hawaiian volcanic edifice stoped into magma chambers, or silicate liquids produced by partial melting of the volcanic edifice, the lithosphere, or the underlying mantle 'plume' and mixed unevenly into magma chambers during crystallization-differentiation.

Despite the fact that many processes could be thought to explain the observed co-variations shown in Figures 1 and 2, most of them seem implausible to us, based on other petrologic and geochemical constraints. Firstly, the sharp break in oxygen isotope systematics between subaerial and submarine Mauna Kea lavas (Figure 1, Wang et al., 2003) is not mirrored in the stratigraphic variation of any previously measured radiogenic isotope index (including Sr, Nd, Hf, Pb, He and Os isotopes). Thus, it seems unlikely that the low $\delta^{18}O$ component(s) sampled by Mauna Kea lavas could be one of the recognized compositionally distinct components of the Hawaiian plume. Secondly, the entrapment pressures of fluid inclusions in Hawaiian olivine phenocrysts indicate they generally crystallize at depths of a few km up to a maximum of ~ 10 km. Fluid inclusion data are not available for the samples we studied, but we see no reason to suspect they are exceptions to this generalization. Thus, the low-$\delta^{18}O$ component(s) must have radiogenic isotope compositions broadly similar to those of primary Mauna Kea magmas, and must have mixed with those primary magmas in the volcanic edifice, or perhaps the uppermost portions of the underlying Pacific lithosphere. We suggest the only processes that readily fit these constraint are the ones in which primary Hawaiian magmas undergo crustal contamination while they are stored and differentiated in the magmatic plumbing system in the volcanic edifice, and that the differences in oxygen isotope systematics among

Mauna Loa, submarine Mauna Kea and subaerial Mauna Kea lavas reflect differences in availability of low-$\delta^{18}O$ crustal contaminants in the plumbing systems through which these lavas erupted. We develop a quantitative model to evaluate this in the next section.

## A MODEL FOR THE COMBINED CRYSTALLIZATION AND CRUSTAL CONTAMINATION OF HAWAIIAN LAVAS

To better understand Figure 2, we calculated the $\delta^{18}O$ values and MgO content of the melts with which these olivines are in equilibrium. MgO contents of parental melts are determined using partition coefficient ($K_D$) of $Fe^{2+}$-Mg between liquid and olivine (Gee and Sack, 1988), along with olivine control line calculated by MELTs algorithm (Ghiorso et al., 1994) using the estimates of primary Mauna Kea and Mauna Loa magma (Baker et al., 1996) as starting composition, assuming QFM buffer, crystallization pressure of 500 bar for submarine lavas and 100 bar for subaerial lavas. $\delta^{18}O$ values of the parental magma for these olivines were computed assuming 0.4‰ oxygen isotope equilibrium fractionation factor between melt and olivine (Eiler, 2001). Calculation results are shown in Figure 3. Along with measured glass samples, subaerial Mauna Kea samples define a steeper trend of decrease in $\delta^{18}O$ values with decreasing MgO wt% of the melts, compared with submarine Mauna Kea samples.

To fit these data, we assume contaminant for Mauna Kea lavas has a major element composition equal to the weighted mean of Mauna Kea HSDP lavas (as expected if the contaminant is the volcanic edifice). Similar results are obtained if one assumes the contaminant is any other mafic composition, including MORBs or oceanic gabbros. We

assume the primary magma has a $\delta^{18}O$ value in equilibrium with the average $\delta^{18}O$ value of the most forsteritic olivines (Figure 2).

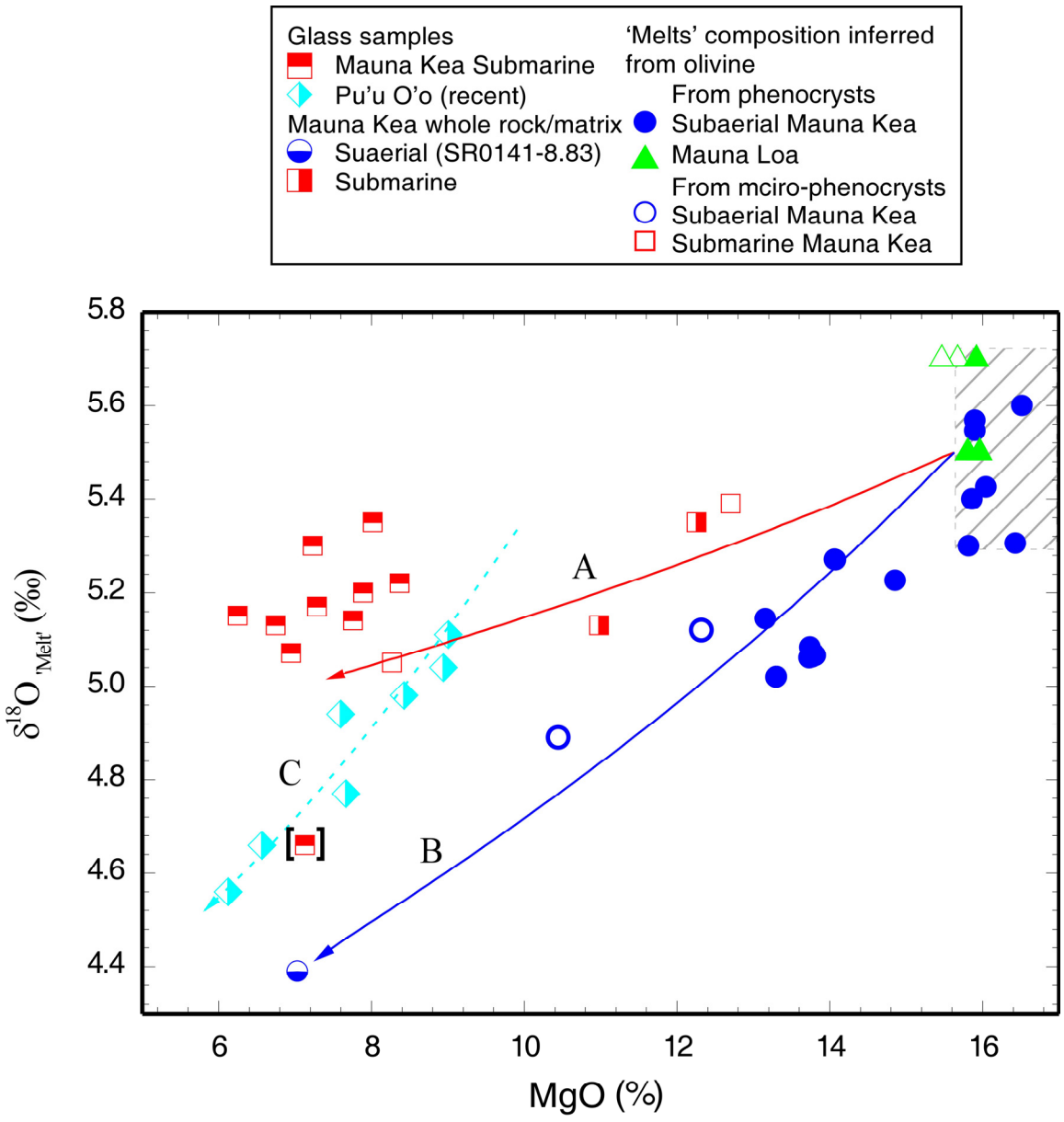


**Figure 3** Relation between MgO contents and $\delta^{18}O$ values in the inferred melt; MgO contents of melts are calculated by Fo contens of crystallized olivine using MELTS algorithm (Ghiorso et al., 1994) given the estimated compositions of primary Mauna Kea and Mauna Loa magmas (Baker et al., 1996); $\delta^{18}O$ values of melts are calculated by assuming 0.4‰ oxygen isotope fractionation between melt and olivine (Eiler, 2001);

curves A, B are fitted using r = 1, $\delta^{18}O_{contaminant}$ = 2.5 or -0.5‰, respectively, curve C is inferred by glass samples only from recent Pu'u O'o eruption (Garcia et al., 1998); some other data sources are also plotted in this figure, including: subaerial Mauna Kea sample with only microphenocrysts ($\delta^{18}O$ of matrix vs. MgO of whole rock), submarine Mauna Kea samples ($\delta^{18}O$ of matrix or glass vs. MgO of whole rock), submarine Mauna Kea glass samples ($\delta^{18}O$ of glass vs. MgO content of glass) and glass samples from recent Pu'u O'o eruption ($\delta^{18}O$ of glass vs. MgO content of whole rock, in which whole rock only contains a few grains of olivines at best and matrix type is also glass).

After these assumptions, only two key variables can vary -- the $\delta^{18}O$ values of the contaminant(s) and the mass ratio of contaminant added to phenocrysts precipitated (referred to hereafter as 'r'). It is generally possible to fit a data trend in Figure 3 equally well using several different values of these variables. For example, one could fit the trend for submarine Mauna Kea lavas either with a relatively high value of $\delta^{18}O_{contaminant}$ (that is, close to the $\delta^{18}O$ of primary basalt) and a high value of r, or with relatively low values of both $\delta^{18}O_{contaminant}$ and r. It is possible that both of these properties varied during the differentiation histories of the lavas we have studied. However, two previous observations suggest to us that $\delta^{18}O$ contaminant values varied substantially, whereas 'r' values varied relatively little: 1) Wang et al. (2003) found a sharp break in oxygen isotope compositions of coarse olivine phenocrysts in Mauna Kea occurs at the transition between submarine and subaerial lavas, and suggested this might be because exceptionally low-$\delta^{18}O$ contaminants made in meteoric-hydrothermal systems first became available once Mauna Kea grew above sea level, whereas before that, only moderately low-$\delta^{18}O$ seawater-hydrothermal systems could contaminate differentiating magmas. For this reason, we propose that the $\delta^{18}O$ of contaminants differed between

submarine Mauna Kea and subaerial Mauna Kea; and perhaps also 2) Garcia et al. (1998) found evidence that Kilauea lavas are most strongly contaminated during re-organizations of the shallow plumbing system in the East rift zone, suggesting it occurs by stoping of the walls and roofs of magma conduits, followed by melting of stoped blocks. In this case, the value of 'r' should be limited by the heat balance of magma cooling and crystallization vs. heating and fusion of wall-rock. We estimate using the MELTs algorithm (Ghiorso et al., 1994) that cooling of primary Mauna Kea magma from its liquidus of ca. 1380 ˚C to its multiple-saturation temperature of ca. 1156 ˚C yields 20.6 wt.% olivine phenocrysts and releases 11.6 kJ/g of heat. This almost exactly equals the 11.8 kJ/g of heat required to raise the temperature of average Mauna Kea tholeiite whole rock (Rhodes and Vollinger, 2004) from its solidus temperature of 840 ˚C to 1156 ˚C (including the heat of fusion). Thus, it seems reasonable to us to assume that stoping and fusion of the walls of magma conduits takes place with an average 'r' value near 1. Assuming 'r' equals 1 throughout the differentiation of all three suites of lavas we examined, the $\delta^{18}O$ values of the contaminants added to those lavas, based on fits of our model to the data in figure 3 are: -0.5 ‰ for subaerial Mauna Kea lavas; 2.5 ‰ for submarine Mauna Kea lavas; and ca. 5.5 ‰ for Mauna Loa lavas.

## SOURCES OF CONTAMINANTS

Our estimates of the $\delta^{18}O$ values of contaminants added to Hawaiian magmas are clearly model-dependent. We infer that all the lavas we have studied are products of broadly similar differentiation processes (Figure 1), and that their extent of contamination is limited by the heat-budget of combined wall-rock assimilation and fractional

crystallization, leaving us with only one factor that can produce the observed variations in slope in Figure 3: difference in the $\delta^{18}O$ of contaminants. Nevertheless, despite the non-uniqueness of this interpretation, it seems plausible to us for the reasons stated above, and so, in this section we consider their implication in the oxygen isotope geochemistry and geology of the Hawaiian volcanic edifice.

First, and most simply, our results indicate that Mauna Loa lavas did not vary in $\delta^{18}O$ during their differentiation, and therefore, either escaped the assimilation-fractional-crystallization processes we infer influenced Mauna Kea lavas, or assimilated wall-rocks similar in $\delta^{18}O$ to primary magmas. In this latter case, the volcanic edifice through which subaerial Mauna Loa lavas erupted must contain few, if any, weathered or hydrothermally altered rocks.

By contrast, our model indicates that submarine Mauna Kea lavas were contaminated by wall rocks having a weighted-average $\delta^{18}O$ value of 2.5 ‰. This value is similar to that observed for the highest-temperature (≥ 350 ˚C) portions of seawater-hydrothermal systems in submarine volcanic ridges, as sampled in ophiolites and in hydrothermally altered basalts from the Costa Rica Rift (Friedrichsen, 1985). It is lower than the average $\delta^{18}O$ of $^{18}O$-depleted parts of ophiolites (ca. 3 to 4 ‰), although we expect that magmas passing through active hydrothermal systems will tend to be preferentially contaminated by country rocks that have undergone the highest temperature alteration (because the magmas themselves are the source of heat, driving the surrounding hydrothermal systems). The source of these rocks could come from either seawater-altered volcanic edifice or lower pacific crust. Pacific lithosphere underneath Hawaii has a range of radiogenic isotope compositions approaching that of Mauna Kea lavas ($^{87}Sr/^{86}Sr$ =

0.7030±0.0004 vs. 0.7036±0.0002; $\varepsilon_{Nd}$ = 9.7±1.2 vs.7.6±1; $^{206}Pb/^{204}Pb$ = 18.54±0.18 vs. 18.54±0.11; Waggoner, 1993, King et al., 1993, Lassiter et al., 1996), and generally has lower concentrations of most trace elements. As a result, even 10-20% mixing of lower Pacific crust into primary magmas might not result in changes in radiogenic isotope composition outside the range of initial variability of primary magmas. Hydrothermally altered volcanic edifice should be similar in radiogenic isotope composition and elemental concentrations to primary magmas. This possibility cannot be completely ruled out based on available geochemical data. Nevertheless, we prefer the interpretation that low-$\delta^{18}O$ contaminants come from the volcanic edifice because it can explain why oxygen isotope systematics change suddenly at the subaerial/submarine transition in Mauna Kea volcano (Wang et al., 2003): the submarine-subaerial transition represents a sudden change in the supply of water to the volcanic edifice (from seawater to meteoric water), and so might lead to a sudden change in the $\delta^{18}O$ value of wall rocks magmas must erupt through. In addition, previous studies have suggested that submarine Hawaiian lavas assimilate altered volcanic edifice from seawater-hydrothermal systems based on correlations between $\delta D$ and $\delta^{11}B$ (Chaussidon, 1994), high Cl concentrations (Clague et al., 1995), and high $Cl/H_2O$ and $B/H_2O$ ratios (Kent et al., 1999; Kent et al., 1999b).

Our model suggests that the $\delta^{18}O$ value of contaminants added to subaerial Mauna Kea lavas averaged -0.5 ‰ -- lower than the minimum observed in submarine hydrothermal systems, and substantially lower than the average for those systems. Thus, the oxygen isotope systematics of this suite of lavas appears to require a component lower in $\delta^{18}O$ than can be produced in seawater-hydrothermal systems. The $\delta^{18}O$ value of

groundwater within Mauna Kea and Kilauea volcanoes are ca. -6.0 to -6.2‰ (Thomas et al., 1996). These values are lower than those typical of rain at Laupahoehoe beach or the Pu'u O'o crater rim (ca. -1.2 ‰; Hinkley et al., 1995), and so presumably sample precipitation that falls at higher altitudes. The $\delta^{18}O$ of Hawaiian groundwater may also reflect partitioning of $^{18}O$ into low-temperature weathering products in the shallow crust. Regardless, meteoric-hydrothermal systems fed by these low-$\delta^{18}O$ waters would be capable of producing altered rocks significantly lower in $\delta^{18}O$ than those observed in submarine hydrothermal systems, and easily as low as -0.5 ‰ at temperatures higher than 450 °C.

Figure 3 also shows $\delta^{18}O$ values of glasses and MgO wt% of whole rock from the recent Pu'u O'o eruption of Kilauea volcano (only using data with glass as matrix type; Garcia et al., 1998). These data show a steep slope similar to the subaerial section of Mauna Kea, but they require MgO wt% = ~ 11 % when the lava has $\delta^{18}O$ value of 5.6 ‰. It indicates that Kilauea lavas from the recent Pu'u O'o eruption should have experienced two-stage magma chamber: 1) a deep magma chamber, where a slight contamination in low-$\delta^{18}O$ rocks occurs and MgO wt% of lava is higher than 11%, these low-$\delta^{18}O$ rocks come from high temperature sea-water altered volcanic edifice and/or pacific crust (a gentle slope in Figure 3); and 2) a shallow magma chamber, where a strong contamination in low-$\delta^{18}O$ rocks occurs and MgO wt% of lava is lower than 11%, these low-$\delta^{18}O$ rocks come from high temperature meteoric-water altered volcanic edifice (manifested by a steep slope in the curve C of Figure 3).

### A DIVERSITY OF HYDROTHERMAL SYSTEMS IN THE HAWAIIAN VOLCANIC EDIFICE

Our finding that the oxygen isotope systematics of Hawaiian lavas varies with the location of eruption has implications for the distribution and character of hydrothermal systems in the Hawaiian volcanic edifice. We suggest that the primary factor controlling the $\delta^{18}O$ value of contaminants is the availability and source of water in the rift zones and summit calderas through which magmas pass before and during eruption. In particular, submarine rift zones obviously have a ubiquitous supply of seawater, and so should contain hydrothermally altered rocks with $\delta^{18}O$ values of ca. 2 to 4‰ (like those in portions of ophiolites and modern ocean crust that have undergone high temperature seawater alteration). Subaerial parts of the volcanic edifice that receive abundant rainfall -- mostly the northeast side of the island of Hawaii -- should contain vigorous meteoric-hydrothermal systems capable of producing altered rocks with $\delta^{18}O$ values lower than ca. 2‰. Subaerial parts of the volcanic edifice that receive relatively little rainfall -- mostly the southwest side of the island, and the summits of Mauna Kea and Mauna Loa -- might well be dry or contain only intermittent or 'patchy' meteoric hydrothermal systems, and thus, permit lavas to erupt without passing through low - $\delta^{18}O$ wall rocks.

## ACKNOWLEDGEMENTS

We would like to thank Chi Ma for help on the electron microscope analysis, George Rossman for discussion and providing gem-quality San Carlos olivine standard, Paul Asimow for teaching the first author to use the MELTS program, and H.P. Taylor and K. Muehlenbachs for providing valuable comments. The principle financial support for this research was a grant from NSF.

# REFERENCES

Armstrong J. T. (1995) A package of correction programs for the quantitative electron microbeam X-ray analysis of thick polished materials, thin films, and particles. *Microbeam Analysis* **4**, 177-200.

Baker M. B., Alves S., and Stolper E. M. (1996) Petrography and petrology of the Hawaii Scientific Drilling Project lavas: Inferences from olivine phenocryst abundances and compositions. *Journal of Geophysical Research-Solid Earth* **101**(B5), 11715-11727.

Chaussidon M., Jambon, A. (1994) Boron content and isotopic composition of oceanic basalts: geochemical and cosmochemical implications. *Earth and Planetary Science Letters* **121**, 277-291.

Clague D. A., Moore J. G., Dixon J. E., and Friesen W. B. (1995) Petrology of submarine lavas from Kilaueas Puna ridge, Hawaii. *Journal of Petrology* **36**(2), 299-349.

Eiler J. M. (2001) Oxygen isotope variations of basaltic lavas and upper mantle rocks. In *Stable Isotope Geochemistry*, Vol. 43, pp. 319-364. Mineralogical. Soc. America.

Eiler J. M., Crawford A., Elliott T., Farley K. A., Valley J. W., and Stolper E. M. (2000a) Oxygen isotope geochemistry of oceanic-arc lavas. *J. Petrol* **41**, 229–256.

Eiler J. M., Farley K. A., Valley J. W., Hofmann A. W., and Stolper E. M. (1996b) Oxygen isotope constraints on the sources of Hawaiian volcanism. *Earth and Planetary Science Letters* **144**(3-4), 453-467.

Friedrichsen H. (1985) Strontium, oxygen and hydrogen isotope studies on primary and secondary minerals in basalts from the Leg 83 section of DSDP hole 504B, Costa Rica Rift. *Initial Reports of the Deep Sea Drilling Project* **83**, 289-296.

Garcia M. O., Ito E., Eiler J. M., and Pietruszka A. J. (1998) Crustal contamination of Kilauea Volcano magmas revealed by oxygen isotope analyses of glass and olivine from Pu'u O'o eruption lavas. *Journal of Petrology* **39**(5), 803-817.

Gee L. L. and Sack R. O. (1988) Experimental petrology of melilite nephelines. *Jornal of Petrology* **29**, 1233-1255.

Ghiorso M. S., Hirschmann M. M., and Sack R. O. (1994) New software models thermodynamics of magmatic systems. *Eos, Transactions, American Geophysical Union* **75**(49), 571.

Harmon R. S. and Hoefs J. (1995) Oxygen isotope heterogeneity of the mantle deduced from global $^{18}O$ systematics of basalts from different geotectonic settings. *Contribution to Mineralogy and Petrology* **120**, 95–114.

Kent A. J. R., Clague D. A., Honda M., Stolper E. M., Hutcheon I. D., and Norman M. D. (1999) Widespread assimilation of a seawater-derived component at Loihi Seamount, Hawaii. *Geochimica et Cosmochimica Acta* **63**(18), 2749-2761.

Kent A. J. R., Norman M. D., Hutcheon I. D., and Stolper E. M. (1999) Assimilation of seawater-derived components in an oceanic volcano: evidence from matrix glasses and glass inclusions from Loihi seamount, Hawaii. *Chemical Geology* **156**(1-4), 299-319.

King A. J., Waggoner D. G., and Garcia M. O. (1993) Geochemistry and petrology of basalts from LEG 136, central Pacific ocean. *Procedings of the Ocean Drilling Program, Scientific Results* **136**, 107-118.

Lassiter J. C., DePaolo D. J., and Tatsumoto M. (1996) Isotopic evolution of Mauna Kea volcano: Results from the initial phase of the Hawaii Scientific Drilling Project. *Journal of Geophysical Research-Solid Earth* **101**(B5), 11769-11780.

Lassiter J. C. and Hauri E. H. (1998) Osmium-isotope variations in Hawaiian lavas: Evidence for recycled oceanic lithosphere in the Hawaiian Plume. *Earth Planet. Sci. Lett.* **164**, 483–496.

Mattey D., Lowry D., and Macpherson C. (1994) Oxygen-isotope composition of mantle peridotite. *Earth and Planetary Science Letters* **128**(3-4), 231-241.

Norman M. D. and Garcia M. O. (1999) Primitive magmas and source characteristics of the Hawaiian plume: petrology and geochemistry of shield picrites. *Earth and Planetary Science Letters* **168**(1-2), 27-44.

Rhodes J. M. and Vollinger M. J. (2004) Composition of basaltic lavas sampled by phase-2 of the Hawaii Scientific Drilling Project: Geochemical stratigraphy and magma types. *Geochemistry Geophysics Geosystems* **5**, art. no.-Q03G13.

Rumble D., III, Farquhar J., Young E. D., and Christensen C. P. (1997) *In situ* oxygen isotope analysis with an excimer laser using $F_2$ and $BrF_5$ reagents and $O_2$ gas as analyte. *Geochimica et Cosmochimica Acta* **61**(19), 4229-4234.

Thomas D. M., Paillet F. L., and Conrad M. E. (1996) Hydrogeology of the Hawaii Scientific Drilling Project borehole KP-1: 2. Groundwater geochemistry and regional flow patterns. *J. Geophys. Res.* **101**(B5), 11683-11694.

Waggoner D. G. (1993) The age and alteration of central Paficic Oceanic Crust near Hawaii, Site 843. *Proceedings of the Ocean Drilling Program, Scientific Results* **136**, 119-132.

Wang Z., Kitchen N. E., and Eiler J. M. (2003) Oxygen isotope geochemistry of the second HSDP core. *Geochemistry Geophysics Geosystems* **4**, art. no.-8712.

Wiechert U., Fiebig J., Przybilla R., Xiao Y., and Hoefs J. (2002) Excimer laser isotope-ratio-monitoring mass spectrometry for *in situ* oxygen isotope analysis. *Chemical Geology* **182**(2-4), 179-194.

Young E. D., Fogel M. L., Rumble D., and Hoering T. C. (1998) Isotope-ratio-monitoring of $O_2$ for microanalysis of $^{18}O/^{16}O$ and $^{17}O/^{16}O$ in geological materials. *Geochimica et Cosmochimica Acta* **62**(18), 3087-3094.

# CHAPTER 4.

# OXYGEN ISOTOPE GEOCHEMISTRY OF SHIELD BUILDING LAVAS FROM KO'OLAU VOLCANO, HAWAII

Zhengrong Wang[1], John M. Eiler[1], Paul Asimow[1], Michael Garcia[2], Eiichi Takahashi[3]

1. Division of Geological and Planetary Sciences, Caltech, Pasadena, California 91125, USA

(Email: wzhr@gps.caltech.edu; eiler@gps.caltech.edu; asimow@gps.caltech.edu )

2. Department of Geology & Geophysics, University of Hawaii, Honolulu, HI 96822, USA

(Email: garcia@soest.hawaii.edu )

3. Department of Earth and Planetary Sciences, Tokyo Institute of Technology,

Tokyo 152-8551, Japan

(Email: etakahas@geo.titech.ac.jp )

**ABSTRACT**

Basaltic lavas from the Ko'olau Scientific Drilling Project (KSDP, collected at 381~511 mbsl) contain olivines with $\delta^{18}O$ values (5.39±0.1‰) higher than typical upper mantle peridotites and Mauna Loa lavas (5.17±0.11‰). Younger basalts (collected at 304~359 mbsl) have olivines with even higher $\delta^{18}O$ values (5.56±0.05‰), similar to olivines from plagioclase-spinel peridotite xenoliths collected on Oahu (5.51±0.05‰) and approaching exceptionally high values previously reported for subaerial (Makapu`u) Ko'olau lavas (5.89±0.12‰). Olivines from dredged samples (including subaerial landslides and submarine Ko'olau volcano) show a wide range of $\delta^{18}O$ values (5.2~6.0‰). Unlike the Mauna Kea series, this full diversity of $\delta^{18}O$ values across all three sample suites (drill core; subaerial lavas; submarine land slides) correlate with trace element and radiogenic isotope compositions of host lavas, defining a compositional continuum from a high-$\delta^{18}O$, extremely enriched end member, toward a more normal-$\delta^{18}O$, 'Mauna Loa-like' composition. This trend is interpreted to reflect mixing between partial melts of high- $\delta^{18}O$ components and normal-$\delta^{18}O$ components of the Hawaiian plume. A magma mixing model is constructed to simultaneously explain the oxygen isotope, major element, trace element and radiogenic isotope variations defined by this trend. The two mixing components are defined as primary melts of Loihi and experimentally determined eclogite melt, and different possible mixing scenarios are discussed. This model indicates that the Ko'olau shield building lavas are mixtures of 75~100 % melt of mantle peridotite with 0~25% melt of eclogite, the protolith of which is Mid-Ocean Ridge Basalt (MORB) with Depleted Mantle Model (DMM) age of at least 1.8±0.3 billions years. $\delta^{18}O$ values of this eclogite component can be predicted to be 11.3

±1.5‰, implying it is an upper crustal (layer 1 or 2) basalt or gabbro with a low-temperature alteration history and contains a small amount of sediment. This basalt experienced partial melting before forming eclogite, therefore leaving a LIL-depleted element pattern. Moreover, this magma mixing model is also consistent with high Ni olivines associated with high silica Ko'olau lavas.

## 1. INTRODUCTION

Subaerial shield-building lavas exposed at the surface of the Ko'olau volcano are a compositional end-member to the geochemical diversity of Hawaiian lavas and thus are of special interest for understanding the sources of Hawaiian volcanism (e.g., HAURI, 1996; EILER et al., 1996a). In comparison with mid-ocean-ridge basalts (MORBs) and other Hawaiian shield-building lavas, these Ko'olau lavas are higher in $SiO_2/Fe_2O_3$, $Al_2O_3/CaO$, La/Nb and Sr/Nb abundance ratios (FREY et al., 1994; HUANG and FREY, 2005) and $^{87}Sr/^{86}Sr$ isotope ratios, and lower in $^{143}Nd/^{144}Nd$, $^{176}Hf/^{177}Hf$, $^{206}Pb/^{204}Pb$, $^{207}Pb/^{204}Pb$ and $^{208}Pb/^{204}Pb$ isotope ratios (RODEN et al., 1994; LASSITER and HAURI, 1998; BLICHERT-TOFT et al., 1999). Many previous studies have argued that these characteristics reflect the fact that the mantle sources of Ko'olau shield-building lavas are enriched in incompatible trace elements and more fertile, or even mafic in major element composition in comparison with the sources of other Hawaiian shield building lavas. Subaerial shield-building Ko'olau lavas are also anomalous for containing olivines with exceptionally high $\delta^{18}O$ values, consistent with their sources being rich in recycled crustal materials, which presumably are also the cause of their enriched and fertile major- and trace-element compositions (EILER et al., 1996a).

Despite the general coherence of the evidence that the sources of Ko'olau shield-building lavas are 'enriched' (that is, with respect to crust-forming elements), there is considerable uncertainty and debate about the exact nature of that source. At one extreme, PUTIRKA (1999) argued that variations in melting depths of a peridotite mantle are sufficient to yield observed differences in Na/Ti, Lu/Hf, and Sm/Yb between Hawaii and the East Pacific Rise (EPR). Therefore, garnet pyroxenite and eclogite are unlikely source components of Hawaiian lavas. At the other extreme, HAURI (1996) proposed a zoned plume model which estimates up to ~20% dacitic melts derived from recycled oceanic crust and sediments in Ko'olau lavas. Moreover, even among those studies that agree that the source of Ko'olau lavas is rich in recycled materials, some describe these materials as basaltic (LASSITER and HAURI, 1998; SOBOLEV et al., 2000) and others as sedimentary (BLICHERT-TOFT et al., 1999). Finally and most problematically, few previous studies have reached quantitative (and therefore testable) conclusions about the amounts of recycled materials in the mantle sources of Ko'olau lavas (HAURI, 1996; EILER et al., 1996a; SOBOLEV et al., 2005).

In this study, we present new oxygen isotope data for olivines from Ko'olau lavas, compile them with previous data from this and other Hawaiian volcanoes, and present a model that attempts to explain these results, along with other geochemical data for these samples in terms of the abundances, and melting properties of compositional components in the mantle sources of these lavas. We take advantage of two recently-available suites of Ko'olau shield building lavas: 1) those sampled from core recovered by the Ko'olau Scientific Drilling Project (KSDP), and 2) samples recovered from submarine landslides off the north shores of Ko'olau and Molokai. We find there has been a secular change in

the $\delta^{18}O$ values of olivines from Ko'olau lavas over the sampled history of shield-building volcanism, from a low of 5.2 ‰ (similar to Mauna Loa lavas) in the oldest samples to a high of 5.9 ‰ in the youngest (Makapu'u stage) lavas. These variations correlate with various major-element, trace-element and radiogenic isotope indices in the same lavas, producing geochemical trends that form the basis of our model for the mantle sources of Ko'olau lavas.

## 2. SAMPLING AND ANALYTICAL TECHNIQUES

Oxygen isotope ratios were analyzed in olivines and plagioclases from twenty two tholeiites from the KSDP core, sampled from depths of between 305.3 and 529.5 meters below sea level (mbsl), and from fifteen samples collected by the KAIKO and SHINKAI 6500 submarine vessels (from the Japan Marine Science and Technology Center and used during joint Japan-US cruises in 1998 and 1999). These data are summarized in Table 1. The KSDP core penetrates subaerial shield building Ko'olau lavas stratigraphically below the Makapu'u stage lavas exposed on the surface at Makapu'u head, and sample some of the same stratigraphic intervals exposed by a highway (H3) tunnel (see JACKSON et al., 1999 and HASKINS and GARCIA, 2004 for detailed sample locations and descriptions). We only analyzed samples from the cored section of the KSDP drill hole and none of the materials recovered by rotary drilling done above 305.3 mbsl. Ko'olau submarine landslide samples are from several named landslide blocks whose locations and descriptions are presented in GARCIA (2002), MOORE and CLAGUE (2002), and TANAKA et al. (2002). Blocks Oahu North-a and Oahu North-b are closest to Ko'olau volcano, and blocks Nuuanu-1, Nuuanu-2 and Nuuanu-3 are further away. The relative distances of

Table 1. Oxygen isotope composition of olivines from KSDP core and landslides of Ko'olau and Molokai volcanoes.

| Unit | Depth(masl[&]) | $\delta^{18}O_{olivine}$ | 1σ | $\delta^{18}O_{plagioclase}$ | 1σ | Sample | $\delta^{18}O_{olivine}$ | 1σ |
|---|---|---|---|---|---|---|---|---|
| KSDP drill core | | | | | | Landslide sample | | |
| 1 | -305.3 | 5.51 | 0.01 | | | Oahu North-a | | |
| 2 | -308.2 | 5.55 | 0.09 | 5.99 | 0.01 | K89-02 | 6.01 | 0.05 |
| 3 | -308.8 | 5.44 | 0.07 | 6.16 | 0.06 | K89-04 | 5.89 | 0.04 |
| 4 | -311.6 | 5.46 | 0.10 | | | K89-05 | 5.87 | 0.07 |
| 5 | -314.4 | 5.46 | 0.05 | | | K89-06 | 5.82 | 0.03 |
| 6 | -317.3 | 5.61 | 0.01 | | | S500-1 | 5.91 | 0.08 |
| 7 | -324.8 | 5.51 | 0.05 | | | S500-2B | 5.80 | 0.06 |
| 8 | -327.7 | 5.52 | 0.01 | | | S500-5B | 5.91 | 0.01 |
| 10 | -334.4 | 5.54 | 0.07 | | | S500-6 | 5.77 | 0.04 |
| 15 | -343.4 | 5.52 | 0.07 | | | Nuuanu-1 | | |
| 20 | -358.9 | 5.52 | 0.03 | | | D4-7 | 5.41 | 0.06 |
| 29 | -381.3 | 5.35 | 0.04 | | | S497-2 | 5.19 | 0.10 |
| 31 | -387.7 | 5.54 | 0.10 | | | S497-6 | 5.24 | 0.02 |
| 32 | -388.3 | 5.29 | 0.05 | | | S497-7 | 5.26 | 0.09 |
| 36 | -394.4 | 5.37 | 0.14 | | | S497-9 | 5.25 | 0.03 |
| 47 | -418.5 | 5.30 | 0.07 | | | Molokai | | |
| 50 | -427.7 | 5.43 | 0.07 | | | S501-2 | 5.04 | 0.06 |
| 52 | -438.9 | 5.33 | 0.02 | | | D8-1 | 4.83 | 0.02 |
| 53 | -439.2 | 5.60 | 0.08 | | | | | |
| 64 | -493.5 | 5.39 | 0.08 | | | | | |
| 65 | -495.9 | 5.35 | 0.10 | | | | | |
| 67 | -510.9 | 5.41 | 0.02 | | | | | |

[&]: meters above sea level

these blocks from Ko'olau volcano appear to be roughly correlated with the original stratigraphic positions in the volcanic edifice of the lavas they contain. Most samples

from these blocks are pieces of subaerial erupted lavas, except for Nuuanu-3 and parts of Nuuanu-2 which are suggested to represent shallow submarine erupted lava fragments (SHINOZAKI et al., 2002; TANAKA et al., 2002). Blocks Wailau-1 and Wailau-2 are believed to have slumped off Molokai volcano; we analyzed them for comparison with our samples of Ko'olau volcano, but do not interpret them as members of the Ko'olau suite.

All mineral separates were prepared by crushing whole-rock chips in a steel percussion mortar and then sieving and ultrasonicating the resulting powder in distilled water or 1N HCl, followed by ultrasonicating in ethanol, drying, and handpicking under a binocular microscope. Mineral fragments containing visible inclusions and alteration products were discarded during handpicking. All data are for large (≥1 mm) phenocrysts of olivine. All mineral separates were analyzed by $CO_2$ laser fluorination technique at California Institute of Technology using methods previously described by EILER et al., (2000b), based on methods developed by SHARP (1990), and VALLEY et al. (1995). A total of 35 UWG-2 (garnet) and 36 SCO3 (olivine) standards were analyzed interspersed with analyses of samples. Results for these standards are as follows: UWG-2 = 5.85 ± 0.08‰, SCO3 = 5.40 ± 0.07‰ (all standard deviations refer to long-term reproducibility of raw measurements and are 1σ). These values compare with accepted values of: UWG-2 = 5.80‰ and SCO3 = 5.35‰ (VALLEY et al., 1995; EILER et al., 2000a; EILER et al., 2000b). All $\delta^{18}O$ values for unknowns measured on a given day were corrected by the difference between measured and accepted values for standards on that day. All measurements of unknown samples were replicated, generally in duplicate but some

between three and five times. Standard deviations for replicate measurements of each sample are reported in Table 1.

## 3. RESULTS AND DISCUSSION

Figure 1d depicts the stratigraphic profile of oxygen isotope compositions of olivines from the KSDP core and Makapu'u stage lavas, which can be compared with stratigraphic profiles for these same lavas in the $CaO/Al_2O_3$ and Sr/Nd ratios and $\varepsilon_{Nd}$ values (Figures 1a-c, data from HASKINS and GARCIA, 2004; HUANG and FREY, 2005; SALTERS, 2005). Olivines from lavas collected between 381 and 511 mbsl in the KSDP core have $\delta^{18}O$ values (5.39±0.1‰) higher than typical upper mantle peridotites (5.2±0.2 ‰; MATTEY et al., 1994, EILER, 2001) and Mauna Loa lavas (5.17±0.11‰, EILER et al., 1996a; EILER et al., 1996b; EILER, 2001; WANG et al., 2003), whereas olivines from lavas collected between 304 and 359 mbsl have even higher $\delta^{18}O$ values (5.56±0.05‰). This later value is similar to olivines from plagioclase-spinel peridotite xenoliths collected on Oahu (5.51±0.05, DUCEA et al., 2002) and approaches exceptionally high values previously reported for subaerial Makapu`u stage lavas (5.89±0.12, EILER et al., 1996a; EILER et al., 1996b; these data are also shown in Figure 1d). Stratigraphic variations in oxygen isotope compositions of olivines generally track stratigraphic variations of other geochemical indices in these same and related lavas. For example, Makapu'u stage lavas average 0.67±0.02 in $CaO/Al_2O_3$ ratio, 45±4 in Sr/Nd ratio and 1.8±1 in $\varepsilon_{Nd}$ value, whereas lavas from the base of the KSDP core (> 500 mbsl) average 0.74±0.06 in $CaO/Al_2O_3$, 31±5 in Sr/Nd and 5.7±0.6 in $\varepsilon_{Nd}$, ($\varepsilon_{Hf}$ values and $^{206}Pb/^{204}Pb$ ratios exhibit stratigraphic trends similar to that for $\varepsilon_{Nd}$ (FEKIACOVA and ABOUCHAMI, 2003; SALTERS,

2005). There are second-order variations in each geochemical index superimposed on the gradual changes in average values we refer to. These oscillations are not generally coherent from one geochemical index to another, and might reflect any or all of uncorrelated differences in primary lava composition, differences in sampling density, or variable effects of post-eruptive alteration.

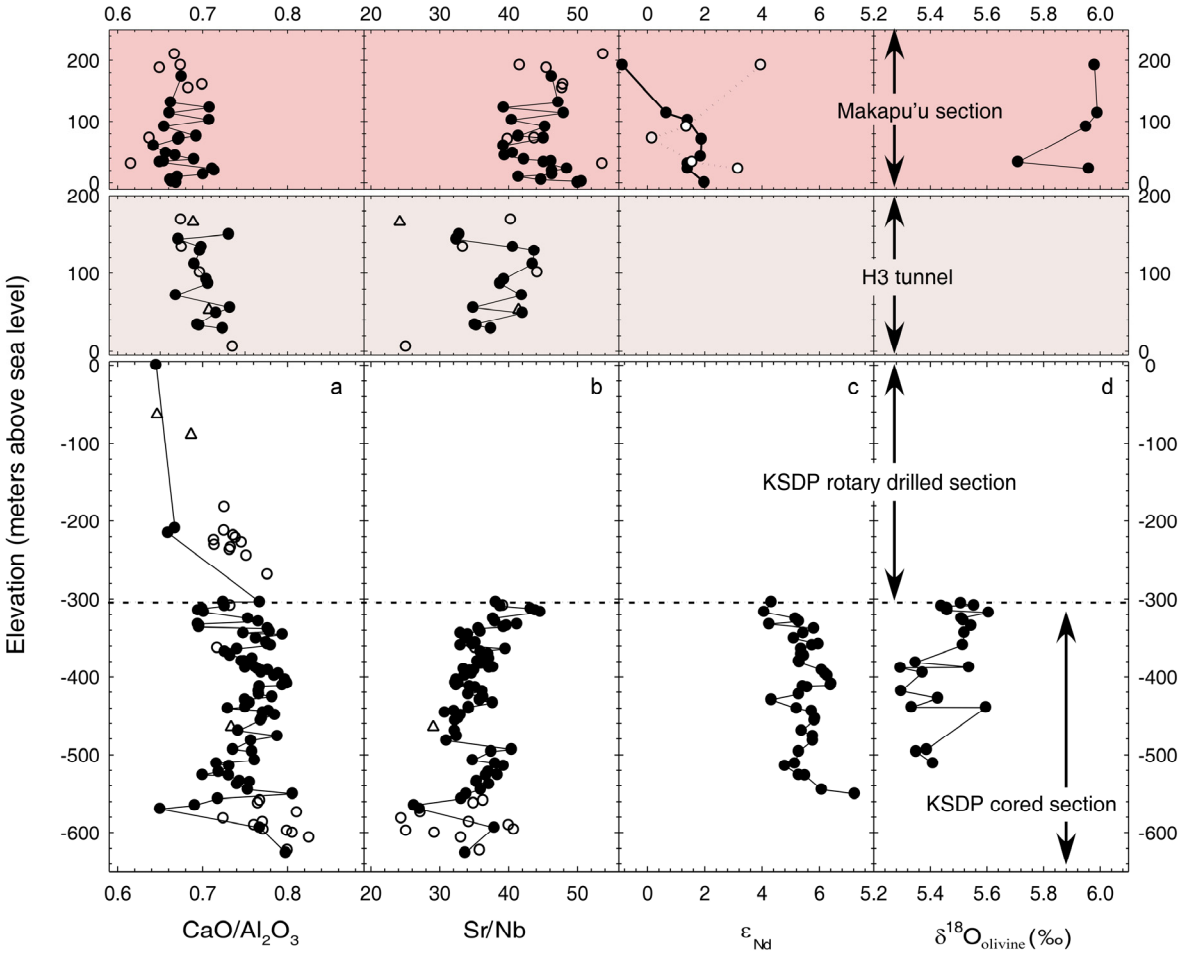


**Figure 1.** Stratigraphic profile of geochemical indices from Makapu'u head, H3 tunnel and KSDP drill core; **a:** $CaO/Al_2O_3$ (HASKINS and GARCIA, 2004); **b:** Sr/Nb (HASKINS and GARCIA, 2004; HUANG and FREY, 2005); **c:** $\varepsilon_{Nd}$ (SALTERS, 2005) and **d:** $\delta^{18}O$ values of olivines (this study).

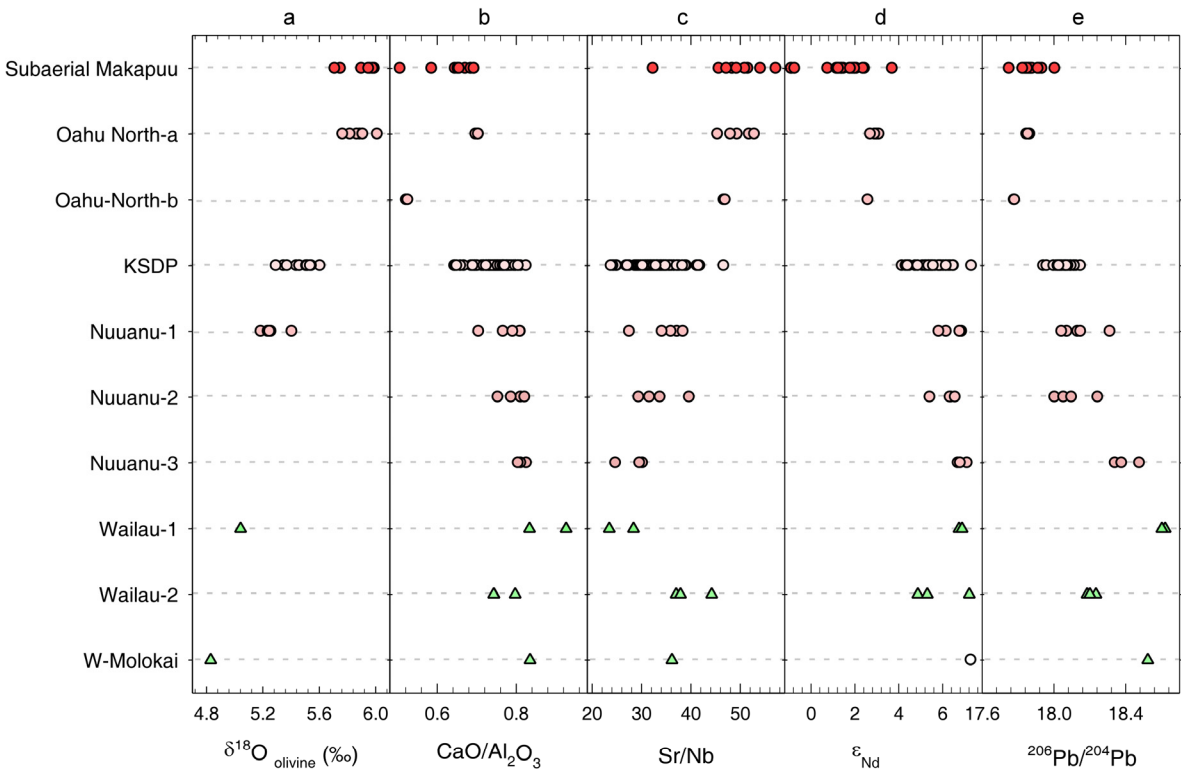


**Figure 2.** Summary of oxygen isotope compositions of olivines **a:** $CaO/Al_2O_3$; **b:** Sr/Nd; **c:** $^{206}Pb/^{204}Pb$; **d:** ratios and $\varepsilon_{Nd}$; and **e:** values for lavas from submarine landslides (oxygen isotope data from this study; other data from TANAKA et al., 2002).

Figure 2 summarizes the oxygen isotope compositions of olivines, $CaO/Al_2O_3$, Sr/Nd and $^{206}Pb/^{204}Pb$ ratios and $\varepsilon_{Nd}$ values for lavas from submarine landslides (oxygen isotope data are from this study. Other data are from TANAKA et al., 2002). The samples are arranged in approximate stratigraphic order, from oldest at the bottom to youngest at the top, based on estimates of positions of the blocks before the landslides. There are monotonic gradients in composition from the Nuuanu-3 block to the Oahu north-a block, defining a trend of increasing $\delta^{18}O$ and Sr/Nb and decreasing $CaO/Al_2O_3$, $\varepsilon_{Nd}$ and $^{206}Pb/^{204}Pb$ as one approaches Oahu (going up section). This reconstructed geochemical stratigraphy generally resembles that observed in the KSDP and Makapu'u point lavas:

i.e., lavas from the Oahu North-a and Oahu North-b blocks are similar in composition to Makapu'u stage lavas, whereas lavas from the Nuuanu-1 and Nuuanu-2 blocks are similar to KSDP lavas (TANAKA et al., 2002) .

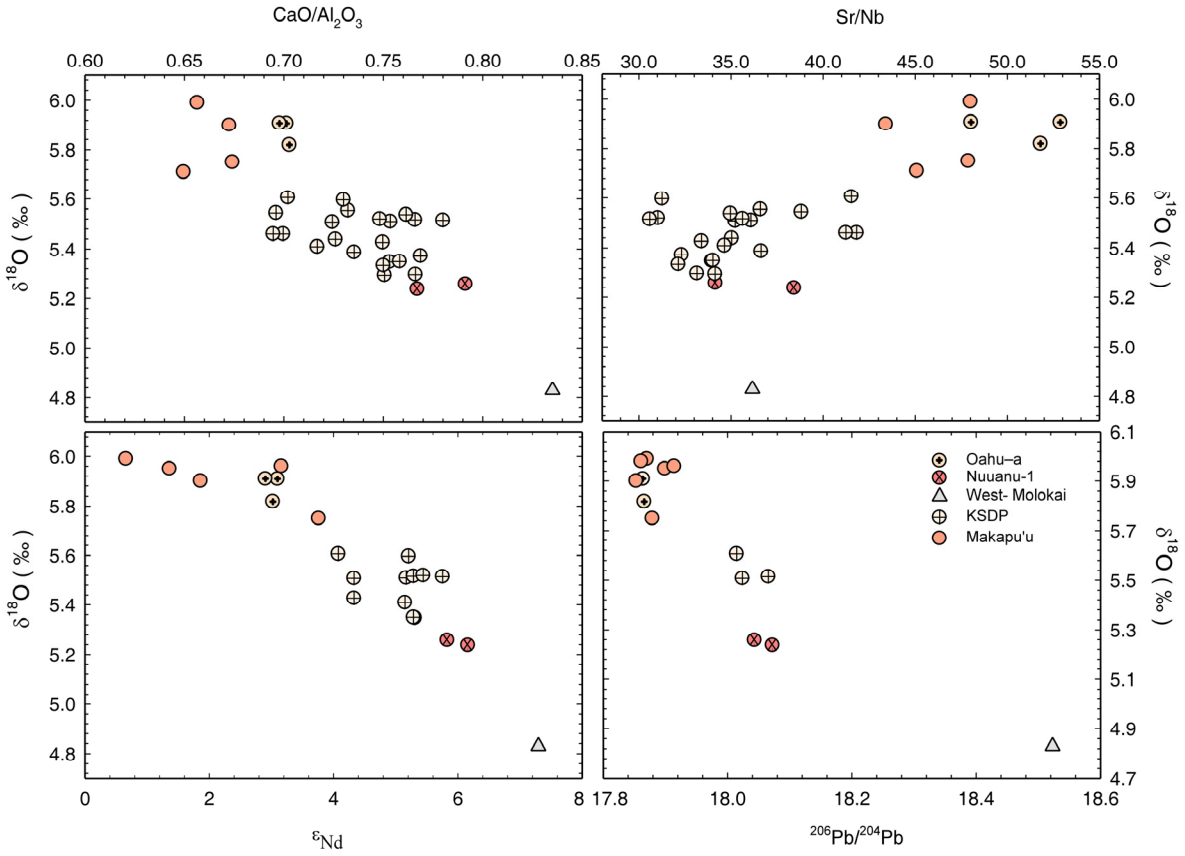


**Figure 3.** Correlation between $\delta^{18}O$ values of olivines and geochemical indices of their host lavas from Ko'olau and Molokai volcanoes; **a:** $\delta^{18}O$-$CaO/Al_2O_3$; **b:** $\delta^{18}O$-Sr/Nb; **c:** $\delta^{18}O$-$\varepsilon_{Nd}$; **d:** $\delta^{18}O$-$^{206}Pb/^{204}Pb$.

Figure 3 compares $\delta^{18}O$ values of olivines from Ko'olau lavas to other geochemical indices measured in the same lavas. In general, the entire sample suite shows correlations of $\delta^{18}O$ with $CaO/Al_2O_3$, Sr/Nb, $\varepsilon_{Nd}$ and $^{206}Pb/^{204}Pb$. These trends define a compositional continuum from a high-$\delta^{18}O$, 'enriched' (i.e., in crust-forming elements) end member to a more normal-$\delta^{18}O$, 'Mauna Loa-like' composition. These geochemical variations and

correlations cannot be explained by variations in degrees of partial melting of a uniform source (i.e., because partial melting cannot produce the observed radiogenic and oxygen isotope range, even if it could be responsible for some variations in major- and trace-element ratios), indicating that Ko'olau shield building lavas sample at least two geochemically distinct reservoirs. The enriched end member of this data array differs strongly in radiogenic isotope composition from local oceanic crust or depleted mantle (based on studies of mantle xenoliths, DUCEA et al., 2002; WEINSTEIN et al., 2004) and differs in trace-element ratios and $\delta^{18}O$ values from the estimated composition of primitive mantle, suggesting that it reflects the presence of recycled crustal materials in the mantle sources of Ko'olau lavas (e.g., HOFMANN and WHITE, 1982; HAURI, 1996; EILER et al., 1996a; LASSITER and HAURI, 1998), which might include any combination of eclogitized basaltic oceanic crust or gabbro cumulates (HAURI, 1996; EILER et al., 1996a; LASSITER and HAURI, 1998; SOBOLEV et al., 2000), pyroxenite (HIRSCHMANN and STOLPER, 1996), and/or pelagic sediments (BLICHERT-TOFT et al., 1999). In the next section of this study, we present a quantitative model to simultaneously explain the oxygen isotope, major element, trace element and radiogenic isotope variations of Ko'olau lavas in terms of the abundance, composition and melting properties of recycled crustal materials in their mantle sources.

## 4. A QUANTITATIVE GEOCHEMICAL MODEL

Geochemical variations of Hawaii shield-building lavas can be circumscribed by three compositional end-members (HAURI, 1996; EILER et al., 1996a). These are commonly referred to as the 'Ko'olau', 'Loihi' and 'Mauna Kea' end-members or

components, based on the name of the volcano whose lavas most closely approach that extreme. Many models have been developed to explain this geochemical diversity of Hawaiian lavas. HAURI (1996) discovered correlations between isotope ratios and olivine-fractionation-corrected major element and trace element compositions (where the composition of each lava has olivine added to or removed from it until the bulk composition reaches $Mg^{\#} = 0.76$). These correlations can be understood as a consequence of mixing between melts from geochemically distinct mantle sources, and are difficult or impossible to explain by variable degrees of melting of a homogeneous source. However, it is not necessary that mixing between geochemically distinct sources occurs at a constant $Mg^{\#}$ (e.g., = 0.76). Taking advantage of recent data from the melting experiments (PERTERMANN and HIRSCHMANN, 2003a; PERTERMANN and HIRSCHMANN, 2003b; PERTERMANN et al., 2004), we develop a quantitative model without assuming a constant $Mg^{\#}$ for mixing. In this model, primary magmas are mixtures of melts of peridotite on the one hand, and melts of eclogite (or possibly pyroxenite) on the other, fit to simultaneously explain the concentrations of all major elements in Ko'olau lavas (and we extend the model to fit "Loa trend" lavas in general). We then compare the fitted amounts of each of these components to the trace-element, radiogenic-isotope and oxygen-isotope compositions of Ko'olau lavas, showing that they correlate with the relative amounts of these two end members (which were defined based on major element data alone), and use those correlations to invert the trace-element and isotopic compositions of those end members. These model compositions are then examined for their significances regarding the origins and melting behaviors of components of the Hawaiian plume.

**4.1 Defining mixing end-members**

Our model assumes that the compositions of all "Loa trend" lavas (emphasizing those from Ko'olau) are mixtures of peridotite melts with melts of eclogite and/or pyroxenite. Figure 4 illustrates the major-element compositions of ca. 6700 Hawaiian lavas including shield, pre-shield and post-shield lavas. Although there is considerable compositional diversity in these data, the first-order trends are consistent with the following interpretation: 1) primary melts of all Hawaiian lavas have MgO content of about 18~20% (or $Mg^{\#}$=0.76), in equilibrium with $Fo_{91\text{-}92}$ olivines (similar to the most magnesian olivines found in Hawaiian lavas; NORMAN and GARCIA, 1999); 2) when undergoing crystallization-differentiation between 18~20 wt.% and ~7 wt.% of MgO, melts are saturated only in olivine and a small amount of spinel (~1 wt.%); 3) when undergoing crystallization-differentiation between ~7 and 6 wt.% MgO, melts are saturated in both olivine and plagioclase; 4) clinopyroxene is saturated shortly after plagioclase between 6 and 5 wt. %; and 5) Ti-Fe oxide starts to precipitate when MgO falls below ca. 5 wt. %. Lavas that substantially deviate from these general trends are explicable by unusually low degrees and/or high pressures of melting (e.g., some low-$SiO_2$, alkali-rich Loihi lavas) and accumulation of excess olivine (e.g., picrites with MgO larger than 20 wt. %).

Figures 4 and 5 show a representative model liquid line of descent (LLD) that we use to interpret and correct for the effects of crystallization-differentiation evident in the measured whole-rock compositions (Figure 4). This model LLD is calculated by first calculating a model primary melt. This was done by starting with the measured composition of Loihi glass KK29-10 (DIXON and CLAGUE, 2001; BYERS et al., 1985) and

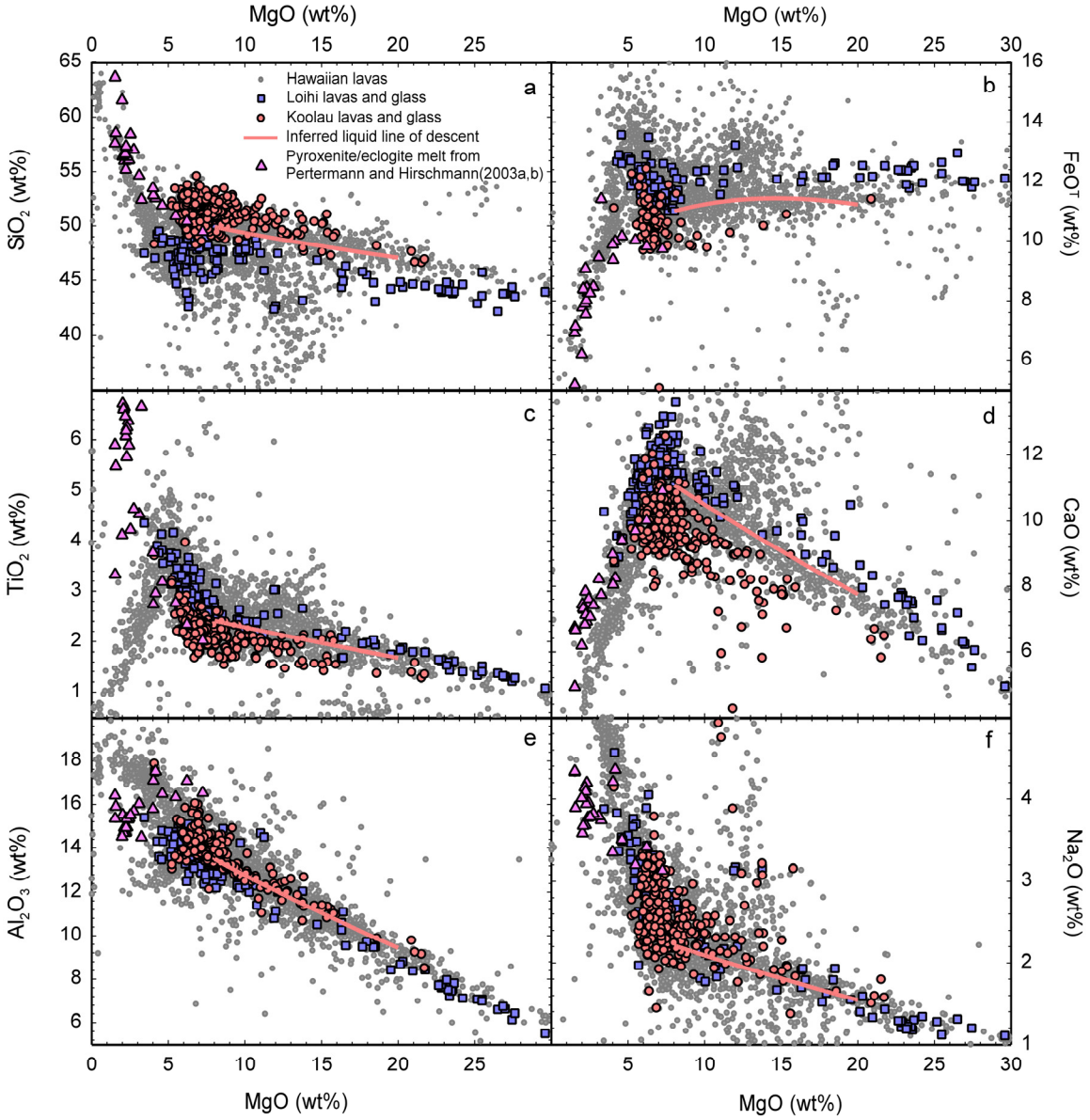


**Figure 4.** Major element variation of about 6700 Hawaiian lavas as a function of MgO. Data are from (http://georoc.mpch-mainz.gwdg.de/georoc/). Loihi and Ko'olau lavas are square and dots, respectively. The liquid line of descent is inferred from some Loihi glass by adding olivines. Compositions of Eclogite/pyroxenite melt from recent melting experiments (PERTERMANN and HIRSCHMANN, 2003a; PERTERMANN and HIRSCHMANN, 2003b; PERTERMANN et al., 2004) are also plotted for comparison (triangles).

then incrementally adding to it (in 0.1% steps) olivines in Fe-Mg exchange equilibrium with the glass ($K_D$ is from HERZBERG and ZHANG, 1996, around 0.29~0.34 as a function of MgO wt. %). The resulting curve through composition space represents the expected differentiation path for olivine-dominated fractionation, which passes through a large proportion of Hawaiian lavas in the dimensions of $SiO_2$-MgO-$FeO^T$-CaO-$Al_2O_3$-$TiO_2$-$Na_2O$, between MgO = 10~20 wt.%. We chose a Loihi glass for this calculation because it lies near the low-$\delta^{18}O$, depleted end of geochemical trends in Figure 3, and thus, is a plausible 'eclogite-melt-free' end-member, and it is magnesian enough to have undergone only olivine fractionation (we ignored 1~2 wt. % spinel precipitation). While we could have chosen other lavas to represent our depleted end-member, trial calculations with other possible compositions showed that all tholeiitic Loihi glasses with MgO > 7.0 wt.% lead to similar final models.

Referring to this LLD, some Hawaiian lavas from different volcanoes are apparently not on the same fractional-crystallization path. Neither can they be explained by olivine accumulations. For example, Makapu'u-stage lavas (the stratigraphically youngest sequence of Ko'olau lavas) are systematically higher in $SiO_2$ and lower in FeO at a given MgO than the LLD defined by Loihi glasses (Figure 4). This difference becomes even more pronounced at MgO = 5~7 wt% where Ko'olau lavas continue to increase in $SiO_2$ and decrease in $FeO^T$ with decreasing MgO, whereas Loihi lavas exhibit the opposite trends (presumably because Loihi lavas are plagioclase saturated below 7 wt.% MgO whereas Ko'olau lavas are not). Figure 4 also plots the melt composition of partial melts of eclogite and pyroxenite having MORB-like major element compositions (PERTERMANN and HIRSCHMANN, 2003a; PERTERMANN and HIRSCHMANN, 2003b). These

experimental melts of mafic materials lie along extensions of the trends in major element composition defined by Hawaiian lavas for all elements other than $TiO_2$ (which are systematically higher in the experimental melts than in Hawaiian lavas). This difference in $TiO_2$ concentration might reflect that the source rock composition or melting condition in the melting experiment is not exactly the same as what is responsible for the formation of Ko'olau lavas. Therefore, we will define melts from PERTERMANN and HIRSCHMANN (2003a, 2003b) as our enriched component. These melt compositions are parameterized as a function of pressure and degree of melting using the Bicubic Spline method (PRESS et al., 2002, chapter 3.3) to interpolate data between experiments. We will also discuss other possibilities in Section 5.

**4.2 Implementation of the model**

We fit the compositions of Hawaiian lavas as mixtures of model Loihi primitive melt with partial melts of eclogite/pyroxenite, followed by crystallization-differentiation. An important aspect of our model is that we force the composition of the eclogite melt component to be within the compositional spectrum of experimental eclogite melts, and use an error-minimization algorithm to determine the composition within that spectrum that best fits major-element trends of Hawaiian lavas. The actual fitting algorithm is performed simultaneously in all major element compositional dimensions of interest (here, $SiO_2$-MgO-$FeO^T$-CaO-$Al_2O_3$-$TiO_2$-$Na_2O$ space) in a least-squares sense, but one can visually understand the procedure by looking at a two-dimensional 'cut' through that composition space (MgO vs. FeO; Figure 5). As shown in Figure 5, we assume the parental melt of a given Ko'olau sample (PK) is the mixture of primary magma of Loihi

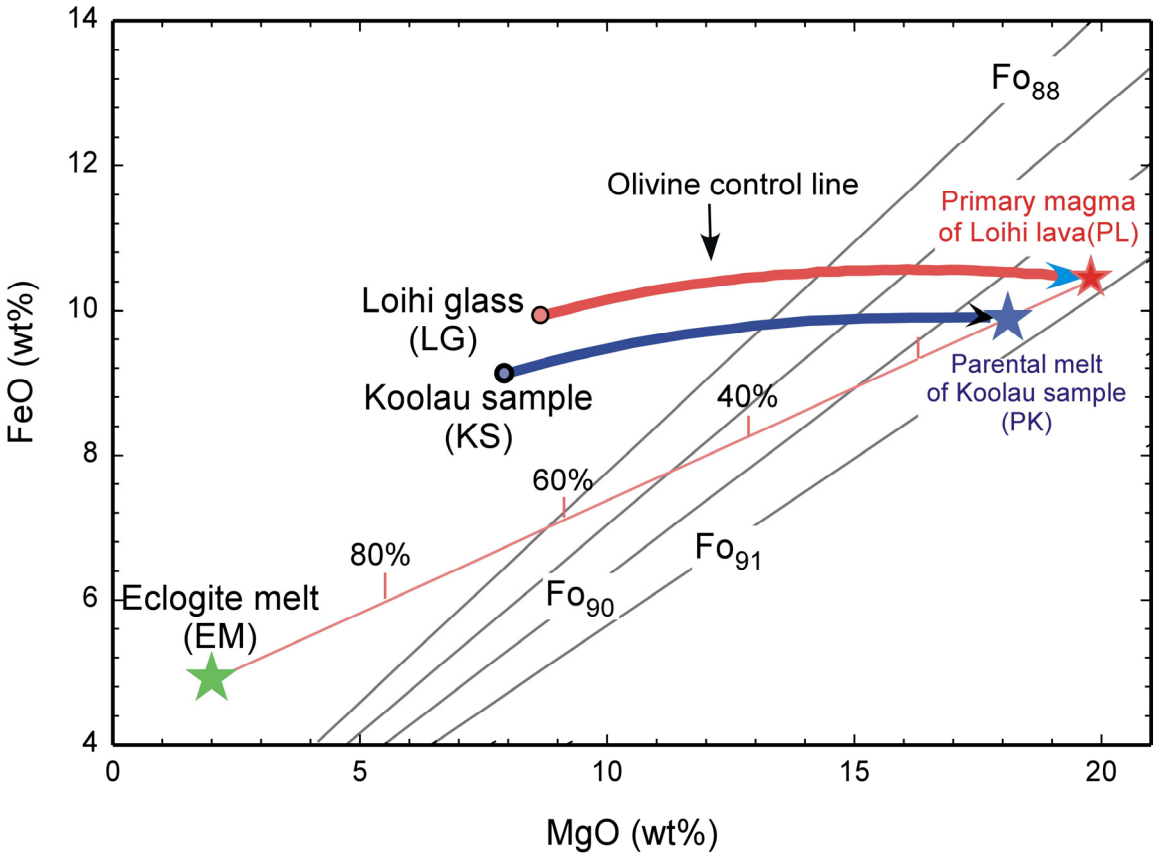


**Figure 5.** Schematic description of model implementation procedures in FeO-MgO space.

lava (PL) and eclogite melt (EM). There are several constraints for the mixing end-members and mixtures: 1) primary magma of Loihi lavas (PL) has to be on the liquid-line of descent calculated for Loihi glass (LG) KK29-10 (DIXON and CLAGUE, 2001; BYERS et al., 1985); 2) parental melt of a given Ko'olau sample (PK) has to be on the olivine control line defined by this Ko'olau sample (KS); and 3) eclogite melt composition is the parameterized melting experiment data (EM). Point PK marks the intersection of olivine control line (defined by a given Ko'olau sample) with the mixing line between model primitive Loihi-like melt and eclogite melt, and is our model estimate for the composition of the primary melt from which this Ko'olau lava differentiated. In the two dimensions

illustrated in Figure 5, it is clear that a wide range of compositions and proportions of eclogite melt could equally well explain the composition of Ko'olau lavas. However, we perform this geometric analysis simultaneously in all major-element dimensions other than $TiO_2$. We also analyze all "Loa-trend" lavas globally and we require that the same eclogite melt composition is sampled by all lavas and that this composition is part of the spectrum of experimental eclogite melts. We iteratively vary the eclogite melt composition within these constraints to minimize the overall error in our model. Note that this model is only applied to Ko'olau lavas with ≥ 6.5 wt.% MgO, which we can confidently infer they underwent fractionation of only olivines. Note also that if a Ko'olau sample has $Mg^{\#} > 0.706$ (melts in equilibrium with $Fo_{88.5}$ olivine, the majority of olivine phenocrysts in Ko'olau lavas, NORMAN and GARCIA, 1999; NORMAN et al., 2002), we assume this sample is a mixture of glass with $Fo_{88.5}$ olivines, and calculate out the composition of glass which is then used in the optimization procedure.

## 4.3 MODELING RESULTS

### 4.3.1 OPTIMIZATION CALCULATION

These optimization processes are carried out for 210 samples from Makapu'u lavas, KSDP drill core, and submarine landslide blocks from Ko'olau volcano. These calculations show that: 1) most lavas require Loihi primary melt to have $Mg^{\#}= 0.77$. This was originally set as a limit for Loihi primary melt in order to co-exist with $Fo_{91.5}$ olivine; 6 out of 210 samples require $Mg^{\#} = 0.702\sim0.77$, which is still valid to be a parental melt of Ko'olau lavas. Variation in $Mg^{\#}$ by 0.03 around $Mg^{\#} = 0.77$ will only change the mixing ratio by 1.2%; 2) eclogite melt from the melting experiment A200K

(PERTERMANN and HIRSCHMANN, 2003a) is the best candidate among the available melting experiments for the enriched component. This melt is produced from starting material G2k at 30 kbar, 1275°C after melting 14% of a MORB-like eclogite with clinopyroxene, garnet, quartz and rutile as coexisting phases (PERTERMANN and HIRSCHMANN, 2003a); the best candidates for pyroxenite melts (PERTERMANN and HIRSCHMANN, 2003a; 2003b) are also produced at similar conditions -- 30 kbar and about 13% partial melting -- but they are not as good as melts from A200K at satisfying the linear mixing relationship in all major element composition space. Our preferred model eclogite melt is similar to the dacitic melt component estimated by HAURI (1996) in $SiO_2$, $Al_2O_3$, FeO, $Na_2O$ and $K_2O$, but significantly different in MgO and CaO; 3) lavas that are strongly altered ($K_2O/P_2O_5$<1.0 or > 3.0) will not normally converge to an acceptable minimum in the optimization procedure, and are therefore not shown in Figure 6 and not considered for further calculation.

Figure 6 shows $Ca_2O_3/Al_2O_3$ (a), Sr/Nb (b), εNd (c) and $\delta^{18}O$ (d) for all Ko'olau volcanoes (except strongly altered samples) as a function of calculated mixing ratios of eclogite melt component required for fitting the major element composition by the mixing of eclogite melt and peridotite melt. Figure 6a is essentially a consistency test of our model, as it compares a major element index with one of the parameters we fit using major element data. However, the other panels of Figure 6 compare our model fits based on major elements to independent trace-element and isotope variables. In summary, Ko'olau lavas from Makapu'u section, KSDP, and submarine landslides contain between 0% and 23% of the eclogite melt component. We estimate that the uncertainty in this mixing proportion for any given sample is approximately 2.5%, (2σ), simply based on

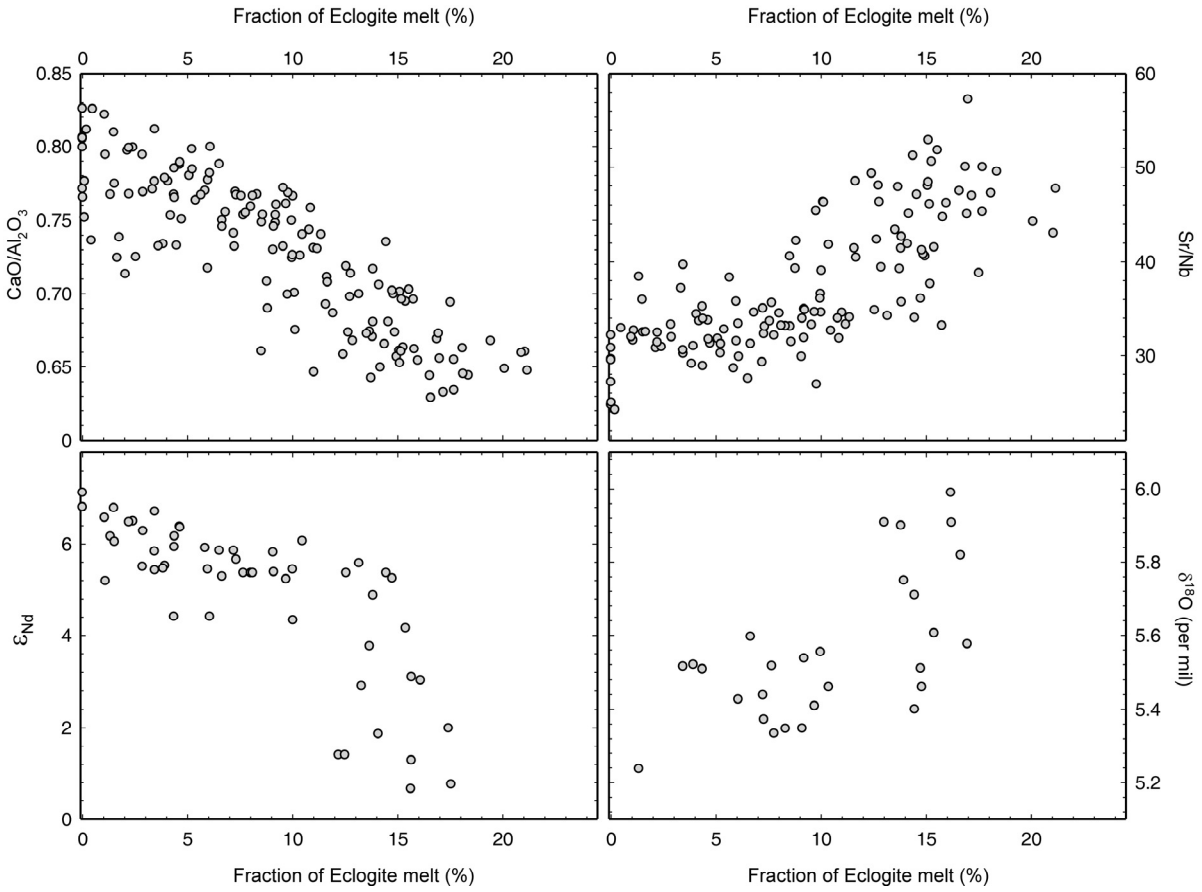


**Figure 6.** Geochemical indices varied with calculated proportion of eclogite melt for Ko'olau samples. **a:** $CaO/Al_2O_3$; **b:** Sr/Nb; **c:** $\varepsilon_{Nd}$; **d:** $\delta^{18}O$ values of olivines.

this being half of the range in mixing proportion for a given value of one of the geochemical indices that correlate with the amount of eclogite melt (although the scatters higher for Figure 6d). We suspect these uncertainties are caused by the geochemical variation in Loihi primary melts and the eclogite component, and the precision in measuring these geochemical quantities. Our model predicts that the $Mg^{\#}$ of primary Hawaiian melts is inversely correlated with the proportion of eclogite melt they contain, from a maximum of 0.77 (pure Loihi-like melt) to a minimum of ~0.75 (23 % eclogite melt; Figure 7). Note that this calculated proportion of eclogite melt is a minimum

quantity, assuming the sample we chose to represent the depleted, Loihi-like end member does not sample any eclogite melt.

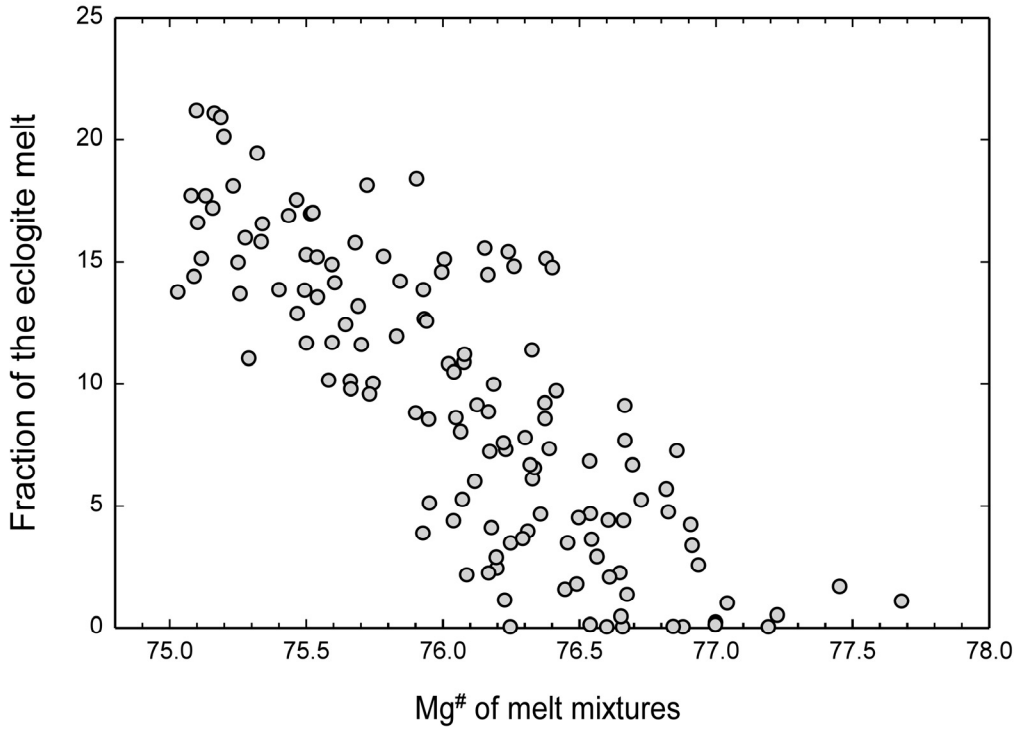


**Figure 7.** Variation in $Mg^{\#}$ of the melt mixtures as a function of calculated proportion of eclogite melt.

#### 4.3.2 INFERRING PROPERTIES OF THE ENRICHED COMPONENT

Using one of the Ko'olau lavas in Figures 6a-d, we can infer the trace element and isotope composition of the eclogite component, and the mixing relationships that could be tested using known geochemical data. In this exercise, we use experimentally determined parameters for the eclogite melt in this inversion, i.e., 14.3% melting of MORB-like eclogite and partition coefficients of trace element between solid and melt (PERTERMANN and HIRSCHMANN, 2003a; PERTERMANN et al., 2004). We chose sample KOO-8 from Makapu'u section of Ko'olau volcano because: 1) it is well-studied in major,

trace element and isotope geochemistry (FREY et al., 1994; RODEN et al., 1994; LASSITER and HAURI, 1998; BLICHERT-TOFT et al., 1999; HUANG and FREY, 2005); 2) it has a mixing ratio of 11.9% which is in the middle of the variation range, so its extrapolation can be tested by other data. However, the disadvantage of this choice of sample is that it might require high precision trace element and radiogenic isotope data to resolve because of the low mixing fraction. Trace element composition of the primary melt of Loihi is estimated using the average of six Loihi volcanic glasses corrected back to $Mg^{\#} = 0.77$ (GARCIA et al., 1993). Major element compositions differences are within 6.7% between the average of these glasses and the primary melts estimated using sample KK29-10, except $K_2O$ about 20%. Isotope compositions of this component were selected from averages of Loihi glasses.

Calculations were made for trace element composition of Loihi primary melts from two datasets (one using ICP-MS and ICP-ES). Trace element compositions for sample KOO-8 are mostly from ICP-MS measurements (HUANG and FREY, 2005). A few of them are from XRF (FREY et al., 1994). Comparison between these two dataset for the same element shows that trace element concentrations calculated for the eclogite melt are sensitive to the precision of the measurement. Nonetheless, the differences between these two datasets for a given element are within a factor of 2.0, except Dy with a factor of 10. Trace element compositions in estimating the isotope composition of eclogite component are data with better precision in these two datasets judged by comparing the precision of standard measurement for each element reported by GARCIA et al., 1993). The average of the two datasets is plotted in Figure 11. Besides these instrumental differences, the standard deviation of trace element for the eclogite is about ~50%, assuming ~10%

Table 2: Spreadsheet for binary mixing calculation results using KOO-8

| Sample | Loihi [R1] | Ko'olau KOO-8 [R2 R2] | Eclogite Melt A200K [R3] | Calculated KOO-8 [a] | | | |
|---|---|---|---|---|---|---|---|
| $SiO_2$ | 47.14 | 49.10 | 63.64 | 49.11 | | | |
| $TiO_2$ | 1.70 | 1.56 | 3.33 | 1.90 | | | |
| $Al_2O_3$ | 9.54 | 10.22 | 15.35 | 10.23 | | | |
| $FeO^T$ | 11.25 | 10.93 | 5.18 | 10.52 | | | |
| MnO | 0.11 | 0.12 | 0.06 | 0.11 | | | |
| MgO | 19.67 | 17.55 | 1.53 | 17.50 | | | |
| CaO | 7.84 | 7.27 | 4.93 | 7.49 | | | |
| $Na_2O$ | 1.56 | 2.24 | 4.34 | 1.89 | | | |
| $K_2O$ | 0.25 | 0.35 | 1.63 | 0.41 | | | |
| $Mg^{\#}$ | 0.770 | 0.755 | 0.345 | 0.758 | | | |
| Optimized proportion of eclogite melt | | | 11.93 | | | | N-MORB |
| | | | | $D_{Total}$ [R4] | Eclogite Glass(14.3%) | NMORB [R5] | Normalized |
| ICP-MS analyses [b] | | | | | | | |
| La | 9.32 | 8.98 | 6.41 | 0.021 | 1.03 | 3.895 | 0.26 |
| Ce | 19.73 | 22.79 | 46.04 | 0.044 | 8.32 | 12.001 | 0.69 |
| Nd | 12.61 | 15.59 | 38.25 | 0.164 | 10.85 | 11.179 | 0.97 |
| Sm | 3.61 | 3.97 | 6.69 | 0.233 | 2.29 | 3.752 | 0.61 |
| Ba | 73.70 | 83.15 | 154.87 | 0.006 | 22.94 | 1.335 | 1.65 |
| Eu | 1.27 | 1.32 | 1.68 | 0.241 | 0.59 | 0.885 | 0.44 |
| Dy | 3.70 | 3.35 | 0.65 | 1.027 | 0.66 | 3.9 | 0.10 |
| Er | 1.82 | 1.63 | 0.25 | 1.795 | 0.43 | 0.589 | 0.10 |
| Yb | 1.32 | 1.28 | 0.93 | 2.553 | 2.16 | 13.87 | 0.55 |
| Lu | 0.19 | 0.18 | 0.07 | 2.903 | 0.19 | 3.507 | 0.33 |
| Y | 17.93 | 18.93 | 26.53 | 1.38 | 35.17 | 35.82 | 0.98 |
| Hf | 2.21 | 2.69 | 6.34 | 0.302 | 2.55 | 2.974 | 0.86 |
| Rb | 6.00 | 5.32 | 0.19 | 0.004 | 0.03 | 1.262 | 0.02 |
| Cs | 0.06 | 0.06 | 0.06 | 0.004[c] | 0.01 | 0.01408 | 0.62 |
| ICP-ES analyses [d] | | | | | | | |
| K | 2689.72 | 2900.50 | 4508.10 | 0.024 | 737.38 | 883.7 | 0.83 |
| Sr | 236.63 | 356.35 | 1265.19 | 0.054 | 239.47 | 113.2 | 2.12 |

Table 2 continued

| Sample | Loihi [R1] | Ko'olau KOO-8 [R2 R2] | Eclogite Melt A200K [R3] | $D_{Total}$ [R4] | Eclogite | NMORB [R5] | N-MORB Normalized |
|---|---|---|---|---|---|---|---|
| Optimized proportion of eclogite melt | | | 11.93 | | Glass(14.3%) | | |
| Ba | 78.11 | 83.15 | 121.37 | 0.006 | 17.98 | 13.87 | 1.30 |
| Zr | 95.30 | 114.33 | 258.77 | 0.233 | 88.68 | 104.24 | 0.85 |
| La | 8.10 | 8.98 | 15.70 | 0.021 | 2.53 | 3.895 | 0.65 |
| Nd | 12.02 | 15.59 | 42.67 | 0.164 | 12.10 | 11.179 | 1.08 |
| Sm | 3.14 | 3.97 | 10.26 | 0.233 | 3.52 | 3.752 | 0.94 |
| Eu | 1.09 | 1.32 | 3.05 | 0.241 | 1.06 | 1.335 | 0.80 |
| Dy | 2.94 | 3.35 | 6.44 | 1.027 | 6.59 | 6.304 | 1.05 |
| Yb | 1.20 | 1.28 | 1.87 | 2.553 | 4.36 | 3.9 | 1.12 |
| Lu | 0.17 | 0.18 | 0.27 | 2.903 | 0.70 | 0.589 | 1.19 |
| Th | 0.55 | 0.50 | 0.11 | 0.0034 | 0.02 | 0.1871 | 0.09 |
| Y | 15.27 | 18.93 | 46.71 | 1.38 | 61.92 | 35.82 | 1.73 |
| Pb* | 0.40[e] | 0.95 | 5.12 | 0.001[f] | 0.74 | 0.489 | 1.50 |
| $\delta^{18}O_{whole\ rock}$ [g] | 5.60 [h] | 6.30 [i] | 11.5 | | | | |
| $^{87}Sr/^{86}Sr$ | 0.70361 [j] | 0.70408 | 0.70475 | | | | |
| $^{143}Nd/^{144}Nd$ | 0.51296 [l] | 0.51271 | 0.51209 | | | | |
| $^{206}Pb/^{204}Pb$ | 18.252 [m] | 17.879 | 17.659 | | | | |
| $^{207}Pb/^{204}Pb$ | 15.433 | 15.447 | 15.455 | | | | |
| $^{208}Pb/^{204}Pb$ | 38.001 | 37.826 | 37.723 | | | | |
| $^{176}Hf/^{177}Hf$ | 0.28311 | 0.28294 | 0.28249 | | | | |

**R1:** defined primary magma of Loihi lavas at $Mg^{\#}$=0.77 calculated from sample KK29-10 (DIXON and CLAGUE, 2001; BYERS et al., 1985); trace element and isotopic compositions are inferred from other Loihi glasses (GARCIA et al., 1993); **R2:** tholeiite from Makapu'u section (FREY et al., 1994; RODEN et al., 1994; LASSITER and HAURI, 1998; BLICHERT-TOFT et al., 1999; HUANG and FREY, 2005); **R3:** experiment determined eclogite melt derived from G2k (PERTERMANN and HIRSCHMANN, 2003a) at 30 kbar, 1275°C after melting 14.2% of a MORB-like eclogite with clinopyroxene, garnet, quartz and rutile as coexisting phases; **R4:** if otherwise noted, we experimentally determined partition coefficient between solid phase and eclogite melt for sample A200K (PERTERMANN et al., 2004); **R5:** N-MORB use HOFMANN (1988); **a:** calculated KOO-8 by mixing Loihi primary magma and eclogite melt with optimized eclogite proportion; note this calculated KOO-8 on the mixing line is very close to KOO-8 on the olivine

control line; **b:** trace element concentration using averages of Loihi glasses and KOO-8 measured by ICP-MS (GARCIA et al., 1993, HUANG and FREY, 2005); **c:** estimated to be same as Rb; **d:** trace element concentration using averages of Loihi glasses by ICP-ES (GARCIA et al., 1993); **e:** Pb concentration is estimated to satisfy Pb = 0.0866×La-0.30 after linear regression over samples measured for both La and Pb ($R^2$ = 0.9) from GEOROC database (http://georoc.mpch-mainz.gwdg.de/georoc/); **f:** estimated value**; g:** assuming fractionation factor between melt and olivine is 0.5 (EILER et al., 2000b); **h:** estimated using the averages of all samples from Loihi (EILER et al., 1996a); **i:** estimated to be 5.8; **j,l,m:** estimated from Loihi glasses which is more like Mauna Kea.

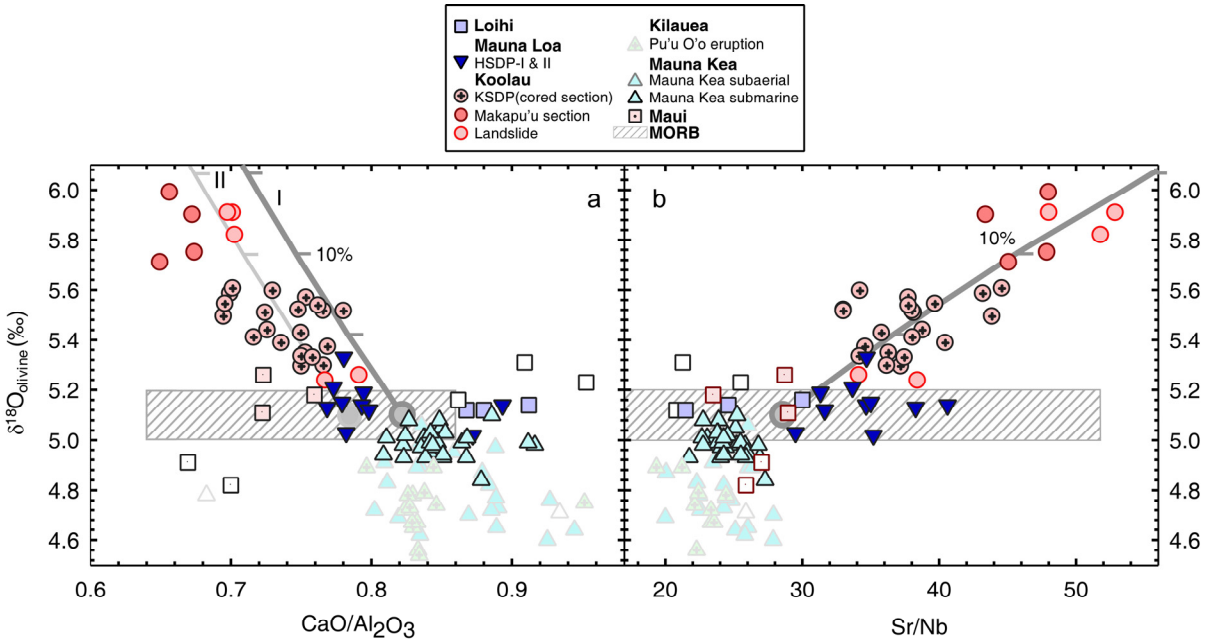


**Figure 8.** Correlation between $\delta^{18}O$ values of olivines and geochemical indices of their host rock **a:** $CaO/Al_2O_3$ ratio; **b:** Sr/Nb ratio. Open symbols are alkali basalts. Faded symbols for Pu'u O'o eruption of Kilauea volcano and subaerial Mauna Kea volcanoes are representing progressive rift zone contamination, therefore deviate from the main mixing trend. Dark grey lines with tick mark at every 5% percent are binary mixing calculation. In panel a, two conditions are plotted; line-I is the direct calculation result and can describe the trend well, but miss major population of data; line-II is a fitting of the data and requires parental magma of Loihi volcano to have a $CaO/Al_2O_3$ ratio of 0.8.

precision for data from Loihi and Ko'olau. Since Pb concentration data are unavailable for most samples measured for Pb isotope ratios of Loihi lavas, we estimate Pb = 0.0866×La-0.30 using linear regression over samples from GEOROC database (http://georoc.mpch-mainz.gwdg.de/georoc/) measured for both La and Pb ($R^2 = 0.9$).

Calculation results are shown in Table 2 and Figures 8 to 11. In Table 2, we also listed calculated KOO-8 by mixing Loihi primary magma and eclogite melt at optimized eclogite proportion. This calculated KOO-8 on the mixing line is very close to KOO-8 on the olivine control line. Figure 8 is a test of our model using the correlation between $\delta^{18}O$ values of olivine and major element ($CaO/Al_2O_3$) and trace element ratio (Sr/Nd). Figure 9 is a test using the correlation between $\delta^{18}O$ values of olivines and radiogenic isotope ratios. Figure 10 is a test using correlations between radiogenic isotope ratios. In Figures 8 to 10, our calculated mixing curves fit well, not only in the direction of progressive changes in the geochemistry of 'Loa trend' lavas, but also through the center of most measured compositions. Isotope composition of shield stage lavas from "Loa trend" volcanoes can be explained by about 0~25% incorporation of melts from our eclogite melt, which is also consistent with calculation results shown in Figure 6. The calculated eclogite component has isotopic composition of $\delta^{18}O_{\text{whole rock}} = 12.0$, $^{87}Sr/^{86}Sr = 0.70475$, $^{206}Pb/^{204}Pb = 17.659$ and $^{176}Hf/^{177}Hf = 0.28249$, $^{143}Nd/^{144}Nd = 0.51209$ with DMM model age of 1.6 billion years.

Figure 11 shows the calculated trace element pattern of this eclogite normalized relative to N-MORB (HOFMANN, 1988). To the first order, HREE pattern of our calculated eclogite is very similar to NMORB, suggesting the protolith of this eclogite is from MORB-like basalts. Highly incompatible elements, Rb, Th, U, Nb and La of this

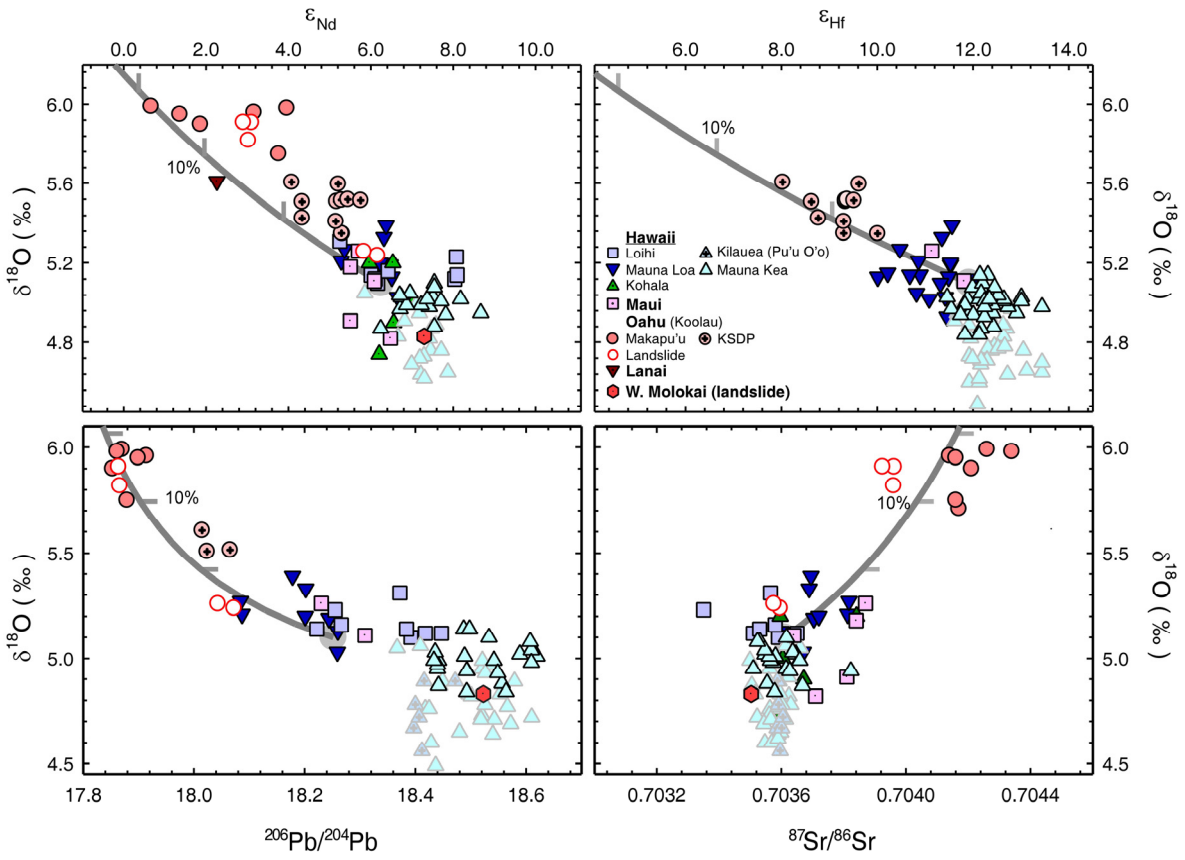


**Figure 9.** Correlation between $\delta^{18}O$ values of olivines and radiogenic isotope ratios: **a:** $\varepsilon_{Nd}$; **b:** $\varepsilon_{Hf}$; **c:** $^{206}Pb/^{204}Pb$; **d:** $^{87}Sr/^{86}Sr$. Faded symbols for Pu'u O'o eruption of Kilauea volcano and subaerial Mauna Kea volcanoes are representing progressive rift zone contamination. Dark grey lines with tick mark at every 5% are binary mixing calculation results between eclogite melt and parental magma of Loihi volcano. The isotopic characters of eclogite end-member are $\delta^{18}O_{whole\ rock}$ = 12.0‰ assuming melt-olivine fractionation of ~0.5‰ (EILER et al., 2000b), $^{87}Sr/^{86}Sr$ = 0.70475, $^{143}Nd/^{144}Nd$ = 0.51209, $^{176}Hf/^{177}Hf$ = 0.28249, $^{206}Pb/^{204}Pb$ = 17.659. Grey diamonds are samples from lherzolite xenoliths from Pali, Oahu (DUCEA et al., 2002), $^{87}Sr/^{86}Sr$ ratios of whole rocks are represented by that of plagioclase, $\varepsilon_{Nd}$ values of whole rock are using that of clinopyroxene due to high concentration of Sr and Nd element, respectively.

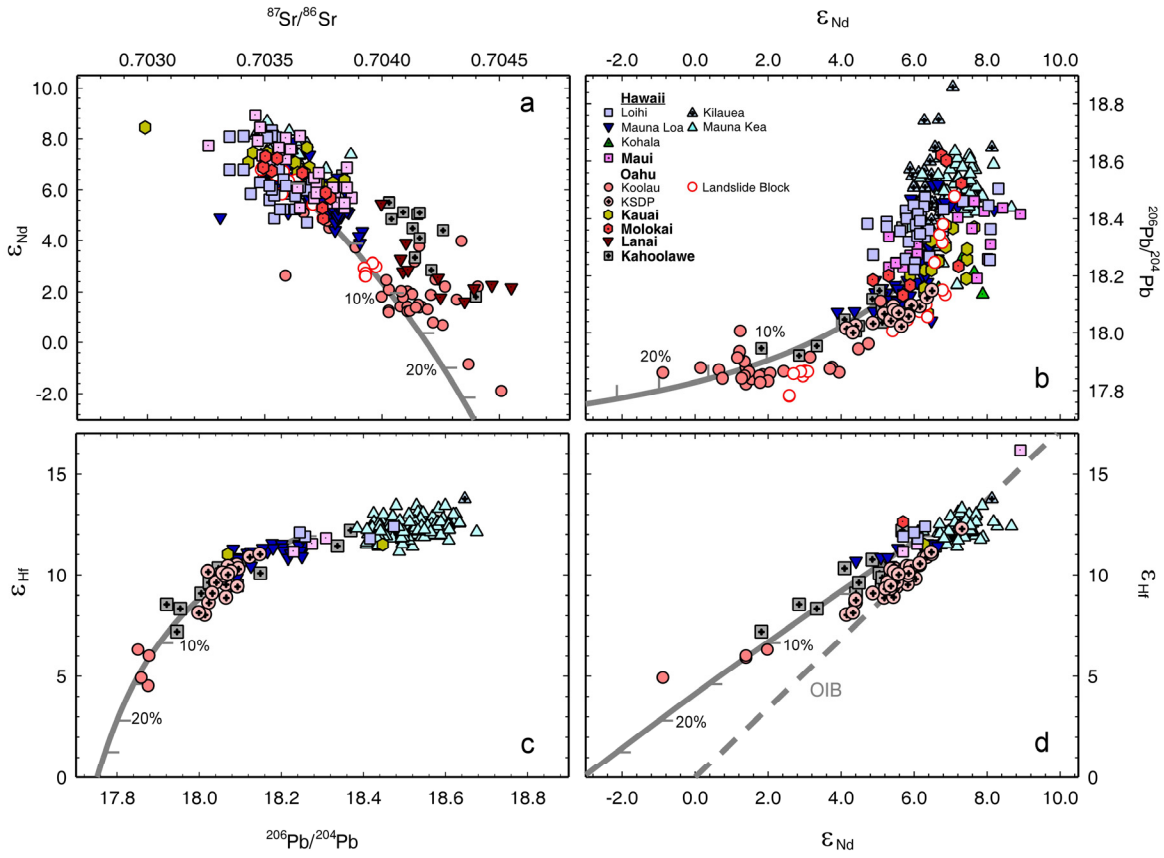


**Figure 10.** Correlation between radiogenic isotope ratios to test our binary mixing models. **a:** $^{87}Sr/^{86}Sr$ vs. $\varepsilon_{Nd}$; B: $\varepsilon_{Nd}$ vs. $^{206}Pb/^{204}Pb$; C: $^{206}Pb/^{204}Pb$ vs. $\varepsilon_{Hf}$; D: $\varepsilon_{Nd}$ vs. $\varepsilon_{Hf}$. Dark grey lines with tick mark at every 5% are binary mixing calculation results between eclogite melt and parental magma of Loihi volcano. The isotopic character of eclogite end-member is $^{87}Sr/^{86}Sr$ = 0.70475, $^{143}Nd/^{144}Nd$ = 0.51209, $^{176}Hf/^{177}Hf$ = 0.28249, and $^{206}Pb/^{204}Pb$ = 17.659.

eclogite melt are strongly depleted compared with MORB, suggesting these MORB-like basalts experienced partial melting before forming eclogite. However, highly incompatible element Pb, Ba and Sr are slightly more enriched than N-MORB, deviating from partial melting pattern as expected from other highly incompatible elements. Their enrichments can be explained by the following possibilities: 1) MORB-like basalts incorporating some pelagic sediments; pelagic sediments are known to be enriched in Ba

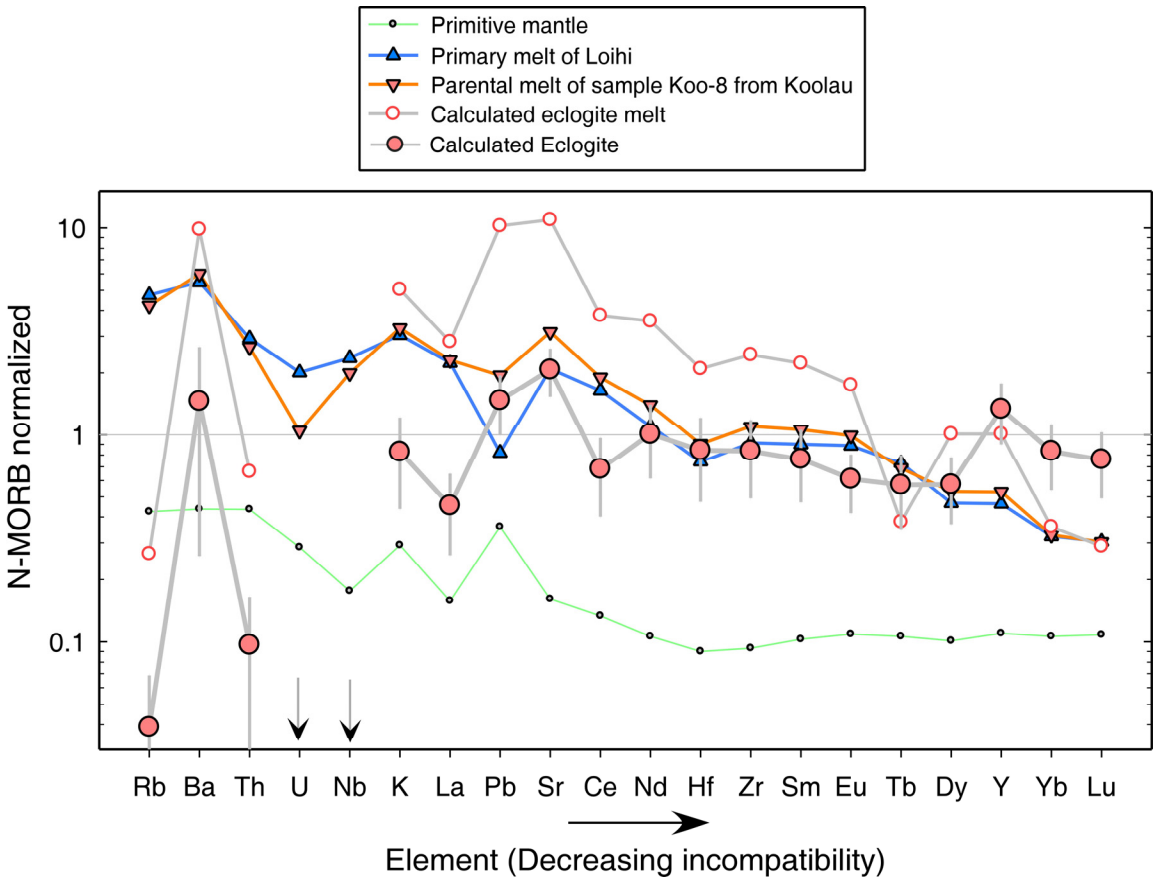


**Figure 11.** N-MORB normalized trace element concentration for the calculated eclogite source rock, compared with primitive mantle (HOFMANN, 1988), primary melt from Loihi and parental magma of sample KOO-8 (FREY et al., 1994; RODEN et al., 1994) from Ko'olau volcano. Calculated eclogite source rock has N-MORB like features, but different from melt inclusion from Mauna Loa. The typical standard deviation for each sample is ~40%.

and Pb relative to N-MORB by more than one hundred times (e.g., HOLE et al., 1984). Therefore a few percent of sediments added to a MORB-like basalt will significantly increase the concentration of Ba and Pb; also this hypothesis is consistent with the calculated extremely high $\delta^{18}O$ values ( = 12.0 ‰) of whole rock and deviation from OIB trend in Figure 10d. 2) Partial melting of the MORB-like basalt might occur in the

plagioclase stability field where plagioclase can hold some Ba, Pb and Sr in the solid phase. Or 3) the MORB-like basalts also include some gabbro which are enriched in plagioclase.

In addition, other properties can be noticed in Figure 11 that are consistent with our model assumptions. As we see, trace element compositions of primary melt of Loihi lavas can be derived from partial melting of primitive mantle as they track well the changes of primitive mantle. Also, primary melt of Loihi lavas and parental melt of Ko'olau lavas are very similar to each other, except the latter is enriched in Pb and Sr, presumably due to the incorporation of eclogite melt.

### 4.3.3 SENSITIVITY TEST AND SOME LIMITATIONS OF THE MODEL

To test the sensitivity of the selection of Ko'olau samples, similar exercises are carried out on three other Makapu`u samples. Results show those general features described above are true, but with variations in real values. For example, each sample will generate mixing lines with similar or slightly different slopes as in Figures 8 to 11, and the scales (tick marks) along each mixing line are a little bit different due to the propagation of ±3% uncertainties in mixing proportions. Nevertheless, the range in derived isotopic compositions of the eclogite component from inversions of the 4 samples is $\varepsilon_{Nd}$ = -9.4±2.5, $\varepsilon_{Hf}$ = -7.6 ± 2.5, $\delta^{18}O_{\text{whole rock}}$ = 11.3 ± 1.5‰, $^{87}Sr/^{86}Sr$ = 0.70484 ± 0.00015, $^{206}Pb/^{204}Pb$ = 17.642 ± 0.025 and DMM age of 1.8±0.3 byrs.

In summary, our mixing model has the power to explain most of the geochemical variation as seen in 'Loa trend' lavas, and predict the properties of the enriched component. However, it also has its own limitations. Even though these limitations do not

alter any conclusion we have drawn, we list them below not only for awareness, but also providing a basis for further test and refinement of this model, experimentally and theoretically.

In the inversion calculation exercises, $TiO_2$, MnO, Nb, Ta, U and most compatible trace elements (Sc, V, Cr, Co, Ni) yield negative concentration. They are caused by the the following reasons: 1) All $TiO_2$ data from known eclogite/pyroxenite melting experiment (PERTERMANN and HIRSCHMANN, 2003a, 2003b) are too high to be a mixing end-member for lavas from Ko'olau volcano as discussed previously. More rutile is required in those experiments to produce melts that are perfect for the enriched end-member; 2) For Mn, U, Ta, and Nb, the concentration differences between the primary melts of Loihi and parental melts of KOO-8 are very small due to only ~12±2.5% eclogite/pyroxenite melt incorporation. Therefore, the errors are very high. Nevertheless, it suggests that concentration of Nb, Ta and U of the calculated eclogite are very low; And 3), for compatible trace element Mn, Sc, V, Cr, Co, Ni, the model we use to calculate the olivine control line is not very good for these elements. Also, the calculated mixing curve (curve I) in Figure 8a is a bit away from the measured value, which is due to high $CaO/Al_2O_3$ in Loihi glasses. If we adopt $CaO/Al_2O_3$ ratio of average Mauna Loa samples, it will fit data perfectly (curve II).

## 5. DISCUSSION

### 5.1 THE SYSTEMATICS OF MIXING BETWEEN DEPLETED AND ENRICHED MELTS IN N-DIMENSIONAL COMPOSITION SPACE

We suppose there is an enriched melt of mafic material whose composition can be defined in terms of all geochemical variables examined in this study ($SiO_2$-MgO-FeO-other, where "other" could be concentration of one element/oxide or another composition vector including CaO, $Al_2O_3$, compatible or incompatible trace-element concentration),

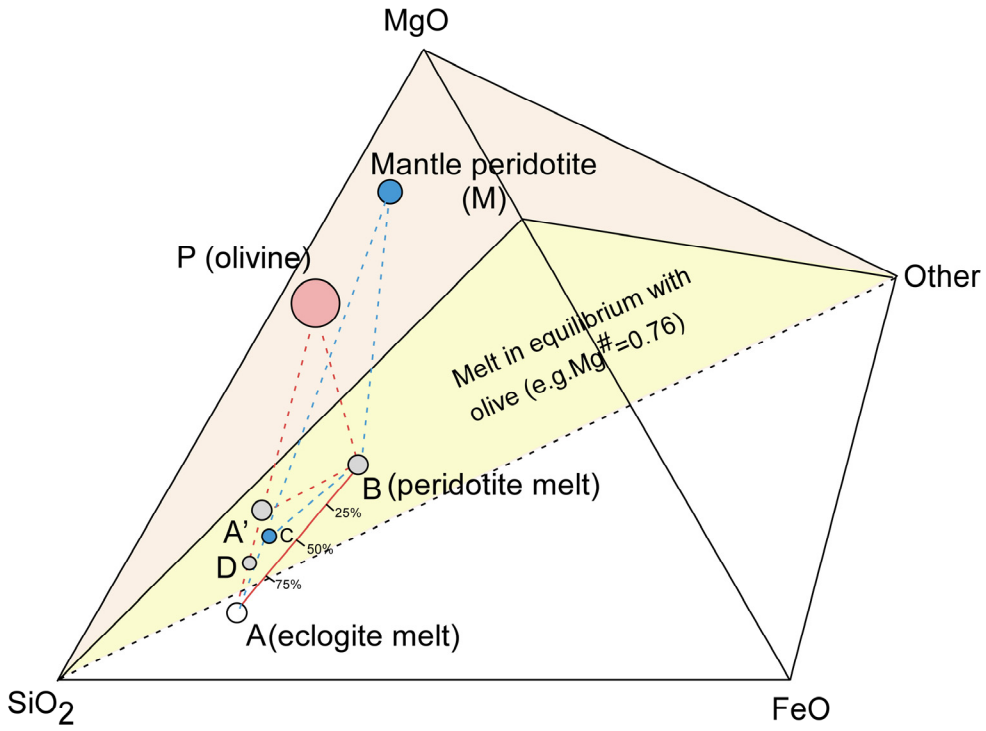


**Figure 12.** Schematic description of the mixing relationship in $SiO_2$-MgO-FeO-other space. A' and C are projections of A on $Mg^{\#}$ = 0.76 plane from P (olivines) and Mantle peridotite (M), respectively. AB, A'B and BC are mixing lines between melts.

and we designate the location of this end-member melt as point 'A' in that multi-dimensional composition space (in Figure 12). Similarly, we can define the composition of a depleted melt (point B) and its mantle peridotite source (point M) in that same space. Mixtures between these two melts lie along the line AB. Note that enriched melt, A, if similar in composition to experimental partial melts of eclogite and pyroxenite, has a $Mg^{\#}$ much lower than that in equilibrium with mantle olivine. Therefore, we also plot at point

A' (in Figure 12) the location of enriched melt after assimilating enough $Fo_{91}$ olivine (point P) to reach an $Mg^{\#}$ of 0.76 (such as might occur if eclogite or pyroxenite melt reacts with peridotite or dunite). Mixtures between this 'mantle-equilibrated' enriched melt and the peridotite melt sit on the curve A'B. It can rigorously be proven that A'B is also a straight line in any compositional space, regardless where point P is (refer to appendix). Although both AB and A'B should be properly thought of as N-dimensional where N is the number of independent compositional variables we consider (nine in our major element consideration), but in four component space, this relationship can be visualized by projecting curve (AB) from point (P) onto the plane of all compositions having $Mg^{\#}$=0.76. This projection should be linear. In reality, if a mixture on mixing line AB has a $Mg^{\#}$ close to the $Mg^{\#}$ =0.76 plane (e.g., mixing ratio of A component is less than 20%), it is in equilibrium with olivines having a composition close to point P. If one then adds this equilibrium olivine to the mixture to drive its composition to the $Mg^{\#}$ =0.76 plane (e.g., HAURI, 1996), the final projection will be linear in concentration space, sitting close to mixing line A'B. This geometric relationship can explain why we can see general linear correlations between element concentrations after back-correcting olivines to a constant $Mg^{\#}$ (e.g. = 0.76). Moreover, it can also explain the hyperbola shaped correlation between isotope or trace element ratios with corrected element concentrations (e.g., HAURI, 1996). For example, let us consider the correlation between $^{143}Nd/^{144}Nd$ vs. olivine-corrected $SiO_2$ wt. %. According to the argument we made above, Nd should linearly correlate with $SiO_2$ on the mixing line A'B -- say $[Nd] = a \times [SiO_2] + b$, where bracket means concentration, a and b are parameters. It is also well known that in a binary mixing (A' and B), isotope ratio ($^{143}Nd/^{144}Nd$) should be proportional to the

inverse of its concentration (1/[Nd]). Therefore, $^{143}Nd/^{144}Nd$ will be proportional to $1/(a\times[SiO_2]+b)$. If we plot $^{143}Nd/^{144}Nd$ vs. olivine-corrected $SiO_2$ wt%, we will still have a hyperbola shaped mixing curve. This is true for any other plot involving isotope ratio and corrected concentrations. Thus, mixing relationships observed in a suite of lavas corrected to $Mg^{\#}$=0.76 reasonably approximate those among primary melts, even if those melts had $Mg^{\#}$'s different from 0.76.

## 5.2 OTHER POSSIBLE MIXING SCENARIOS

Besides direct mixing of melts modeled in Section 4, there are other possible mixing scenarios that could produce similar geochemical diversity as manifested by Ko'olau lavas. Some key features of these processes can be shown in four component space ($SiO_2$-MgO-FeO-others, Figure 12), and can be applied to multiple component systems.

### 5.2.1 MIXING OF PERIDOTITE MELT WITH OLIVINE-BUFFERED HYBRID MELT

The first derivative is the mixing between peridotite melt (B) and a hybrid melt (D) between A and A' after eclogite melt is equilibrated with peridotic or dunitic component around MOHO. Exercises described in Section 4 cannot distinguish this process (on DB) from direct mixing (on AB). For the same melt mixture, there will be a mixing ratio difference between calculation along A'B and DB. Again, this difference will be very small if the mixture is close to B, e.g., calculation along A'B and AB for sample KOO-8 will yield ~2% difference in mixing ratio, which is the maximum for the differences between DB and AB. Nevertheless, as long as we know where A is, we can always infer A from A'. In traditional isotope ratio space, A, A' and D are even located at a similar

location. Therefore, any mixing between B and a melt (D) between A' and A is a possible scenario.

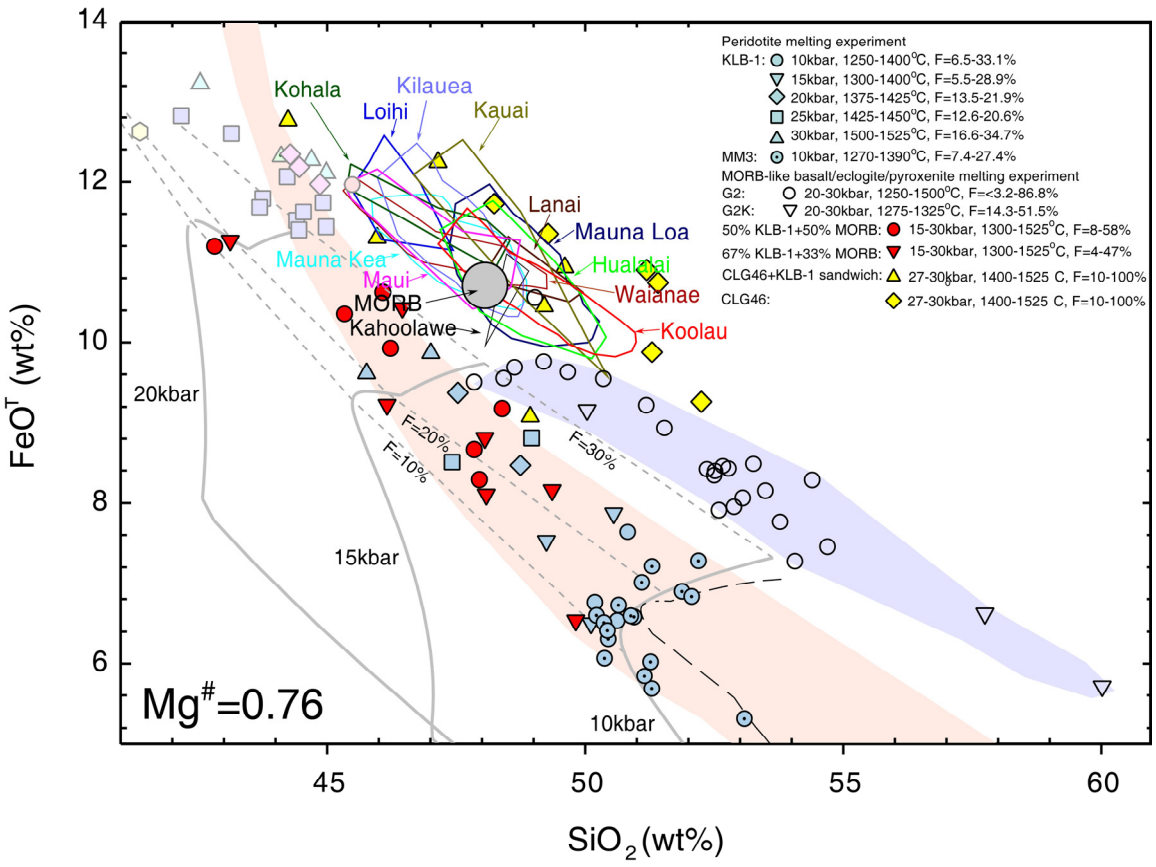


**Figure 13.** Comparison between Hawaiian lavas and melts from melting experiments: mantle peridotite melt (HIROSE and KUSHIRO, 1993; BAKER and STOLPER, 1994; BAKER et al., 1995), mantle peridotite and MORB mixtures (KOGISO et al., 1998), MORB-like eclogite/pyroxenite (PERTERMANN and HIRSCHMANN, 2003a; PERTERMANN and HIRSCHMANN, 2003b; PERTERMANN et al., 2004), and basalt or basalt-mantle peridotite sandwiches (TAKAHASHI and NAKAJIMA, 2002) are projected onto $Mg^{\#}$ = 0.76 plane by adding or removing $Fo_{91.3}$ in batch. Curves labeled by pressure and extent of melting are isobars and equal-fraction batch melts of peridotite KLB-1 using pMELTS (GHIORSO et al., 2002).

Moreover, it is also possible that the position A is non-unique in concentration space. Any melt which is lying on the plane determined by P ($Fo_{89\sim91}$) and projection A'B could be a possible end-member. We can use the geometrical arguments explained in Section 5.1 to determine which family of experimentally determined compositions of eclogite and pyroxenite melts are reasonable candidates for the enriched component sampled by Ko'olau lavas. Figure 13 plots results of this projection for compositions of silicate liquids generated experimentally by melting peridotite (HIROSE and KUSHIRO, 1993; BAKER and STOLPER, 1994; BAKER et al., 1995), peridotite-basalt mixtures (KOGISO et al., 1998) or 'sandwiches' (TAKAHASHI and NAKAJIMA, 2002), eclogite and/or pyroxenite (PERTERMANN and HIRSCHMANN, 2003a; PERTERMANN and HIRSCHMANN, 2003b; PERTERMANN et al., 2004). We also show in Figure 13 the projection for compositions of partial melts of peridotite KLB-1 at various conditions, calculated using the pMELTS algorithm (GHIORSO et al., 2002; note this model is known to predict well the composition of melts at a given melt fraction, although it overestimates the pressure corresponding to that melt fraction when pressure is over 10 kbar). Comparison of the trend for Ko'olau lavas with this set of experimental and model melts shows that candidates for the enriched component sampled by Ko'olau lavas are liquids from melting experiments performed on either MORB-like eclogite/pyroxenite or Archaean basalt CLG 46 in the pyroxenite or eclogite stability field. In this study, isotope geochemistry tests conducted in Section 4 demonstrate that melt from A200K should be very close to the real answer (A). We will discuss the second alternatives in Section 5.2.3.

### 5.2.2 MIXING OF PERIDOTITE MELT WITH PYROXENITE MELT

Another possibility is that this eclogite first interacts with mantle peridotite (M) to form pyroxenite, and later, this pyroxenite melts almost completely (thus, on AM line), and then mixes with the peridotite melt (e.g., on CB). This possibility is proposed by SOBOLEV et al., (2005), based on the following evidence and assumptions: 1) olivines from Hawaiian lavas have extremely high Ni content relative to olivines from MORB, Iceland or Gorgona at a given Fo content and among them, Ni content in olivines from Ko'olau lavas are highest in Hawaiian lavas at a given Fo content (as shown in Figures 14 and 15); 2) both eclogite melt and any mantle peridotite melt have Ni content much lower than melts supposedly in equilibrium with these olivines, such that a simple mixing model would fail. One consequence of this interaction is to reduce the mode of olivine and therefore, the bulk partition coefficient of Ni between melt and solid phase ( $D_{Ni}^{rock/melt}$ ) during melting. This mechanism has been brought up before in order to explain the correlation between Ni content in olivines and Opx abundance in mantle peridotite xenoliths from Archean cratons (KELEMEN et al., 1998). This model can explain extremely high Ni content in olivines from Ko'olau volcanoes that are associated with high $SiO_2$.

However, detailed analyses indicate that this high Ni content in olivines from Ko'olau volcanoes are also consistent with even a simple magma mixing model. In Figure 14, symbols are adopted from SOBOLEV et al., (2005), taken from GEOROC. Different curves are calculated Ni content in olivines, given the following conditions: 1) direct mixing between peridotite melt (B) with 950 ppm Ni and eclogite melt (A) with 50 ppm Ni at different mixing proportion (on AB in Figure 12); 2) using BEATTIE (1993)

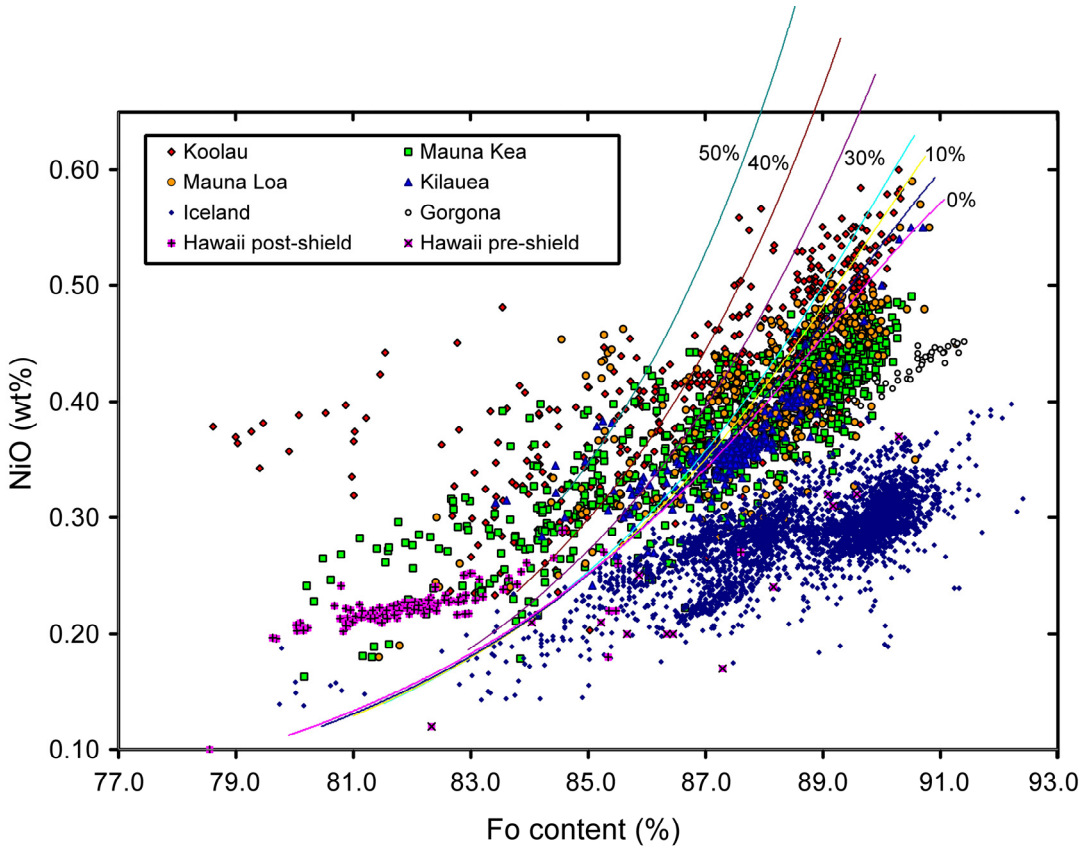


**Figure 14.** Variation of NiO wt% in olivines from Hawaii as a function of Fo content. Symbols are from SOBOLEV et al. (2005), taken from GEOROC. Solid lines are olivine control line for the mixtures after direct mixing eclogite melt and peridotite melt at variable proportion. $D^{olivine/melt}$ for Ni is from the parameterization of BEATTIE (1993).

formulation to describe partition coefficient of NiO, FeO and MgO between olivine and melt. The calculated results can describe the general pattern of NiO variation as a function of Fo content when Fo>85%. Importantly it indicates, at a given Fo number (at Fo > 84% in Figure 14), mixtures with more eclogite component will have high Ni content. This rather surprising result can be explained by the dependence of $D_{Ni}^{rock/melt}$ on melt composition. It is a well-know fact that $D_{Ni}^{rock/melt}$ is roughly proportional to 1/MgO because Ni and Fe have to compete with Mg for the distribution into cation sites in

olivine (HART and DAVIS, 1978; BEATTIE, 1993). An increase in $SiO_2$ content will also help in the formation of olivines. Therefore, low MgO and high $SiO_2$ can significantly facilitate Ni partitioning into olivines. This dependency of $K_D$ on melt composition dominates over the contrary decrease of Ni concentration in the melt after mixing. For comparison, we also investigated a special case as shown in Figure 15, where we use the eclogite melt (A) to assimilate ~20% mantle peridotite (point M) with 2080 ppm Ni to reach $Mg^{\#} = 0.77$ (point C), then mix this mixture with mantle peridotite melt (B) along BC line. In this case, the mixture has more Ni in the liquid, e.g., 30 % mixing of point C with peridotite melt (B) will have 140 ppm increase in the mixture, but there is ~ 0.03 wt% decrease in NiO of olivines first crystallized from the liquid compared with mixing on AB at similar mixing ratio. In this second case in Figure 15, one interesting feature is the cross-over point at $Fo_{88.5}$, from which the relative sequence of Ni enrichment for olivines from Hawaiian lavas reverses at a given Fo number. This point reflects the switch from partition-coefficient-controlled partitioning to Ni concentration-controlled partitioning between olivine and melts. The position of this point depends on the relative difference in the chemistry between the two mixing component (e.g. MgO, NiO, $SiO_2$ and FeO concentrations), i.e., if the difference is small, this cross-over point will be closer to the first olivine crystallized. Because the difference in melt chemistry between our first exercise (Figure 14) is much larger for the second one (in Figure 15), the cross-over point in the first case is at about $Fo_{84}$. In principle, this effect of the increase in partition coefficient due to the melt chemistry could be tested by other olivine-compatible trace elements such as Co, Sc and Yb.

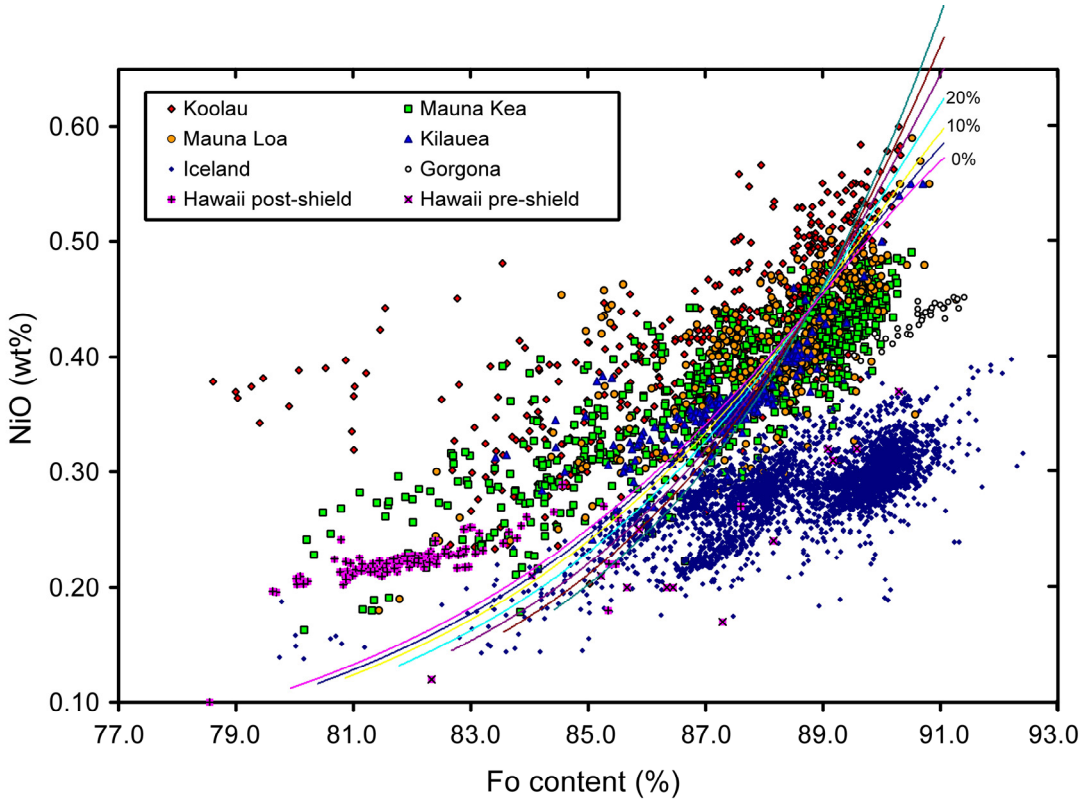


**Figure 15.** Variation of NiO wt% in olivines from Hawaii as a function of Fo content. Solid lines are olivine control line for the mixtures after eclogite melt has reach $Mg^{\#}$ = 0.77 by reacting with mantle peridotite.

Also as noted in Figure 14 and 15, the calculated curves are steeper than Hawaiian olivines. This feature stands out at Fo < 86%, where data from Hawaiian olivines have only a slight decrease. These deviations exist even when a different Ni partitioning formulation is used (HART and DAVIS, 1978; BEATTIE, 1993; Baker, personal communication), and can be explained by any combination of the following possible reasons: 1) partition coefficient at low MgO concentration normally has larger errors due to the difficulty in controlling the experiment, and it is hard to calibrate; 2) when liquid phase is multiply-saturated by plagioclase or pyroxene at low MgO wt.%, Ni concentration in the liquid phase tends to decrease slowly due to the precipitation of these

phases which do not significantly concentrate Ni; and 3) the concentration of sulphur in the melt significantly increases after Fo < 86%; a recent study shows that sulphur plays an important role in Ni partitioning between olivine and melts by competing with olivine to form a Ni-S complex in melts (LI et al., 2003). Therefore, these discrepancies between model and observation imply that our calculated Ni content in the primary melts can be overestimated by a factor of ~3 after back-correcting olivine fractionation. This can explain why we cannot get reasonable estimates for compatible trace elements discussed in Section 4.

### 5.2.3 SOURCE-MIXING, MELTING OF AN INHOMOGENEOUS SOURCE

A third possibility of the mixing is that eclogite melt first reacts with mantle peridotite and then freezes down through producing a series of pyroxenite and peridotite mixtures (on MC and close to M). Later, these inhomogeneous mixtures melt at different degrees depending on pressure and temperature conditions. KOGISO et al. (1998) have conducted experiments to melt the mixture of mantle peridotite and basalt with average MORB composition. These experiments indicate that alkali-basalts from Ocean-Island-Basalt could be produced by melting an inhomogeneous source at a much lower pressure than by melting pyrolitic peridotite. TAKAHASHI and NAKAJIMA (2002) later experimentally studied the melting behavior of Archaean basalt (high FeO, but low $Al_2O_3$ and CaO) and basalt-peridotite "sandwiches". Melt of Archaean basalt and mantle peridotite sandwiches can produce parental magmas of some alkalitic and tholeiitic lavas from Hawaii, but only 80~100% melting of this Archaean basalt could possibly serve as the $SiO_2$-rich end member of Ko'olau lavas as shown in Figure 13 and discussed in Section 5.2.1. However,

it is still unclear how isotope and trace element composition will evolve during progressive melting of peridotite-basalt mixtures (i.e., how far away those melting vectors are from the plane determined by MBAC in Figure 13 in any compositional space). However, it is conceivable that this process is undistinguishable from the magma mixing if the melting degree is large (e.g., >30%) for incompatible elements and some isotope compositions. More systematic experiments and thermodynamic modeling are needed to explore the consequences of melting these inhomogeneous sources.

## 6. CONCLUSIONS

Across all three sample suites (KSDP drill core, Makapu`u subaerial lavas and submarine land slides), $\delta^{18}O$ values of olivines correlate with trace element and radiogenic isotope compositions of host lavas, defining a compositional continuum from a high-$\delta^{18}O$, extremely enriched end member, toward a more normal $\delta^{18}O$, 'Mauna Loa-like' composition.

We interpret this trend as reflecting mixing between partial melts of high-$\delta^{18}O$ components and normal-$\delta^{18}O$ components of the Hawaiian plume, and have constructed a model to simultaneously explain the oxygen isotope, major element, trace element and radiogenic isotope variations defined by this trend. This model indicates that the Ko'olau shield-building lavas are mixtures of 75-100% melt of mantle peridotite with 0-25% melt of eclogite, the protolith of which is Mid-Ocean Ridge Basalt (MORB) with Depleted Mantle Model (DMM) age of at least 1.8±0.3 billions years. $\delta^{18}O$ values of this eclogite component can be predicted to be 11.3 ± 1.5‰, implying it is an upper crustal (layer 1 or 2) basalt or gabbro with a low-temperature alteration history, containing a small amount

of sediment. This basalt also experienced partial melting before forming eclogite and therefore left a depleted LIL pattern.

Detailed modeling analyses show that this magma mixing model is consistent with mixing directly and indirectly between melts. High NiO wt% in olivines from Ko'olau volcano is better explained by an increase in partition coefficient due to changes in magma chemistry, rather than by an increase in Ni concentration in the source. Source mixing is also a possible scenario, but not explored here due to limited knowledge about the melting behavior of this inhomogeneous source. At high temperature when both mantle peridotite and eclogite melt together, the eclogite component tends to have less mixing proportion because of the relative volume contrast in the source. When the plume cools, the eclogite component will increase in the mixing proportion when less mantle peridotite is able to melt. This can explain why we can only see a large eclogite component in the very late stage of Ko'olau shield. Although it is still not clear how large this piece of oceanic crust is in the Hawaiian plume source, it certainly affects the geochemistry of some other 'Loa trend' volcanoes, e.g., Mauna Loa and Kahoolawe.

## ACKNOWLEDGEMENTS

We would like to thank Ed Stolper, Michael Baker, Alexander Sobolev, Huiyu Li, and Paula Smith for inspiration and helpful discussion, and Zhongyuan Ren for sending us Hawaiian samples for analysis. This research is funded by NSF.

**REFERENCES**

Baker M. B., Hirschmann M. M., Ghiorso M. S., and Stolper E. M. (1995) Compositions of near-solidus peridotite melts from experiments and thermodynamic calculations. *Nature* **375**(6529), 308-311.

Baker M. B. and Stolper E. M. (1994) Determining the composition of high-pressure mantle melts using diamond aggregates. *Geochimica et Cosmochimica Acta* **58**(13), 2811-2827.

Beattie P. (1993) On the occurrence of apparent non-henry law behavior in experimental partitioning studies. *Geochimica et Cosmochimica Acta* **57**(1), 47-55.

Blichert-Toft J., F.A. F., and Albarede F. (1999) Hf isotope evidence for pelagic sediments in the source of Hawaiian basalts. *Science* **285**(6), 879-882.

Byers C. D., Garcia M. O., and Muenow D. W. (1985) Volatiles in pillow rim glasses from Loihi and Kilauea volcanos, Hawaii. *Geochimica et Cosmochimica Acta* **49**(9), 1887-1896.

Dixon J. E. and Clague D. A. (2001) Volatiles in basaltic glasses from Loihi seamount, Hawaii: Evidence for a relatively dry plume component. *Journal Of Petrology* **42**(3), 627-654.

Ducea M., Sen G., Eiler J., and Fimbres J. (2002) Melt depletion and subsequent metasomatism in the shallow mantle beneath Ko'olau volcano, Oahu (Hawaii). *Geochemistry Geophysics Geosystems* **3**, art. no.-1015.

Eiler J. M. (2001) Oxygen isotope variations of basaltic lavas and upper mantle rocks. *Reviews in Mineralogy & Geochemistry* **43**, 319-364.

Eiler J. M., Crawford A., Elliott T., Farley K. A., Valley J. W., and Stolper E. M. (2000b) Oxygen isotope geochemistry of oceanic-arc lavas. *Journal of Petrology* **41**(2), 229-256.

Eiler J. M., Farley K. A., Valley J. W., Hofmann A. W., and Stolper E. M. (1996a) Oxygen isotope constraints on the sources of Hawaiian volcanism. *Earth and Planetary Science Letters* **144**(3-4), 453-467.

Eiler J. M., Schiano P., Kitchen N., and Stolper E. M. (2000a) Oxygen isotope evidence for recycled crust in the sources of mid-ocean ridge basalts. *Nature* **403**, 530–534.

Eiler J. M., Valley J. W., and Stolper E. M. (1996b) Oxygen isotope ratios in olivine from the Hawaii Scientific Drilling Project. *Journal of Geophysical Research-Solid Earth* **101**(B5), 11807-11813.

Fekiacova Z. and Abouchami W. (2003) Pb isotopic evolution of Ko'olau volcano (Oahu, Hawaii). *Eos Trans. AGU* **84**(46), Fall Meet. Suppl., Abstract V32A-0991.

Frey F. A., Garcia M. O., and Roden M. F. (1994) Geochemical characteristics of Ko'olau volcano - Implications of intershield geochemical differences among Hawaiian volcanos. *Geochimica et Cosmochimica Acta* **58**(5), 1441-1462.

Garcia M. O. (2002) Submarine picritic basalts from Ko'olau volcanoe, Hawaii: implications for parental magma compositions and mantle source. In *Hawaiian volcanoes: Deep underwater perspectives*, Vol. 128, pp. 391-401. American Geophysical Union.

Garcia M. O., Jorgenson B. A., Mahoney J. J., Ito E., and Irving A. J. (1993) An evaluation of temporal geochemical evolution of Loihi summit lavas - Results

from Alvin submersible dives. *Journal of Geophysical Research-Solid Earth* **98**(B1), 537-550.

Ghiorso M. S., Hirschmann M. M., Reiners P. W., and Kress V. C. (2002) The pMELTS: A revision of MELTS for improved calculation of phase relations and major element partitioning related to partial melting of the mantle to 3 GPa. *Geochemistry Geophysics Geosystems* **3**, art. no.-1030.

Hart S. R. and Davis K. E. (1978) Nickel partitioning between olivine and silicate melt. *Earth and Planetary Science Letters* **40**(2), 203-219.

Haskins E. H. and Garcia M. O. (2004) Scientific drilling reveals geochemical heterogeneity within the Ko'olau shield, Hawai'i. *Contributions to Mineralogy and Petrology* **147**, 162-188.

Hauri E. H. (1996) Major-element variability in the Hawaiian mantle plume. *Nature* **382**(6590), 415-419.

Herzberg C. and Zhang J. Z. (1996) Melting experiments on anhydrous peridotite KLB-1: Compositions of magmas in the upper mantle and transition zone. *Journal of Geophysical Research-Solid Earth* **101**(B4), 8271-8295.

Hirose K. and Kushiro I. (1993) Partial melting of dry peridotites at high-pressures - Determination of compositions of melts segregated from peridotite using aggregates of diamond. *Earth and Planetary Science Letters* **114**(4), 477-489.

Hirschmann M. M. and Stolper E. M. (1996) A possible role for garnet pyroxenite in the origin of the "garnet signature" in MORB. *Contributions to Mineralogy and Petrology* **124**(2), 185-208.

Hofmann A. W. (1988) Chemical differentiation of the earth - the relationship between mantle, continental-crust, and oceanic-crust. *Earth and Planetary Science Letters* **90**(3), 297-314.

Hole M. J., Saunders A. D., Marriner G. F., and Tarney J. (1984) Subduction of pelagic sediments: Implications for the origin of Ce-anomalous basalts from the Mariana Island. *Journal of the Geological Society* **141**(3), 453-472.

Huang S. and Frey F. A. (2005) Temporal geochemical variation within the Ko'olau shield: a trace element perspective (Submitted to Contributions of Minealogy and Petrology).

Jackson M. C., Wilmoth R. A., and Frey F. A. (1999) Geology and petrology of basaltic lavas and dikes of Ko'olau volcano in the trans-Ko'olau exploratory tunnels, Oahu, Hawaii. *Bulletin of Volcanology* **60**, 381-401.

Kelemen P. B., Hart S. R., and Bernstein S. (1998) Silica enrichment in the continental upper mantle via melt/rock reaction. *Earth and Planetary Science Letters* **164**(1-2), 387-406.

Kogiso T., Hirose K., and Takahashi E. (1998) Melting experiments on homogeneous mixtures of peridotite and basalt: application to the genesis of ocean island basalts. *Earth and Planetary Science Letters* **162**, 45-61.

Lassiter J. C. and Hauri E. H. (1998) Osmium-isotope variations in Hawaiian lavas: evidence for recycled oceanic lithosphere in the Hawaiian plume. *Earth and Planetary Science Letters* **164**(3-4), 483-496.

Li C., Ripley E. M., and Mathez E. A. (2003) The effect of S on the partitioning of Ni between olivine and silicate melt in MORB. *Chemical Geology* **201**(3-4), 295-306.

Mattey D., Lowry D., and Macpherson C. (1994) Oxygen-isotope composition of mantle peridotite. *Earth and Planetary Science Letters* **128**(3-4), 231-241.

Moore J. G. and Clague D. A. (2002) Mapping the Nuuanu and Wailau landslides in Hawaii. In *Hawaiian Vlcanoes: Deep Underwater Perspectives*, Vol. 128, pp. 223-244. American Geophysical Union.

Norman M. D. and Garcia M. O. (1999) Primitive magmas and source characteristics of the Hawaiian plume: Petrology and geochemistry of shield picrites. *Earth and Planetary Science Letters* **168**(1-2), 27-44.

Norman M. D., Garcia M. O., Kamenetsky V. S., and Nielsen R. L. (2002) Olivine-hosted melt inclusions in Hawaiian picrites: Equilibration, melting, and plume source characteristics. *Chemical Geology* **183**(1-4), 143-168.

Pertermann M., Hirschmann M., Hametner K., Guenther D., and Schmidt M. (2004) Experimental determination of trace element partitioning between garnet and silica-rich liquid during anhydrous partial melting of MORB-like eclogite. *Geochemistry Geophysics Geosystems* **5,** Q05A01.

Pertermann M. and Hirschmann M. M. (2003a) Anhydrous partial melting experiments on MORB-like eclogite: Phase relations, phase compositions and mineral-melt partitioning of major elements at 2-3 GPa. *Journal of Petrology* **44**(12), 2173-2201.

Pertermann M. and Hirschmann M. M. (2003b) Partial melting experiments on a MORB-like pyroxenite between 2 and 3 GPa: Constraints on the presence of pyroxenite in basalt source regions from solidus location and melting rate. *Journal of Geophysical Research-Solid Earth* **108**(B2), art. no.-2125.

Press W. H., Teukolsky S. A., Vetterling W. T., and Flannery B. P. (2002) Numerical recipes in C++: The art of scientific computing. 1002 p.

Putirka K. (1999) Melting depths and mantle heterogeneity beneath Hawaii and the East Pacific Rise: Constraints from Na/Ti and rare earth element ratios. *Journal of Geophysical Research-Solid Earth* **104**(B2), 2817-2829.

Roden M. F., Trull T., Hart S. R., and Frey F. A. (1994) New He, Nd, Pb, and Sr isotopic constraints on the constitution of the Hawaiian plume - Results from Ko'olau volcano, Oahu, Hawaii, USA. *Geochimica et Cosmochimica Acta* **58**(5), 1431-1440.

Salters. (2005) Nd-Hf study of KSDP (in preparation).

Sharp Z. D. (1990) A laser-based microanalytical method for the *in situ* determination of oxygen isotope ratios of silicates and oxides. *Geochimica et Cosmochimica Acta* **54**(5), 1353-1357.

Shinozaki K., Ren Z.-Y., and Takahashi E. (2002) Geochemical and petrological characteristics of Nuuanu and Wailau landslide blocks. In *Hawaiian volcanoes: Deep underwater perspectives*, Vol. 128, pp. 297-310. American Geophysical Union.

Sobolev A. V., Hofmann A. W., and Nikogosian I. K. (2000) Recycled oceanic crust observed in 'ghost plagioclase' within the source of Mauna Loa lavas. *Nature* **404**(6781), 986-990.

Sobolev A. V., Hofmann A. W., Sobolev S. V., and Nikogosian I. K. (2005) An olivine free mantle source of Hawaiian shield basalts. *Nature* **434**, 590-597.

Takahashi E. and Nakajima K. (2002) Melting procecss in the Hawaiian plume: An experimental study. In *Geophyical Monograph*, Vol. 128, pp. 403-418.

Tanaka R., Nakamura E., and Takahashi E. (2002) Geochemical evolution of Ko'olau volcano, Hawaii. In *Hawaiian volcanoes: Deep underwater perspectives*, Vol. 128, pp. 311-332. American Geophysical Union.

Valley J. W., Kitchen N., Kohn M. J., Niendorf C. R., and Spicuzza M. J. (1995) UWG-2, a garnet standard for oxygen isotope ratios: Strategies for high precision and accuracy with laser heating. *Geochimica et Cosmochimica Acta* **59**(24), 5223-5231.

Wang Z., Kitchen N. E., and Eiler J. M. (2003) Oxygen isotope geochemistry of the second HSDP core. *Geochemistry Geophysics Geosystems* **4**, art. no.-8712.

Weinstein J. P., Fodor R. V., and Bauer G. R. (2004) Ko'olau shield basalt as xenoliths entrained during rejuvenated- stage eruptions: Perspectives on magma mixing. *Bulletin of Volcanology* **66**(2), 182-199.

## Appendices

### Mixing relationship in $SiO_2$-FeO-MgO-other space

As shown in Figure A1, suppose A, B and M are the flowing composition vector, where M is a mixture of A and B (on AB):

$$A=\begin{Bmatrix} A_{SiO_2} \\ A_{FeO} \\ A_{MgO} \\ A_{other} \end{Bmatrix}; B=\begin{Bmatrix} B_{SiO_2} \\ B_{FeO} \\ B_{MgO} \\ B_{other} \end{Bmatrix}; M=\begin{Bmatrix} M_{SiO_2} \\ M_{FeO} \\ M_{MgO} \\ M_{other} \end{Bmatrix} \tag{4.1}$$

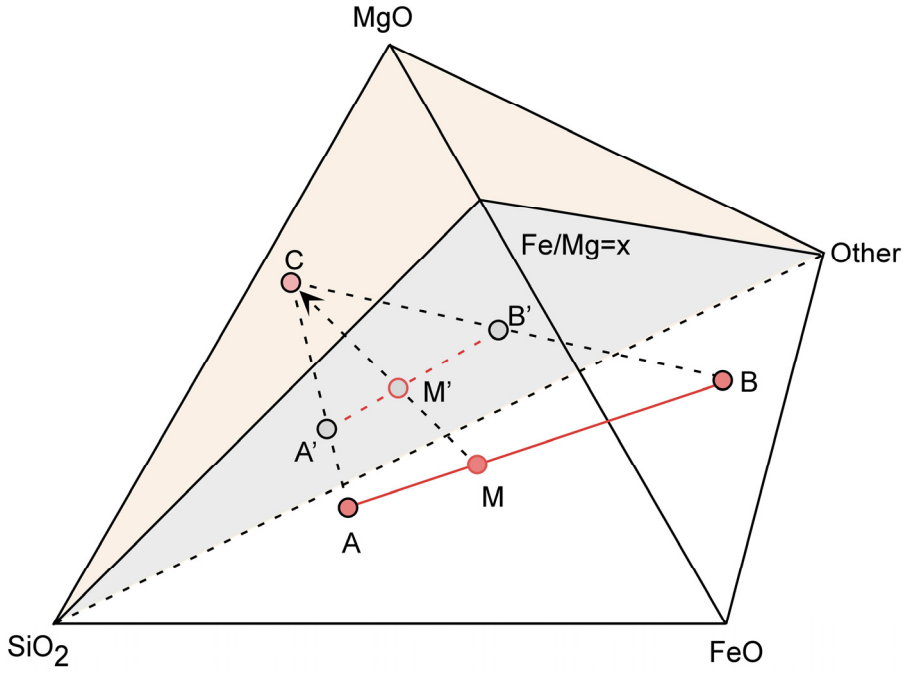


**Figure A1**: Schematic relationship of projection of a line (AB) from a point (C) to a plane (constant Fe/Mg) in $SiO_2$-FeO-MgO-other space.

and they shall satisfy the following mixing relationship:

$$(1-F)A+FB=M \tag{4.2}$$

where F is the proportion of B component (eclogite melt). We can project A, B and M to A', B' and M' which has a constant FeO/MgO ratio $x$ by adding a component C (C can be $Fo_{91.3}$ or rocks) with the following composition by amount of $y$:

$$C = \begin{Bmatrix} C_{SiO_2} \\ C_{FeO} \\ C_{MgO} \\ C_{other} \end{Bmatrix} \qquad (4.3)$$

Then $y$ for A→A', B→B' and M→M' can be described using the following expression:

$$A' = \frac{1}{1+y_A} A + \frac{y_A}{1+y_A} C; \text{where } y_A = \frac{A_{FeO} - xA_{MgO}}{xC_{MgO} - C_{FeO}} \qquad (4.4)$$

$$B' = \frac{1}{1+y_B} B + \frac{y_B}{1+y_B} C; \text{where } y_B = \frac{B_{FeO} - xB_{MgO}}{xC_{MgO} - C_{FeO}} \qquad (4.5)$$

$$M' = \frac{1}{1+y_M} M + \frac{y_M}{1+y_M} C; \text{where } y_M = \frac{M_{FeO} - xM_{MgO}}{xC_{MgO} - C_{FeO}} \qquad (4.6)$$

Eqn (4.6) can be simplified as follows:

$$y_M = \frac{\left[(1-F)A_{FeO} + FB_{FeO}\right] - x\left[(1-F)A_{MgO} + FB_{MgO}\right]}{xC_{MgO} - C_{FeO}} = (1-F)y_A + Fy_B \qquad (4.7)$$

If there exists a F' satisfying the following equation for any given F, then we can conclude that the projection is linear:

$$(1-F')A' + F'B' = M' \qquad (4.8)$$

Now it is a matter to look for whether there exists such a F'. If eqn (4.8) holds, then:

$$(1-F')\left(\frac{1}{1+y_A} A + \frac{y_A}{1+y_A} C\right) + F'\left(\frac{1}{1+y_B} B + \frac{y_B}{1+y_B} C\right) = \frac{1}{1+y_M} M + \frac{y_M}{1+y_M} C \qquad (4.9)$$

$$\frac{(1-F')}{1+y_A} A + \frac{F'}{1+y_B} B + \left(\frac{y_A(1-F')}{1+y_A} + \frac{F'y_B}{1+y_B}\right) C = \frac{(1-F)}{1+y_M} A + \frac{F}{1+y_M} B + \frac{y_M}{1+y_M} C \qquad (4.10)$$

Since A, B and C are arbitrary choices, it requires the following expression to hold in order for eqn (4.8) to be true:

$$\begin{cases} \dfrac{(1-F')}{1+y_A} = \dfrac{(1-F)}{1+y_M} \\ \dfrac{F'}{1+y_B} = \dfrac{F}{1+y_M} \\ \left( \dfrac{y_A(1-F')}{1+y_A} + \dfrac{y_B F'}{1+y_B} \right) = \dfrac{y_M}{1+y_M} \end{cases} \tag{4.11}$$

In fact, this equation array is redundant, i.e., (1st eqn + 2nd eqn) above could automatically give the third one. From the 1st equation, we can solve F':

$$F' = 1 - \frac{(1-F)(1+y_A)}{1+y_M} = \frac{1+(1-F)y_A + Fy_B - (1-F) - (1-F)y_A}{1+y_M} = \frac{F(1+y_B)}{1+y_M} \tag{4.12}$$

As we see, this F' also satisfies the 2nd equation in eqn 4.11. Therefore, eqn (4.13) is the solution for all equations in eqn (4.11). It means that we can find a F' which satisfies eqn (4.8) for any given F. More importantly, this demonstrates that the projection is linear in any composition space, regardless of the selection of *x* (= FeO/MgO), component A, B and C (even if C is not olivine).

# PART 2.

# THEORETICAL STUDY ON EQUILIBRIUM THERMODYNAMICS OF MULTIPLY-SUBSTITUTED ISOTOPOLOGUES

# CHAPTER 5

# EQUILIBRIUM THERMODYNAMICS OF MULTIPLY-SUBSTITUTED ISOTOPOLOGUES OF MOLECULAR GASES

**Zhengrong Wang, Edwin A. Schauble*, and John M. Eiler**

Division of Geological and Planetary Sciences, M/C 100-23,

California Institute of Technology, Pasadena, CA 91125, USA

(*wzhr@gps.caltech.edu*, *schauble@ess.ucla.edu*, *eiler@gps.caltech.edu*)

*(Published in Geochimica et Cosmochimica Acta, Vol. 68, No. 23, pp. 4779–4797, 2004)*

---

* Present address: Department of Earth and Space Sciences, P.O. Box 951567, UCLA, Los Angeles, CA 90095-1567

**ABSTRACT**

Isotopologues of molecular gases containing more than one rare isotope (multiply-substituted isotopologues) can be analyzed with high precision ($1\sigma < 0.1$ ‰), despite their low natural abundances (~ ppm to ppt in air), and can constrain geochemical budgets of natural systems. We derive a method for calculating abundances of all such species in a thermodynamically equilibrated population of isotopologues, and present results of these calculations for $O_2$, CO, $N_2$, NO, $CO_2$ and $N_2O$ between 1000 and 193 to 77 K. In most cases, multiply-substituted isotopologues are predicted to be enriched relative to stochastic (random) distributions by ca. 1 to 2 per mil at earth-surface temperatures. This deviation, defined as $\Delta_i$ for isotopologue $i$, generally increases linearly with 1/T at temperatures ≤ 500 K. An exception is $N_2O$, which shows complex temperature dependences and 10's of per-mil enrichments or depletions of abundances for some isotopologues. These calculations provide a basis for discriminating between fractionations controlled by equilibrium thermodynamics and other sorts of isotopic fractionations in the budgets of atmospheric gases. Moreover, because abundances of multiply-substituted isotopologues in thermodynamically equilibrated populations of molecules vary systematically with temperature, they can be used as geothermometers. Such thermometers are unusual in that they involve homogeneous rather than heterogeneous equilibria (e.g., isotopic distribution in gaseous $CO_2$ alone, rather than difference in isotopic composition between $CO_2$ and co-existing water). Also, multiple, independent thermometers exist for all molecules having more than one multiply-substituted isotopologue (e.g., thermometers based on abundances of $^{18}O^{13}C^{16}O$ and

$^{18}O^{12}C^{18}O$ are independent). Thus, temperatures estimated by this method can be tested for internal consistency.

## 1. INTRODUCTION

Stable isotope geochemistry is principally concerned with bulk isotopic compositions of natural materials (e.g., $\delta^{13}C$ or $\delta^{18}O$ values). In gases, these bulk compositions effectively depend only on the abundances of molecules containing one rare isotope, hereafter referred to as singly-substituted isotopologues (e.g., $^{13}C^{16}O_2$ or $^{18}O^{12}C^{16}O$). However, there also exist molecules having more than one rare isotope, hereafter referred to as multiply-substituted isotopologues (e.g., $^{18}O^{13}C^{16}O$). UREY (1947) and BIGELEISEN and MAYER (1947) recognized that multiply-substituted isotopologues have unique thermodynamic properties, different from both isotopically normal and singly-substituted isotopologues of the same molecule. Similarly, the kinetic theory of gases predicts that multiply substituted isotopologues undergo distinctive fractionations during processes such as diffusion or gravitational settling (PRESENT, 1958; KAYE, 1987 and references therein), and it seems likely to us that they also exhibit distinctive kinetic fractionations during metabolic or photochemical reactions. It follows that distributions of multiply substituted isotopologues in nature could provide unique constraints on geological, geochemical and cosmochemical processes. Similar statements could be made about distributions of rare isotopes within condensed phases, although calculation and analysis of such isotopic 'clumps' involve several difficulties beyond those encountered with gaseous molecules. We intend to address them in the near future, but consider them beyond the scope of this paper.

The geochemistry of singly-substituted stable isotopologues is a large and diverse field, but virtually nothing is known about the natural abundances of their multiply-substituted relatives. We suspect this is because commonly available gas-source mass spectrometers do not provide meaningful measurements of abundances of these very rare species, and in the absence of such data, there has been little incentive to explore their geochemistry. EILER and SCHAUBLE (2004) report precise (sub-0.1 ‰) measurements of synthetic and atmospheric $^{18}O^{13}C^{16}O$ at natural isotopic abundances. These data both document the existence of anomalies and variations in the abundances of multiply-substituted isotopologues, and more generally, demonstrate a set of techniques that could also be used to study multiply-substituted $O_2$, $N_2$, CO, NO, $N_2O$ and perhaps other gases. These techniques do not appear to be appropriate for precise analysis of multiply deuterated molecules (e.g., $D_2$ or $CH_2D_2$). Therefore, although such analyses might become possible in the future, we will not consider these species in this study.

Theory describing partition functions of multiply-substituted isotopologues was derived long ago (UREY, 1947; BIGELEISEN and MAYER, 1947), but has not been systematically evaluated. This theoretical framework is a prerequisite for applied study because it provides a context for interpreting measured abundances of these species. This theory is particularly useful for recognizing and interpreting isotopic variations caused by equilibrium thermodynamics, much as calculations by RICHET et al. (1977) provide a context for interpreting differences in bulk stable isotope composition between different molecular gases. In this paper, we develop a method for calculating the relative abundances of all stable isotopologues of molecular gases based on principles of statistical thermodynamics and various matrix algebra operations. We also combine that

method with existing spectroscopic data to calculate expected abundances of isotopologues of thermodynamically equilibrated populations of $N_2$, $O_2$, CO, NO, $CO_2$, and $N_2O$ between 1000 and 193 to 77 K.

## 2. METHODOLOGY

In order to calculate the abundances of all isotopologues of a given molecule at thermodynamic equilibrium and a specified temperature, we: (1) define the set of possible isotopologues for that molecule; (2) select a subset of these isotopologues that can uniquely define the bulk isotopic composition of a given population of molecules (e.g., its $^{18}O/^{16}O$ ratio, including contributions from all isotopologues); (3) define the set of independent isotope exchange reactions between all isotopologues; (4) use principles of statistical thermodynamics to evaluate the equilibrium constants of those reactions as functions of temperature (BIGELEISEN and MAYER, 1947; RICHET et al., 1977; O'NEIL, 1986); and, finally, (5) calculate the proportions of all possible isotopologues that are consistent with both the bulk isotopic composition and the calculated equilibrium constants. Most steps of this algorithm make use of widely known mathematical principles and are defined and illustrated by example in Section 2.1. Evaluation of equilibrium constants (step 4) involves principles of physical chemistry that are less widely understood and are described separately in Section 2.2.

### 2.1 ALGORITHM

It is relatively straightforward to calculate the abundances of multiply-substituted isotopologues of diatomic molecules of elements having only two isotopes. For example,

A

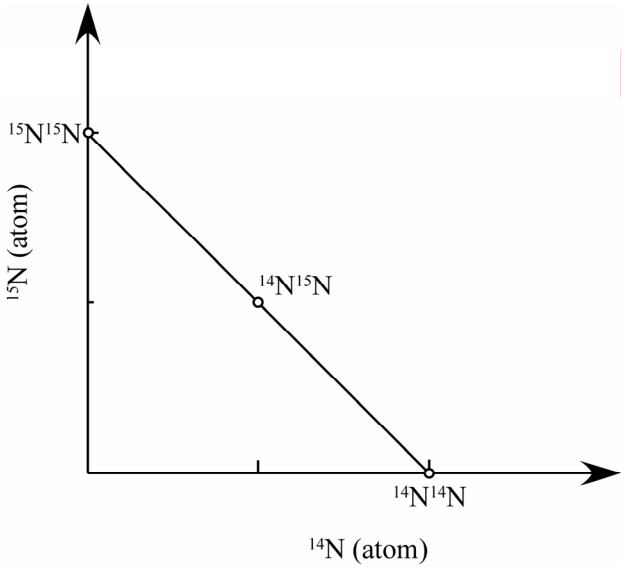


B

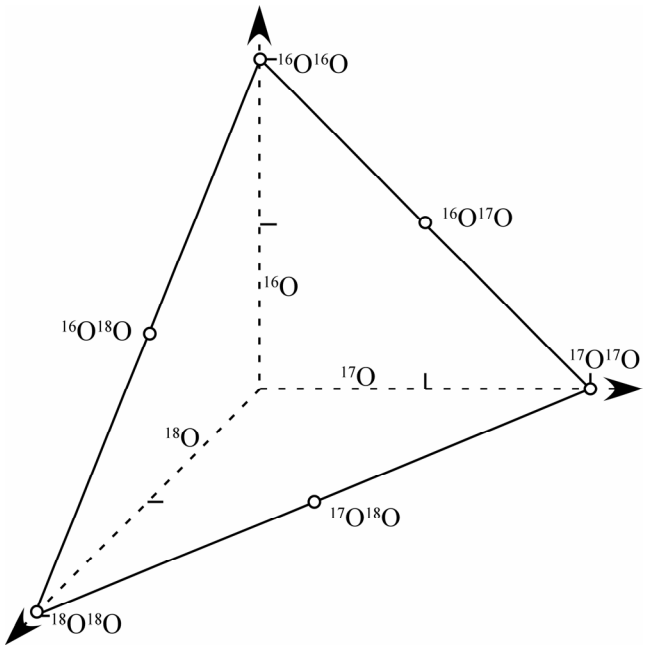


Figure 1. A: Projection of the composition of isotopologues of $N_2$ into the composition space $^{14}N$-$^{15}N$; note all isotopologues of $N_2$ lie on a straight line. B: Projection of composition of isotopologues of $O_2$ into the composition space $^{16}O$-$^{17}O$-$^{18}O$; note all isotopologues of $O_2$ lie on a plane.

there is only one isotope exchange reaction involving the three stable isotopologues of molecular nitrogen:

$$^{14}N^{14}N + {}^{15}N^{15}N \overset{K}{\rightleftharpoons} 2^{14}N^{15}N \qquad (5\text{-}1)$$

and at equilibrium, proportions of these three isotopologues are uniquely defined by the equilibrium constant for this reaction ($K$), the known bulk isotopic composition of that population (i.e., its $^{15}N/^{14}N$ ratio), and the equations describing isotopic mass balance in this system (i.e., $n_{^{14}N} = n_{^{14}N^{15}N} + 2n_{^{14}N^{14}N}$, and $n_{^{15}N} = n_{^{14}N^{15}N} + 2n_{^{15}N^{15}N}$, where $n_i$ is the number of molecules of isotopologue $i$).

However, molecules containing three or more atoms and/or containing elements with more than two isotopes have several independent isotope exchange reactions, each of which has an equilibrium constant that constrains the proportions of isotopologues. These systems also have only one possible distribution of isotopologues when thermodynamically equilibrated at a given temperature, but that distribution is less easy to infer by inspection. We developed a method for handling such systems based on Gauss-Jordan reduction of a matrix. This method is inspired by composition-space analysis commonly used in petrology (THOMPSON, 1982).

We first project isotopic composition of every isotopologue of a molecule of interest into the composition space defined by the isotopes that molecule can contain. Figures 1A and B illustrate examples of projections of isotopologues of $N_2$ into the composition space $^{14}N$-$^{15}N$ and of $O_2$ into the composition space $^{16}O$-$^{17}O$-$^{18}O$. Molecules containing five or more isotopologues (e.g., CO, NO, $CO_2$, and $N_2O$) cannot easily be illustrated in such plots, but follow the same principles. All such projections can be formulated as matrices of simultaneous linear equations. For example, the stable isotopes making up

$CO_2$, $^{12}C$, $^{13}C$, $^{16}O$, $^{17}O$ and $^{18}O$, can be used to define a five end member composition space, and the twelve possible isotopologues of $CO_2$ can be projected into that space using the set of linear equations making up the following matrix:

$$\begin{pmatrix} {}^{16}O{}^{12}C{}^{16}O \\ {}^{16}O{}^{13}C{}^{16}O \\ {}^{16}O{}^{12}C{}^{17}O \\ {}^{16}O{}^{12}C{}^{18}O \\ {}^{16}O{}^{13}C{}^{17}O \\ {}^{17}O{}^{12}C{}^{17}O \\ {}^{16}O{}^{13}C{}^{18}O \\ {}^{17}O{}^{12}C{}^{18}O \\ {}^{17}O{}^{13}C{}^{17}O \\ {}^{18}O{}^{12}C{}^{18}O \\ {}^{17}O{}^{13}C{}^{18}O \\ {}^{18}O{}^{13}C{}^{18}O \end{pmatrix} = \begin{pmatrix} 1 & 0 & 2 & 0 & 0 \\ 0 & 1 & 2 & 0 & 0 \\ 1 & 0 & 1 & 1 & 0 \\ 1 & 0 & 1 & 0 & 1 \\ 0 & 1 & 1 & 1 & 0 \\ 1 & 0 & 0 & 2 & 0 \\ 0 & 1 & 1 & 0 & 1 \\ 1 & 0 & 0 & 1 & 1 \\ 0 & 1 & 0 & 2 & 0 \\ 1 & 0 & 0 & 0 & 2 \\ 0 & 1 & 0 & 1 & 1 \\ 0 & 1 & 0 & 0 & 2 \end{pmatrix} \begin{pmatrix} {}^{12}C \\ {}^{13}C \\ {}^{16}O \\ {}^{17}O \\ {}^{18}O \end{pmatrix}$$

$$\downarrow \qquad\qquad \downarrow \qquad\qquad \downarrow \qquad\qquad (5\text{-}2)$$

$$M \qquad\qquad C \qquad\qquad A$$

We define $C$ here as the transformation matrix, $M$ as the molecular species matrix and $A$ as the isotope component matrix. Equation (5-2) can be simplified to:

$$E \cdot M = C \cdot A \qquad (5\text{-}3)$$

where E is 12 by 12 identity matrix.

The rank and dimensionality of matrix $C$ define the set of linearly independent isotopologues needed to describe the bulk isotopic composition of the population. This set of isotopologues is referred to as the system components. The number of these system components always equals the number of isotopes contributing to a pool of isotopologues minus one (i.e., four in the case of the stable isotopes of $CO_2$), although several different choices of these four system components are possible and the choice of a preferred set is arbitrary and does not affect the final calculation result. However, we believe it is least

confusing to use isotopically normal and singly-substituted isotopologues as the system components because these species are the most abundant and familiar, and they control the bulk isotopic compositions. We can select the preferred set of independent isotopologues by placing them in the first four positions of matrix *M*; subsequent matrix operations will identify these as the system components, as illustrated below. We diagonalize matrix *C* using Gauss-Jordan reduction and document the necessary operations in matrix *E*. This can be done by hand or by using *PLU* decomposition -- a tool included in several commercial software packages including MAPLE® or MATLAB®. Any m × n real matrix can be decomposed as the product of *PLU* (where *P* is a permutation m × m matrix, *L* is a real lower triangular m × m matrix with 1 as each diagonal element, and *U* is an upper triangular m × n matrix). The result is expressed as follows:

$$C = PLU \tag{5-4}$$

Because matrices *P* and *L* are invertible, we can multiply both sides of the equation (5-4) by their inverse to find:

$$(PL)^{-1} \cdot M = U \cdot A \tag{5-5}$$

The rank of the characteristic matrix, *U*, equals the rank of matrix *C* and therefore, the number of system components that define the bulk isotopic composition of the population. Moreover, the locations of non-0 rows in matrix *U* correspond to the location of those system components in matrix *M*. The first n rows (counting from the top, where n equals the rank of matrix *U*) in matrices $(PL)^{-1}$ and *U* define the relationships between system components and isotope components. The remaining rows of matrix $(PL)^{-1}$ contain the

stoichiometric coefficients for isotopologues in the set of linearly independent isotope exchange reactions for this molecule.

In the case of $CO_2$, the matrix $(PL)^{-1}$ and matrix $U$ are:

$$(PL)^{-1} = \begin{pmatrix} 1 & 0 & 0 & 0 & 0 & 0 & 0 & 0 & 0 & 0 & 0 & 0 \\ 0 & 1 & 0 & 0 & 0 & 0 & 0 & 0 & 0 & 0 & 0 & 0 \\ -1 & 0 & 1 & 0 & 0 & 0 & 0 & 0 & 0 & 0 & 0 & 0 \\ 0 & 0 & -1 & 1 & 0 & 0 & 0 & 0 & 0 & 0 & 0 & 0 \\ 1 & -1 & -1 & 0 & 1 & 0 & 0 & 0 & 0 & 0 & 0 & 0 \\ 1 & 0 & -2 & 0 & 0 & 1 & 0 & 0 & 0 & 0 & 0 & 0 \\ 1 & -1 & 0 & -1 & 0 & 0 & 1 & 0 & 0 & 0 & 0 & 0 \\ 1 & 0 & -1 & -1 & 0 & 0 & 0 & 1 & 0 & 0 & 0 & 0 \\ 2 & -1 & -2 & 0 & 0 & 0 & 0 & 0 & 1 & 0 & 0 & 0 \\ 1 & 0 & 0 & -2 & 0 & 0 & 0 & 0 & 0 & 1 & 0 & 0 \\ 2 & -1 & -1 & -1 & 0 & 0 & 0 & 0 & 0 & 0 & 1 & 0 \\ 2 & -1 & 0 & -2 & 0 & 0 & 0 & 0 & 0 & 0 & 0 & 1 \end{pmatrix} \tag{5-6}$$

$$U = \begin{pmatrix} 1 & 0 & 2 & 0 & 0 \\ 0 & 1 & 2 & 0 & 0 \\ 0 & 0 & -1 & 1 & 0 \\ 0 & 0 & 0 & -1 & 1 \\ 0 & 0 & 0 & 0 & 0 \\ 0 & 0 & 0 & 0 & 0 \\ 0 & 0 & 0 & 0 & 0 \\ 0 & 0 & 0 & 0 & 0 \\ 0 & 0 & 0 & 0 & 0 \\ 0 & 0 & 0 & 0 & 0 \\ 0 & 0 & 0 & 0 & 0 \\ 0 & 0 & 0 & 0 & 0 \end{pmatrix} \tag{5-7}$$

In this case, the rank of $U$ is four, indicating that the rank of the transformation matrix $C$ is four, that four independent isotopologues are needed to describe the bulk composition of this system (as expected), and that they are the first four isotopologues in matrix $M$ ($^{16}O^{12}C^{16}O$, $^{16}O^{13}C^{16}O$, $^{16}O^{12}C^{17}O$ and $^{16}O^{12}C^{18}O$). The independent exchange reactions

are defined by the bottom eight rows of matrix $(PL)^{-1}$ (i.e., excluding the first four rows — the rank of matrix $U$). These reactions can be expanded as follows:

$$\text{row 5: } {}^{16}O^{12}C^{16}O + {}^{16}O^{13}C^{17}O \overset{K_1}{\rightleftharpoons} {}^{16}O^{13}C^{16}O + {}^{16}O^{12}C^{17}O \quad K_1 = \frac{x_2 x_3}{x_1 x_5} \tag{5-8-i}$$

$$\text{row 6: } {}^{16}O^{12}C^{16}O + {}^{17}O^{12}C^{17}O \overset{K_2}{\rightleftharpoons} 2\ {}^{16}O^{12}C^{17}O \qquad K_2 = \frac{x_3^2}{x_1 x_6} \tag{5-8-ii}$$

$$\text{row 7: } {}^{16}O^{12}C^{16}O + {}^{16}O^{13}C^{18}O \overset{K_3}{\rightleftharpoons} {}^{16}O^{13}C^{16}O + {}^{16}O^{12}C^{18}O \quad K_3 = \frac{x_2 x_4}{x_1 x_7} \tag{5-8-iii}$$

$$\text{row 8: } {}^{16}O^{12}C^{16}O + {}^{17}O^{12}C^{18}O \overset{K_4}{\rightleftharpoons} {}^{16}O^{12}C^{17}O + {}^{16}O^{12}C^{18}O \quad K_4 = \frac{x_3 x_4}{x_1 x_8} \tag{5-8-iv}$$

$$\text{row 9: } 2\ {}^{16}O^{12}C^{16}O + {}^{17}O^{13}C^{17}O \overset{K_5}{\rightleftharpoons} {}^{16}O^{13}C^{16}O + 2\ {}^{16}O^{12}C^{17}O \quad K_5 = \frac{x_4^2}{x_1 x_{10}} \tag{5-8-v}$$

$$\text{row 10: } {}^{16}O^{12}C^{16}O + {}^{18}O^{12}C^{18}O \overset{K_6}{\rightleftharpoons} 2\ {}^{16}O^{12}C^{18}O \qquad K_6 = \frac{x_4^2}{x_1 x_{10}} \tag{5-8-vi}$$

$$\text{row 11: } 2\ {}^{16}O^{12}C^{16}O + {}^{17}O^{13}C^{18}O \overset{K_7}{\rightleftharpoons} {}^{16}O^{13}C^{16}O + {}^{16}O^{12}C^{17}O + {}^{16}O^{12}C^{18}O \quad K_7 = \frac{x_2 x_3 x_4}{x_1^2 x_{11}} \tag{5-8-vii}$$

$$\text{row 12: } 2\ {}^{16}O^{12}C^{16}O + {}^{18}O^{13}C^{18}O \overset{K_8}{\rightleftharpoons} {}^{16}O^{13}C^{16}O + 2\ {}^{16}O^{12}C^{18}O \quad K_8 = \frac{x_4^2 x_2}{x_1^2 x_{12}} \tag{5-8-viii}$$

where $K_i$ indicates the equilibrium constant for exchange reaction $i$, and $i$ equals the row number minus four. Assuming ideal mixing of all isotopologues of a given molecule, equations relating $K_i$ to the mole fractions of reactant and product isotopologues are given next to each reaction, where $x_j$ is the mole fraction of the isotopologue in row $j$ of matrix $M$ (e.g., $x_1$ is the mole fraction of $^{16}O^{12}C^{16}O$).

Given known values of $K_i$ for all independent isotope exchange reactions (calculated in Section 2.2, below), one need only define the mole fractions of the system components

(i.e., $^{16}O^{12}C^{16}O$, $^{16}O^{13}C^{16}O$, $^{16}O^{12}C^{17}O$ and $^{16}O^{12}C^{18}O$ for our example) to solve the set of eight non-linear equations, 5-8i through 5-8viii, and thereby retrieve the mole fractions of all dependent isotopologues. The mole fractions of the system components can be calculated based on independently defined bulk concentrations of isotopes in the population of isotopologues being considered (e.g., concentrations of $^{13}C$, $^{12}C$, $^{16}O$, $^{17}O$ and $^{18}O$ spread among all isotopologues of $CO_2$ for our example) and the known $K_i$ values. We do so by simultaneous solution of a number of mass balance equations equal to the number of system components (i.e., four mass balance equations for our example). These mass-balance equations are of two kinds: (1) one stipulating that the sum of mole fractions of all isotopologues equals one (i.e., $\sum_{i=1}^{n} x_i = 1$, summed over all n isotopologues; e.g., $n = 12$ for our example); and (2), several stipulating that the sum of mole fractions of all isotopologues containing a given isotope, multiplied by the stoichiometric coefficient for that isotope in that isotopologue (e.g., two for $^{16}O$ in $^{16}O^{13}C^{16}O$), equals the known concentration of that isotope in the entire population of isotopologues. $n$-1 independent equations of this second type are needed, where $n$ equals the number of system components (e.g., three independent equations of this type are needed for our system). For our example, the resulting four equations are:

$$x_2 + \frac{x_2 x_3}{K_1 x_1} + \frac{x_2 x_4}{K_3 x_1} + \frac{x_2 x_3^2}{K_5 x_1^2} + \frac{x_2 x_3 x_4}{K_7 x_1^2} + \frac{x_2 x_4^2}{K_8 x_1^2} = x_{^{13}C} \qquad \text{(5-9-i)}$$

$$2x_1 + 2x_2 + x_3 + x_4 + \frac{x_2 x_3}{K_1 x_1} + \frac{x_2 x_4}{K_3 x_1} = 2x_{^{16}O} \qquad \text{(5-9-ii)}$$

$$x_4 + \frac{x_2 x_4}{K_3 x_1} + \frac{x_3 x_4}{K_4 x_1} + \frac{2x_4^2}{K_6 x_1} + \frac{x_2 x_3 x_4}{K_7 x_1^2} + \frac{2x_2 x_4^2}{K_8 x_1^2} = 2x_{^{18}O} \qquad \text{(5-9-iii)}$$

$$x_1 + x_2 + x_3 + x_4 + \frac{x_2 x_3}{K_1 x_1} + \frac{x_3^2}{K_2 x_1} + \frac{x_2 x_4}{K_3 x_1} + \frac{x_3 x_4}{K_4 x_1} + \frac{x_2 x_3^2}{K_5 x_1^2} + \frac{x_4^2}{K_6 x_1} + \frac{x_2 x_3 x_4}{K_7 x_1^2} + \frac{x_2 x_4^2}{K_8 x_1^2} = 1 \quad \text{(5-9-iv)}$$

For the special case that each value of $K_i$ equals the mass-action constant for the relevant balanced reaction (e.g., when $K_i$ values for equations 5-8i through 5-8viii are 1, 4, 1, 2, 4, 4, 2 and 4, respectively), the exact solution for equation 5-9i through 5-9iv is that the concentration of each of the system components equals the product of the concentrations of the isotopes it contains (e.g., $x_1 = x_{^{12}C} x_{^{16}O}^2$, $x_3 = 2 x_{^{16}O} x_{^{12}C} x_{^{17}O}$). This is referred to as the stochastic or random distribution and corresponds to the expected distribution at infinite temperature. For the general case that $K_i$ values are controlled by enhanced thermodynamic stabilities of certain isotopologues relative to others and differ from the stochastic distribution, we solve equations 5-9i through 5-9iv numerically using line search procedures and a quasi-Newton method (also called the variable metric method). Programs for such numerical procedures can be found in Numerical Recipes (e.g., PRESS et al., 2002, chapter 10.1 and 10.7) or Matlab® (referring to Matlab help files). We recommend using the concentrations of isotopologues corresponding to the stochastic distributions as initial guesses for these numerical solutions. Other choices will yield the same result, just more slowly.

To test the precision of our numerical methods for solving equation 5-9i through 5-9iv, we calculated the concentration of each isotopologue of $CO_2$ for a population having the stochastic distribution of isotopes using both: (1) the exact solution; and (2) the numerical method in which the initial guess for concentrations of independent isotopologues differed greatly from the stochastic distribution (i.e., so that the numerical algorithm must converge on the final result from a highly aberrant initial condition).

Differences between these two methods, defined as $\left( \frac{x_{numeric}}{x_{exact}} - 1 \right)$, are less then $5.0 \times 10^{-13}$ for all twelve $CO_2$ isotopologues for assumed bulk isotopic compositions within the natural range. This error is trivial compared to the variations in expected abundances of isotopologues calculated in Section 3.

### 2.2 EVALUATION OF EQUILIBRIUM CONSTANTS

In this section, we describe how equilibrium constants ($K_i$ values) can be evaluated using classical statistical thermodynamics and spectroscopic data. We frame our discussion around calculation of the equilibrium constant for the isotope exchange reaction, 5-8iii above which involves isotopologue $^{18}O^{13}C^{16}O$, data for which is reported by EILER and SCHAUBLE (2004). The same principles apply to other isotope exchange reactions of $CO_2$ and other gases discussed in Section 3 of this paper.

The equilibrium constant of isotope exchange reaction 5-8iii ($K_3$) can be expressed as:

$$K_3 = \frac{Q_{^{16}O^{13}C^{16}O} \cdot Q_{^{16}O^{12}C^{18}O}}{Q_{^{16}O^{12}C^{16}O} \cdot Q_{^{16}O^{13}C^{18}O}} \qquad (5\text{-}10)$$

where $Q_i$ is partition function for each isotopologue, $i$. Each partition function, $Q_i$ in this equation is the product of translational, vibrational (including zero point), and rotational energies, the rotation-vibration interaction energy, and electronic energy. For isotope exchange reactions involving molecules in the ground state, the electronic energy is ignored if one adopts the Born-Oppenheimer approximation (as we do), because it is independent of isotopic mass. Thus, only terms associated with the energies of translation, rotation and vibration need be considered. UREY (1947) presented a simplified calculation of the components of the partition function that are most important

for isotope exchange reactions. He considered only the vibrational energy, approximated intra-molecular bonds as oscillators, and adopted the Teller-Redlich product rule. Urey's solution for polyatomic molecules, stated in terms relevant for evaluation of the partition function ratio, $\frac{Q_{^{16}O^{13}C^{16}O}}{Q_{^{16}O^{12}C^{16}O}}$ (as an example) is:

$$\left(\frac{Q_{^{16}O^{13}C^{16}O}}{Q_{^{16}O^{12}C^{16}O}}\right)=\frac{\sigma_{^{16}O^{12}C^{16}O}}{\sigma_{^{16}O^{13}C^{16}O}}\prod_{i=1}^{3n-5}\frac{u_i^{^{16}O^{13}C^{16}O}}{u_i^{^{16}O^{12}C^{16}O}}\frac{e^{-\frac{u_i^{^{16}O^{13}C^{16}O}}{2}}}{1-e^{-u_i^{^{16}O^{13}C^{16}O}}}\frac{1-e^{-u_i^{^{16}O^{12}C^{16}O}}}{e^{-\frac{u_i^{^{16}O^{12}C^{16}O}}{2}}} \qquad (5\text{-}11)$$

where $\sigma_{^{16}O^{12}C^{16}O}$ and $\sigma_{^{16}O^{13}C^{16}O}$ are symmetry numbers of $^{16}O^{12}C^{16}O$ and $^{16}O^{13}C^{16}O$ (both equal two); $n$ is the number of atoms in the molecule of interest (both equal three); $u_i=\frac{hc\varpi_i}{kT}$ ($\varpi_i$ is the normal vibrational wave number for $^{16}O^{12}C^{16}O$ or $^{16}O^{13}C^{16}O$ at each vibrating mode $i$; $h$ is Plank's constant; $c$ is light speed; $k$ here is Boltzmann constant; $T$ is absolute temperature). There are $3n$-6 normal vibrational modes for non-linear polyatomic molecules, while there are only $3n$-5 for linear polyatomic molecules such as $CO_2$ and $N_2O$ because the bending vibrational mode is doubly-degenerate. Note that a factor of $\prod_i^n m_i^{\frac{3}{2}}$ (where $m_i$ is the mass of atom $i$ of n atoms that form the molecule) for each molecule is omitted in this expression because this factor will be eventually cancelled out when calculating equilibrium constants (refer to DAVIDSON, 1962). Expressions having the form of equation 5-11 have been widely used to predict equilibrium constants of isotope exchange reactions among gaseous species and their temperature dependence (e.g., RICHET et al., 1977). The equilibrium constant of isotope exchange reaction such as 5-8i through 8viii can be calculated by combining two or more

expressions having the form of equation 5-11. For example, $K_3$ equals the product of two partition function ratios, $\left(\frac{Q_{^{16}O^{13}C^{16}O}}{Q_{^{16}O^{12}C^{16}O}}\right)\cdot\left(\frac{Q_{^{16}O^{12}C^{18}O}}{Q_{^{16}O^{13}C^{18}O}}\right)$, as shown in equation 5-10, each of which can be calculated using equation 5-11.

For molecules with known zero point energies (obtained from *ab initio* and quantum mechanic molecular models), the partition function ratio is evaluated starting with the first vibration quantum number, rather than using $\frac{1}{2}\sum_{i}^{3n-5}\varpi_i$ to estimate the zero point energy. After this modification, the partition function ratio $\frac{Q_{^{16}O^{13}C^{16}O}}{Q_{^{16}O^{12}C^{16}O}}$ becomes:

$$\left(\frac{Q_{^{16}O^{13}C^{16}O}}{Q_{^{16}O^{12}C^{16}O}}\right)=\frac{\sigma_{^{16}O^{12}C^{16}O}}{\sigma_{^{16}O^{13}C^{16}O}}e^{-(u_0^{\,^{16}O^{13}C^{16}O}-u_0^{\,^{16}O^{12}C^{16}O})}\prod_{i=1}^{3n-5}\frac{u_i^{\,^{16}O^{13}C^{16}O}}{u_i^{\,^{16}O^{12}C^{16}O}}\frac{1-e^{-u_i^{\,^{16}O^{12}C^{16}O}}}{1-e^{-u_i^{\,^{16}O^{13}C^{16}O}}} \qquad (5\text{-}12)$$

where $u_0^{\,^{16}O^{13}C^{16}O}=\frac{hc\varpi_0^{\,^{16}O^{13}C^{16}O}}{kT}$, indicating the contribution from the zero point energy. We used equations 5-11 and 5-12 to evaluate equilibrium constants of reactions involving multiply-substituted isotopologues when approximating intra-molecular bonds as oscillators. Equation 5-12 is better than equation 5-11 in describing partition function ratios at low temperatures, and was used whenever possible.

Because molecules both vibrate and rotate, centrifugal forces acting on intra-molecular bonds make it difficult to separate vibrational and rotational contributions to the partition function and require that we treat these bonds as an. It is commonly assumed that this effect leads to insignificant corrections in calculated partition functions. However, it is conceivable that these terms could influence the stabilities of multiply-

substituted molecules so we have evaluated them for all cases we deemed computationally tractable. For diatomic molecules, we use the an non-rigid rotor model (PITZER, 1953; see DAVIDSON, 1962, for a broader summary). In this model, the energy in each quantum level is described as a function of quantum numbers $v$ and $J$:

$$\frac{\varepsilon_{v,J}}{hc} = \varpi_e(v+\tfrac{1}{2}) - \varpi_e x_e(v+\tfrac{1}{2})^2 + B_e J(J+1) - DJ^2(J+1)^2 - \alpha(v+\tfrac{1}{2})J(J+1) \qquad (5\text{-}13)$$

where $\varpi_e$ is the vibration wave number and is related to the second derivative of the potential curve at its minimum; $\varpi_e x_e$ describes the anharmonicity of the potential curve, $x_e$ is the cubic anharmonic correction term and is half of the relative deviation of the harmonic vibration wave number ($\varpi_e$) from the first vibrational spacing ($\varpi_0$); which can be directly measured from infrared or Raman spectroscopic data; $B_e = \frac{h}{8\pi^2 I_e c}$ and is the rotational constant, where $I_e$ is moment of inertia of the diatomic molecule; $c$ is speed of light; and $h$ is Plank's constant. $J$ and $v$ are the rotational and vibrational quantum numbers, respectively. $D = \frac{4B_e^3}{\varpi_e^3}$ and describes centrifugal stretching, and $\alpha$ is the vibration-rotation coupling constant.

After removing small, higher order terms and integrating v and J, the contribution of the rovibration partition function to the overall partition function can be separated into the product of three parts: 1) $Q_0$ is from the zero point energy contribution (RICHET et al., 1977); 2) $Q_{harm\text{-}rigid}$, has the same meaning as in the harmonic oscillator and rigid motor models, above; and 3) $Q_{corr}$ is the deviation from the harmonic oscillator and rigid motor model due to anharmonicity. These terms can be shown to have the following form (Eq.8-40 in DAVIDSON, 1962):

$$Q^{v-r} = Q_0 Q_{harm-rigid} Q_{corr} \tag{5-14}$$

$$Q_0 = e^{-\frac{(\frac{\varpi_e}{2} - \frac{\varpi_e x_e}{4})hc}{kT}} \tag{5-15}$$

$$Q_{harm-rigid} = \frac{1}{\sigma y} \frac{1}{1 - e^{-u}} \tag{5-16}$$

$$Q_{corr} = 1 + \frac{2\gamma}{y} + \frac{\delta}{e^u - 1} + \frac{2xu}{(e^u - 1)^2} + \frac{y}{3} + \frac{y^2}{15} \tag{5-17}$$

where $u = \frac{hc(\varpi_e - 2\varpi_e x_e)}{kT}$ , $y = \frac{hc(B_e - \frac{\alpha}{2})}{kT}$ , $\gamma = \frac{D}{B_e - \frac{\alpha}{2}}$ and $\delta = \frac{\alpha}{B_e - \frac{\alpha}{2}}$ . The full partition function $Q_i$ including translational energy is:

$$Q_i = M_i Q_i^{v-r} \tag{5-18}$$

where $M_i$ is the mass of isotopologue $i$. We used equations 5-13 through 5-18 to evaluate equilibrium constants of reactions involving multiply-substituted isotopologues when describing intra-molecular bonds of diatomic molecules with an anharmonic model.

Anharmonic models of partition functions for polyatomic molecules are more complex than equations 5-13 through 5-18 (e.g., NIELSEN, 1951) and can only be approximated by numerically solving the Schrödinger equation using an accurate rovibrational potential energy surface, and considering the first several thousand rovibrational state energies. This would be unreasonably time-consuming for the relatively broad overview of isotopologues and temperatures we consider. However, we tested the validity of our simpler approximations by conducting a limited set of more accurate calculations of this type for CO and $CO_2$. The results, presented in the Appendix, are effectively indistinguishable from those produced using the Urey method at temperatures of less than 275 K. We suspect that differences between these methods at

higher temperatures reflect limitations of the spectroscopic data for multiply-substituted isotopologues at higher quantum states, and do not reflect methodological errors. We conclude that the harmonic oscillator approximation (equations 5-11 and 5-12), in addition to being applicable to a large range of molecules and conditions, is sufficiently accurate for our purposes. We therefore focus on results of these simpler calculations in the following section.

## 3. APPLICATION TO COMMON MOLECULAR GASES

In this section, we use the algorithm developed in Section 2 to calculate the equilibrium proportions of all stable isotopologues of $N_2$, $O_2$, NO, CO, $CO_2$ and $N_2O$ between 1000 and 193 to 77 K, based on published spectroscopic data. The lower temperature limit for each molecule is chosen to be its 1-atm boiling, or for $CO_2$, sublimation temperature (77.3 K for $N_2$, 81.6 for CO, 90.2 K for $O_2$, 121.3 for NO, 184.6 K for $N_2O$, and 192.6 for $CO_2$; LIDE and FREDERIKSE, 1994). This lower limit is somewhat arbitrary, but focuses on the temperature ranges appropriate for most geochemical and cosmochemical problems of possible interest.

The input data and results of these calculations are organized below by molecular species, from the simplest (symmetric, diatomic molecules) to the most complex ($N_2O$). The precision and accuracy of our model calculations depend chiefly on the quality of the spectroscopic data, on the accuracy and completeness of the harmonic and anharmonic models of intra-molecular bonds, and on the assumption of ideal mixing of all isotopologues of a given molecule. Before presenting our results, we first define terms that are useful for expressing the systematics of multiply-substituted isotopologues.

### 3.1 DEFINITION AND PROPERTIES OF Δ

In order to appreciate the magnitude of isotopic variations that could result from distinctive partition functions of multiply-substituted isotopologues, it is useful to compare abundances of these species calculated as described in Section 2 of this paper to those expected if all isotopes are randomly distributed among all isotopologues (the stochastic distribution). We define here the variable, $\Delta_i$ to describe this difference:

$$\Delta_i = \left( \frac{R_{i-e}}{R_{i-r}} - 1 \right) \times 1000 \tag{5-19}$$

where $R_{i\text{-}e}$ is the abundance of an isotopologue of interest $i$, divided by the abundance of the isotopologue having no rare isotopes in the same pool of molecules evaluated at thermodynamic equilibrium. For example, $R_{^{18}O^{13}C^{16}O\text{-}e} = \frac{[^{18}O^{13}C^{16}O]_e}{[^{16}O^{12}C^{16}O]_e}$. $R_{i\text{-}r}$ is that same ratio in a pool of $CO_2$ molecules of the same bulk isotopic composition, but having the stochastic distribution of isotopologues. $R_{i\text{-}r}$ is a simple function of the abundances of isotopes contributing to a pool of isotopologues (e.g., $R_{^{18}O^{13}C^{16}O\text{-}r} = \frac{[^{18}O^{13}C^{16}O]_r}{[^{16}O^{12}C^{16}O]_r} = \frac{2[^{18}O][^{13}C][^{16}O]}{[^{12}C][^{16}O]^2} = \frac{2[^{18}O][^{13}C]}{[^{16}O][^{12}C]}$). Values of $\Delta_i$ have units of per mil deviation from the stochastic distribution, and are independent of bulk isotopic composition over the range of natural abundances of rare isotopes (because $\Delta_i$ values of singly-substituted isotopologues are close to zero for these isotopic compositions, in which case $\Delta_i$ values of multiply-substituted isotopologues depend only on $K_i$ values). Positive and negative values of $\Delta_i$ correspond to enrichments and depletions, respectively, in the isotopologue, $i$, relative to the stochastic distribution.

### 3.2 RELATIONSHIP BETWEEN Δ AND *K* VALUES

An isotope exchange reaction involving only one doubly-substituted isotopologue of a given molecule can be written as:

$$A_1 + A_4 \overset{K}{\rightleftharpoons} A_2 + A_3 \tag{5-20}$$

where $A_4$ is the doubly-substituted isotopologue, $A_1$ is the isotopologue having no rare isotopes, and $A_2$ and $A_3$ are singly-substituted isotopologues (note $A_2$ and $A_3$ can be the same isotopologue; e.g., reaction 5-8ii and 8vi). Based on the law of mass action and assuming ideal mixing of stable isotopes on a given molecular site, the following expressions can be used to describe the equilibrium constants for such reactions:

$$K = \frac{[A_2][A_3]}{[A_1][A_4]} \tag{5-21}$$

$$K_r = \frac{[A_{2-r}][A_{3-r}]}{[A_{1-r}][A_{4-r}]} \tag{5-22}$$

where $K_r$ refers to the equilibrium constant for the stochastic (random) distribution. Also, from the definition of $\Delta_i$ in equation 5-19 we know:

$$\frac{[A_i]}{[A_1]} = \left(\frac{\Delta_i}{1000} + 1\right) \cdot \frac{[A_{i-r}]}{[A_{1-r}]} \tag{5-23}$$

After dividing equation 5-21 by equation 5-22 on both sides and replacing the concentration ratios with Δ values following equation 5-23, we find:

$$\frac{K}{K_r} = \frac{\left(\frac{\Delta_2}{1000} + 1\right)\left(\frac{\Delta_3}{1000} + 1\right)}{\left(\frac{\Delta_1}{1000} + 1\right)\left(\frac{\Delta_4}{1000} + 1\right)} \tag{5-24}$$

Taking the natural logarithm of both sides of equation 5-24 and rearranging, we find the following expression for the $\Delta_4$:

$$\ln\left(\frac{\Delta_4}{1000}+1\right)=\ln\left(\frac{\Delta_2}{1000}+1\right)+\ln\left(\frac{\Delta_3}{1000}+1\right)-\ln\left(\frac{\Delta_1}{1000}+1\right)-\ln\frac{K}{K_r} \qquad (5\text{-}25)$$

Because we defined $A_1$ as the isotopologue having no rare isotopes, $\Delta_1$ by definition equals 0. When $\Delta_i$ is small (ca. < 10 per mil), equation 5-25 can be reduced to:

$$\Delta_4 \approx \Delta_2 + \Delta_3 - 1000\ln\frac{K}{K_r} \qquad (5\text{-}26)$$

based on the approximation that $ln(1+x) \approx x$ when $x$ is much smaller than 1.

For all populations of isotopologues of diatomic and symmetric tri-atomic molecules (i.e., $CO_2$, but not $N_2O$) having bulk isotopic compositions within the range typical of natural materials, $\Delta_i$ values of singly-substituted isotopologues are near 0 (ca. < 0.01 ‰) at temperatures of interest. In this case, the following simple relationship exists between value of $K$ and value of $\Delta_4$ :

$$\Delta_4 \approx -1000\ln\frac{K}{K_r} \qquad (5\text{-}27)$$

Asymmetric tri-atomic molecules (among whose different isotopologues the highest symmetry is $C_{\infty v}$) such as $N_2O$ are exceptions for which $\Delta_i$ values of singly-substituted isotopologues can be far from 0 (see Section 3.5). In the interests of completeness, we present both $\Delta_i$ values and $K_i$ values for all isotope exchange reactions for each molecule considered in the following section. In general, these two sets of variables have simple relationships to one another, as in equation 5-27. However, it is important to note that while the $K$ values are independent of bulk composition, $\Delta_i$ values can differ significantly from the values we show for highly-enriched bulk isotopic compositions.

### 3.3 Δ VALUES FOR ISOTOPIC MASSES

While it is possible to precisely measure abundances of doubly-substituted isotopologues of some molecular gases, the instruments used for this purpose today do not have sufficient mass resolution to separate isotopologues that are isobars of one another. For example, measurements of $^{16}O^{13}C^{18}O$ presented by EILER and SCHAUBLE (2004) must be corrected for minor contributions from $^{17}O^{12}C^{18}O$ and $^{17}O^{13}C^{17}O$ (much as conventional measurements of $\delta^{13}C$ must be corrected for contributions from the isobar, $^{16}O^{12}C^{17}O$; SANTROCK et al., 1985 and references therein). We report $\Delta_i$ values for all individual isotopologues in this paper, both for completeness in our theoretical treatment and because it may be possible in the future to resolve some of these isobars. However, we also report $\Delta_i$ values calculated in the same fashion as defined in equation 5-19, but including contributions from all isotopologues having a single nominal cardinal mass. For example, $\Delta_{47}$ for $CO_2$ is calculated as:

$$\Delta_{47} = \left( \frac{\frac{[^{16}O^{13}C^{18}O] + [^{17}O^{12}C^{18}O] + [^{17}O^{13}C^{17}O]}{[^{16}O^{12}C^{16}O]}}{\frac{[^{16}O^{13}C^{18}O]_r + [^{17}O^{12}C^{18}O]_r + [^{17}O^{13}C^{17}O]_r}{[^{16}O^{12}C^{16}O]_r}} - 1 \right) \times 1000 \qquad (5\text{-}28)$$

These $\Delta_i$ values calculated for a given cardinal mass obscure important details of the geochemistry of some isotopologues, but are useful because they provide a practical guide to the isotope effects that are measurable using existing technology.

### 3.4 DIATOMIC MOLECULES

Abundances of isotopologues of $N_2$, NO, CO, and $O_2$ were calculated using both the harmonic oscillator approximation (equation 5-11 and 5-12) and the anharmonic model

(equations 5-13 through 5-17). Results of these calculations are presented in Figures 2 through 5 and in Table 2. We use molecular constants for $^{14}N^{14}N$, $^{14}N^{16}O$, $^{12}C^{16}O$ and $^{16}O_2$ taken from HUBER and HERZBERG (1979) (see Table 1). Properties of other isotopologues of these molecules were calculated based on spectroscopic data and the following relationship from DUNHAM (1932):

$$\frac{\varpi_1}{\varpi_2} = \sqrt{\frac{\mu_2}{\mu_1}};\ \frac{\varpi_1 x_{e1}}{\varpi_2 x_{e2}} = \frac{\mu_2}{\mu_1}; \frac{B_{e1}}{B_{e2}} = \frac{\mu_2}{\mu_1}; \frac{\alpha_{e1}}{\alpha_{e2}} = \left(\frac{\mu_2}{\mu_1}\right)^{\frac{3}{2}} \tag{5-29}$$

where $\mu = \frac{m_1 m_2}{m_1 + m_2}$ and is the reduced mass; $\varpi_i$, is the normal mode wave number (as above); $x_e$ is the cubic anharmonic correction term; $B_e$ is the rotational constant; $\alpha_e$ is vibration-rotation coupling constant; and subscripts 1 or 2 refer to different isotopologues of the same molecule. Isotopic masses and average natural abundances are from WALKER et al. (1989).

Table 1. Molecular constants for diatomic molecules of $^{16}O^{16}O$, $^{14}N^{14}N$, $^{12}C^{16}O$ and $^{14}N^{16}O$, data are from HUBER and HERZBERG (1979). $r_e$ is the equilibrium inter-nuclear distance; other terms are defined in the text.

| | $\varpi_e$ (cm$^{-1}$) | $\varpi_e x_e$ (cm$^{-1}$) | $B_e$ | $\alpha_e$ | $r_e$ (Å) |
|---|---|---|---|---|---|
| $^{14}N^{14}N$ | 2358.570 | 14.324 | 1.63745 | 0.01791 | 1.21260 |
| $^{14}N^{16}O$ | 1904.204 | 14.075 | 1.70493 | 0.01710 | 1.15077 |
| $^{12}C^{16}O$ | 2169.814 | 13.288 | 1.93128 | 0.01750 | 1.12832 |
| $^{16}O^{16}O$ | 1580.193 | 11.981 | 0.04747 | 0.01593 | 1.20752 |

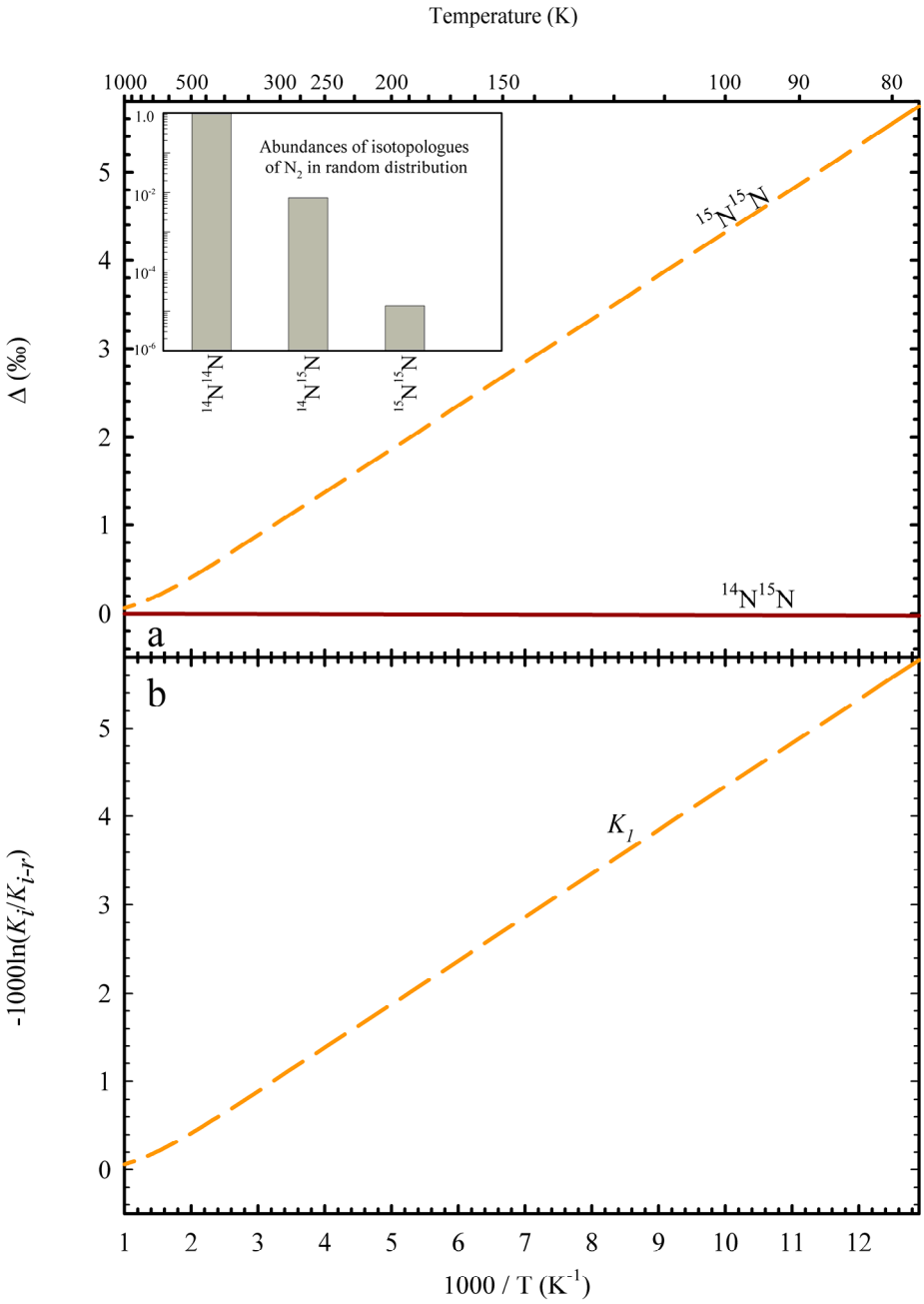


**Figure 2.** A: Variation of Δ values of all isotopologues of $N_2$ with 1/T; the inset shows the abundances of all isotopologues of $N_2$ for the stochastic distribution and an $^{15}N/^{14}N$ ratio equal to atmospheric $N_2$. B: Variation of $-1000 \cdot \ln(K_i / K_{i\text{-}random})$ ($i$ = 1) with 1000/T for the isotope exchange reaction in equation 5-30.

**$N_2$**: The two required system components for $N_2$ were chosen to be $^{14}N^{14}N$ and $^{14}N^{15}N$. The independent exchange reaction that goes with these system components is:

$$^{14}N^{14}N + {}^{15}N^{15}N \overset{K_1}{\rightleftharpoons} 2\,^{14}N^{15}N \qquad (5\text{-}30)$$

Results of our calculations for $N_2$ using the harmonic oscillator approximation are shown in Figures 2A and 2B and Table 2. Figure 2A shows $\Delta_i$ values of all isotopologues of $N_2$ as functions of 1/T; the inset shows the abundances of all isotopologues of $N_2$ for the stochastic distribution and a bulk isotopic composition equal to terrestrial atmospheric $N_2$ (IUPAC, 1994). Note that $\Delta_{^{14}N^{15}N}$ does not differ significantly from zero at any temperature within the range considered, i.e., this isotopologue is present in very nearly the abundance predicted for the stochastic distribution. In contrast, $\Delta_{^{15}N^{15}N}$ is ca. 1 per mil at room temperature and increases with decreasing temperature. At temperatures less than ca. < 400 K, $\Delta_{^{15}N^{15}N}$ varies linearly with 1/T. Figure 1B shows values of $-1000\cdot\ln(K_1/K_{1\text{-}r})$ as a function of 1/T, where $K_r$ is the equilibrium constant of reaction 5-30 ($K_{1\text{-}r} = 4$ for the stochastic distribution). The value of $\Delta_{30}$ exactly equals $\Delta_{^{15}N^{15}N}$.

If nitrogen in the earth's atmosphere were in equilibrium with respect to reaction 5-30, we would expect a ca. 1 ‰ excess of $^{15}N^{15}N$ beyond the stochastic distribution. This should be readily detectable using existing analytical methods, provided contributions from $^{14}N^{16}O$ and $^{12}C^{18}O$ (common products of fragmentation and oxidation reactions in mass spectrometer sources) can be minimized (it is unlikely they could be mass resolved by an practical instrument). Given the slow rates of gas-phase isotope exchange reactions for most simple molecules, we think it likely that the earth's atmosphere is not in thermodynamic equilibrium, and instead that its $^{15}N^{15}N$ content reflects the net effects

of fractionations accompanying various biological and photochemical sources and sinks. Given the very long lifetime of $N_2$ in air, we think it possible that any such net enrichments or deficits could be large.

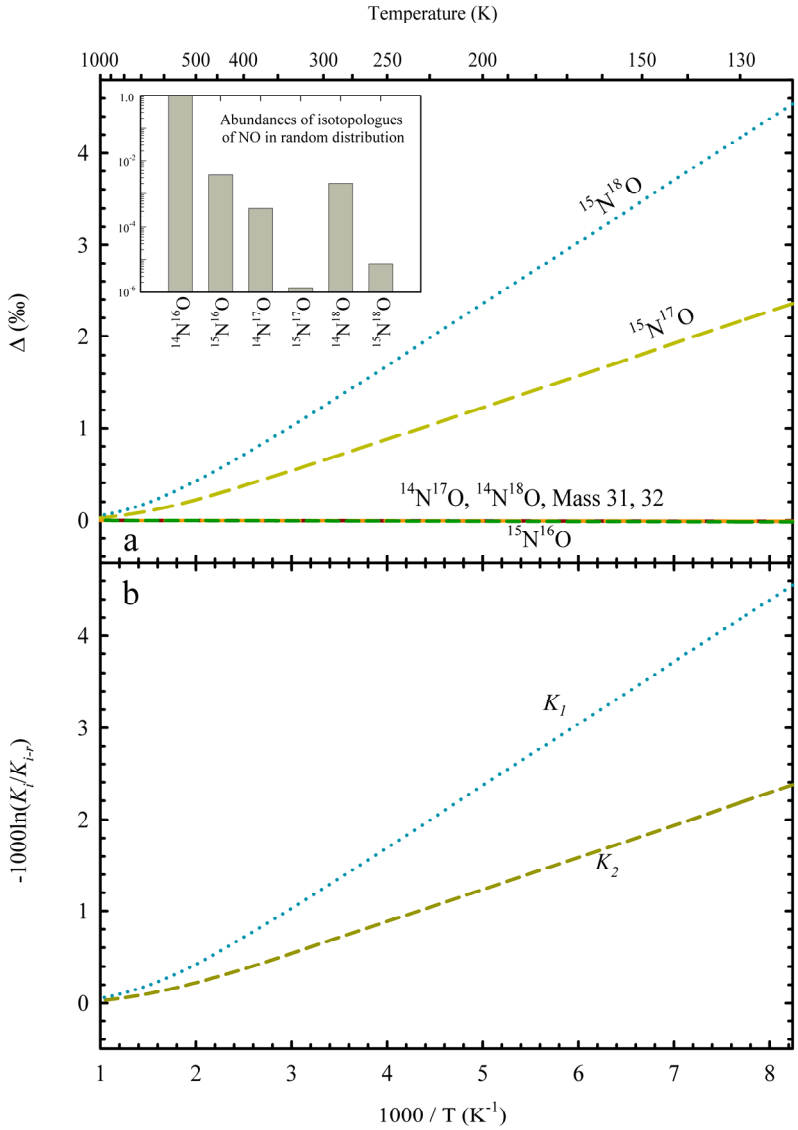


**Figure 3.** A: Variation of Δ values of all isotopologues of NO with 1/T; the inset shows the abundances of all isotopologues of NO for the stochastic distribution, an $^{15}N/^{14}N$ ratio equal to atmospheric $N_2$ and an oxygen isotope composition equal to VSMOW. B: Variation of $-1000 \cdot \ln(K_i / K_{i\text{-}random})$ ($i$ = 1 or 2) with 1000/T for the isotope exchange reactions in equations 5-31i and 31ii.

**NO**: The four required system components for NO were chosen to be $^{14}N^{16}O$, $^{15}N^{16}O$, $^{14}N^{17}O$ and $^{14}N^{18}O$. The two independent exchange reactions that go with these system components are:

$$^{14}N^{16}O + {}^{15}N^{17}O \overset{K_1}{\rightleftharpoons} {}^{15}N^{16}O + {}^{14}N^{17}O \qquad \text{(5-31-i)}$$

$$^{14}N^{16}O + {}^{15}N^{18}O \overset{K_2}{\rightleftharpoons} {}^{15}N^{16}O + {}^{14}N^{18}O \qquad \text{(5-31-ii)}$$

Results of our calculations for NO using the harmonic oscillator approximation are shown in Figures 3A and B and Table 2. Figure 3A shows the dependence of $\Delta$ values on $1/T$; the inset shows the abundances of all isotopologues for NO having the stochastic distribution, a bulk isotopic composition of N equal to atmospheric $N_2$ (IUPAC, 1994), and of O equal to VSMOW (IUPAC, 1994). Values of $\Delta_{^{15}N^{18}O}$ and $\Delta_{^{15}N^{17}O}$ are approximately 1‰ at earth-surface temperatures, increase with decreasing temperature, and vary linearly with 1/T at temperatures less than 500 K. Figure 3B shows the dependences of $-1000 \cdot \ln(K_i/K_{i\text{-}r})$ ($i$ = 1 or 2) on 1/T ($K_{i\text{-}r}$ = 1 for both reactions). As for $N_2$, there is a simple relationship between $\Delta_i$ values and related $K_i$ values (see Section 3.2). The $\Delta_{32}$ value (a weighted sum of $\Delta_{^{15}N^{17}O}$ and $\Delta_{^{14}N^{18}O}$) approximately equals 0 despite significant enrichments in $^{15}N^{17}O$ because the abundance ratio, $\frac{[^{15}N^{17}O]}{[^{14}N^{18}O]}$ is very small; $\Delta_{33}$ exactly equals $\Delta_{^{15}N^{18}O}$.

The atmospheric budget of NO is influenced by emissions from soils (particularly fertilized agricultural fields) and a complex set of photochemical sources and sinks (including transfer between NO and $NO_2$). The budget has not been well studied by conventional stable isotope techniques, perhaps because of the low mixing ratio of nitric

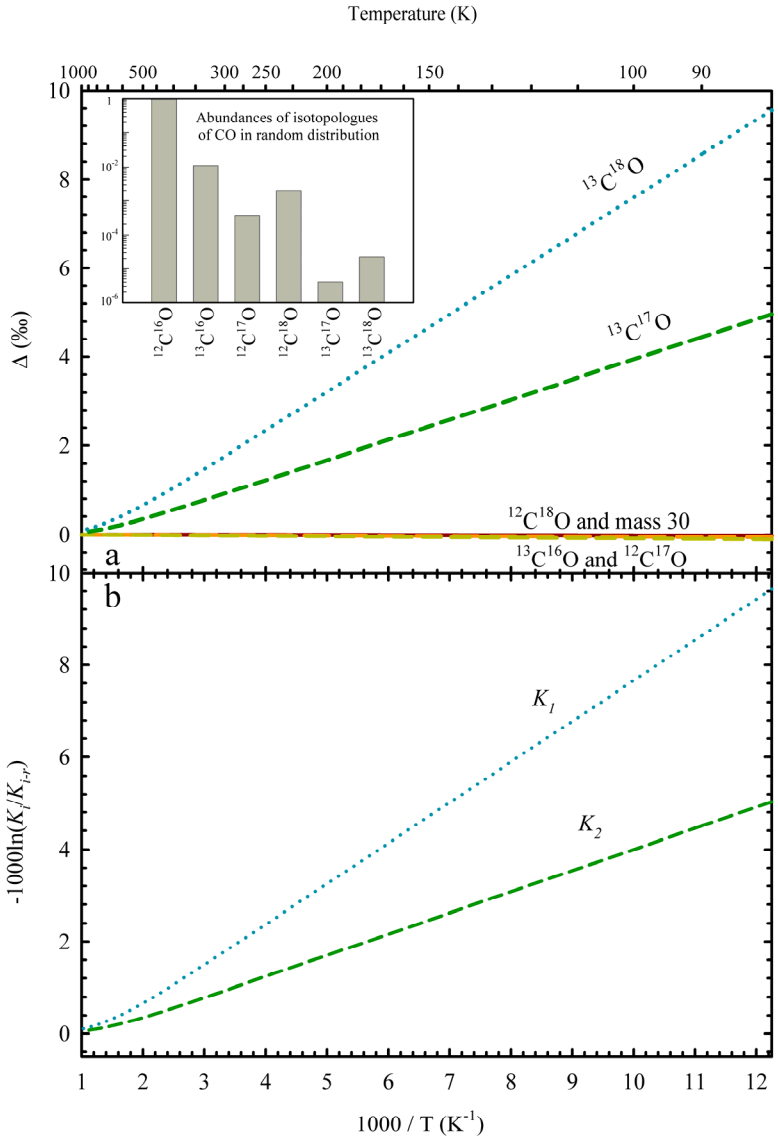


**Figure 4.** A: Variation of Δ values of all isotopologues of CO with 1/T; the inset shows the abundances of all isotopologues of CO for the stochastic distribution, a $^{13}C/^{12}C$ ratio equal to PDB, and an oxygen isotope composition equal to VSMOW. B: Variation of $-1000 \cdot \ln(K_i / K_{i\text{-}random})$ ($i$ = 1 or 2) with respect to 1000/T for the isotope exchange reactions in equations 5-32i and 5-32ii.

oxide in air (tens of pptv). We can think of no basis for confidently predicting the abundances of $^{15}N^{17}O$ and $^{15}N^{18}O$ in air, although it seems reasonable to suspect they

could be sensitive to the balance between soil sources vs. atmospheric photochemical sources and sinks.

**CO**: The four required system components for CO were chosen to be $^{12}C^{16}O$, $^{13}C^{16}O$, $^{12}C^{17}O$ and $^{12}C^{18}O$. The two independent exchange reactions that go with these system components are:

$$^{12}C^{16}O + {}^{13}C^{17}O \overset{K_1}{\rightleftharpoons} {}^{13}C^{16}O + {}^{12}C^{17}O \qquad \text{(5-32-i)}$$

$$^{12}C^{16}O + {}^{13}C^{18}O \overset{K_2}{\rightleftharpoons} {}^{13}C^{16}O + {}^{12}C^{18}O \qquad \text{(5-32-ii)}$$

Results of our calculations for CO using the harmonic oscillator approximation are shown in Figures 4A and 4B and Table 2. Figure 4A shows the dependence of Δ values on 1/T; the inset shows the abundances of all isotopologues for CO having the stochastic distribution, a $^{13}C/^{12}C$ ratio equal to PDB (CRAIG, 1957) and an oxygen isotope composition equal to VSMOW (IUPAC, 1994). Values of $\Delta_{^{13}C^{18}O}$ and $\Delta_{^{13}C^{17}O}$ are approximately 1‰ at earth-surface temperatures, increase with decreasing temperature, and vary linearly with 1/T at temperatures < 600 K. Figure 4B shows the dependence of $-1000 \cdot \ln(K_i/K_{i\text{-}r})$ ($i$ = 1 or 2) on 1/T ($K_{i\text{-}r}$ = 1 for both reactions). The $\Delta_{30}$ value (equal to the weighted sum of $\Delta_{^{12}C^{18}O}$ and $\Delta_{^{13}C^{17}O}$) approximately equals 0 because the abundance ratio, $\frac{[^{13}C^{17}O]}{[^{12}C^{18}O]}$ is very small; $\Delta_{31}$ exactly equals $\Delta_{^{13}C^{18}O}$.

The natural atmospheric budget of CO includes sources from fossil-fuel and biomass combustion and photo-oxidation of volatile hydrocarbons, and sinks to soil uptake and oxidation by atmospheric radicals. It is difficult to predict the expected impact of these processes on abundances of multiply-substituted isotopologues, although experience with

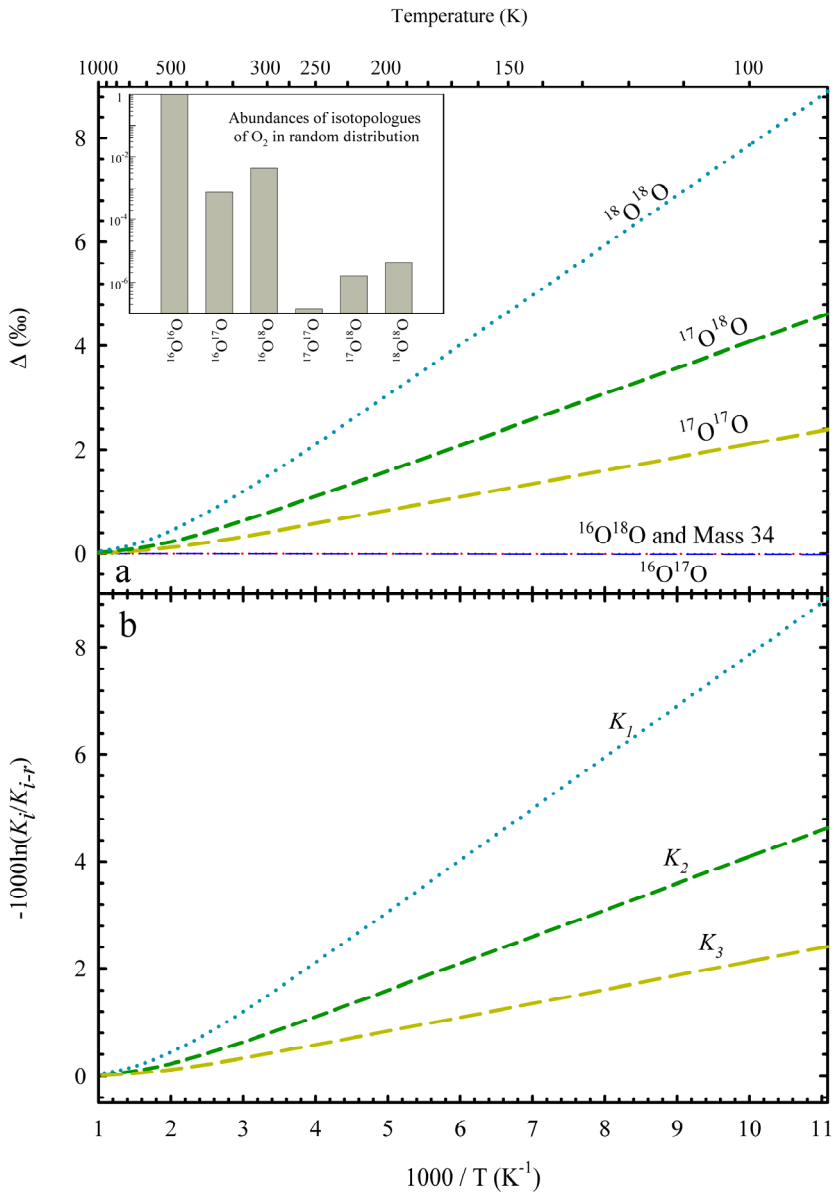


**Figure 5.** A: Variation of Δ values of all isotopologues of $O_2$ with 1/T; the inset shows the abundances of all isotopologues of $O_2$ for the stochastic distribution and an oxygen isotope composition equal to VSMOW. B: Variation of $-1000 \cdot \ln(K_i/K_{i\text{-}random})$ ($i$ = 1 to 3) with 1000/T for the isotope exchange reactions in equation 5-33i through 5-33iii.

$CO_2$ (discussed below) suggests combustion sources will be near the stochastic distribution. Losses to soil are suspected to be rate-limited by soil diffusion and may

involve fractionations controlled by the kinetic theory of gases (see EILER and SHAUBLE, 2004 for examples of such fractionations of $^{18}O^{13}C^{16}O$). Photo-chemical sources and sinks are less easily predicted and suggest we must await experimental study.

**$O_2$**: The three required independent system components for $O_2$ are chosen to be $^{16}O^{16}O$, $^{16}O^{17}O$ and $^{16}O^{18}O$. The set of three independent reactions that go with these system components is:

$$^{16}O^{16}O + {}^{18}O^{18}O \overset{K_1}{\rightleftharpoons} 2\,{}^{16}O^{18}O \qquad \text{(5-33-i)}$$

$$^{16}O^{16}O + {}^{17}O^{18}O \overset{K_2}{\rightleftharpoons} {}^{16}O^{17}O + {}^{16}O^{18}O \qquad \text{(5-33-ii)}$$

$$^{16}O^{16}O + {}^{17}O^{17}O \overset{K_3}{\rightleftharpoons} 2\,{}^{16}O^{17}O \qquad \text{(5-33-iii)}$$

Results of our calculations for $O_2$ using the harmonic oscillator approximation are shown in Figures 5A and 5B and Table 2. Figure 5A shows $\Delta$ values of all isotopologues of $O_2$ as functions of 1/T; the inset shows the abundances of all isotopologues for $O_2$ having the stochastic distribution and an oxygen isotope composition equal to VSMOW (IUPAC, 1994). Values of $\Delta_{^{17}O^{17}O}$, $\Delta_{^{17}O^{18}O}$ and $\Delta_{^{18}O^{18}O}$ are ca. 1‰ at earth-surface temperatures, increase with decreasing temperature, and vary linearly with 1/T at temperatures less than ca. 400 K. Figure 5B shows values of $-1000\cdot\ln(K_i/K_{i\text{-}r})$ ($i$ = 1, 2 and 3) as functions of 1/T. The value of $\Delta_{34}$ (equal to the weighted sum of $\Delta_{^{16}O^{18}O}$ and $\Delta_{^{17}O^{17}O}$) approximately equals 0 because the abundance ratio, $\frac{[^{17}O^{17}O]}{[^{16}O^{18}O]}$, is very small; $\Delta_{35}$ exactly equals $\Delta_{^{17}O^{18}O}$ and $\Delta_{36}$ exactly equals $\Delta_{^{18}O^{18}O}$.

The atmospheric budget of $O_2$ is dominated by photosynthetic sources and respiration sinks, resulting in a distinctive heavy-isotope enrichment referred to as the Dole effect

(DOLE, 1937), which has been ascribed to fractionations during respiration (LANE and DOLE, 1956). In the absence of other fractionations, the kinetic theory of gases predicts this should lead to several tenths of per mil depletions of $\Delta_{^{17}O^{18}O}$ and $\Delta_{^{18}O^{18}O}$ rather than values of ca. +1‰ predicted for thermodynamic equilibrium. However, the Dole effect is also influenced by stratospheric ozone chemistry and by fossil-fuel and biomass combustion. In particular, atmospheric $O_2$ is anomalously low in $\delta^{17}O$ given its $\delta^{18}O$ value (i.e., it lies below the terrestrial fractionation line defined by earth rocks and waters on a plot of $\delta^{17}O$ vs. $\delta^{18}O$; LUZ et al., 1999). This phenomenon has been ascribed to non-mass-dependent isotopic fractionations associated with ozone chemistry (LUZ et al., 1999), or to unusual mass dependence of diffusive fractionations during respiration (YOUNG et al., 2002). While the fractionation of $^{18}O^{18}O$ and $^{17}O^{18}O$ during natural ozone chemistry are not well known, we speculate that they could differ from those predicted for thermodynamic equilibrium and diffusive fractionation, and therefore might constrain contributions of these various processes to the overall atmospheric budget.

Results of calculations for $N_2$, NO, CO, and $O_2$ using an anharmonic model of intra-molecular bonds and temperatures of 200 K, 300 K and 1000 K are listed in Table 2, where they can be compared with results using the harmonic oscillator approximation. Note that $\Delta$ values calculated using the harmonic oscillator model are slightly larger at low temperatures (ca. 200 K) and slightly lower at high temperatures (ca. 1000 K) than those calculated using the anharmonic non-rigid rotor model. Thus, results plotted in Figures 2 through 5 contain small systematic errors reflecting imperfections in the harmonic oscillator model. However, these errors are a small fraction of $\Delta$ values at any given temperature and we conclude that the harmonic oscillator model is sufficiently

accurate for the purposes of interpreting measured abundances of multiply-substituted isotopologues.

Table 2. Calculated Δ for isotopologues of $N_2$, NO, CO and $O_2$, at select temperature using harmonic or anharmonic oscillator models.

| | 200 K | | 300 K | | 1000 K | |
|---|---|---|---|---|---|---|
| | Harmonic | Anharmonic | Harmonic | Anharmonic | Harmonic | Anharmonic |
| **$N_2$** | | | | | | |
| $^{14}N^{15}N$ | -0.0069 | -0.0069 | -0.0039 | -0.0039 | -0.0002 | -0.0002 |
| $^{15}N^{15}N$ | 1.8619 | 1.8603 | 1.0456 | 1.0441 | 0.0636 | 0.0642 |
| **NO** | | | | | | |
| $^{15}N^{16}O$ | -0.0053 | -0.0053 | -0.0028 | -0.0028 | -0.0001 | -0.0001 |
| $^{14}N^{17}O$ | -0.0046 | -0.0046 | -0.0024 | -0.0024 | -0.0001 | -0.0001 |
| $^{15}N^{17}O$ | 1.2261 | 1.2240 | 0.6476 | 0.6458 | 0.0277 | 0.0281 |
| $^{14}N^{18}O$ | -0.0088 | -0.0088 | -0.0046 | -0.0046 | -0.0002 | -0.0002 |
| $^{15}N^{18}O$ | 2.3560 | 2.3518 | 1.2413 | 1.2378 | 0.0525 | 0.0533 |
| **CO** | | | | | | |
| $^{13}C^{16}O$ | -0.0073 | -0.0073 | -0.0040 | -0.0040 | -0.0002 | -0.0002 |
| $^{12}C^{17}O$ | -0.0189 | -0.0188 | -0.0104 | -0.0103 | -0.0005 | -0.0005 |
| $^{12}C^{18}O$ | -0.0362 | -0.0361 | -0.0198 | -0.0198 | -0.0010 | -0.0010 |
| $^{13}C^{17}O$ | 1.6735 | 1.6714 | 0.9197 | 0.9179 | 0.0487 | 0.0487 |
| $^{13}C^{18}O$ | 3.2134 | 3.2094 | 1.7623 | 1.7589 | 0.0924 | 0.0924 |
| **$O_2$** | | | | | | |
| $^{16}O^{17}O$ | -0.0036 | -0.0036 | -0.0017 | -0.0017 | -0.0001 | -0.0001 |
| $^{16}O^{18}O$ | -0.0069 | -0.0068 | -0.0033 | -0.0033 | -0.0001 | -0.0001 |
| $^{17}O^{17}O$ | 0.8274 | 0.8254 | 0.4063 | 0.4047 | 0.0128 | 0.0137 |
| $^{17}O^{18}O$ | 1.5899 | 1.5862 | 0.7782 | 0.7751 | 0.0243 | 0.0261 |
| $^{18}O^{18}O$ | 3.0569 | 3.0498 | 1.4910 | 1.4850 | 0.0460 | 0.0495 |

Note that all values of Δ for the diatomic molecules discussed above vary linearly with 1/T when temperature is lower than ca. 600 to 400 K. This reflects the same factors that control the temperature dependence of better-known inter-molecular isotope exchange reactions (e.g., BIGELEISEN and MAYER, 1947; O'NEIL, 1986). BIGELEISEN and MAYER (1947) showed that expressions for partition function ratios such as eqn 5-11, can be approximated as follows:

$$\frac{Q_2}{Q_1} = 1 + \left( \frac{1}{2} - \frac{1}{U_2} + \frac{1}{e^{-U_2} - 1} \right) (U_1 - U_2) = 1 + G(U_1 - U_2) \qquad (5\text{-}34)$$

where $U_i = hc\omega_i/kT$. Because vibrational wave numbers for the molecules considered in this section are generally between 1600 to 2400 $cm^{-1}$, $U_2$ values are generally larger than 5 when temperature is below 400 K. In this case, $G$ approaches a value of 0.5 and partition function ratios vary linearly with 1/T. At higher temperatures, where $U_2$ values are smaller than 5, $G$ converges toward a value of $U_2/12$ and partition function ratios instead vary linearly with $1/T^2$. Hence, equilibrium constants for the isotope exchange reactions we consider should vary linearly with 1/T below ca. 600 to 400 K, and non-linearly with 1/T at higher temperatures.

### 3.5 TRI-ATOMIC MOLECULES

As the number of atoms in a molecule increases, it becomes increasingly difficult to predict the equilibrium distribution of isotopologues both due to gaps in the spectroscopic data and the larger number of independent isotope exchange reactions that must be considered. Moreover, anharmonic models of intra-molecular bonds are more difficult to formulate and evaluate because the vibrational-rotational potential energy surface is

Table 3. Calculated zero point energies and normal mode wave numbers for all isotopologues of $CO_2$ and $N_2O$, using potential energy surfaces from ZÚÑIGA et al. (2001) and ZÚÑIGA et al. (1999).

| | Zero point energy($cm^{-1}$) | $\varpi_1$($cm^{-1}$) | $\varpi_2^+$($cm^{-1}$) | $\varpi_3$($cm^{-1}$) |
|---|---|---|---|---|
| $CO_2$ | | | | |
| $^{16}O^{12}C^{16}O$ | 2525.394 | 1348.479 | 670.315 | 2387.185 |
| $^{16}O^{13}C^{16}O$ | 2472.905 | 1348.479 | 651.237 | 2319.243 |
| $^{16}O^{12}C^{17}O$ | 2507.955 | 1328.175 | 667.609 | 2377.682 |
| $^{16}O^{12}C^{18}O$ | 2492.277 | 1309.544 | 665.205 | 2369.462 |
| $^{16}O^{13}C^{17}O$ | 2455.240 | 1328.154 | 648.452 | 2309.472 |
| $^{17}O^{12}C^{17}O$ | 2490.437 | 1308.042 | 664.892 | 2367.872 |
| $^{16}O^{13}C^{18}O$ | 2439.355 | 1309.467 | 645.976 | 2301.041 |
| $^{17}O^{12}C^{18}O$ | 2474.686 | 1289.553 | 662.478 | 2359.382 |
| $^{17}O^{13}C^{17}O$ | 2437.498 | 1308.042 | 645.654 | 2299.360 |
| $^{18}O^{12}C^{18}O$ | 2458.866 | 1271.185 | 660.056 | 2350.649 |
| $^{17}O^{13}C^{18}O$ | 2421.542 | 1289.536 | 643.168 | 2290.624 |
| $^{18}O^{13}C^{18}O$ | 2405.519 | 1271.185 | 640.673 | 2281.620 |
| $N_2O$ | | | | |
| $^{14}N^{14}N^{16}O$ | 2362.891 | 1293.360 | 594.047 | 2273.531 |
| $^{14}N^{15}N^{16}O$ | 2324.403 | 1291.559 | 580.468 | 2224.518 |
| $^{15}N^{14}N^{16}O$ | 2339.811 | 1276.422 | 590.511 | 2250.898 |
| $^{15}N^{15}N^{16}O$ | 2301.072 | 1275.062 | 576.848 | 2201.112 |
| $^{14}N^{14}N^{17}O$ | 2347.536 | 1270.870 | 591.559 | 2269.847 |
| $^{14}N^{15}N^{17}O$ | 2308.882 | 1268.802 | 577.922 | 2220.888 |
| $^{15}N^{14}N^{17}O$ | 2324.378 | 1254.108 | 588.008 | 2246.910 |
| $^{15}N^{15}N^{17}O$ | 2285.474 | 1252.506 | 574.286 | 2197.158 |
| $^{14}N^{14}N^{18}O$ | 2333.729 | 1250.451 | 589.349 | 2266.682 |
| $^{14}N^{15}N^{18}O$ | 2294.920 | 1248.131 | 575.659 | 2217.776 |
| $^{15}N^{14}N^{18}O$ | 2310.497 | 1233.829 | 585.785 | 2243.483 |
| $^{15}N^{15}N^{18}O$ | 2271.441 | 1231.997 | 572.009 | 2193.768 |

$^+$: $\omega_2$ is doubly-degenerate.

complicated and the interaction between rotation and vibration is often strong. For these reasons, the only tri-atomic (or higher order) molecules we consider are $CO_2$ and $N_2O$, both of which have full spectroscopic data and accurate potential energy surfaces available in the literature (CHEDIN, 1979; CHEDIN and TEFFO, 1984; ZÚÑIGA et al., 1999; ZÚÑIGA et al., 2001). The models we present for these molecules are based upon the same type of 'Urey-type' treatment of vibrational energies discussed above. The Appendix presents additional calculations made using higher-order theory to test the validity of the approximations used in this approach. These tests suggest the 'Urey' method of calculating partition function ratios is adequate for our purposes, even for tri-atomic molecules.

**$CO_2$:** The four required system components for $CO_2$ were chosen to be $^{16}O^{12}C^{16}O$, $^{16}O^{13}C^{16}O$, $^{16}O^{12}C^{17}O$ and $^{16}O^{12}C^{18}O$. The set of eight independent exchange reactions that go with these system components are listed above in equations 5-8i through 5-8viii (Section 2.1). Zero point energy and normal mode frequencies of $CO_2$ isotopologues (Table 3) were calculated using the potential energy surface from ZÚÑIGA et al. (2001). Results of our calculations for $CO_2$ using the harmonic oscillator approximation are shown in Figures 6A and 6B and Table 4. Figure 6A shows $\Delta$ values of all isotopologues of $CO_2$ as functions of 1/T. The inset shows the abundances of all isotopologues for $CO_2$ having the stochastic distribution, a $^{13}C/^{12}C$ ratio equal to PDB (CRAIG, 1957) and an oxygen isotope composition equal to VSMOW (IUPAC, 1994). Values of $\Delta_{^{18}O^{13}C^{18}O}$, $\Delta_{^{17}O^{13}C^{18}O}$, $\Delta_{^{17}O^{13}C^{17}O}$, $\Delta_{^{16}O^{13}C^{18}O}$, $\Delta_{^{16}O^{13}C^{17}O}$ and $\Delta_{^{18}O^{12}C^{18}O}$ are all between ca. 0.5 and 2‰ at earth-surface temperatures, increase with decreasing temperature, and vary linearly with 1/T at temperatures < 400 K. Figure 6B shows values of $-1000 \cdot \ln(K_i / K_{i\text{-}r})$ ($i$ = 1 through

8) as functions of 1/T (values of $K_{i\text{-}r}$ for these reactions are listed in Section 2 immediately following equation 5-9). The $\Delta_{46}$ value (equal to the weighted sum of $\Delta_{^{16}O^{12}C^{18}O}$, $\Delta_{^{17}O^{12}C^{17}O}$ and $\Delta_{^{16}O^{13}C^{17}O}$) is approximately 0 due to low abundances of $^{17}O^{12}C^{17}O$ and $^{16}O^{13}C^{17}O$ compared with that of $^{16}O^{12}C^{18}O$ (Figure 5A). Similarly, $\Delta_{47}$ (equal to the weighted sum of $\Delta_{^{16}O^{13}C^{18}O}$, $\Delta_{^{17}O^{12}C^{18}O}$ and $\Delta_{^{17}O^{13}C^{17}O}$) is only slightly greater than $\Delta_{^{16}O^{13}C^{18}O}$, and $\Delta_{48}$ (equal to the weighted sum of $\Delta_{^{18}O^{12}C^{18}O}$ and $\Delta_{^{17}O^{13}C^{18}O}$) is only slightly greater than $\Delta_{^{18}O^{12}C^{18}O}$ at any given temperature. Alternate calculated abundances of $CO_2$ isotopologues using spectroscopic data from CHEDIN (1979) and CHEDIN and TEFFO (1984) are also provided in Table 4 for comparison. Differences between these results and those based on the ZÚÑIGA et al. (2001) potential energy surface model are up to ~ 0.3 ‰ at 200 K (though generally < 0.1 ‰). These differences are detectable with existing analytical methods (EILER and SCHAUBLE, 2004) and suggest that analyses of $\Delta_i$ values in equilibrated mixtures of $CO_2$ isotopologues could be used to chose between or otherwise constrain models of the $CO_2$ molecule.

To the best of our knowledge, $^{18}O^{13}C^{16}O$ is the only multiply substituted isotopologue to be precisely measured in atmospheric samples. These data are presented in EILER and SCHAUBLE (2004). Briefly, the atmosphere is enriched by ca. 0.7 to 0.8 ‰ in $\Delta_{47}$, consistent with thermodynamic equilibrium at earth-surface temperatures being the first-order control, but with a small (~0.2 ‰) but consistent deficit in $\Delta_{47}$ that might reflect diffusive fractionations during photosynthetic carbon fixation and additions to air of high-temperature anthropogenic $CO_2$. Variations in $\Delta_{47}$ with time and location are likely to result from variable temperatures of equilibration between air and seawater or plant

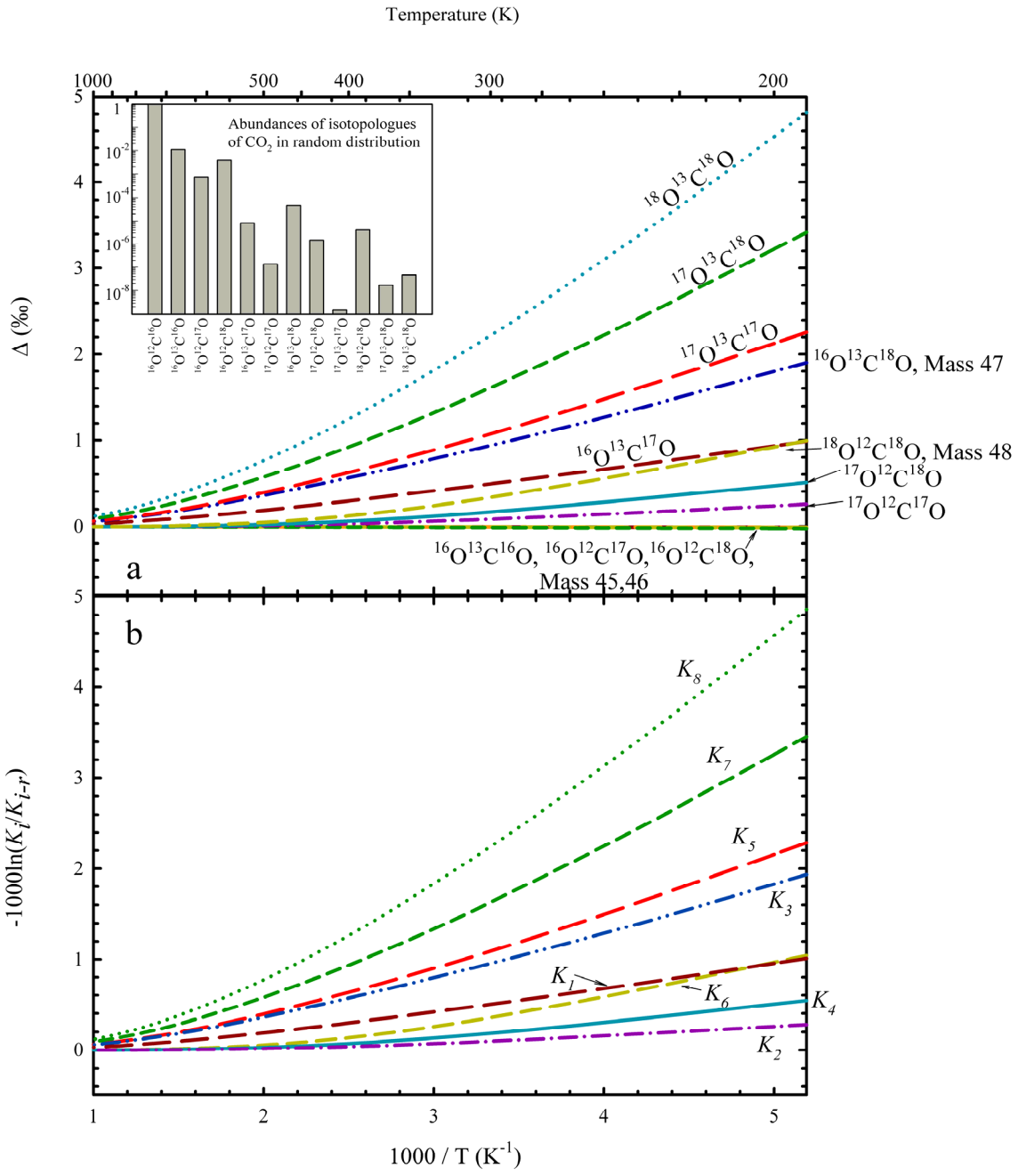


**Figure 6.** A: Variation of Δ values of all isotopologues of $CO_2$ with 1/T; the inset shows the abundances of all isotopologues of $CO_2$ for the stochastic distribution, a $^{13}C/^{12}C$ ratio equal to PDB, and an oxygen isotope composition equal to VSMOW. B: Variation of $-1000 \cdot \ln(K_i / K_{i\text{-}random})$ ($i$ = 1 to 8) with 1000/T for the isotope exchange reactions in equations 5-8i through 5-8viii.

leaf-water, and variable contributions of anthropogenic sources. It is possible that the abundances of multiply-substituted isotopologues of $CO_2$ in the stratosphere where photochemical reactions contribute significantly to its budget will differ even more greatly from the existing tropospheric measurements.

**$N_2O$:** The four required system components for $N_2O$ were chosen to be $^{14}N^{14}N^{16}O$, $^{14}N^{15}N^{16}O$, $^{14}N^{14}N^{17}O$ and $^{14}N^{14}N^{18}O$. The set of eight independent exchange reactions that go with these system components are:

$$^{14}N^{14}N^{16}O + {}^{15}N^{15}N^{16}O \overset{K_1}{\rightleftharpoons} {}^{14}N^{15}N^{16}O + {}^{15}N^{14}N^{16}O \quad \text{(5-35-i)}$$

$$^{14}N^{14}N^{16}O + {}^{15}N^{14}N^{17}O \overset{K_2}{\rightleftharpoons} {}^{15}N^{14}N^{16}O + {}^{14}N^{14}N^{17}O \quad \text{(5-35-ii)}$$

$$2{}^{14}N^{14}N^{16}O + {}^{15}N^{15}N^{17}O \overset{K_3}{\rightleftharpoons} {}^{14}N^{15}N^{16}O + {}^{15}N^{14}N^{16}O + {}^{14}N^{14}N^{17}O \quad \text{(5-35-iii)}$$

$$^{14}N^{14}N^{16}O + {}^{14}N^{15}N^{17}O \overset{K_4}{\rightleftharpoons} {}^{14}N^{15}N^{16}O + {}^{14}N^{14}N^{17}O \quad \text{(5-35-iv)}$$

$$^{14}N^{14}N^{16}O + {}^{14}N^{15}N^{18}O \overset{K_5}{\rightleftharpoons} {}^{14}N^{15}N^{16}O + {}^{14}N^{14}N^{18}O \quad \text{(5-35-v)}$$

$$^{14}N^{14}N^{16}O + {}^{15}N^{14}N^{18}O \overset{K_6}{\rightleftharpoons} {}^{15}N^{14}N^{16}O + {}^{14}N^{14}N^{18}O \quad \text{(5-35-vi)}$$

$$2{}^{14}N^{14}N^{16}O + {}^{15}N^{15}N^{18}O \overset{K_7}{\rightleftharpoons} {}^{14}N^{15}N^{16}O + {}^{15}N^{14}N^{16}O + {}^{14}N^{14}N^{18}O \quad \text{(5-35-vii)}$$

$$^{14}N^{15}N^{16}O \overset{K_8}{\rightleftharpoons} {}^{15}N^{14}N^{16}O \quad \text{(5-35-viii)}$$

Zero point energies and normal mode frequencies for $N_2O$ (Table 3) were calculated using the potential energy surface of ZÚÑIGA et al. (1999). Results of our calculations for $N_2O$ using the harmonic oscillator approximation are shown in Figures 7A through 7C, 8a and 8b, and Table 4. Figures 7A through 7C show $\Delta$ values of all isotopologues of $N_2O$ as functions of 1/T; the inset to Figure 7A shows abundances of all isotopologues for $N_2O$ having the stochastic distribution, a $^{15}N/^{14}N$ ratio equal to atmospheric $N_2$ (IUPAC, 1994), and an oxygen isotope composition equal

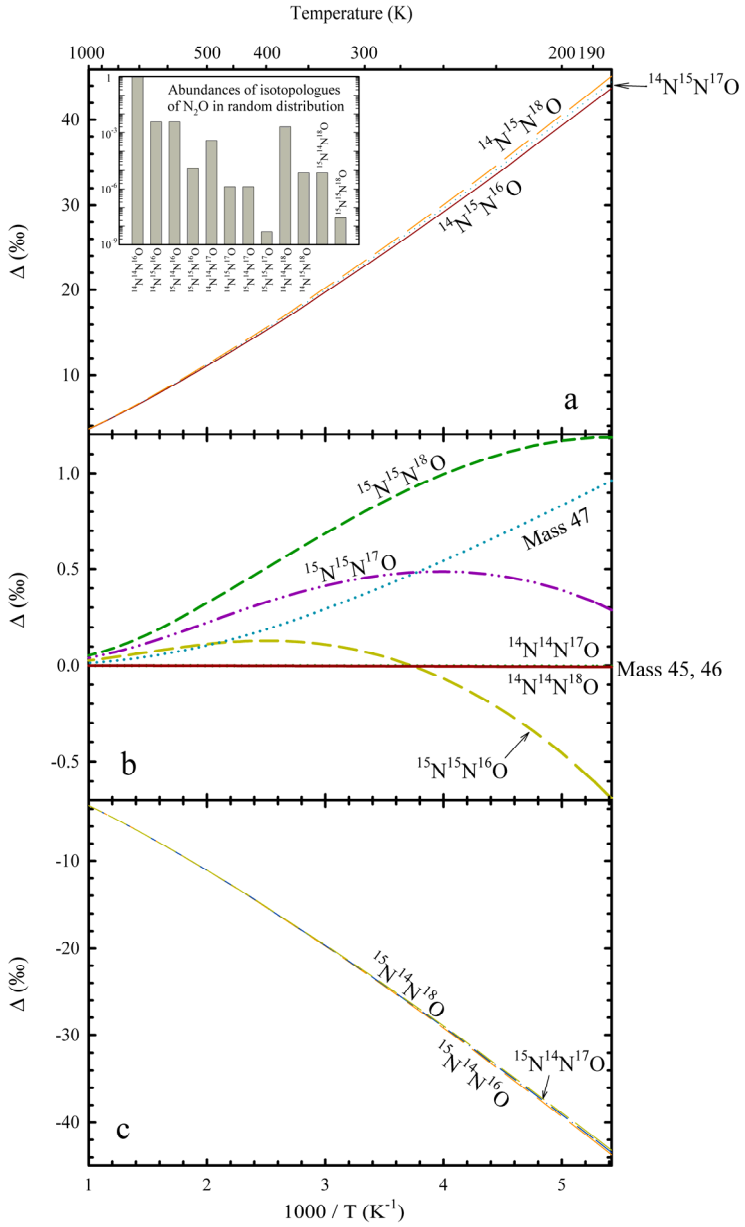


**Figure 7.** A: Variation of Δ values of isotopologues $^{14}N^{15}N^{x}O$, where $x$ = 16,17, or 18, with 1/T; the inset shows the abundances of all isotopologues of $N_2O$ for the stochastic distribution, a $^{15}N/^{14}N$ ratio equal to atmospheric $N_2$, and an oxygen isotope ratio equal to VSMOW. B: Variation of Δ values of isotopologues $^{14}N^{14}N^{x}O$, where $x$ = 17 or 18, and $^{15}N^{15}N^{x}O$, where $x$ = 16,17, or 18, with 1/T. C: Variation of Δ values of isotopologues, $^{15}N^{14}N^{x}O$, where $x$ =16,17, or 18, with 1/T.

to VSMOW (IUPAC, 1994). Figures 8A and 8B show values of $-1000 \cdot \ln(K_i / K_{i\text{-}r})$ (i = 1 through 8) as functions of 1/T. Note that unlike all other molecules considered in this study, relationships between $-1000 \cdot \ln(K_i / K_{i\text{-}r})$ and $\Delta_i$ values are not simple for $N_2O$. Values of $-1000 \cdot \ln(K_i / K_{i\text{-}r})$ for reactions 5-34i through 34vii have magnitudes and temperature dependences resembling those of analogous reactions of other molecules considered in this study, whereas $-1000 \cdot \ln(K_i / K_{i\text{-}r})$ for reaction 5-34viii is exceptionally large and strongly dependent on temperature. The aberrant behaviors of $N_2O$ isotopologues (discussed below) can be attributed to this large equilibrium constant for reaction 5-34viii.

There are several noteworthy differences between results for $N_2O$ and $CO_2$, despite similarities in masses of isotopologues and their constituent atoms. First, values of $\Delta_{^{15}N^{15}N^{x}O}$ (where x = 16, 17, or 18) differ significantly from zero at low temperature, but do not increase monotonically with decreasing temperature. Second, values of $\Delta_{^{14}N^{15}N^{x}O}$ are large positive numbers more than an order of magnitude larger than $\Delta$ values for any $CO_2$ isotopologue. Finally, values of $\Delta_{^{15}N^{14}N^{x}O}$ are large negative numbers also more than an order of magnitude larger in absolute value than $\Delta$ values for any $CO_2$ isotopologue, and the only $\Delta$ values of any isotopologue considered in this study that are significantly less than 0. Note that large positive and negative $\Delta$ values for the $^{14}N^{15}N^{18}O$ and $^{14}N^{15}N^{18}O$ isotopologues are similar in absolute value to one another at any given temperature, so that $\Delta_{47}$ (equal to the weighted sum of $\Delta_{^{14}N^{15}N^{18}O}$, $\Delta_{^{15}N^{14}N^{18}O}$, and $\Delta_{^{15}N^{15}N^{17}O}$) is only ca. 0.5 ‰ at earth-surface temperatures and has a temperature dependence resembling doubly-substituted isotopologues of other molecules we considered.

The unusual behaviors of $N_2O$ result from the affinity of $^{15}N$ for the central position in $N_2O$, stabilizing $^{14}N^{15}N^{x}O$ species relative to $^{15}N^{14}N^{x}O$ species. The zero-point

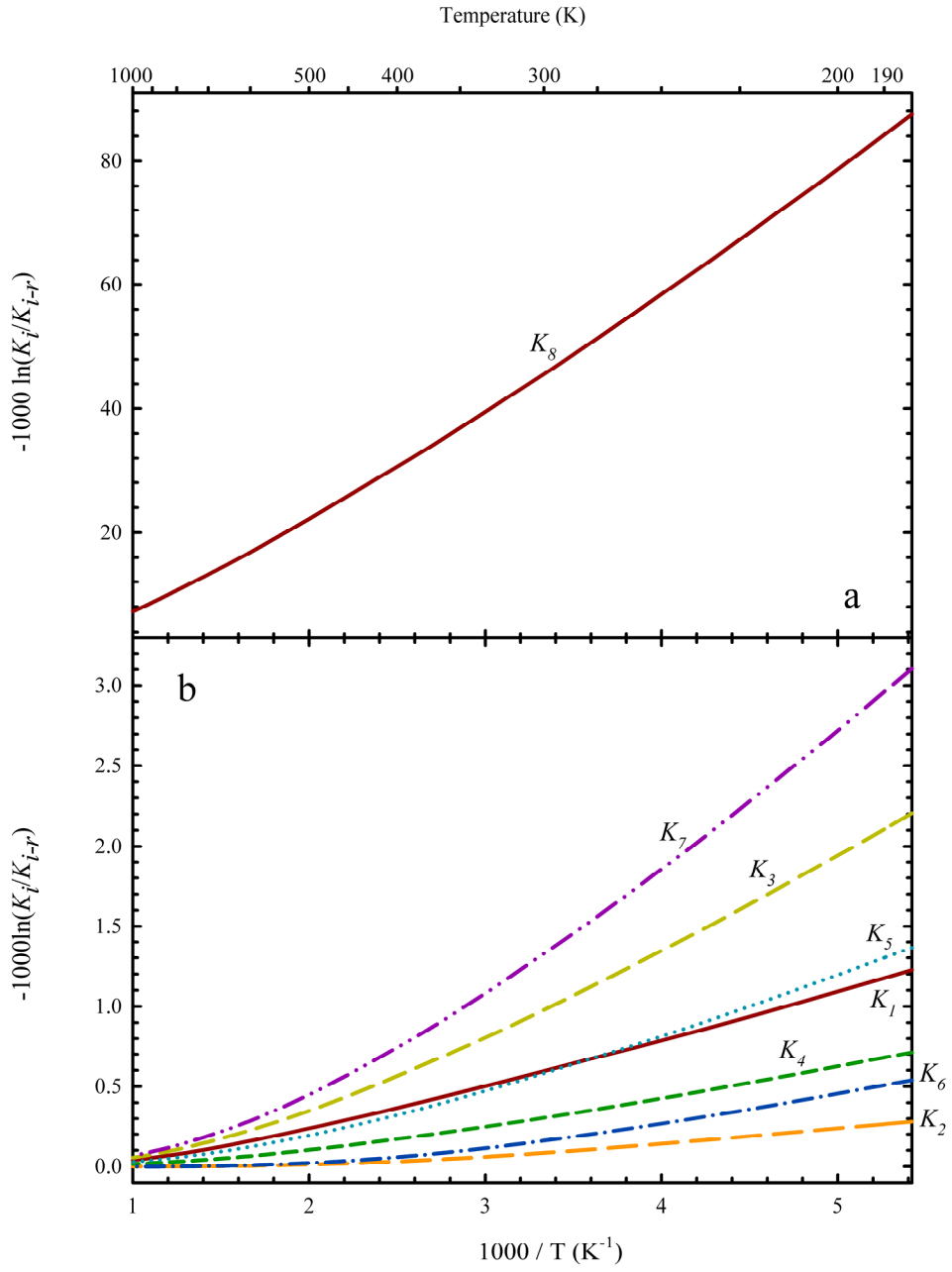


**Figure 8.** A: Variation of -1000·ln($K_i$ /$K_{i\text{-}random}$) ($i$ = 8) with 1000/T for the isotope exchange reaction in equation 5-34viii. B: Variation of -1000· ln($K_i$ /$K_{i\text{-}random}$) ($i$ = 1 to 7) with 1000/T for the isotope exchange reactions in equations 5-34i through 5-34vii.

energies of $^{14}N^{15}N^{x}O$ species are ca. 15.5 $cm^{-1}$ less than those of $^{15}N^{14}N^{x}O$ species having the same mass (Table 3). These differences lead to ca. 80‰ enrichment of $^{14}N^{15}N^{16}O$

relative to $^{15}N^{14}N^{16}O$ at 200 K. Furthermore, the complex temperature dependence of $\Delta_{^{15}N^{15}N^{16}O}$ can be explained by different temperature dependencies of the reduced partition functions of $\Delta_{^{14}N^{15}N^{16}O}$ and $\Delta_{^{15}N^{14}N^{16}O}$. Similar to equation 5-25, the relationship between $\Delta_{^{15}N^{15}N^{16}O}$ and $K_1$ is:

$$\ln\left(\frac{\Delta_{^{15}N^{15}N^{16}O}}{1000}+1\right)=\ln\left(\frac{\Delta_{^{15}N^{14}N^{16}O}}{1000}+1\right)+\ln\left(\frac{\Delta_{^{14}N^{15}N^{16}O}}{1000}+1\right)-\ln\frac{K_1}{K_{1-r}} \qquad (5\text{-}36)$$

At low temperatures (e.g. < 250 K), $\ln\left(\frac{\Delta_{^{15}N^{14}N^{16}O}}{1000}+1\right)+\ln\left(\frac{\Delta_{^{14}N^{15}N^{16}O}}{1000}+1\right)$ is a negative number and smaller than $\ln\frac{K_1}{K_{1-r}}$, giving rise to the negative $\Delta_{^{15}N^{15}N^{16}O}$ value; while at high temperatures, it is a small negative number close to zero.

Alternative calculations of the abundances of $N_2O$ isotopologues using spectroscopic data, zero point energies and normal mode frequencies from ZÚÑIGA et al. (2003) are also listed in Table 4 for comparison. These results are generally similar to those based on the ZÚÑIGA et al. (1999) potential energy surface, although a notable exception is the ca. 2.5 ‰ difference in $\Delta_{^{15}N^{15}N^{16}O}$ at low temperature. This difference is difficult to understand given agreement for all other isotopologues; one possible explanation is that the spectroscopic data for $^{15}N^{15}N^{16}O$ from ZÚÑIGA et al. (2003) are not consistent with those for other isotopologues considered in that study.

The atmospheric budget of $N_2O$ is dominated by sources from the terrestrial biosphere and oceans and photochemical sinks (RAHN and WAHLEN, 2000; TOYODA et al., 2002; MCLINDEN et al., 2003). Recent research on its budget has been motivated, in part, by the fact that it is a greenhouse gas with a large, though indirect anthropogenic source

Table 4. Comparison of calculated Δ values for isotopologues of $N_2O$ and $CO_2$ at select temperatures, using data in Table 3 (I) and data from ZÚÑIGA et al. (2001) for $CO_2$ and ZÚÑIGA et al. (2003) for $N_2O$ (II).

| | 200 K | | 300 K | | 1000 K | |
|---|---|---|---|---|---|---|
| | I | II | I | II | I | II |
| **$CO_2$** | | | | | | |
| $^{16}O^{13}C^{16}O$ | -0.0082 | -0.0082 | -0.0043 | -0.0043 | -0.0003 | -0.0003 |
| $^{16}O^{12}C^{17}O$ | -0.0117 | -0.0121 | -0.0060 | -0.0062 | -0.0003 | -0.0004 |
| Mass 45 | -0.0084 | -0.0085 | -0.0044 | -0.0044 | -0.0003 | -0.0003 |
| $^{16}O^{12}C^{18}O$ | -0.0225 | -0.0228 | -0.0114 | -0.0116 | -0.0007 | -0.0007 |
| $^{16}O^{13}C^{17}O$ | 0.9347 | 0.9477 | 0.4888 | 0.4982 | 0.0306 | 0.0327 |
| $^{17}O^{12}C^{17}O$ | 0.2370 | 0.4537 | 0.0848 | 0.2124 | -0.0007 | 0.0181 |
| Mass 46 | -0.0205 | -0.0208 | -0.0104 | -0.0106 | -0.0006 | -0.0006 |
| $^{16}O^{13}C^{18}O$ | 1.7977 | 1.8093 | 0.9384 | 0.9482 | 0.0582 | 0.0609 |
| $^{17}O^{12}C^{18}O$ | 0.4674 | 0.5187 | 0.1681 | 0.2011 | -0.0010 | 0.0056 |
| $^{17}O^{13}C^{17}O$ | 2.1273 | 2.3922 | 1.0738 | 1.2332 | 0.0616 | 0.0865 |
| Mass 47 | 1.7552 | 1.7680 | 0.9138 | 0.9243 | 0.0563 | 0.0592 |
| $^{18}O^{12}C^{18}O$ | 0.9217 | 1.0100 | 0.3329 | 0.3900 | -0.0013 | 0.0104 |
| $^{17}O^{13}C^{18}O$ | 3.2220 | 3.5192 | 1.6078 | 1.7888 | 0.0892 | 0.1187 |
| Mass 48 | 0.9311 | 1.0202 | 0.3381 | 0.3956 | -0.0010 | 0.0108 |
| $^{18}O^{13}C^{18}O$ | 4.5322 | 4.6997 | 2.2192 | 2.3296 | 0.1169 | 0.1391 |
| **$N_2O$** | | | | | | |
| $^{14}N^{15}N^{16}O$ | 39.3299 | 39.3517 | 22.8067 | 22.8072 | 3.6144 | 3.6031 |
| $^{15}N^{14}N^{16}O$ | -39.3302 | -39.3736 | -22.8089 | -22.8282 | -3.6146 | -3.6116 |
| $^{14}N^{14}N^{17}O$ | -0.0032 | -0.0030 | -0.0015 | -0.0013 | -0.0001 | 0.0000 |
| Mass 45 | -0.0003 | -0.0106 | -0.0011 | -0.0101 | -0.0001 | -0.0041 |
| $^{15}N^{15}N^{16}O$ | -0.4564 | 2.4191 | 0.0727 | 2.5882 | 0.0261 | 1.1336 |
| $^{14}N^{15}N^{17}O$ | 39.9751 | 39.9314 | 23.1163 | 23.0706 | 3.6293 | 3.6018 |
| $^{15}N^{14}N^{17}O$ | -39.1061 | -39.1274 | -22.7294 | -22.7313 | -3.6155 | -3.6056 |
| $^{14}N^{14}N^{18}O$ | -0.0062 | -0.0065 | -0.0028 | -0.0030 | -0.0001 | -0.0002 |
| Mass 46 | -0.0086 | 0.0103 | -0.0020 | 0.0146 | 0.0001 | 0.0074 |
| $^{15}N^{15}N^{17}O$ | 0.3899 | 0.3162 | 0.4538 | 0.3991 | 0.0401 | 0.0197 |
| $^{14}N^{15}N^{18}O$ | 40.5659 | 40.5792 | 23.3982 | 23.3915 | 3.6426 | 3.6272 |
| $^{15}N^{14}N^{18}O$ | -38.8990 | -38.8564 | -22.6568 | -22.6107 | -3.6163 | -3.5874 |
| Mass 47 | 0.8333 | 0.8612 | 0.3708 | 0.3904 | 0.0131 | 0.0199 |
| $^{15}N^{15}N^{18}O$ | 1.1670 | 1.1484 | 0.8012 | 0.7867 | 0.0527 | 0.0454 |

(resulting from the use of agricultural fertilizers). Stable isotope data are a prominent part of this research, and take advantage of large isotopic contrasts between biosphere sources and the mean atmosphere. The large, distinctive thermodynamic fractionations predicted for $N_2O$ isotopologues (Figures 7 and 8), combined with strong isotopic fractionations associated with photolysis (BLAKE et al., 2003) suggest that measurements of multiply-substituted isotopologues could contribute additional constraints to this problem.

## 4. DISCUSSION AND CONCLUSIONS

Results of our calculations can be summarized as follows:

1. Whereas most singly-substituted isotopologues do not have measurable deviations from the stochastic distribution, multiply-substituted isotopologues typically have per mil level enrichments at earth-surface temperatures.
2. In most cases, deviations from the stochastic distribution ($\Delta$ values) increase approximately linearly with 1/T at temperatures < ca. 600 to 400 K.
3. Abundances of multiply-substituted isotopologues of $N_2O$ are exceptions to the preceding generalizations. They vary complexly with temperature, and include tens of per mil enrichments and depletions of $^{14}N^{15}N^{x}O$, and $^{15}N^{14}N^{x}O$, respectively (where $x$ = 16, 17, 18). We speculate that similarly complex and large enrichments and depletions exist for other tri-atomic and higher order, asymmetric molecules (i.e., those with highest symmetry of $C_{\infty v}$ among their isotopologues).

These results provide a framework for interpretation of the natural abundances of multiply-substituted isotopologues. For example, contributions of processes involving

low-temperature, thermodynamically controlled isotopic exchange (e.g., air-sea and air-leaf water exchange of $CO_2$) could be identified as contributors to budgets of atmospheric gases. Moreover, the size and temperature dependence of $\Delta$ values of most multiply-substituted isotopologues suggest they can be used as geothermometers. Such thermometers differ from more familiar ones based on differences in bulk stable isotopic composition between co-existing phases. They instead involve homogeneous equilibria (e.g., isotopic distribution within a population of gaseous $CO_2$ molecules alone) and are effectively independent of bulk isotopic composition of that population. Furthermore, multiple, independent thermometers exist for all molecules having more than one multiply-substituted isotopologue (e.g., $^{18}O^{13}C^{16}O$ and $^{18}O^{12}C^{18}O$ for $CO_2$). Thus, temperatures estimated by this method can be tested for internal consistency. Finally, the zero-point-energy differences between multiply-substituted isotopologues and their isotopically 'normal' and singly-substituted relatives (Table 3) are also likely to manifest themselves in kinetic fractionations during non-equilibrium reactions (e.g., YUNG and MILLER, 1997). Our calculations provide guidance as to the sizes and directions of these effects.

It remains to be seen which of the isotope exchange reactions modeled here are manifested in natural atmospheric gases, other than initial evidence that $^{18}O^{13}C^{16}O$ in air is dominantly controlled by thermodynamic equilibrium (EILER and SCHAUBLE, 2004). Furthermore, it must be determined which of these reactions resist continuous re-equilibration in the atmosphere and in the laboratory during sample preparation and analysis. Evidence to-date suggests that such re-equilibration does not occur for $CO_2$ over timescales of days to weeks at atmospheric pressures and temperatures, and does not

take place during most vacuum and gas-chromatography sample preparation techniques nor during dual-inlet mass spectrometry (EILER and SCHAUBLE, 2004). Further work will be needed to establish whether this also holds true of other common molecular gases.

Measurements of multiply-substituted isotopologues place special demands on techniques of sample preparation and mass spectrometry. These are detailed by EILER and SCHAUBLE (2004). Briefly, they include: 1) Enough multiple static collectors to simultaneously measure isotopically 'normal', singly-substituted, and multiply-substituted isotopologues (e.g., for $CO_2$ at least four collectors needed and six are preferred); 2) High sensitivity (e.g. ability to stably register ion beams for species making up ca. 5-50 ppm of ca. μmolar samples) and high precision ($1\sigma < 0.1$ ‰). Fortunately, commonly available faraday cups and counting systems, when appropriately configured and read through $10^{12}$ Ohm resistors, appear to be sufficient for this task. 3) Sample preparation procedures that remove potential interferences from other common molecular gases (e.g., $^{16}O_3$ on $^{18}O^{12}C^{18}O$), and more problematically halocarbons and hydrocarbons. Finally, 4) as with more familiar measurements of singly-substituted isotopologues, measurements of some multiply-substituted isotopologues must be ion-corrected to account for 'internal isobars' of one isotopologue of the analyte gas on another (e.g., $^{16}O^{13}C^{18}O$ and $^{17}O^{12}C^{18}O$ for $CO_2$). We are not aware of any instrument capable of resolving these isobars and also capable of high-precision measurements of isotope ratios. Therefore, at present, all such isobars are corrected for the following procedures similar to the $^{17}O$ correction applied to conventional measurements of $\delta^{13}C$ of $CO_2$ (SANTROCK et al., 1985 and references therein). The related problem of resolving isotopomers (e.g., $^{14}N^{15}N^{18}O$ vs. $^{15}N^{14}N^{18}O$) should be addressable by either 1) spectroscopic methods (e.g.,

YUNG and MILLER, 1997), or 2) mass spectrometry of fragments (e.g., by monitoring $^{15}N^{18}O$ and $^{14}N^{18}O$ fragments during analysis of $N_2O$).

**ACKNOWLEDGEMENTS**

We thank Desheng Wang, Yiqin Gao, Wei-Chen Chen, Mitchio Okumura and Paul Asimow for discussion and inspiration, Paul Wennberg and Zhonghua Yang for their explanation of HITRAN; L. S. Rothman for offering HITRAN2k dataset; David Cole and two other anonymous reviewers who provided constructive comments and suggestions. This work is supported by a Packard Foundation grant to J.M.E., support to J.M.E. from the Davidow Endowment to Caltech, and from General Motors.

**REFERENCES**

Authier N., Bagland N., and Lefloch A. (1993) The 1992 Evaluation of Mass-Independent Dunham Parameters for the Ground-State of CO. *Journal of Molecular Spectroscopy* **160**(2), 590-592.

Bigeleisen J. and Mayer M. G. (1947) Calculation of equilibrium constants for isotopic exchange reactions. *J. Chem. Phys* **15**, 261-267.

Chedin A. (1979) The Carbon Dioxide Molecule: Potential, Spectroscopic, and Molecular Constants from its Infrared Spectrum. *Journal of Molecular Spectroscopy* **76**, 430-491.

Chedin A. and Teffo J.-L. (1984) The Carbon Dioxide Molecule: A New Derivation of Potential, Spectroscopic, and Molecular Constants. *Journal of Molecular Spectroscopy* **107**, 333-342.

Craig, H. (1957) Isotopic standards for carbon and oxygen and correction factors for mass-spectrometric analysis of carbon dioxide. *Geochim. Cosmochim. Acta,* **12**, 133-149

Davidson N. (1962) Statistical mechanics. **McGraw-Hill Series in advanced chemistry**, pp. 540.

Dole, M. (1935) The relative atomic weight of oxygen in water and air, *J. Am. Chem. Soc.*, **57**, 2731.

Dunham J. L. (1932) The Energy levels of a rotating vibrator. *Physical Review* **41**, 721-731.

Eiler J. and Schauble E. (2004) $^{18}O^{13}C^{16}C$ in earth's atmosphere, *GCA,* **68 (**23), 4767 - 4777.

Gamache R. R., Hawkins R. L., and Rothman L. S. (1990) Total internal partition sums in the temperature range 70-3000K: atmospheric linear molecules. *Journal of Molecular spectroscopy* **142**, 205-219.

Goorvitch D. (1994) Infrared CO Line List for the Chi(1)Sigma(+) State. *Astrophysical Journal Supplement Series* **95**(2), 535-552.

Herzberg G. (1945) Infrared and Raman Spectra of polyatomic molecules. D. Van Nostrand Company, Inc.

Huber K. P. and Herzberg G. (1979) Constants of Diatomic Molecules. **Molecular Spectra and Molecular Structure. IV**, 716.

IUPAC(International Union of Pure and applied Chemistry) (1994) Commission on Atomic Weights and Isotopic Abundances, Atomic weights of the elements 1993. *Pure and Applied Chemistry*, **66**, 2423-2444.

Kaye, Jack A.(1987) Mechanisms and observation for isotope fractionation of molecular species in planetary atmospheres, *Rev. Geophys*, **25**(8): 1609-1658.

Lane, G. A. and M. Dole, (1956) Fractionation of oxygen isotopes during respiration, *Science*, **123**, 574-576.

Lide David R. and Frederikse, H.P.R.(1994) CRC handbook of chemistry and physics, 74th edition, **4**-36~114, CRC press, Inc.

Luz B., Barkan, E., Bender, M.L., Thiemens, M.H. and Boering, K.A., (1999) Triple-isotope composition of atmospheric oxygen as a tracer of biosphere productivity. *Nature,* **400,** 547–550.

McLinden C. A., Prather M. J., Johnson M. S., (2003) Global modeling of the isotopic analogues of $N_2O$: Stratospheric distributions, budgets, and the $^{17}O^{18}O$ mass-independent anomaly, *J. Geophysical Research -Atmosphere*, **108**(D8): art. no. 4233.

Nielsen H. H. (1951) The vibration-rotation energies of molecules. *Reviews of Modern Physics* **23**(2), 90-136.

O'Neil J. R. (1986) Theoretical and experimental aspects of isotopic fractionation. **Reviews in Mineralogy Volume 16: Stable isotopes in high temperature geological processes, Ed.J.W. Valley, H.P. Taylor, Jr., J.R. O'Neil**, 1-40.

Pitzer K. S. (1953) Quantum Chemistry. **Prentice-Hall chemistry series**.

Press W. H., Teukolsky S. A., Vetterling W. T., and Flannery B. P. (2002) Numerical Recipes in C++: The Art of Scientific computing. 1002 p.

Present R.D. (1958) Kinetic theory of gases, **International Series in pure and applied physics, Ed. Leonard I. Schiff,** pp. 280.

Rahn T., and M. Wahlen, A reassessment of the global isotopic budget of atmospheric nitrous oxide, *Global Biogeochem. Cycles*, **14**, 537–543, 2000.

Richet P., Bottinga Y., and Javoy M. (1977) A review of hydrogen, carbon, nitrogen, oxygen, sulphur, and chlorine stable isotope fractionation among gaseous molecules. *Ann. Rev. Earth Planet. Sci.* **5**, 65-110.

Rothman L. S. and Young L. D. G. (1981) Infrared Energy-Levels and Intensities of Carbon-Dioxide. *Journal of Quantitative Spectroscopy & Radiative Transfer* **25**(6), 505-524.

Rothman L. S., Hawkins R. L., Wattson R. B., and Gamache R. R. (1992) Energy-Levels, Intensities, and Linewidths of Atmospheric Carbon-Dioxide Bands. *Journal of Quantitative Spectroscopy & Radiative Transfer* **48**(5-6), 537-566.

Rothman L. S., Barbe A., Benner D. C., Brown L. R., Camy-Peyret C., Carleer M. R., Chance K., Clerbaux C., Dana V., Devi V. M., Fayt A., Flaud J. M., Gamache R. R., Goldman A., Jacquemart D., Jucks K. W., Lafferty W. J., Mandin J. Y., Massie S. T., Nemtchinov V., Newnham D. A., Perrin A., Rinsland C. P., Schroeder J., Smith K. M., Smith M. A. H., Tang K., Toth R. A., Vander Auwera J., Varanasi P., and Yoshino K. (2003) The HITRAN molecular spectroscopic database: edition of 2000 including updates through 2001. *Journal of Quantitative Spectroscopy & Radiative Transfer* **82**(1-4), 5-44.

Santrock J., Studley, S.A. and Hayes, J.M., (1985) Isotopic analyses based on the mass spectrum of carbon dioxide. *Anal. Chem.* **57**, pp. 1444–1448.

Thompson J. B., Jr. (1982) Composition space: an algebraic and geometric approach. **Reviews in Mineralogy 10: Characterization of Metamorphism through Mineral Equilibria, Ed. J.M.Ferry**, 1-31.

Toyoda S., N. Yoshida, T. Urabe, S. Aoki, T. Nakazawa, S. Sugawara, and H. Honda**,** Fractionation of $N_2O$ isotopomers in the stratosphere, *J. Geophys. Res.*, **106**, 7515–7522, 2001.

Urey H. C. (1947) The thermodynamic properties of isotopic substances. *J. Chem. Soc. (London),*, 561-581.

Varberg T. D. and Evenson K. M. (1992) Accurate Far-Infrared Rotational Frequencies of Carbon-Monoxide. *Astrophysical Journal* **385**(2), 763-765.

Walker F. W., Parrington J. R., and Feiner F. (1989) Nuclides and isotopes.

Young Edward D; Galy, Albert; Nagahara, Hiroko (2002) Kinetic and equilibrium mass-dependent isotope fractionation laws in nature and their geochemical and cosmochemical significance, *Geochimica et Cosmochimica Acta*, **66**(6):1095-1104.

Yung Y. L. and Miller C. (1997) Isotopic Fractionation of Stratospheric Nitrous Oxide. *Science* **278**, 1778-1780.

Zúñiga J., Alacid M., Bastida A., Carvajal F. J., and Requena A. (1999) Determination of highly excited rovibrational states for $N_2O$ using generalized internal coordinates. *The Journal of Chemical Physics* **110**(13), 6339-6352.

Zúñiga J., Bastida A., Alacid M., and Requena A. (2001) Variational calculations of Rovibrational Energies for $CO_2$. *Journal of Molecular Spectroscopy* **205**, 62-72.

Zúñiga J., Bastida A., and Requena A. (2003) Theoretical calculations of vibrational frequencies and rotational constants of the $N_2O$ isotopomers. *Journal of Molecular Spectroscopy* **217**, 43–58.

## APPENDIX

The calculations presented in Section 3 of this study are based on several approximations made in the derivation of the Urey equation and its quantum-mechanical relatives. In this appendix, we present several calculations using higher-order theory made to test the accuracy of the harmonic oscillator and rigid rotor models. We make these tests for CO and $CO_2$ because their spectroscopic properties are relatively well known.

### ALTERNATE MODELS FOR CO

Table A1 shows the calculated Δ value for each isotopologue of CO at select temperatures based on three different methods: 1) the harmonic oscillator model (i.e., eqn. 5-11 in this paper); 2) an anharmonic model using the PITZER (1953) treatment (i.e., eqns 5-14 through 5-17); and, 3) a model in which each vibrotational partition function was calculated by numerical summation over several vibrational and rotational quantum energy levels using the following equation:

$$Q_{v,J}(T) = \sum_{v=0}\sum_{J=0}(2J+1)\cdot e^{-\frac{hcE(v,J)}{kT}} \qquad \text{(A-5-37)}$$

Input data for the first two methods are listed in Table 1, and are taken from HUBER and HERZBERG (1979). Three different sets of constraints were used for the third method: 1) a model using five Dunham parameter equations, in which data from Table 1 and eqn. 5-13 were used to calculate energy at each quantum level, with vibrational and rotational quantum numbers up to 70 and 200, respectively; 2) a model using a larger number of

Dunham parameters. In particular, 43 mass-independent Dunham parameters from AUTHIER (et al., 1993) were used to evaluate the energy for every isotopologue at

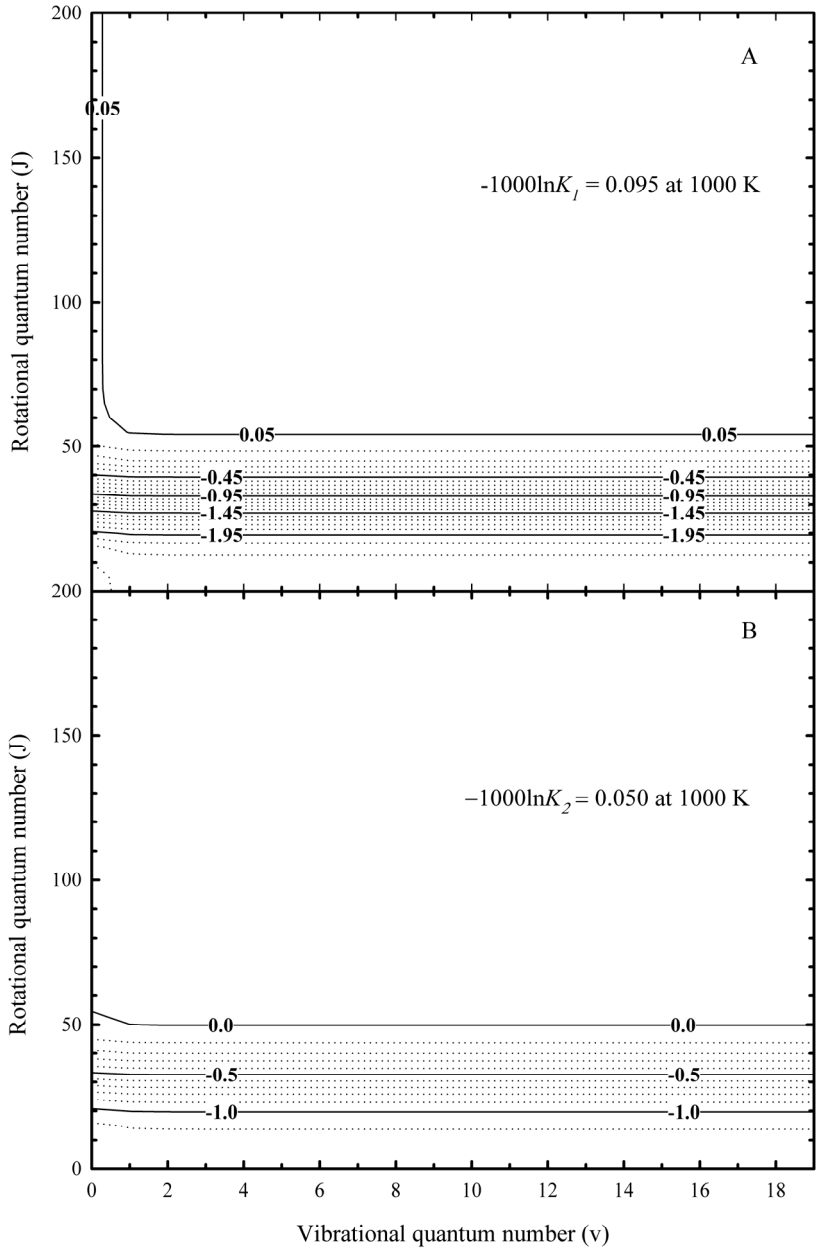


Figure A1. Sensitivity test for the value of A: -1000·ln$K_1$ and B: -1000·ln$K_2$ in 5- 32i and 32ii as a function of maximum vibrational and rotational quanta calculated.

each quantum level, including the zero point energy, and vibrational and rotational quantum numbers were calculated up to 70 and 200, respectively; and 3) a model based on the HITRAN database (**Hi**gh Resolution **Tran**smission), HITRAN2k (ROTHMAN et al., 2003). This database compiles 4477 transmissions between low and high energy states of all six isotopologues of the CO molecule from which we can deduce the energy of each state involved. The line-list for CO molecule in this database is mainly from GOORVITCH (1994), modified to incorporate experimental data from VARBERG and EVENSON (1992). The zero point energy from GOORVITCH (1994) was also adopted. After calculating the energy levels at each quantum number, eqn A-5-37 and eqn 5-18 were used to calculate the full partition function. Results of these calculations summarized in Table A1 indicate that differences between these models are effectively irrelevant for our purposes.

We also explored the number of energy levels required to calculate $-1000 \cdot \ln K_i$ ($i$ = 1,2) in eqn 5-32i and ii at 1000 K. Forty three Dunham parameters were used for this test. As shown in Figure A1-A and B, values of $-1000 \cdot \ln K_i$ ($i$ = 1,2) converge to within 0.05 per mil when vibrational energy levels larger than 2 and rotational energy levels larger than 60. At lower temperatures, an even smaller number of energy levels is required for convergence.

### ALTERNATE MODELS FOR $CO_2$

The spectroscopic properties of $CO_2$ are relatively well studied, but remain incomplete. ROTHMAN et al. (1992) present spectroscopic data for eight isotopologues: $^{16}O^{12}C^{16}O$ (155 vibrational energy levels); $^{16}O^{13}C^{16}O$ (78 vibrational energy levels); $^{16}O^{12}C^{18}O$ (59 vibrational energy levels); $^{16}O^{12}C^{17}O$ (26 vibrational energy levels);

$^{16}O^{13}C^{18}O$ (16 vibrational energy levels); $^{16}O^{13}C^{17}O$ (10 vibrational energy levels); $^{18}O^{12}C^{18}O$ (12 vibrational energy levels); $^{17}O^{12}C^{18}O$ (3 vibrational energy levels). These data are insufficient for a full analysis of Δ values for most multiply substituted isotopologues. However, the 16 known energy levels for $^{16}O^{13}C^{18}O$ is better than other multiply substituted isotopologues and sufficient for a first-order analysis. We calculated the rotational energy for each vibration level using spectroscopic constants $B_v$, $D_v$ and $H_v$ as follows:

$$E(v,J) = G_0 + G_v + B_v J(J+1) - D_v\left[J(J+1)\right]^2 + H_v\left[J(J+1)\right]^3 \qquad \text{(A-5-38)}$$

Where $G_0$ is zero point energy listed in Table 3, $G_v$ is the energy at each vibrational level with $J = 0$, and $G_v$, $B_v$, $D_v$ and $H_v$ are listed in ROTHMAN et al. (1992). Partition functions are directly summed over given vibrational quantum energy levels and calculated rotational quantum energy levels with $J$ up to 200 using an equation similar to 5-35, but including other factors:

$$Q_{v,J}(T) = \sum_{v_1,v_2,v_3=0} \sum_{l}^{v_2} g_{vl} g_{NS} \sum_{N} \left[2(N+l)+1\right] \cdot e^{-\frac{hcE(v,J)}{kT}} \qquad \text{(A-5-39)}$$

where $v_1$, $v_2$ and $v_3$ are quantum numbers of three fundamental vibrational modes (please refer to ROTHMAN and YOUNG, 1981 for notation details); $l$ and $N$ are angular momentum quantum numbers; $l$ can take values of $v_2$, $v_2$-2, $v_2$-4,…,1 or 0 and $N$ can take any non-negative integer; the sum of vector $\vec{l}$ and $\vec{N}$ is the total angular momentum vector $\vec{J}$, i.e., $\vec{J} = \vec{N} + \vec{l}$, therefore total angular momentum quantum number $J$ can take possible values of $(N + l)$, $(N + l - 1)$, ⋯, $|N - l|$. Here the maximum of $J$ (i.e., $J = N + l$) is chosen, which can take values of $J$, $(J - 1)$, $(J - 2)$, ⋯, $-J$, contributing to $2J + 1$ degeneracy; $g_{NS}$ is statistical weight caused by nuclear spin, and generally composed of two parts: (1)

nuclear spin degeneracy factor for unpaired nuclei: this factor is $(2I_1+1)(2I_2+1)(2I_3+1)$ and the same for all levels of a molecule (where $I_i$ denotes the nuclear spin number of

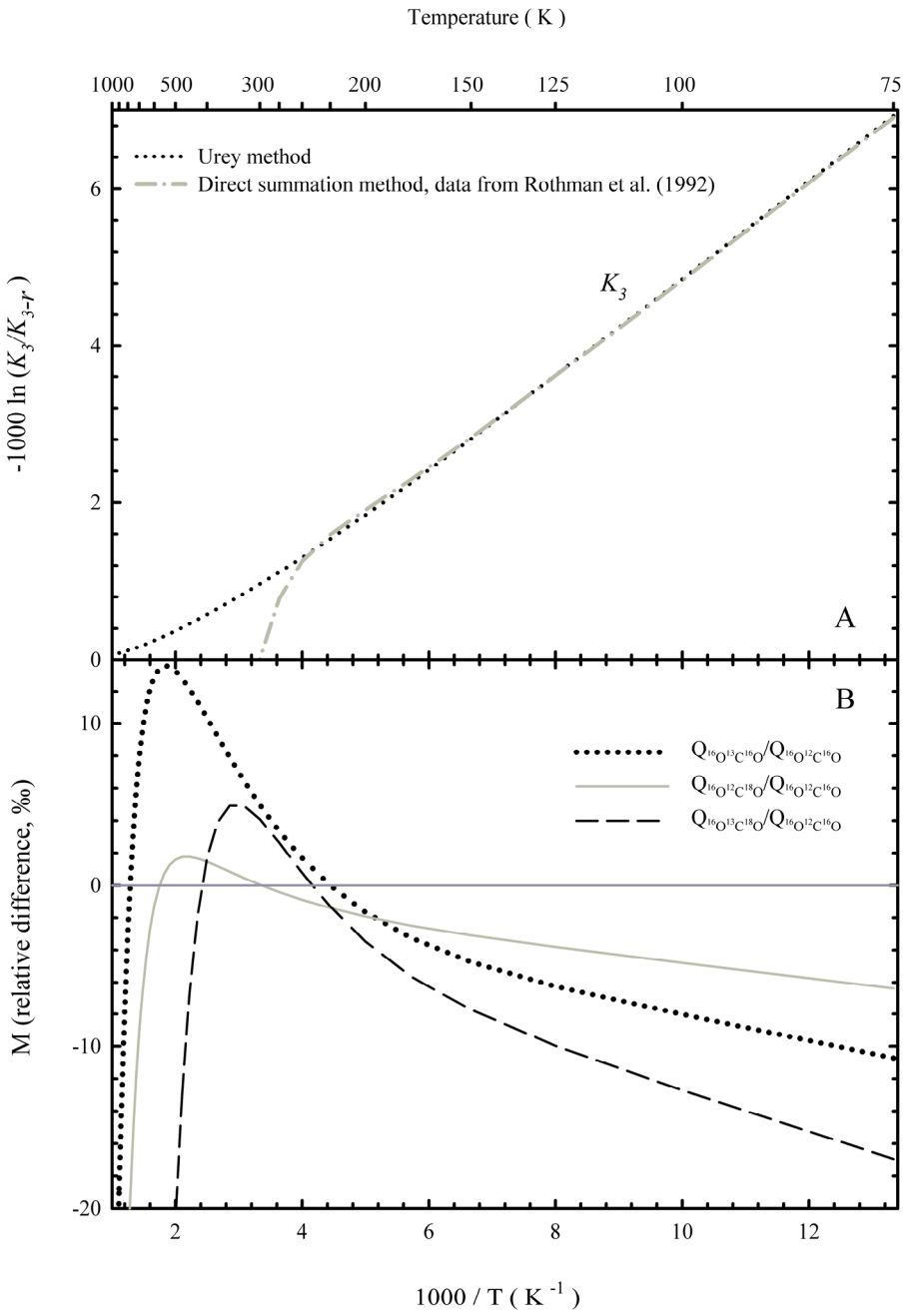


Figure A2. A: Comparison of $-1000\cdot\ln(K_3/K_{3\text{-}r})$ in eqn 5-8iii calculated using Urey method with using direct summation method as a function of 1000/T; B: Relative difference $M_i$ (defined in equation A-5-5) between partition function ratios calculated using Urey method and using direct summation method as a function of 1000/T.

atom *i*), and therefore, will be cancelled out during the calculation of equilibrium constants (we ignored this part during our calculation of partition function); (2) nuclear spin degeneracy factor for coupling of equivalent nuclear pairs with rotational wavefunctions; This factor may differ between alternate rotational levels of one isotopologue, and therefore, is included in our calculation of partition function (HERZBERG, 1945, GAMACHE et al., 1990). Since our consideration excludes $^{17}OC^{17}O$ isotopologues due to the lack of spectroscopic data of them, $g_{NS}$ is 1 or 0 depending on the symmetric or anti-symmetric rotational energy levels, i.e., when two oxygen atoms are the same isotopes (point group $D_{\infty h}$), $g_{NS} = 1$ for symmetric rotational states ($N$ is even integer, e.g. 0,2,4, ···) and $g_{NS} = 0$ for antisymmetric rotational states ($N$ is odd integer, e.g. 1,3,5, ···). Otherwise, when two oxygen atoms are different isotopes (point group $C_{\infty v}$), $g_{NS} = 1$ for both symmetric and antisymmetric rotational state. $g_{vl}$ is a statistical weight factor due to internal rotation, $g_{vl} = 1$ when $l = 0$ and $g_{vl} = 2$ when $l > 0$.

Results of these calculations are shown in Figure A2-A for temperatures from 75 to 1000 K. Deviation in $-1000 \cdot \ln K_3$ from that calculated using the 'Urey' method (eqns. 5-11 through 5-13) are small (< 0.1 per mil) below 260 K, but significant at higher temperatures. We suspect this reflects the absence of spectroscopic data for high-energy quantum states for $^{16}O^{13}C^{18}O$, and we conclude that the approximations associated with the Urey model are sufficiently accurate for our purposes.

Comparison also has been made for partition function ratios between calculations using these two methods. We use eqn A-5-38 and 5-18 to calculate partition function of each isotopologue of $^{16}O^{12}C^{16}O$, $^{16}O^{13}C^{16}O$, $^{16}O^{12}C^{18}O$ and $^{16}O^{13}C^{18}O$. To calculate the right partition function ratio, we have to multiply eqn 5-12 by a factor of

$\prod_i^n m_i^{\frac{3}{2}}$ according to Teller-Redlich product rule (refer to DAVIDSON, 1962), where $m_i$ is the mass of atom $i$ of n atoms that form the molecule, i.e.,

$$\left(\frac{Q_{^{16}O^{13}C^{16}O}}{Q_{^{16}O^{12}C^{16}O}}\right)=\left(\frac{m_{^{13}C}}{m_{^{12}C}}\right)^{\frac{3}{2}}\frac{\sigma_{^{16}O^{12}C^{16}O}}{\sigma_{^{16}O^{13}C^{16}O}}\prod_{i=1}^{3n-5}\frac{u_i^{^{16}O^{13}C^{16}O}}{u_i^{^{16}O^{12}C^{16}O}}\frac{e^{-\frac{u_i^{^{16}O^{13}C^{16}O}}{2}}}{1-e^{-u_i^{^{16}O^{13}C^{16}O}}}\frac{1-e^{-u_i^{^{16}O^{12}C^{16}O}}}{e^{-\frac{u_i^{^{16}O^{12}C^{16}O}}{2}}} \quad \text{(A-5-40)}$$

We omit this factor in eqn 5-12 because this factor will be eventually cancelled out during the calculation of equilibrium constants. We define M as the relative difference in per mil between partition function ratios calculated using direct summation method and Urey's method as:

$$M_i=\left(\frac{\left(Q_i/Q_{^{16}O^{12}C^{16}O}\right)_{Numerical}}{\left(Q_i/Q_{^{16}O^{12}C^{16}O}\right)_{Urey}}-1\right)\times 1000 \quad \text{(A-5-41)}$$

where $i$ = $^{16}O^{13}C^{16}O$, $^{16}O^{12}C^{18}O$ and $^{16}O^{13}C^{18}O$. Figure A2-B shows the difference between these two model changes with temperature. To the first order, there are up to 20 per mil difference between these two methods at temperatures lower than 500 K, and the deviation in $-1000\cdot\ln K_3$ between two models can be approximated into $M_{^{16}O^{13}C^{18}O}-M_{^{16}O^{13}C^{16}O}-M_{^{16}O^{12}C^{18}O}$ within 0.1 per mil. As we can see in Figure A2-B, even though individual $M_i$ is up to -19 per mil at temperature lower than 250 K, the deviation in $-1000\cdot\ln K_3$ is smaller than 0.1 per mil. This difference seems to be qualitatively correlative to number of vibrational levels used in the direct summation calculation. At temperature higher than 300 K, $Q_{^{16}O^{13}C^{18}O}$ began to show increasingly higher deviation with increasing temperature from Urey method. This is caused by greater contribution from higher vibrational energy levels of $^{16}O^{13}C^{18}O$ whose information is not available to

us yet. The lack of several vibrational energy levels from 2000 $cm^{-1}$ to 3000 $cm^{-1}$ (e.g., 11102e,f and 03301e,f; notations follow ROTHMAN and YOUNG, 1981 and ROTHMAN et al., 1992) during the calculation will especially reduce the value of $\frac{Q_{^{16}O^{13}C^{18}O}}{Q_{^{16}O^{12}C^{16}O}}$ even at low temperatures (< 300 K), and therefore, lower down the value of $-1000 \cdot \ln K_3$. Hence, we believe that the deviation of $-1000 \cdot \ln K_3$ calculated using direct summation method from the calculation results of the Urey method shown in Figure A2-A is due to the insufficiency in vibrational energy levels known for isotopologue $^{16}O^{13}C^{18}O$, rather than due to the calculation method, and we conclude that the approximations associated with the Urey model are sufficiently accurate for our purposes.

Table A1. Comparison of calculated $\Delta_i$ for CO molecule at select temperature using three methods (plase refer to text for details)

| Temperature | Harmonic approximation | | | | | Anharmonic approximation | | | | |
|---|---|---|---|---|---|---|---|---|---|---|
| (K) | $^{13}C^{16}O$ | $^{12}C^{17}O$ | $^{12}C^{18}O$ | $^{13}C^{17}O$ | $^{13}C^{18}O$ | $^{13}C^{16}O$ | $^{12}C^{17}O$ | $^{12}C^{18}O$ | $^{13}C^{17}O$ | $^{13}C^{18}O$ |
| 100 | -0.0172 | -0.0444 | -0.0853 | 3.9421 | 7.5867 | -0.0172 | -0.0444 | -0.0853 | 3.9392 | 7.5812 |
| 150 | -0.0106 | -0.0274 | -0.0525 | 2.4292 | 4.6691 | -0.0106 | -0.0274 | -0.0525 | 2.4268 | 4.6646 |
| 200 | -0.0073 | -0.0189 | -0.0362 | 1.6735 | 3.2134 | -0.0073 | -0.0188 | -0.0361 | 1.6714 | 3.2094 |
| 250 | -0.0053 | -0.0138 | -0.0263 | 1.2206 | 2.3415 | -0.0053 | -0.0137 | -0.0263 | 1.2187 | 2.3378 |
| 300 | -0.0040 | -0.0104 | -0.0198 | 0.9197 | 1.7623 | -0.0040 | -0.0103 | -0.0198 | 0.9179 | 1.7589 |
| 400 | -0.0024 | -0.0062 | -0.0118 | 0.5503 | 1.0523 | -0.0024 | -0.0062 | -0.0118 | 0.5487 | 1.0491 |
| 500 | -0.0015 | -0.0039 | -0.0074 | 0.3429 | 0.6544 | -0.0015 | -0.0038 | -0.0073 | 0.3415 | 0.6516 |
| 600 | -0.0009 | -0.0025 | -0.0047 | 0.2202 | 0.4194 | -0.0009 | -0.0025 | -0.0047 | 0.2190 | 0.4171 |
| 700 | -0.0006 | -0.0016 | -0.0031 | 0.1453 | 0.2763 | -0.0006 | -0.0016 | -0.0031 | 0.1444 | 0.2746 |
| 800 | -0.0004 | -0.0011 | -0.0021 | 0.0985 | 0.1870 | -0.0004 | -0.0011 | -0.0021 | 0.0978 | 0.1859 |
| 900 | -0.0003 | -0.0008 | -0.0015 | 0.0684 | 0.1299 | -0.0003 | -0.0008 | -0.0015 | 0.0681 | 0.1293 |
| 1000 | -0.0002 | -0.0005 | -0.0010 | 0.0487 | 0.0924 | -0.0002 | -0.0005 | -0.0010 | 0.0487 | 0.0924 |

Table A1. (Continued)

| Temperature | 5 parameter Dunham equation | | | | | HITRAN data calculation | | | | |
|---|---|---|---|---|---|---|---|---|---|---|
| (K) | $^{13}C^{16}O$ | $^{12}C^{17}O$ | $^{12}C^{18}O$ | $^{13}C^{17}O$ | $^{13}C^{18}O$ | $^{13}C^{16}O$ | $^{12}C^{17}O$ | $^{12}C^{18}O$ | $^{13}C^{17}O$ | $^{13}C^{18}O$ |
| 100 | -0.0172 | -0.0444 | -0.0853 | 3.9413 | 7.5852 | -0.0172 | -0.0444 | -0.0853 | 3.9412 | 7.5823 |
| 150 | -0.0106 | -0.0274 | -0.0525 | 2.4287 | 4.6682 | -0.0106 | -0.0274 | -0.0525 | 2.4281 | 4.6654 |
| 200 | -0.0073 | -0.0189 | -0.0361 | 1.6733 | 3.2131 | -0.0073 | -0.0189 | -0.0361 | 1.6724 | 3.2100 |
| 250 | -0.0053 | -0.0138 | -0.0263 | 1.2207 | 2.3417 | -0.0053 | -0.0137 | -0.0263 | 1.2195 | 2.3383 |
| 300 | -0.0040 | -0.0104 | -0.0198 | 0.9202 | 1.7633 | -0.0040 | -0.0104 | -0.0198 | 0.9186 | 1.7595 |
| 400 | -0.0024 | -0.0062 | -0.0119 | 0.5518 | 1.0552 | -0.0024 | -0.0062 | -0.0118 | 0.5496 | 1.0504 |
| 500 | -0.0015 | -0.0039 | -0.0074 | 0.3456 | 0.6596 | -0.0015 | -0.0039 | -0.0074 | 0.3428 | 0.6537 |
| 600 | -0.0010 | -0.0025 | -0.0048 | 0.2238 | 0.4266 | -0.0010 | -0.0025 | -0.0047 | 0.2203 | 0.4196 |
| 700 | -0.0006 | -0.0017 | -0.0032 | 0.1499 | 0.2853 | -0.0006 | -0.0016 | -0.0031 | 0.1443 | 0.2763 |
| 800 | -0.0004 | -0.0012 | -0.0022 | 0.1037 | 0.1974 | -0.0004 | -0.0010 | -0.0021 | 0.0911 | 0.1834 |
| 900 | -0.0003 | -0.0008 | -0.0016 | 0.0743 | 0.1414 | -0.0003 | -0.0005 | -0.0013 | 0.0421 | 0.1142 |
| 1000 | -0.0002 | -0.0006 | -0.0012 | 0.0552 | 0.1050 | -0.0001 | 0.0002 | -0.0005 | -0.0208 | 0.0483 |
| | 43 Dunham parameters | | | | | | | | | |
| 100 | -0.0172 | -0.0444 | -0.0853 | 3.9412 | 7.5849 | | | | | |
| 150 | -0.0106 | -0.0274 | -0.0525 | 2.4281 | 4.6670 | | | | | |
| 200 | -0.0073 | -0.0189 | -0.0361 | 1.6724 | 3.2113 | | | | | |
| 250 | -0.0053 | -0.0137 | -0.0263 | 1.2195 | 2.3393 | | | | | |
| 300 | -0.0040 | -0.0104 | -0.0198 | 0.9186 | 1.7603 | | | | | |
| 400 | -0.0024 | -0.0062 | -0.0118 | 0.5496 | 1.0510 | | | | | |
| 500 | -0.0015 | -0.0039 | -0.0074 | 0.3428 | 0.6542 | | | | | |
| 600 | -0.0010 | -0.0025 | -0.0047 | 0.2205 | 0.4201 | | | | | |
| 700 | -0.0006 | -0.0016 | -0.0031 | 0.1459 | 0.2776 | | | | | |
| 800 | -0.0004 | -0.0011 | -0.0021 | 0.0992 | 0.1886 | | | | | |
| 900 | -0.0003 | -0.0008 | -0.0015 | 0.0693 | 0.1315 | | | | | |
| 1000 | -0.0002 | -0.0006 | -0.0011 | 0.0495 | 0.0939 | | | | | |